Modélisation électrique de laser semi-conducteurs pour les communications à haut débit de données

Wosen Eshetu Kassa

UNIVERSITÉ PARIS-EST

THÈSE DE DOCTORAT

Spécialité : ÉLECTRONIQUE, OPTRONIQUE ET SYSTEMES

Wosen Eshetu KASSA

ECOLE DOCTORALE MSTIC

MATHEMATIQUES ET SCIENCES ET TECHNOLOGIES DE L'INFORMATION ET DE LA COMMUNICATION

Electrical modeling of semiconductor laser for high data rate wireless communication

Laboratoire ESYCOM et au Conservatoire national des arts et métiers (le Cnam)

12 Mai 2015

Jury:

Rapporteurs :

Olivier Llopis, Directeur de recherche CNRS, LAAS
Philippe Gallion, Professeur, Télécom Paris

Examinateurs :

Benoit Charbonnier, Ingénieur de recherche, CEA-LETI
Frédéric Van Dijk, Ingénieur de recherche, III-V Lab.
Daniel Bourreau, Maître de conférences, Télécom Bretagne

Directrice de thèse : Catherine Algani, Professeur des universités, le Cnam

Co-encadrants : Anne-Laure Billabert, Maître de conférences HDR, le Cnam
Salim Faci, Maître de conférences, le Cnam

To my parents

“There is no greatness where there is not simplicity, goodness, and truth.” ― Leo Tolstoy

ACKNOWLEDGMENT

I would like to express my utmost gratitude to my PhD director Prof. Catherine Algani, and supervisors Dr. Anne-Laure Billabert and Dr. Salim Faci. Their invaluable assistance, support, guidance, kindness and constant encouragement helped me to develop as a researcher.

My sincere gratitude to Dr. Olivier Llopis, Prof. Philippe Gallion, Dr. Benoit Charbonnier, Dr. Frédéric Van Dijk, Dr. Daniel Bourreau for accepting to be the jury members of my PhD dissertation. Special thanks to the reviewers: Dr. Olivier Llopis, and Prof. Philippe Gallion for their thoughtful suggestions and comments on the manuscript. I also want to thank Dr. Frédéric Van Dijk and Dr. Mickael Faugeron for their collaboration with ESYCOM team for phase noise measurement at III-V lab.

I would like to thank all of my colleagues at ESYCOM laboratory and all who contributed to creating a friendly working atmosphere.

Last but not least, I wish to express my love and gratitude to my family who always believed in me.

Abbreviations

1G	First Generation
2G	Second Generation
3G	Third Generation
4G	Fourth Generation
5G	Fifth Generation
AC	Alternating Current
ADS	Agilent Design System
ADC	Analog To Digital Converters
AM	Amplitude Modulation
APD	Avalanche Photodiode
ASK	Amplitude Shift Keying
BBoF	Baseband Over Fiber
BS	Base Station
BER	Bit-Error-Rate
BPSK	Binary Phase Shift Keying
CAD	Computer-Aided-Design
CCCS	Current Controlled Current Source
CNR	Carrier Noise Ratio
CO	Central Office
CW	Continuous Wave
cm-wave	Centimeter-Wave
CPE	Common Phase Error
DAA	Detect And Avoid
DAC	Digital To Analog Converter
DAS	Distributed Antenna System
dB	Decibels
dBc	Decibels Relative To Carrier
dBm	Decibels Milliwatt
DBR	Distributed Bragg Reflector
DC	Direct Current
DCF	Dispersion Compensation Fiber
DFB	Distributed Feedback
DH	Double Heterostructure
DM	Direct Modulation
DR	Dynamic Range
DSB	Double Side Band
DSF	Dispersion Shift Fiber
EAM	Electro-Absorption Modulator

EEL	Edge Emitting Lasers
E/O	Electro-Optical
EM	External Modulation
EOM	Electro-Optic Modulator
EVM	Error Vector Magnitude
FBG	Fibre Bragg Grating
FCC	Federal Communications Commission
FEC	Forward Error Correction
FM	Frequency Modulation
FM-IM	Frequency Modulation – Intensity Modulation
FFT	Fast Fourier Transform
FTTH	Fibre To The Home
FP	Fabry-Perot
FSR	Free Spectral Range
Gbps	Gigabit Per Second
GHz	Gigahertz
GPRS	General Packet Radio Service
GSM	Global System For Mobile Communications
HAN	Home Area Network
HB	Harmonic Balance
HDMI	High Definition Multimedia Interface
HDTV	High-Definition Tv
WPAN	Wireless Personal Area Network
IEEE	Institute Of Electrical And Electronics Engineers
ICI	Inter-Carrier Interference
IF	Intermediate Frequency
IFoF	Intermediate Frequency Over Fiber
IIP3	Input Third Order Intercept Point
IM	Intensity Modulation
IM-DD	Intensity Modulation – Direct Detection
IMT	International Mobile Telecommunications
IP3	Third Order Intercept
ISI	Inter-Symbol Interference
Kpbs	Kilobit-Per-Second
LAN	Local Area Network
Laser	Stimulated Emission Of Radiations
LED	Light Emitting Diode
LDC	Low Duty Cycle
L-I	Light-Current
LO	Local Oscillator

LTE	Long Term Evolution
mA	Milli-Ampere
MAC	Medium Access Control
MAN	Metropolitan Area Network
Mbps	Megabit-Per-Second
MB-OFDM	Multiband Orthogonal Frequency Division Multiplexing
MHz	Mega-Hertz
MIMO	Multiple Input Multiple Output
MMF	Multimode Fibre
MLE	Maximum Likelihood Estimation
MQW	Multiple Quantum-Well
MZM	Mach-Zehnder Modulator
mm-wave	Millimeter-Wave
NF	Noise Figure
O/E	Opto-Electrical
OFDM	Orthogonal Frequency Division Multiplexing
O/O	Optical-To-Optical
OIP3	Output Third Order Intercept Point
OPLL	Optical Phase-Locked Loop
OIL	Optical Injection Locking
OLT	Optical Line Terminal
ONU	Optical Network Unit
PAN	Personal Area Networks
PAPR	Peak-To-Average
PD	Photodetector
PHY	Physical Layer
PIN	P-Type-Intrinsic-N-Type
PM-AM	Phase Modulation – Amplitude Modulation
POF	Plastic Optical Fiber
PON	Passive Optical Network
PRBS	Pseudo Random Binary Sequence
PSD	Power Spectral Density
PSK	Phase Shift Keying
QAM	Quadrature Amplitude Modulation
QPSK	Quadrature Phase Shift Keying
QW	Quantum Well
RF	Radio Frequency
RFoF	Radio Frequency Over Fiber
RoF	Radio Over Fiber
RIN	Relative Intensity Noise

SC	Single Carrier
SCH-QW	Separate Confinement Heterostructure - Quantum Well Lasers
SDD	Symbolically Defined Device
SFDR	Spurious Free Dynamic Range
SMF	Single Mode Fibre
SNR	Signal To Noise Ratio
SSB	Single Side Band
TDM-PON	Time Division Passive Optical Networks
TFC	Time Frequency Code
THz	Tera-Hertz
TIA	Trans-Impedance Amplifier
UMTS	Universal Mobile Telecommunication System
UTC	Uni-Travelling Carrier
UWB	Ultra-Wideband
VCSEL	Vertical Cavity Surface Emitting Laser Diode
WCDMA	Wideband Code Division Multiple Access
WDM	Wavelength Division Multiplexing
WDM-PON	Wavelength Division Multiplexing-Passive Optical Network
WLAN	Wireless Local Area Network
Wi-Fi	Wireless Fidelity
WiMax	Worldwide Interoperability For Microwave Access
xQAM	X-Quadrature Amplitude Modulation
xDSL	X-Digital Subscriber Line
YAG	Yttrium Aluminum Garnet

Table of Content

Abstract

The advancement of digital optical communication in the long-haul and access networks has triggered emerging technologies in the microwave/millimeter-wave domain. The performance of these hybrid systems is highly influenced not only by the optical link impairments but also electrical circuit effects. The optical and electrical effects can be well studied at the same time using computer aided tools by developing equivalent circuit models of the photonic link components namely semiconductor lasers, modulators, photodetectors and optical fiber.

In this thesis, circuit representations of the photonic link components are developed so that different complex systems can be analyzed in an efficient manner. Since the optical light source is the main limiting factor of the optical link, particular attention is given to modeling the most important characteristics of single mode semiconductor lasers such as static response and dynamic response, intensity noise and phase noise properties. The conventional large signal laser equivalent circuit model which represents the envelope of the optical signal is modified to include the laser phase noise properties. This modification is particularly necessary to study systems like optical remote heterodyne detection where the optical phase noise is important. Measurement results of the laser characteristics are compared with simulation results in order to validate the equivalent circuit model under different conditions. It is shown that the equivalent circuit model can precisely predict the component behaviors for system level simulations.

To demonstrate the capability of the equivalent circuit model of the photonic link to analyze microwave/millimeter-wave systems, the new circuit model of the laser along with the behavioral models of other components are used to characterize two different radio-over-fiber (RoF) links: intensity modulation – direct detection (IM-DD) and optical heterodyne RoF systems. Wireless signal with specifications complying with IEEE 802.15.3c standard for the millimeter-wave frequency band is transmitted over the RoF links and the system performance is analyzed based on EVM evaluation. This study shows that effective analysis of microwave/millimeter-wave photonics systems is achieved by using circuit models which allows us to take into account both electrical and optical behaviors at the same time.

1

Introduction

By far the most successful application of wireless communication has been the cellular telephone system. According to the recent trends in information and communication technologies (ICT), the ubiquitous availability of mobile-telephone services is close to 100 percent of the world population, almost all of the population covered by the mobile signal. The global ICT development chart is shown in Fig. 1.1 [1]. While growth in mobile-cellular penetration is flattening, reaching 95.5% by the end of 2014, mobile broadband continues to grow strongly, on average by around 40% annually between 2010 and 2014. On the other hand, fixed-broadband uptake is growing steadily: at around 10% compound annual growth rate. This shows there is a strong growth in mobile internet uptake. In the view of the steep growth of the broadband and the widespread deployment of mobile infrastructure, there is a high expectation that the mobile-broadband services will become equally as available as mobile-cellular telephony in the near future. Additionally, growth in household access to the internet has also accelerated over the past four years.

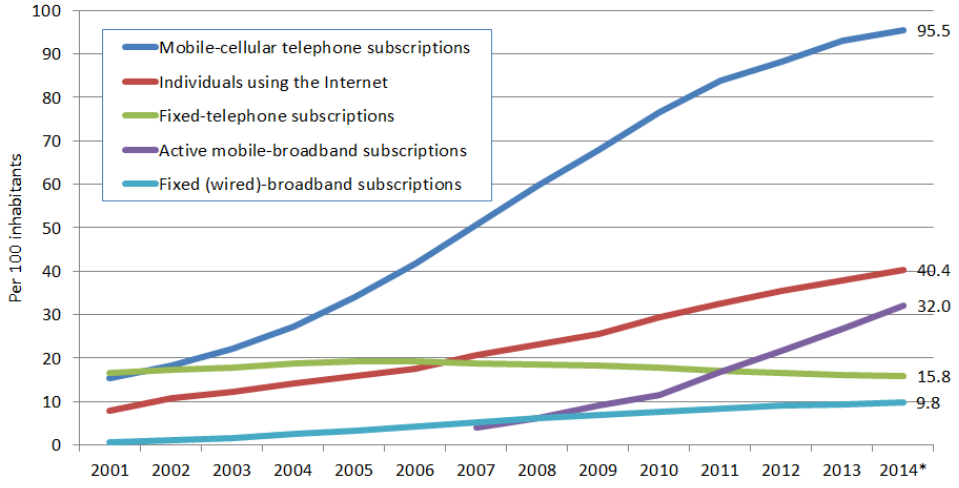

Fig. 1.1. Global ICT developments.

Not only is the mobile telephone communications growing, Wireless Local Area Networks (WLANs), which came on the scene in 1997 [2], have also experienced phenomenal growth. WLANs have now made their way into homes, riding on the back of xDSL and cable access modems, which are integrated with WLAN Radio Access Points (RAPs). Because of the fact that Wi-Fi is becoming a complement to 3G and 4G services and is a mainstay of the majority of devices, there has been tremendous growth in the number of Wi-Fi connectivities in recent times. In 2013 it was anticipated that the number of Wi-Fi connections would surpass 6.3 million compared to 4.9 million in 2012 [3].

Currently available broadband wireless services and standards such as Wi-Fi, GSM, and UMTS are concentrated in the lower microwave band. Even the new wireless standards such as long term evolution (LTE+) and worldwide interoperability for microwave access (WiMax) still operate in the lower microwave regions (2–5GHz). This places a heavy burden on the already congested wireless spectrum in the microwave region. This is the fundamental driver that has led to new wireless technologies which can exploit the large unused bandwidths of millimeter-wave frequency regions for the provision of future broadband wireless services particularly in the unlicensed millimeter-wave band (57–64 GHz). The deployment of broadband access network which allows the delivery of service more than 1Gbit/s also contributed for the release of new radio standards delivering data of multi-Gbit/s. The radio coverage at this frequency is limited to very small area, single room which allows frequency reusability without interference. This rapid growth of wireless communication is driven by the ease of installation and technological maturity. The possibility of developing fabricating reliable digital and RF circuits using miniaturization technologies allows producing smaller portable wireless devices [4]. For instance small size antenna in the 60GHz band allows advanced integration of radio terminal such as cellphones, and laptops.

Emerging standards for high data rate communication cannot be supported by traditional transmission systems such as free space and coaxial cable transmission lines, because electrical transmission of high frequency radio signal over those media is not feasible. In free space, the losses due to atmospheric oxygen and reflections increase with the radio frequency. In traditional co-axial cable transmission, the losses increase with frequency which makes long distance transmission using these methods impossible without using regenerating equipments. Optical links have been appeared to be the best alternative to transmit radio signals with much better performance and installation cost compared to the other methods [4] [5]. The method to transmit radio signals over an optical link is usually referred as radio over fiber (RoF) system (Fig. 1.2).

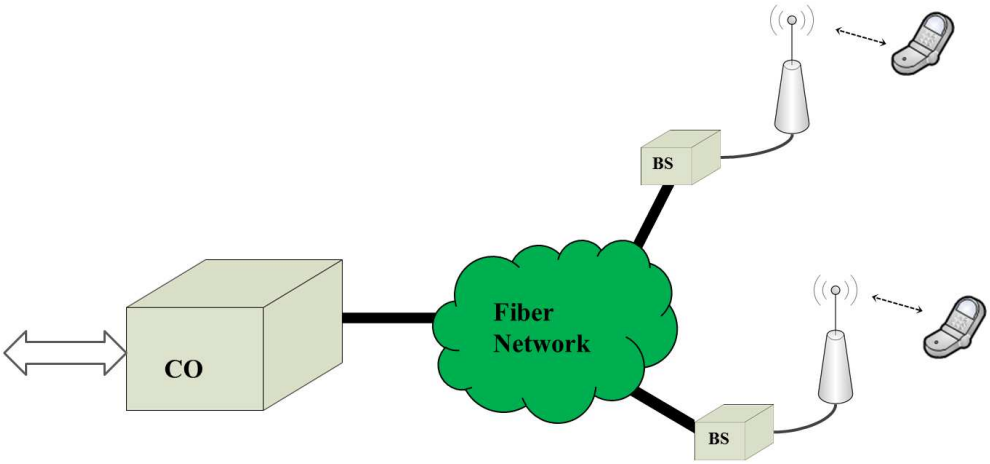

Fig. 1.2. Typical RoF architecture in the access network.

Fig. 1.2 shows typical RoF system integrated with the existing fiber infrastructures. At the heart of this hybrid optical-wireless system is fiber optic communication which serves as a back bone for the broadband interconnection between the central office (CO) and the antenna, base station (BS). The hybrid network incorporating WDM technology for fixed wireless access operating in the millimeter-wave band is being actively pursued to provide untethered connectivity for ultrahigh bandwidth communications. The architecture of such radio networks requires a large number of antenna base-stations with high throughput to be deployed to maximize the geographical coverage with the main switching and routing functionalities located in a centralized location. Therefore, the complexity of the antenna at the BS must be reduced while providing high throughput.

Although the optical-wireless integration is able to simplify the backhaul infrastructure and offers significant benefits to future service providers, the implementation of the hybrid fiber-wireless network is not straightforward because of issues regarding high frequency wireless signal transmission signal impairments, spectrum allocation, performance optimization and integration with existing infrastructure have to be considered. One of the major technical challenges in implementing such networks lies in the mitigation of these various optical impairments that the wireless signals experience while being transmitted over the optical link in the hybrid network.

The other issue that is being actively investigated in many research centers is the use of fiber links for short range communications in the home area network (HAN). To cope up with the support new standards in the millimeter-wave band that have the capacity of multi-Gbit/s transmission, optical fiber communication provides untethered connectivity. Fibers at home would be the natural extension of the transparent FTTH network and an ideal to support the current and upcoming standards for years to come.

* * *

Since the development of low-loss optical fiber in the late 1960s, different light generation and detection methods have been developed making optical communication mature technology every passing year. The idea of using optical links for microwave/RF communication is to take advantage of all the benefits of fiber optics. Through time, analog optical links have incorporated different techniques to improve the performance of the optical link for RF signal transmission.

The design of an optical link for radio frequency transmission is impossible without the proper choice of different opto-electrical (O/E) and electro-optical (E/O) components to meet system requirements. The fundamental elements of an optical link are devices that offer signal modulation, or control, and detection as depicted in Fig. 1.3. In general, the radio over fiber link could consist of passive optical components and active optoelectronic devices such as semiconductor lasers, optical modulator, optical amplifier, optical fiber, photodetector. Semiconductor lasers are the most widely used optical light sources thanks to the possibility of being directly modulated by microwave frequencies. The modulation frequency is however limited by the relaxation resonance frequency of the device, which depends on a number of factors including photon lifetime, differential gain, carrier recombination time and optical output power. The achievement of high direct modulation bandwidths requires an optimization of both the internal structure of the semiconductor laser and the design of the laser package because electrical parasitic effect associated with the laser chip and package will also limit the frequency response. Another alternative to expand modulation bandwidth is to modulate the light externally using external optical modulators such as electro-optic modulators (EOM) and electro-absorption modulators (EAM). As for the fiber optic, there are different types of fibers that have different features and capabilities. The choice of the fiber type depends on the link distance because much of the fiber impairments depend on the length of the fiber. The optical detector is also another important component that needs careful choice based on the system requirement.

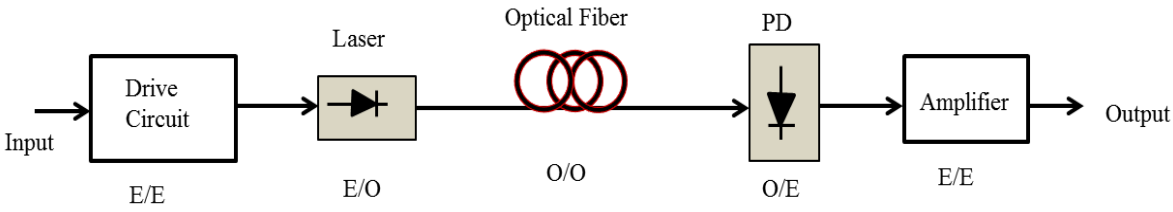

Fig. 1.3. Block diagram a RoF system.

The function of E/O and O/E is to act like a transducer which can convey a microwave signal from input to the output with little signal degradation, ideally like a transparent tube. However, the optical link puts some constraints on the system performance because of impairments from the RoF components such as laser intensity and phase noise, laser and modulator nonlinearities, fiber dispersion, fiber attenuation, saturation and noise effects from the photodetector. These are the most crucial parameters in determining signal degradation. This shows the importance of techniques to improve the link performance and of course to improve the design and fabrication of E/O and O/E components.

The microwave fiber-optic link design always begins with a definition of specifications for the link, and can be considered complete when the design meets those specifications. Based on these definitions, the system has to be verified and analyzed for different working circumstances. The design of such systems greatly benefits from computer-aided-design (CAD) tools that allow the optimization and verification of a particular system before its actual realization, thereby significantly reducing the design cycle and cost. The successful system design which meets system specifications depends on accurate modelling of optoelectronic devices. These models should be consistent with measured characteristics while predicting system performances under small-signal and large-signal conditions.

In the component level, there exist two types of models namely the physical model and circuit model. Although physical models of optoelectronic components are used for device development optimization and characterization, equivalent circuit models are widely used in circuit analysis and design procedures. One advantage of equivalent circuit model is that it can be applied by using a general purpose commercial circuit design software packages. The equivalent circuit model also facilitates the design of monolithic and integrated circuits because it allows the accurate simulation of a laser's terminal characteristics in a circuit-level simulation environment. Another advantage of the equivalent circuit modeling is that it is possible to make independent investigation of different parameters of the device and their interaction with other device parameters. The objective of this thesis lies on developing appropriate equivalent circuit model of single mode semiconductor lasers for different configurations of RoF systems.

The choice of design software is also an important issue to study system performance as to whether to use a software tool in the optical or electrical domain. The choice has to be made based on the type of system that is to be analyzed. Optical systems and networks can be successfully studied using optical domain commercial softwares supplied by companies like RSoft, Optiwave, VPIsystems etc. These softwares offer rate equation based laser models, fiber models (single and multi-mode) and photodetector models. However, to study radio over fiber systems where the RF property of the optical link is needed, it would be desirable to use electrical domain simulators so as to take advantage of the already mature tools in the domain and to consider the driver circuit, matching and parasitic circuit effects of the active devices. Since electrical domain commercial softwares do not have built-in optical and opto-electrical components, the problem with this choice is to represent RoF components in the electrical domain. For this purpose we need equivalent circuit models of devices such as semiconductor laser, photodetector and modulators to construct the RoF link in an electrical simulator where we can apply circuit analysis theory to evaluate system properties.

Some of the commercially available general purpose electrical domain CAD tools include Advanced Design Systems (ADS), MWOFFICE (AWR), APLAC (Helsinkji University). These tools have many capabilities such as fast algorithms for the steady-state solution in nonlinear operation, comprehensive libraries for active and passive components, circuit description through schematic, layout editing facilities, optimization and tunability. The extent to which these tools can be used for designing real analog optical systems depends on how precisely the equivalent circuit models of the device (laser or photodetector) represent the devices' properties. In this work, ADS from KEYSIGHT TECHNOLOGIES is chosen to

study RoF systems. This software provides full, standards-based design and verification options with wireless libraries and circuit system co-simulations in a single platform [6]. The RF circuit analysis simulation tools can be categorized as linear and nonlinear simulators. S-parameter and AC simulator are among the linear frequency domain simulators; while harmonic balance (HB), DC controller and circuit envelop (Env) simulation controllers are used to run nonlinear simulations. Harmonic balance and envelope simulators are essential tools to perform nonlinear analysis both in time domain and frequency domain. Besides, the noise simulation features based on mixing algorithms for intensity and phase makes these tools preferable. The Ptolemy co-simulation feature can also be used to perform simulation of digital signal transmission over analog circuits in the same platform. This helps us to examine the effects of optical links on the performance of the digital end-to-end communication. Generally speaking the circuit analysis and co-simulation features of ADS can be used to obtain realistic investigation of a RoF system.

In this thesis the equivalent circuit model of RoF components are developed with the aim of building a tool that can be used to analyze different types of RoF links for design and verification purposes. These tools could assist the definition of specifications for the link and selection of appropriate devices for generating, modulating and detecting the light, and selection of electronic circuits to modify the system performance. Even though circuit models of all RoF components are developed, focus is made on the equivalent circuit model of single mode semiconductor lasers from the rate equation and considering its parasitic and matching circuit.

The interest in modelling of laser diodes in many research centers is directly linked to the progress that has been made in the application of microwave and millimeter-wave photonic links. Since laser diodes exhibit both electronic and photonic behaviors, it is necessary to take both effects into account which increases the complexity in modeling the dynamic of laser diodes. Device models usually combine all the device's internal physical mechanisms. However, to incorporate physical properties of the laser diode into one model is time consuming and very complex if only specific property of the device is needed. Besides for implementation, device models need specialized CAD tools such as MINILASE, CLASID [7]. Therefore, simplified equivalent circuit models with considerably less computational burden are desired for the design and analysis of radio over fiber systems. Besides circuit-level laser models facilitate the design of monolithic and integrated optoelectronic circuits because it allows the accurate simulation of a laser's terminal characteristics in a standard circuit-level simulation environment.

There have been substantial works done in the literature to develop the circuit model of semiconductor lasers under small-signal and large-signal environments. The small-signal equivalent circuit model of laser was studied in [8] [9] [10] [11] based on rate-equation descriptions of a laser's behavior. For realistic representation of semiconductor lasers, the general rate equations in the large-signal condition should be considered. In fact the small-signal models can be derived from the large-signal models by imposing the small-signal approximation.

The large-signal equivalent circuit model of single mode semiconductor laser was first derived by Tucker [12]. In this equivalent circuit model, lumped circuit elements and current sources are used to represent the rate equation elements. It has been suggested that a complete equivalent circuit model of laser diodes should integrate both the intrinsic model and parasitic circuit models to evaluate the electrical and optical behaviors within the same simulator.

Considerable amount of work has been done in the literature on the laser equivalent circuit model and its implementation on circuit simulators [12] [13] [14] [15] [16] [17]. These models have particular importance to study analog optical links and to evaluate the limitations of the laser diode such as nonlinear distortion and noise figure. A major drawback of the circuit models in general has been the absence of laser phase representation which is particularly important for coherent and heterodyne RoF applications. Laser phase representation in the model also helps to investigate the interaction of phase noise and chirp with the fiber dispersion which could lead to zero transmission unless the system is designed carefully. In this work, we proposed a method to include the optical phase noise in the model [15] using a system simulation approach. This is a direct extension of previous works done at ESYCOM-CNAM laboratory which integrates the large-signal laser model with the noise model and parasitic circuits. The previous laser model [15] has been used to perform simulations of semiconductor laser diodes in the nonlinear regime were performed using ADS to investigate harmonic and intermodulation distortions in directly modulated laser radio over fiber systems [18] [19] [20].

Like the usual laser circuit models, the new laser model is represented by a network of two ports where the input represents the electrical contact between the laser and bias circuits and the output represents the optical output signal. But in the new model the output signal represents the optical '*field*' instead of optical power. This method allows simulation of phase noise effects on the system performance for microwave photonic systems. It is demonstrated that the phase model is effectively integrated with the large-signal and noise model of the laser. The new laser model can therefore estimate the intensity noise, phase noise, nonlinear distortion and other characteristics of the laser diode under small-signal and large-signal conditions. The laser can work well for more complex systems such as optical phase locked loops. The model is validated by performing comparison between simulation results of the equivalent circuit model and measurement results. A distributed-feedback (DFB) laser made in III_V lab [21] is characterized and a very good agreement between simulation and measurement of laser characteristics is achieved confirming the precision of the model to accurately represent the laser for system simulation purposes.

The thesis is organized as follows:

In **Chapter 2** background studies of radio over fiber systems and wireless communication systems is given from the general application point of view. The convergence of wireless communication systems towards Gigabit transmission in the millimeter-wave band is discussed. The principles of radio over fiber and its properties are introduced. This chapter also includes techniques to generate high frequency radio signals for applications in the 60 GHz spectrum.

Chapter 3 is dedicated to the analysis and circuit modeling of RoF components: single mode semiconductor laser, photodiodes, fiber and modulators. Great deal of attention is given to the properties and modeling techniques of single mode semiconductor lasers. After theoretical analysis of static response, noise and modulation characteristics are given based on rate equation analysis, the development of the equivalent circuit modeling of the laser for microwave applications is studied thoroughly. The inclusion of phase noise to the large-signal model which is of particular importance for thesis is shown in details. Besides the complete laser model is validated by comparing measurements and simulation results.

In **Chapter 4**, the RF properties of the RoF link are studied. Simulation results of IM-DD links and heterodyne links are given to compare their performance in terms of noise figure and gain performance indicators. It is shown that the laser phase noise is a major problem for optical heterodyne systems. Optical phase locked loop is integrated to the system to generate high purity RF signal.

Finally **Chapter 5** deals with the performance analysis of RoF system when a wireless signal complying with IEEE standards in 60GHz band is transmitted over the optical links. The performance of DM and EM IM-DD and optical heterodyne RoF links are analyzed using EVM simulation to investigate their performances at different emission levels.

2

Background Studies on Radio over Fiber Technologies

2.1. Introduction

Radio networks provide users with attractive feature of untethered connectivity for a range of applications including cellular communication, WLANs, personal area networks (PANs), and broadband fixed wireless access. The revolution of smart devices and the increasing demand for broadband services has also led to the consideration of wireless networks operating at higher frequencies and extending well into the millimeter-wave band where the total capacity of an antenna at the BS can approach 7 Gbit/s [4] [22]. The application of optical fiber links in radio communication networks for the generation, transport and distribution of radio signals is becoming a reality as service provider worldwide have already deployed optical infrastructure for radio transmission. Some of the applications that use analog optical links include indoor distributed antenna systems offering mobile radio services, current and next generation microcellular mobile networks, indoor wireless local area networks and fixed broadband radio access which can provide very high bandwidth services to users [23]. Radio over fiber technology is also finding several other applications such as in radar systems in order to provide high quality RF distribution. Analog optical systems are preferable in radar systems where the weight of the system is one of the important concerns [24].

The theory covered in this chapter is essential for the discussion in the coming chapters. Various international standards of wireless communication are revised in the context of their potential future wireless and optical links for RoF application is given with the basics of conventional (centimeter-wave) and 60GHz wireless communications. The second section is devoted to fundamentals of radio over fiber technologies, their advantages and disadvantages over traditional communication systems. Finally, brief discussion of two types of RoF systems is given.

2.2. Wireless communication systems

The rapid growth of wireless communications is mainly attributed to their ease of installation in comparison to fixed networks. However, technological advancement, and competition among mobile operators have also contributed to the growth [22]. So far there have been four mobile telephone standards, launched in succession approximately every decade. The first-generation (1G) mobile systems were analog, and were commissioned in the 1980s. In the 1990s, second-generation (2G) digital mobile systems such as the Global System for Mobile communications (GSM) came on the scene. The GSM standard has been extremely successful internationally and it is currently the mainstream mobile communication system working in radio spectrum around 900, and 1800 MHz. Despite the few kbps data rate supported by GSM, the first and second generations of mobile telephones were intended for voice transmission and support circuit-switched services. The third generation of wireless cellular phone such as universal mobile telecommunication system (UMTS) provides both voice and data applications [25]. This allows people to make phone calls, send text and multimedia messages, and browse the internet. The fourth generation (4G) offers higher data speeds and more mobility such as advanced LTE+ and WiMax.

The 4G system provides a comprehensive and secure all IP based mobile broadband to smartphones, laptop computer and other mobile devices. The use of multiple input multiple output (MIMO) technology improves communication performance and increases the potential throughput by using additional antennas at both the transmitter and receiver end. The requirement speed of 4G services by international mobile telecommunication advanced (IMT-advanced) standard is targeted to reach a peak download at 100 Mbit/s for high mobility communication in a moving vehicle and 1 Gbit/s for low mobility communication (such as pedestrians and stationary users) [26].

The 5G systems on the other hand are not officially launched but expected to provide all the major features offered by the 4G mobile technology and IMT-advanced system. 5G mobile system is all-IP based model for wireless and mobile networks interoperability. They are expected to remove the limitations of network access range and uses multi user multiple input and multiple (MIMO) output techniques for cost and energy efficiency [27]. There is an increasing trend of hybrid systems where radio signals can be transported by fiber technologies on the existing fiber infrastructure to support future generation networks.

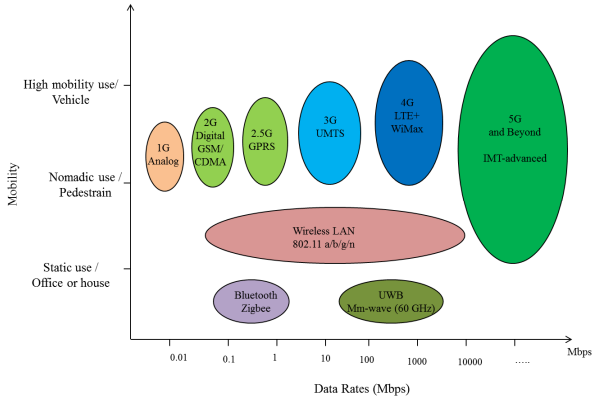

Fig. 2.1. Wireless access technologies [28].

On the other hand, WLANs or IEEE standards 802.11-a/b/g/n provide wireless coverage in one or more rooms in a building supporting multi Mbps. The cost, data speed, and easy integration of WLAN have gained great popularity. IEEE 802.11 series standards have different speed and frequency ranges, shown in summary Table 1 [29], and the range of these varies from 30 -100 m based on location.

Table 1. Summary of wireless access technologies

Technology	Frequency band	Bit rate	Signal range	Typical usage
GSM	900/1800 MHz	9.6 kpbs	35 km	Voice, data
GPRS	900/1800 MHz	160 kpbs	35 km	Data, WAP
UMTS	873/1900 MHz	2 Mpbs	2 km	Voice, data, multimedia
Bluetooth	2.4 GHz	2.1 Mpbs	10 m	WPAN
ZigBee	2.4 GHz	250 kpbs	10 m	
UWB cm-wave	3.1 – 10.6 GHz	> 100 Mpbs	10 m	
UWB mm-wave	57 – 64 GHz	> 1 Gbps	10 m	
802.11a	5 GHz	54 Mpbs	100 / 30 m	WLAN
802.11b	2.4 GHz	11 Mpbs	110 / 35 m	
802.11g	2.4 GHz	54 Mpbs	110 / 35 m	
802.11n	2.4 / 5 GHz	600 Mbps	250 / 70 m	

WPAN is another paradigm that provides short range wireless connectivity between consumer electronic devices such as tablets and mobile phones. Bluetooth (IEEE 802.15.1 standard) was the first low data rate standard for WPAN networks [30]. It enables wireless connectivity between mobile phones, computers, and electronic appliances with data rates up to 3 Mbps. ZigBee (IEEE 802.15.4 standard) wireless technologies is designed for data rates up to 250 kbps, primarily for wireless sensor applications [31]. This technology is mainly devoted for low data rate, low power consumption, and low cost wireless networking.

The first popular standards for WLAN (IEEE 802.11a/b) provide up to 54 Mb/s at 5 GHz, and 802.11b up to 11 Mb/s at 2.4 GHz, both in unlicensed spectrum bands. These standards are designed primarily to serve the needs of a laptop PC in the home and office, and later to allow connectivity “on the road” in airports, hotels, Internet cafes, and shopping malls. To minimize interference from other equipment, both use forms of spread-spectrum transmission and are heavily encoded. Later in 2009, IEEE 802.11n which uses MIMO (multiple input, multiple output or spatial streaming) is introduced to improve the maximum single-channel data rate to over 100 Mb/s. Currently, the wireless connectivity at home with Wi-Fi is available until data rate of 300Mbit/s. Recently, a very high throughput 802.11ac, an extension of 802.11n, has been published in 2014, providing a minimum of 500 Mbit/s single link and 1 Gbit/s overall throughput. The latter standard reuses the techniques seen in 11n but with wider bandwidths and higher constellation diagrams [32].

The demand for Gigabit data rates over wireless connections for a range of consumer applications such as in wireless access networks, future home area networks, remote antenna, radar systems and other multimedia application brings about its own constraint on the available bandwidth in the microwave band. Such data rates demand large spectrum allocation which could not be supported by the congested lower microwave band spectrum (2.4 GHz and 5 GHz bands). But the 60 GHz area is relatively uncongested and there is substantial overlap

of almost 3.5 GHz of contiguous spectrum available worldwide to support multi-GHz modulation bandwidths applications.

This upward trend demands new standards that can achieve data rates until 1Gbit/s in the centimeter-wave band and beyond 1Gbit/s in the millimeter-wave band. Among the standardization in the 60GHz is 802.11ad which has been published in December 2012. This standard is designed to be compatible with 802.11 ac at the Medium Access Control (MAC) or Data Link Layer; the difference stays only at the physical layer. Bearing in mind the number of existing devices, backward compatibility with existing standards using the same frequency range is a "must". All the 802.11 series of standards are backward compatible. Devices could then have three radios: 2.4 GHz for general use which may suffer from interference, 5 GHz for more robust and higher speed applications, and 60 GHz for ultra-high-speed within a room – and support session switching amongst them. IEEE 802.11ad was published in December 2012 and products based on this technology are now commercially available [33].

Transmission at 60 GHz covers less distance for a given power, mainly due to the increased free space path loss, and substantial RF absorption peak in the 60 GHz band due to a resonance of atmospheric oxygen molecules. Therefore, communication at 60 GHz is limited to only few meters. However, the fact that these low-power transmissions will not propagate very far can be considered as an advantage because it reduces the likelihood of co-channel interference and increases the possible frequency re-use density. Lower electromagnetic pollution for healthy environment and reduced opportunity for "theft, hacking" of protected content by eavesdropping on nearby transmissions are some of the advantages of the 60 GHz transmission.

Meanwhile, industrial groups have begun exploiting new radio standards that has the potential to provide high throughput service. These standards use UWB technology in the centimeter-wave (3.1- 10.6 GHz) and millimeter-waves (57-66GHz) bands. Main characteristics of these standards are summarized in Table 2.

Table 2. Characteristics of wireless access technologies [34]

Technology	UWB cm-wave	UWB mm-wave
Standard	WiMedia	IEEE 802.15.3c IEEE 802.15.11ad ECM 387, WirelessHD, WiGig
MAC	IEEE 802.15.3 MAC WiMedia MAC	IEEE 802.15.3c MAC ECMA 387 MAC
Modulation	MB-OFDM	SC (BPSK, QPSK, 8-PSK, 16-QAM, 64-QAM) OFDM
Coding	Convolution code	Convolution code
Bandwidth	3 x 528 MHz	2 GHz
Data rate	480 Mbps	7 Gbps
Range	10 m	10 m
Band allocation	Unlicenced	Unlicenced
Environment	Indoor	Indoor

2.2.1. Conventional UWB Communication (3.1- 10.6 GHz)

According to the definition of the Federal Communications Commission (FCC) of the United States in February, 2002 , a signal is considered UWB if either the -10 dB bandwidth of the signal is larger than 500 MHz or its fractional bandwidth (2.1) is at least 0.2 [35]. The fractional bandwidth is defined as

$$B_f = \frac{Bandwidth\ (10dB)}{Center\ frequency} \tag{2.1}$$

UWB wireless communication is one of the most important candidates for short range wireless signals at high data rates (>1 Gbps). The FCC has allocated the centimeter wave spectrum (3.1 – 10.6 GHz) for UWB communication in their first report. Thus UWB spectrum covers a large band of frequencies that have been home to a number of different wireless systems and services such as WiMAX, 3G/4G, satellite communications, various types of radars, and radiolocation. Some applications of UWB technology in consumer networks include wireless USB, wireless high-definition video, next-generation Bluetooth, peer-to-peer connections.

The maximum emission level of cm-wave UWB signal is very low to a value -41.3 dBm/MHz to avoid interference with existing services in the same spectrum. Comparison of emitted power levels of some wireless systems (Table 2.3) shows that there is roughly 50 and 60 dB difference in PSD levels of UWB/WCDMA and UWB/WLAN systems respectively. This allows coexistence with other technologies but limits transmission distance to few meters.

Table 3. PSD of some wireless systems [34]

Wireless System	Transmit PSD (dBm/MHz)
WCDMA	18
WLAN	7 / 17
Bluetooth 2.0	-19.2 / -15.23
UWB	-41.25

There exist two kinds of modulation schemes of UWB transmission namely UWB-impulse radio and multiband-OFDM (MB-OFDM). UWB-impulse radio is based on the transmission of very short pulses optimized to occupy the entire allowable frequency band. On the other hand MB-OFDM is a multiband scheme that divides the UWB spectrum into 14 bands called sub-bands each with 528 MHz bandwidth (figure 2.2). The first 12 sub-bands are grouped into 4 band groups and the last two sub-bands are grouped into a fifth band group as shown in Fig. 2.2. The sixth band group contains the sub-bands 9, 10, and 11. Band group 6 is the only available band worldwide. To tackle this problem, the European and other regulators have proposed other mechanisms to avoid interference between incumbent users of spectrums: detect and avoid (DAA) and low duty cycle (LDC) are some of the methods [36].

The MB-OFDM transmits information on 110 subcarriers overlapped in the frequency domain without interference. In addition, 12 pilot subcarriers are used for coherent detection. Each group of OFDM signals are hopped at different frequency sub-bands with a sequence determined by a time frequency hopping codes (TFC).

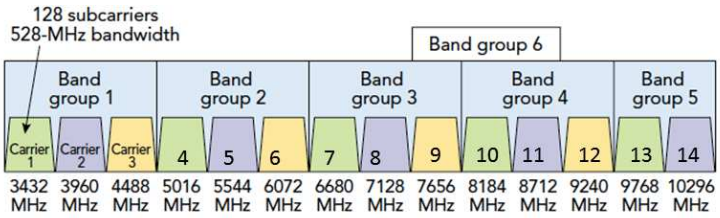

Fig. 2.2. The UWB centimeter-wave band spectrum.

2.2.2. 60-GHz UWB transmission

By definition, millimeter-wave ranges from 30 to 300 GHz. From this range, a band of interest for the short distance wireless communication is known as the U and E bands (U band: 40 - 60 GHz, E band: 60-90 GHz). Roughly speaking, 60 GHz band refers to the range from 50 to 60+ GHz. There has been a significant amount of available unlicensed spectrum in this band worldwide (Fig. 2.3). It is because of this opportunity that millimeter-wave communication systems are growing wireless technologies that enables transmission of data at speeds up to 7 Gbit/s leading to publication of several standardizations in the last decade [34]. In addition to the huge and unexploited available bandwidth, advancements in the low cost fabrication technology and low loss packaging material are other drives for the development of new technologies in this band.

Due to the high loss linked to atmospheric air has limited transmission distances to around ~10m [37], transmission at 60 GHz is limited to only few meters. To extend the network coverage, large numbers of BSs are needed [38]. These BSs should be equipped with low phase noise millimeter-wave oscillators to achieve high data rate communication. However, the fact that this low-power transmissions will not propagate very far can be considered as an advantage. Because it reduces the likelihood of co-channel interference and increases the possible frequency re-use density.

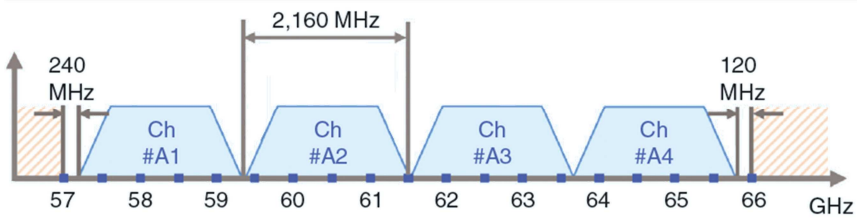

Fig. 2.3. Spectral allocation in the UWB millimeter-wave band.

The UWB (MB-OFDM) in the cm-wave band can support maximum of 480 Mb/s. But this cannot support uncompressed video such as HDMI (high definition multimedia interface) which goes beyond 2 Gb/s. To enhance the data-rate of UWB transmitter above 480 Mb/s brings additional problems in terms of cost, complexity, and power consumption. With the 60 GHz solution, we can avoid the data-rate limitations for wide range of applications with capacity more than 1 Gb/s data rate.

Applications in the 60 GHz include high definition video streaming, file transfer, wireless Gigabit Ethernet, wireless backhaul and others (Fig. 2.4). However, issues for the 60 GHz radio transmission including high-data rate, high antenna directivity, and shadowing are being investigated.

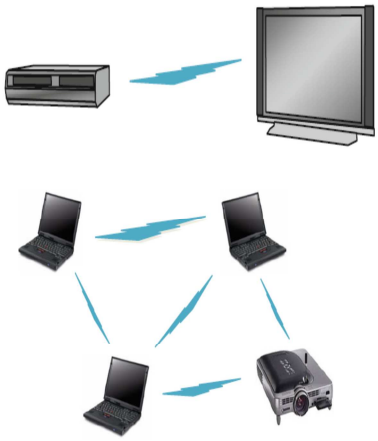

Fig. 2.4. Conference room networks at 60 GHz [34].

2.3. Optical Access Networks

Optical access networks are those networks that feed the metro or core network by gathering data from end users. With the installation of fiber to the home networks (FTTH) already happened in many countries worldwide, delivery of high speed services to end users becomes a possibility. The ultimate goal is to provide new multimedia services like video on demand, videoconferencing, high-definition TV (HDTV), e-learning, interactive games, Voice over IP. Therefore, FTTH systems which provide the fastest possible speed are currently being deployed worldwide. According to the latest figures [39], the number of FTTH subscribers in Europe (including Russia) has reached 20.1 million with more than 77.8 million homes/buildings passed. While Japan continues to lead the world in terms of the number of FTTH subscribers, and South Korea has the highest penetration in the world and is the first country in the world to reach over 50% penetration of households using FTTH.

To satisfy the future bandwidth demand, next-generation passive optical network (PON) architectures which are based on wavelength division multiplexing (WDM) technique are being explored [40]. In a WDM-PON the bandwidth of the fiber is shared between the subscribers, and each subscriber is assigned a pair of wavelength channels for up/down links. This means that each subscriber gets a dedicated point-to-point optical channel to the optical line terminal (OLT) and can send data at any time independent of other subscribers, although they are sharing a common point-to-multipoint physical architecture (Fig. 2.5). A WDM multiplexer/demultiplexer or array waveguide grating (AWG) is used to combine/separate the multiple-wavelength signals instead of the optical power splitter in a time division PON (TDM-PON) configuration. This decreases the insertion power loss in WDM-PONs and improves its ability to scale up to serve a large number of users sharing a single PON. However, there are some challenges in developing a practical system since each optical network unit (ONU) requires a specified wavelength source and N separate transceivers at the OLT to realize a connection to each subscriber.

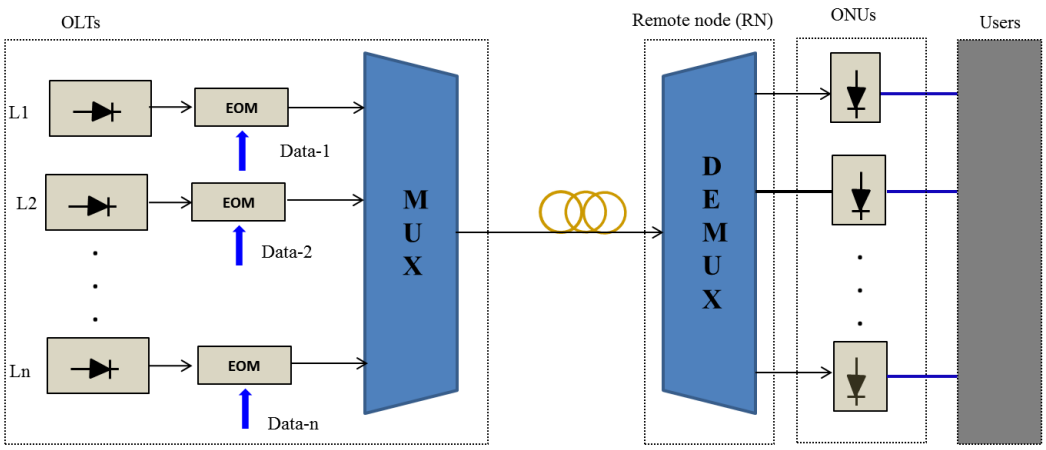

Fig. 2.5. WDM-PON configuration.

2.4. Radio over Fiber Technologies

While digital optical communication has tremendous success over the last few decades, analog photonic communication has also attracted attention because of its simplicity and the benefits offered by the optical fiber [41] [42]. Radio-over-fiber is generally defined as a system where the radio frequency signal is transmitted from the central location to another destination at the BS over an optical link (Fig. 2.6). The quality of service offered by the optical link compared to the conventional coaxial cable communication is remarkable making it possible to centralize the RF signal processing functions at the BS. The BS is limited only to E/O and O/E conversions.

Depending on the type of signal transmitted over the optical link, RoF systems can be classified as baseband over fiber (BBoF), intermediate frequency over fiber (IFoF), and radio frequency over fiber (RFoF). As shown in Fig. 2.6 RFoF involves the transmission of the actual RF signal over the fiber, while in IFoF and BBoF the desired microwave signal is generated at the receiver through up-conversion with a local oscillator, which is either provided separately. Therefore, based on the transmission method used, the receivers at the BS may be more or less complex. Table 4 summarizes the advantages and disadvantages of each method.

Table 4. Types of RoF systems.

Type of System	Advantages	Disadvantages
RFoF	-Simplified BSs	-Fiber dispersion affects the double sidebands -Needs high bandwidth O/E and E/O components
IFoF	-Relaxed bandwidth requirements on O/E and E/O components. -Tolerant to chromatic dispersion	-needs mm-wave mixers and LO at BS or remote LO delivery is necessary -Affected by phase noise
-BBoF	-Digital fiber optic link – relatively cheap -Tolerant to fiber dispersion and nonlinearity.	- needs mm-wave mixers and LO

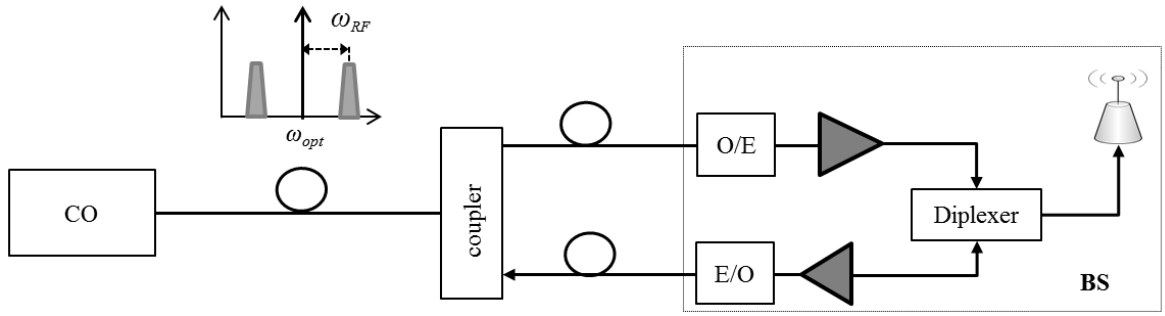

(a)

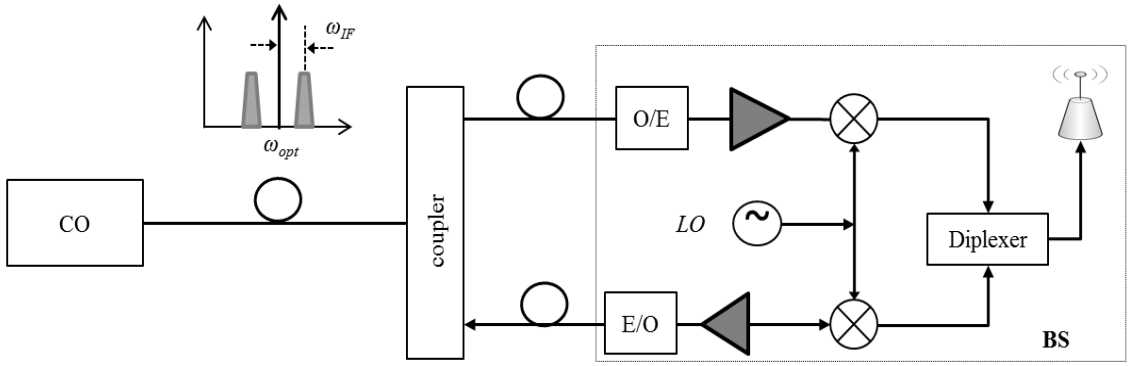

(b)

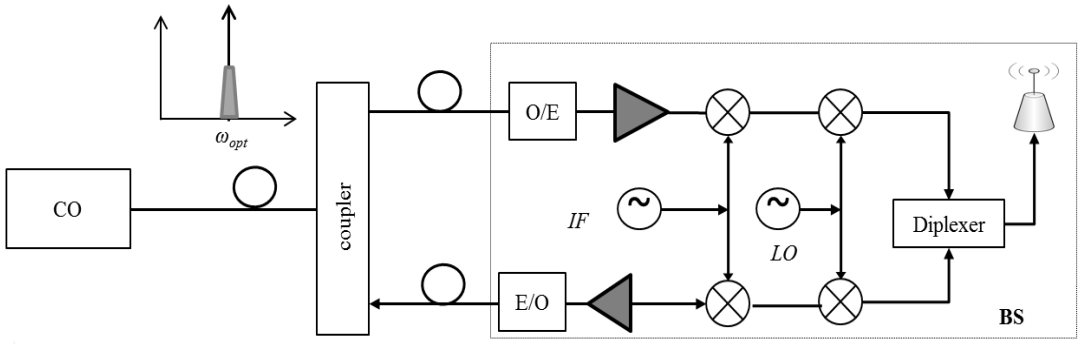

(c)

Fig. 2.6. Radio over fiber systems (a) RF over fiber (b) IF over fiber (c) Baseband over fiber [43].

2.4.1. Advantages of RoF technologies

Thanks to the low attenuation of optical fibers, RoF technology is the best way to distribute high frequency signal since traditional transmission media such as wireless and wired transmission lines experience unacceptably high attenuation such as for millimeter-wave communication.

Commercially available single model fibers (SMF) have attenuation losses below 0.2 dB/km in the 1.3 and 1.55 µm spectral windows. Polymer optical fiber exhibits higher attenuation ranging from 10 – 40 dB/km in the 500 – 1300 nm regions [44]. These losses are much lower than those encountered in coaxial cable whose losses are higher by three orders of magnitude

at higher frequencies. For instance, the attenuation of RG-214 is > 500 dB/km for frequencies above 5 GHz. Therefore, by transmitting microwaves in the optical form, transmission distances are increased several folds and the required transmission powers can be reduced greatly.

The other importance of using RoF is linked to the high bandwidth offered by the optical fiber. Apart from the high capacity for transmitting microwave signals, the high bandwidth offered by optical fibers permits to perform microwave functions such as modulation, filtering, up and down conversion at the BS allowing the use of WDM for dynamic resource allocation.

Immunity to Electro-Magnetic Interference is a very attractive property of optical fiber communications, especially for microwave transmission. This is so because signals are transmitted in the form of light through the fiber. Because of this immunity, fiber cables are preferred even for short connections at mm-waves. Related to EMI immunity is the immunity to eavesdropping, which is an important characteristic of optical fiber communications, as it provides privacy and security.

Lower installation cost and reduced power consumption are also other advantages of using optical links for short and long range wireless communication systems. This is mainly because RoF systems allow centralizing most of the functions at the BS and the large number BSs have a very simple function of O/E and E/O conversions. This contributes to the reduction of installation cost and power consumption.

2.4.2. Limitations of RoF technologies

Since RoF involves analog modulation, and detection of light, it is fundamentally an analog transmission system. Therefore, signal impairments such as noise and distortion, which are key parameters in analog communication systems, are important in RoF systems as well. These impairments tend to limit the signal-to-noise ratio (SNR) and Dynamic Range of the RoF links [45]. Wireless system performance is usually analyzed by using error vector magnitude (EVM) from which it is possible to estimate the bit error rate. The noise added due to the optical link causes low SNR resulting significant increase of EVM, while the distortion limits the dynamic range by causing high inter-symbol interference (ISI) which again increases the EVM. Due to this reason, analog optical links are limited to shorter length compared to their digital counter parts.

Noise in analog optical fiber links include contributions of the laser's Relative Intensity Noise (RIN), the laser's phase noise, the photodiode's shot noise, the amplifier's thermal noise, the fiber's dispersion, and optical amplifiers amplified spontaneous emission. Semiconductor lasers have the dominant contribution of noise to the RoF link. In SMF based RoF systems, chromatic dispersion may limit the fiber link lengths and may also cause phase de-correlation leading to increased RF carrier phase noise. Because single mode semiconductor lasers usually have side mode accompanying the main longitudinal mode. Due to fiber dispersion, these modes travel through the optical fiber at different speed and received at the photo-detector at different times causing phase and amplitude fluctuation on the radio

signal. In Multi-Mode Fiber (MMF) based RoF systems, modal dispersion severely limits the available link bandwidth and distance.

The other limitation of RoF link is its nonlinearity. To compensate the signal attenuation due to the fiber, increasing the RF power is a solution. However, this will have consequence of having a non-linear system which reduces the dynamic range causing limited radio coverage. The sources of nonlinearity in the RoF link are associated with the laser source and photo-detector and electrical amplifiers.

2.4.3. Applications scenarios of broadband RoF technologies

The main interest of using radio signal transmission over fiber is basically related to the advantages offered by the optical communication system. The large bandwidth and low loss are some of the main advantages of using the optical link instead of the traditional wired and wireless systems. Fiber optic links solutions generally are recommended for all applications where high data rate transmission is required, standard architectures become too complex, data transmission needs to be secured, electromagnetic interference is a concern, weigh reduction is important, reduced power consumption is needed. However, the limited dynamic range of RoF systems make them restricted to only shorter length applications compared to the digital fiber optic communications (e.g. terrestrial links). Long distance communication using analog optical links are used in cable television industry and other remote antennae for military radar applications [24]. Some examples of analog photonic applications are shown in Fig. 2.7 among which the interest of this thesis is on the radio transmission over fiber both for indoor and outdoor applications.

RoF systems can readily be used for in-building (indoor) distribution of wireless signals of both mobile and data communication (e.g. WLAN, and HAN) systems, because most indoor applications do not require high spurious-Free dynamic range (SFDR). For high frequency applications such as in 60 GHz transmission, the cell size will be small due to high losses through the walls, bringing the benefits of RoF such as installation cost. The in-building fiber infrastructure may then be used for both wired and wireless applications as shown in Fig. 2.7 (a). To further reduce the system installation and maintenance cost, multimode fiber (MMF) or plastic optical fibers (POFs) can be used since as the effect of dispersion is minimal for shorter length fibers. In-building data communication LANs are often based on MMF.

In mobile telephone networks (outdoor), the role of RoF is mainly for radio coverage extension, and capacity distribution and allocation [45]. The first case includes applications for railway and motorway tunnels, and other dead spot areas where their need of network coverage do not justify the cost of installing and operating new radio systems. In this case the RoF solution extends the reach of an existing BS to one or more locations. The other case includes applications for subway stations, exhibition grounds, downtown street levels, and other densely populated environment where the traffic requirement leads to dedicated radio channels that need to be distributed appropriately. Examples of this case are reported in situations like airports and shopping malls.

Another application for RoF network architectures is shown in Fig. 2.7 (b). In this configuration, a large metropolitan area network (MAN) supports WDM channels, each

carrying data rates up to 10 Gb/s. A number of centralized switching nodes are interconnected together via an optical MAN ring. Each switching node provides control, switching, and routing to the remote node or BSs. The CO can be connected to several remote nodes using ring or star topology as shown in the figure. In either arrangement, the optical WDM channels at the CO are de-multiplexed and dropped from the MAN to the remote terminals. Then, each optical channel is directed to the specified BS for signal detection and radio distribution. There are many host applications that employ the analog optical links. Different architectures are proposed for the integration of RoF with WDM-PON systems to support up to 10 Gbps wireless signal and 112 Gbps baseband signal [46] [47].

RoF applications can also be categorized based on the optical link distance as short range and long haul analog links. Short range analog optical links are used in wide applications from WLAN in millimeter-wave band, and broadband wireless access networks to road vehicle communication networks for intelligent transportation system. On the other hand; high definition TV (HDTV), internet video, cable TV, and remote antennae are some of the applications that can be classified as long haul analog systems [48] [[49].

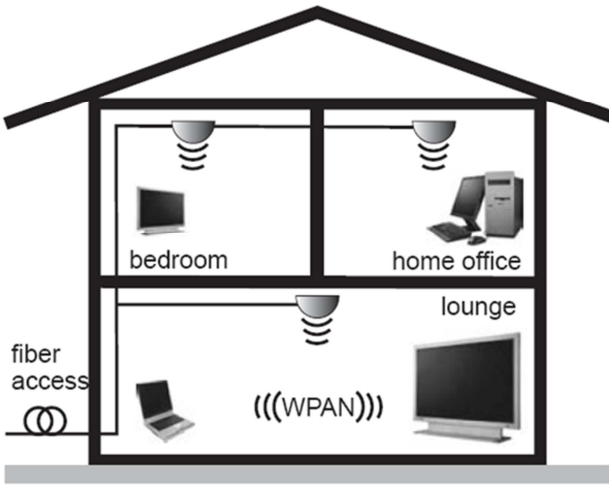

(a) Home area network [4]

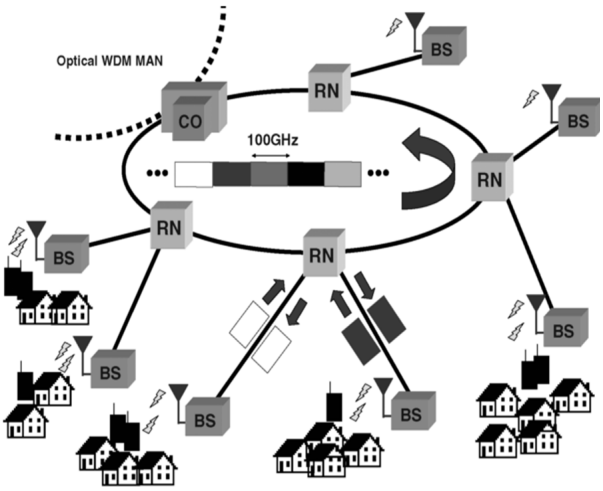

(b) RoF in metropolitan network [43]

(c) Radar (Thales)

(d) Navy (Thales)

Fig. 2.7. Applications of RoF systems

2.5. Photonic generation of millimeter-wave signals

The main system functions of microwave photonics can be divided into three main categories namely transport of microwave and millimeter-wave signals over the optical fiber [50], filtering and processing of microwave signals in the optical domain, generation of microwave [51], millimeter-waves [52].

One of the main functions of the optical link in analog optical applications is for transmission of the radio signal to remote areas due to the advantage of the low attenuation, flexibility, immunity to electromagnetic interference and high bandwidth characteristics of the optical fiber. This is usually done by modulating the intensity of the light with microwave frequencies up to few tens of GHz through different techniques. However, the E/O and O/E devices in the RoF link have to meet a number of requirements to enable higher link gain, lower noise and wider dynamic range [53]. These requirements include a continuous-wave (CW) laser with higher output power and low relative intensity noise, a direct modulated laser with greater slope efficiency, lower relative intensity noise, and higher bandwidth, external modulators with lower V_π and high power handling ability, and photo-detectors with higher responsivity, bandwidth and saturation power.

The other function is for the signal generation. One good example of this function is the generation of millimeter-wave for multi-Gb/s wireless communication. In this case, because of the fiber dispersion which can lead to zero transmission in the millimeter-wave band, the optical link is better used to generate the radio signal rather than transporting the signal. This function proves its effectiveness compared to the traditional methods of radio signal generations using electronic oscillators as we approach to the THz region. Besides the generation of high frequency radio signals using the optical solutions makes it possible to transport the signal over the optical fiber. Intensity modulation of the light using either direct or external modulation is the usual technique to generate radio signals, but these methods are limited by the laser modulation bandwidth and the dispersion-induced fading at the millimeter-wave frequencies. However, one can generate microwave and millimeter-wave signals by a number of other methods such as heterodyne of two lasers, bimodal laser, active and passively mode locked lasers.

Radio over fiber systems can exploit both the phase and intensity of the optical field [54] to transport and generate the RF carrier, but the most popular methods are direct and external modulation of the intensity the light. At the receiver, direct detection method is usually used for intensity modulated signals which are often named as intensity modulation-direct detection (IM-DD). However, coherent and heterodyne detection methods can be used to recover the transmitted information. Coherent detections are more suited for phase/frequency modulated systems which can achieve better performance than from IM-DD systems in terms of signal-to-noise ratio and dynamic range but laser phase noise is a major technical problem for such techniques.

2.5.1. Intensity Modulation-Direct Detection

IM-DD systems are the simplest configuration of RoF systems. The radio signal modulates the intensity of the light and the photodetector recovers the radio signal. If the RF signal itself is modulated with a data, the modulation format will be preserved after detection. The light

source is usually semiconductor laser which can also serve as an optical modulator. Depending on whether the laser is used in CW mode or in modulation, the IM-DD method can be further classified as direct modulation (DM) and external modulation (EM) methods.

DM is the most widely used method in analog optical links because of its simplicity and cost effectiveness. However, this system is limited by the nonlinear distortion and bandwidth limitation of the laser diode. Electro-optical bandwidth up to 35 GHz is achieved experimentally using direct modulated lasers [55] [56], but the key limitation is the rate of the unwanted frequency modulation (chirp) increases for high modulation frequencies. Currently, commercially available direct-modulated lasers exhibit typical bandwidths of about 10 GHz at the maximum. Thus for millimeter-wave applications, local oscillator is required at the BS for up-conversion and down-conversion.

The bandwidth limitation and nonlinear distortion of the directly modulated laser can be reduced by using an optical modulator. In this case, the laser works in a CW mode and the intensity of the light is modulated externally. MZM and EAM are widely used optical modulators. Fig. 2.8 shows DM and EM based RoF links. In this example, an RF signal of frequency f_{RF}, which carries OFDM signal, modulates a single-frequency optical carrier at frequency f_{opt} creating sidebands $f_{opt} \pm f_{RF}$. The photodetector then converts the optical signal to electrical signal to recover the original signal at frequency of f_{RF} which has experienced attenuation, distortion and noise due to the optical link.

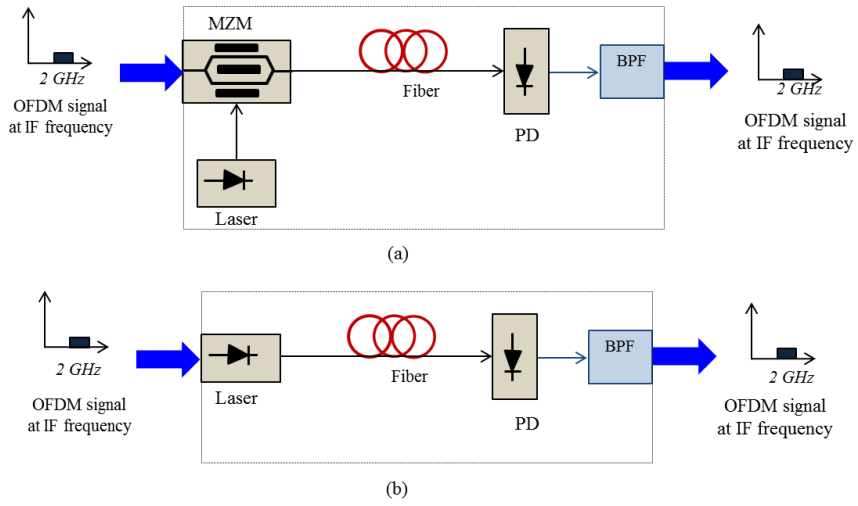

Fig. 2.8. IM-DD system (a) DM RoF link (b) EM RoF link.

The data signal is carried in sidebands on both sides of the optical carrier which is known as double sideband (DSB) operation. Transmission of such a signal through a fiber will cause a phase shift between the two sidebands due to the chromatic dispersion effect causing destructive interference at detection. The problem is even devastating if multimode fibers are used because of modal dispersion. Therefore, the fiber dispersion limits the maximum reach of IM-DD systems. However, there are some methods to suppress one sideband to reduce the power fading in the EM case. This can be achieved either by filtering one band optically or by using dual drive modulators to obtain single sideband (SSB) modulation. Nevertheless, this increases the complexity and cost of the system and has lower receiver sensitivity than DSB due to the large DC power component at the optical carrier.

2.5.2. Optical remote heterodyne method using two free running lasers

When two optical signals at different central frequencies are injected to the photodetector, an RF signal is generated at a frequency equal to the spectral difference of the optical signals. While performing optical to electrical conversion, the photodetector also acts as a mixer thereby making it a key component in heterodyne based RoF systems. This method can generate very high frequency signals only limited by the photodiode bandwidth, removing the need of local oscillator at the BS for millimeter-wave transmission. An example of an optical remote heterodyne system is shown in Fig. 2.9 where an electronic feedback circuit is added to reduce the phase noise influence at the BS.

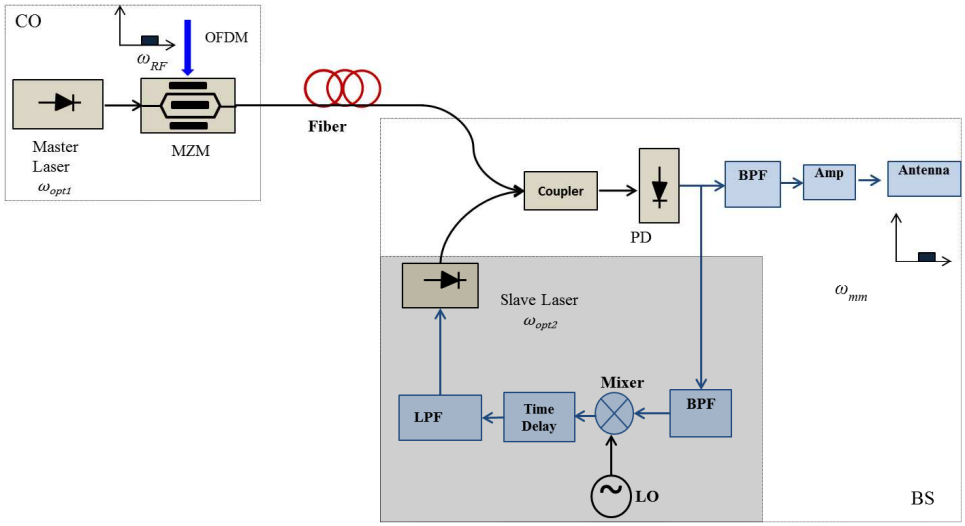

Fig. 2.9. Architecture of optical heterodyne for millimeter-wave applications.

Optical heterodyne method yields high-detected power (higher link gain) and higher carrier-to-noise ratio (CNR). This is so because both the optical powers of the two signals contribute to the power of the generated microwave/mm-wave signal. However, it needs very fast photodiode to generate high frequency signals [42]. Besides it has an inherent advantage concerning chromatic dispersion. Reducing chromatic dispersion effects is very important in phase noise sensitive modulation formats such as xQAM, where dispersion causes a power penalty [2].

Another important attribute of optical heterodyne is that it permits low-frequency data modulation at the CS hence high-frequency electro-optical modulators are not required. Therefore, in contrast to IM-DD, the optical source at the CS may be driven either with baseband data or by a low-frequency RF signal. Low-frequency modulators generally have low half-wave voltages, V_π and therefore require lower drive levels. Consequently, low-frequency modulators are easier to linearize. These advantages make optical heterodyning a promising technique for future generation networks.

The working principle of optical heterodyne systems can be explained if we assume the unmodulated laser outputs beating at the photodiode, the two optical signals with angular frequencies, ω_{opt1} and ω_{opt2} can be represented by

$$\vec{E}_1(t) = E_1 \exp\left(j\left(\omega_{opt\,1}\, t + \phi_{opt\,1}\right)\right)\ \vec{u} \tag{2.2}$$

$$\vec{E}_2(t) = E_2 \exp\left(j\left(\omega_{opt\,2}\, t + \phi_{opt\,2}\right)\right)\ \vec{u} \tag{2.3}$$

where E_1 and E_2 are amplitude terms, ϕ_{opt1} and ϕ_{opt2} are phase terms of the two optical waves, and $\vec{u}$ is the unit vector.

The resulting photocurrent after detection is proportional to the square of the sum of the electrical fields of the optical signal. After a DC block and removing higher order terms, the photocurrent can be written as

$$I_{RF} = r_{PD} E_1 E_2 \cos\left(\omega_{RF} t + \phi_{RF}\right) \tag{2.4}$$

$$\text{where}\quad \omega_{RF} = \omega_{opt\,2} - \omega_{opt1} \text{ and } \phi_{RF} = \phi_{opt\,2} - \phi_{opt\,1} \tag{2.5}$$

where r_{PD} is the responsivity of the photodetector.

Equation (2.5) shows that the stability of the instantaneous frequency of the resulting signal depends on the instantaneous frequency difference between the two optical carriers being mixed. Therefore, it is important to control the instantaneous frequency difference accurately in order to keep the frequency of the generated signal stable. It also shows that the phase noise of the generated signal is influenced by the optical linewidth of the two optical carriers.

The transfer of phase noise from the two free running lasers to the generated RF signal can be shown by writing the auto-correlation of the photocurrent which is related to the root mean square of the phase difference (phase variance) between time t and $t + \tau$ as follows

$$\left\langle \Delta\phi_{RF}(t)^2 \right\rangle = \left\langle \left(\Delta\phi_{RF}(t+\tau) - \Delta\phi_{RF}(t)\right)^2 \right\rangle \tag{2.6}$$

Substituting (2.5) into (2.6), the phase variance of the photocurrent is given by

$$\left\langle \Delta\phi_{RF}(t)^2 \right\rangle = \left\langle \phi_{opt2}(t+\tau) - \phi_{opt1}(t+\tau) - \left(\phi_{opt\,2}(t) - \phi_{opt\,1}(t)\right) \right\rangle^2 \tag{2.7}$$

Since the two lasers are completely uncorrelated, there is no relation between their respective phases. Due to the averaging, the product of ϕ_{opt1} and ϕ_{opt2} becomes zero, therefore, the root mean square becomes the sum of root mean squares of the two phases from the two optical signals:

$$\left\langle \Delta\phi_{RF}(t)^2 \right\rangle = \left\langle \Delta\phi_{opt\,1}(t)^2 \right\rangle + \left\langle \Delta\phi_{opt\,2}(t)^2 \right\rangle \tag{2.8}$$

From (2.8), we can conclude that the phase noise spectrum of the generated RF signal by optical heterodyning is the sum of phase noise spectrums of the two free running lasers. The linewidth of the RF signal is given by the sum of linewidths of the two lasers.

In conclusion, the generation of RF signals by beating of optical waves from two free running laser diodes leads to a linewidth enlargement. In the case of correlated lasers, the product of ϕ_{opt1} and ϕ_{opt2} is different from zero in (2.7). Hence the generated signal will have smaller linewidth as compared to (2.8).

As reported in [57], experimental data shows that millimeter-wave signals generated by two uncorrelated light sources are highly influenced by the high phase noise of semiconductor lasers. Two DFB lasers around λ=1.54 μm are used to generate the millimeter-wave carrier between 60 and 70 GHz. One of the lasers is modulated by a 140 Mb/s pseudo random binary sequence (PRBS) signal. The two lasers being located at the CS, the two optical signals are combined and transmitted over a single mode fiber of lengths up to 12 km. The unmodulated millimeter-wave carrier is observed to have linewidth of approximately 4 MHz due to the uncorrelated lasers phase noises.

Therefore the major drawback of optical heterodyning is the strong influence of laser phase noise and optical frequency variations on the purity and stability of the generated RF carriers. Since semiconductor lasers have large spectral widths, extra measures to reduce the linewidth of the generated RF signals, have to be taken. There are different methods that are being proposed to tackle the phase noise influence of heterodyne method using two lasers by maintaining phase correlation between the two optical fields. The two main methods that are used to maintain the phase correlation are Optical phase-Locked Loop (OPLL) and Optical injection locking (OIL).

OPLL can be implemented using solid-state lasers such as Nd: YAG [58] or external cavity semiconductor lasers [59]. But the use of semiconductor lasers without external linewidth narrowing arrangements is more attractive for its potential compactness to implement monolithic optoelectronic integration [60] [61]. To reduce the high phase noise of semiconductor lasers, large feedback bandwidth is required to achieve high performance. Therefore cheap DFB lasers can be applied for an OPLL for different applications where there are demands of low phase noise levels such as in coherent optical sensing, satellite systems and millimeter-wave radar systems. Experimental results show that wideband heterodyne OPLL can be achieved for microwave carriers from 3-18 GHz [62]. Authors have used master laser of linewidth 2 MHz and slave laser of linewidth 6 MHz to obtain the beat signal of linewidth 8 MHz in the free running case. After applying OPLL to the system, noise level of -125 dBc/Hz is obtained close to the carrier and less than -102 dBc/Hz at all carrier offsets. The linewidth of locked beat signal is not given due to its measurement difficulty, but estimated total variance over 1GHz bandwidth is found to be 0.04 rad^2.

If this OPLL is to be applied for home area networks to generate pure millimeter-wave carriers at the BS [63], the master and slave lasers can be located at the CS and the BS will do photodetection and amplification. This method simplifies the BS and it can help to extend millimeter-wave band wireless signal transmission within buildings, stadiums or other public areas. Block diagram of OPLL is given in Fig. 2.9. A local oscillator and photodetector are needed at the central station to detect the phase of the beat signal which will be feedback to the slave laser. The slave laser will then follow the master laser phase noise profile. By appropriate design of loop gain and response time, the phase noise of the millimeter-wave signal at the BS can be reduced considerably [61] – [64].

On the other hand, optical injection locking is another way of locking the free running lasers to the master laser by using optical injection. The master laser which is directly modulated at an RF frequency creates several sidebands around its central frequency. If the slave lasers are

chosen to be located near the appropriate sidebands, the photodetector mixes the optical harmonics to give a multiple of the RF signal modulating the master laser. The main advantage of OIL is that it offers good phase noise reduction and cheap broad-linewidth lasers can be used. But its small frequency detuning range and high complexity limits its application [2].

Optical heterodyne detection using two uncorrelated lasers coupled with electrical self-heterodyne or envelop detection at the receiver has been under investigated [65], [66] to achieve high performance millimeter wave generation. These methods reduce the complexity of the central and BSs while keeping a low phase noise millimeter-wave carrier. Systems employing these techniques have two free running lasers at the CS, while the base station includes a photodiode, high power amplifier, and antenna, and the mobile unit (user) uses envelop detection to recover the laser phase noise free signal [67] [68]. But this architecture is sensitive to chromatic dispersion since the two optical frequencies have different group delay while propagating through the fiber optic. This effect could reduce the maximum reach of the link. On the other hand, if the heterodyning laser is located at the BS, the system will be resilient chromatic dispersion but the BS will have higher complexity as shown in Fig. 2.9.

2.5.3. Optical heterodyne using dual mode laser

A further another approach to create correlation between the harmonic with less complexity is using dual mode laser source [69]. The phase noises of the two beating harmonics are correlated because they are generated from the same cavity. Despite the poor frequency stability and the phase noise level [70], this method attracts more interest for different fields such as radar, and short range wireless personal area networks [71] due to its compactness and tunability.

Mode-locked lasers are an alternative solution to generate millimeter-wave signals. These lasers are realized from multi-mode lasers by integrating saturable absorber in the laser cavity to create self-oscillation (passive-mode locking). These lasers emit short pulses at a repetition frequency corresponding to the laser's free spectral range (FSR). Mode-locking frequencies of up to 1 THz have been achieved and linewidth of less than 200 kHz is reported in [72].

2.5.4. Optical heterodyne using external modulation technique

Millimeter-wave generation using EM technique is usually employed using cascaded MZMs [73] [74]. As shown in Fig. 2.10, this method consists to two MZMs, the first is used to modulate the digital signal at intermediate frequency (e.g. OFDM) and the second modulator is used for the optical up-conversion. It creates sidebands whose spectral width is equal to the desired millimeter-wave signal. Beating of the sidebands gives the desired signal after the photodetector at the BS. Since the two beating harmonics are correlated, the signal generated after the photodetector has low phase noise. However these kinds of systems are sensitive to chromatic dispersion [75]. To avoid the chromatic dispersion impact, an optical filter such as fiber Bragg grating (FBG) can be used to filter out one of the sidebands [76]. 60-GHz wireless communication compatible with WDM-PON system is investigated in [77] using MZM based optical self-heterodyning method. At the user end, the envelop detection or self-heterodyne method can be applied to demodulate the data being transmitted.

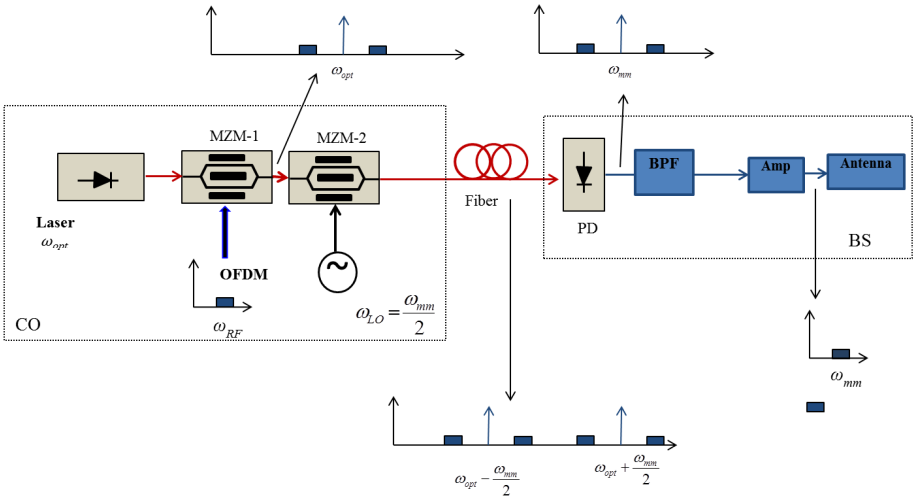

Fig. 2.10. Millimeter-wave generation using MZM based self-heterodyne method.

2.6. Summary

This chapter briefly summarizes the basics of hybrid optical/wireless communication systems. As the wireless systems are converging to the millimeter-wave, optical links have proved their efficiency to support the demand needed for these systems. Different techniques are discussed to generate millimeter-wave signal using optical components. The main issue is to generate high frequency radio signal with high spectral purity and low complexity.

The performance of a DM RoF system is mainly limited by the laser bandwidth, RIN, chirp and nonlinearities. External modulation can be used to tackle the problem of chirp and bandwidth limitations for applications above 10GHz. Systems based on optical frequency harmonics can generate high frequency signals without the limitation of the laser bandwidth. The simplest heterodyne system is composed of two free running lasers. However, the laser phase noise has direct impact on the detected signal leading to spectral broadening and degradation of the information-bearing RF carrier. This influence can be mitigated by introducing phase correlation between two laser sources using an electrical or optical feedback method. If two free running lasers have to be used without any correlation, the phase noise contribution could be reduced by using RF heterodyning or envelop detection at receiver (user end). These methods are best suited method for high frequency applications in the millimeter-wave band. Since transmission distance of millimeter-wave is only few meters (unless high gain antenna is employed), many BSs are required to extend network coverage. Therefore, BSs are required to be as simple as possible.

3

Circuit Modeling of Radio over Fiber Links

3.1. Introduction

This chapter deals with circuit modeling of radio over fiber components for different RoF links. Modeling E/O, O/O and O/E components can be complex since the optical and electrical properties of the devices must be incorporated. Circuit modeling of RoF components is an effective approach to represent components' behaviors making it possible to integrate electrical drive circuit and parasitic effects.

The optical source, semiconductor laser, is characterized by its electrical properties (bias current versus junction voltage) and optical properties (static response, dynamic response, and noise). The input impedance and parasitic of the laser package are some of the electrical effects that requires attention. The equivalent circuit model of the laser has to include all these properties in a very compact and simplified manner.

At the optical detection, properties like the optical to electrical conversion, noise, nonlinearity and impedance matching must be considered. The optical modulator properties such as insertion loss, modulation property, and driver circuit effects need to be incorporated in the analysis. As for the fiber optics, dispersion and attenuation are considered to be the main parameters that could limit the system performance for short range applications. For longer fiber transmission systems, nonlinearity of the fiber such as stimulated Brillouin scattering plays an important role as it has lower threshold than Kerr effect.

This chapter focuses on the detailed modeling and analysis of the laser properties. After discussing the theoretical background about semiconductor lasers, the equivalent circuit model of the laser is developed from the rate equations. Since the developed circuit model contains several parameters which depend on cavity properties and the physical dimensions of the device, it is challenging to obtain the optimum sets of parameters. To obtain these parameters, we have used optimization and tuning routines available in ADS by comparing simulation and measurement curves. For this purpose, measurement of laser characteristics such as RIN, phase noise, the static response, and dynamic response are required. A set of parameters that gives the best fitting between measured and simulated curves are then used for system simulations.

Development of circuit models of other RoF components leads to system study by cascading the models in different configurations. This allows easy evaluation of RoF properties such as link gain, noise figure and dynamic range. The models are flexible to study different RoF systems in terms of light modulation and detection. Both IM-DD and heterodyne detection techniques can be studied with these models.

3.2. Semiconductor lasers

Lasers are devices that generate or amplify highly monochromatic radiation in the infrared region, optical region, or beyond. According to recent developments, sophisticated laser diodes can have more few hundreds of KHz linewidth and high power up to 100mW [21]. Their small dimension, low power consumption, possibility of direct modulation, high efficiency, and mass productivity are some of the outstanding advantages of semiconductor lasers. Together with the optical fiber technology, semiconductor lasers have brought a dramatic change in the communication systems to meet the increasing demand for high speed communication. New applications in the local area data communication and telecommunication networks continue to emerge as these devices become more reliable and efficient.

In a solid semiconductor material, there are four basic electronic transitions that can occur between the valence and conduction bands: spontaneous emission (photon emission), stimulated generation (photon absorption), stimulated emission (coherent photon emission), trap-assisted and Auger recombination (Fig. 3.1). Light is generated due to spontaneous emission and stimulated emission. Based on these two phenomena, there are two kinds of devices that are used as light sources: light amplification by stimulated emission of radiations (Laser) and light emitting diode (LED).

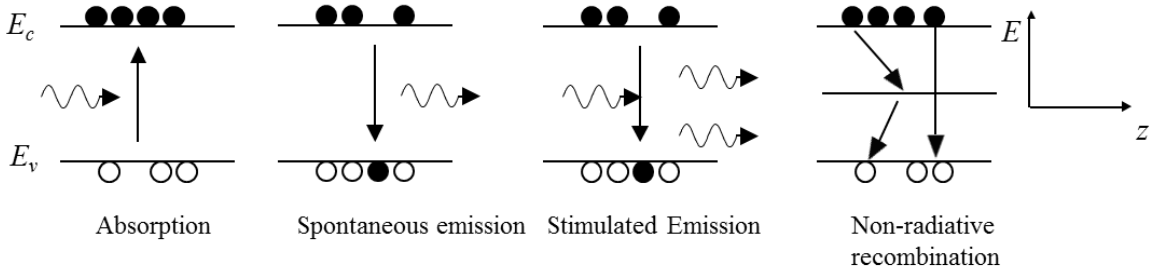

Fig. 3.1. Electronic transitions between the conduction and valence bands in semiconductor materials.

The primary mechanism within LED is that large number of spontaneous emissions occurs inside the material and no photon feedback is provided. This mechanism results in an incoherent emission since the emission time and direction would be random which makes them unsuitable for optical communication. Whereas in lasers both spontaneous emission and stimulated emission occurs, the stimulated emission is dominant allowing the emission of monochromatic light. It is for this reason that lasers are integral elements of an optical communication system.

The optical gain medium in semiconductor laser diodes consists of a material which absorbs incident radiation over some wavelength range of interest and incorporates a resonant optical

cavity. When external energy is applied in the form of electrical or optical energy, the electrons within the material will be excited to a non-equilibrium state which can cause spontaneous and stimulated emission. If the energy incident radiation is higher than the bandgap energy between the electron in the excited state and the available state in the valence band (hole), the electron and the hole recombine emitting a photon which has the same energy as the incident photon. So the incident radiation is amplified rather than absorbed by stimulating the de-excitation of these electrons along with the generation of additional radiation. If the resulting gain is sufficient to overcome the losses of some resonant optical mode of the cavity, relatively monochromatic light can be produced. In semiconductor lasers, after the light is emitted by spontaneous emission, the resulting photons are amplified since they are reflected back and forth in the resonant cavity which provides the necessary positive feedback for the radiation to be amplified, so that a lasing oscillation can be established and sustained with sufficient injection of electrical energy (electron injection).

The range of emission wavelengths of semiconductor lasers covers the optical spectrum from near ultraviolet to far infrared depending on the materials used in the lasing region. The most important criterion to select the semiconductor material for a specific heterostructure laser is related to the lattice matching between the two semiconductors of different band gaps. Long-wavelength lasers in the range of 1.1 to 1.6 µm are desirable in optical fiber communication since the optical fiber attenuation in this window is very low. For these ranges of wavelengths, $In_xGa_{1-x}As_yP_{1-y} - InP$ combination is the most suitable choice in terms of perfect lattice matching. For wavelength range of 0.8 to 0.9 µm, GaAs materials can be used to realize the laser.

Apart from the bandgap of the semiconductor material, for radiative recombination to happen in the active region, the injected carriers and the generated photons have to be confined in the active region. There are different structures to achieve both carrier and photon confinement. Double heterostructure (DH) is the simplest case to have carrier confinement by forming potential well across the transverse axis while the photon confinement is achieved by the index of refraction profile between the cladding layers and the intrinsic region. The active region (intrinsic region) is made of a material with high index of refraction. This index of refraction profile creates an optical waveguide of few micrometers thickness. The carrier confinement effect in DH is one of the most important features of modern diode lasers. By further reducing the dimension of the active region to form a very small layer called quantum well (QW), the characteristics of the laser changes fundamentally. Laser diode structures with this profile are called separate confinement heterostructure - quantum well lasers (SCH-QW). The surrounding intermediate bandgap region is used to confine photons. QW lasers achieve low threshold current while keeping high gain profile, high intrinsic modulation bandwidth, and narrow linewidth, however they are usually more temperature sensitive than conventional non-QW devices. The following analyses about the characteristics of semiconductor lasers are based on [78].

3.2.1. Types of Lasers

Practical laser diodes can be of the two categories (Fig. 3.2): those with in-plane cavities (edge emitting lasers, EEL) and those with vertical cavities (vertical cavity surface emitting lasers, VCSEL). The main difference is that the optical cavity of EEL is in the lateral axis where feedback can be accomplished using cleaved-facet mirror and emission at the edge of the device. Whereas in VCSELs, the cavity is in the vertical direction which is also the direction of growth of the device, and feedback is achieved by using a multilayer reflective stack grown below and above the active region.

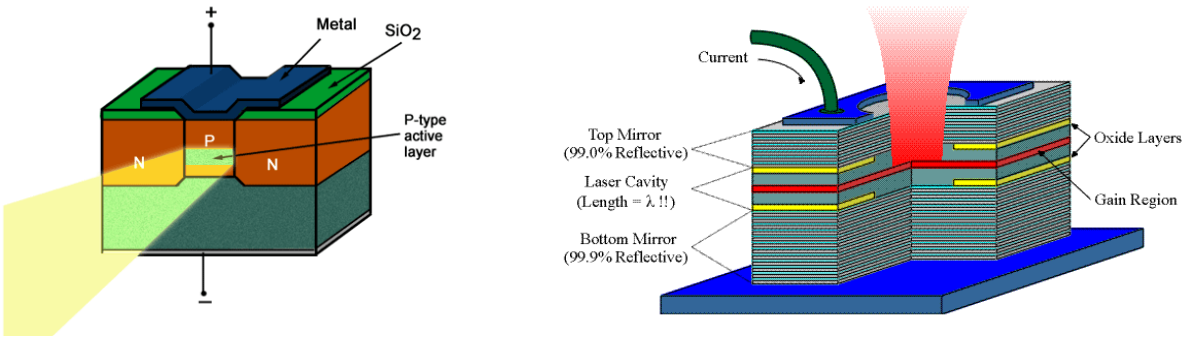

(a) (b)

Fig. 3.2. Schematic of (a) in-plane and (b) vertical-cavity surface-emitting lasers.

Further classification of semiconductor lasers is based on the frequency selective mirrors put in the axial mode propagation direction to determine the emission frequency and tunability. Some of the lasers include but not limited to Fabry-Perot (FP) lasers, distributed Bragg reflector (DBR) lasers, distributed feedback (DFB) lasers, and External cavity lasers.

Fabry-Perot Laser

Fabry-Perot (FP) laser diodes are those whose mirrors are simply the flat cleaved surfaces at the either ends of the laser chip for creating positive feedback. The large index of refraction discontinuity at the semiconductor – air interface provides a reflection coefficient of around 30%. FP lasers are the default configuration for a laser (the usual population inversion, stimulated emission and positive feedback). These lasers are characterized by longitudinally multimode spectra with a wavelength spread of several nm to several ten nm.

Distributed Bragg Reflector lasers

The other alternative to create a resonant cavity in the active region is to put layers of different materials at the two ends of the active region. These layers would create high effective reflectivity at Bragg wavelength, hence the name Distributed Bragg Reflector. These kinds of lasers can emit single longitudinal mode which is linked to the Bragg wavelength.

Many important diode lasers use distributed passive grating reflectors for one or both cavity mirrors (Fig. 3.3 (a)). A DBR typically has two separate grating regions on either side of the gain region, and the grating doesn't overlap the gain region. With the in-plane lasers, the reason is to use their frequency selectivity for single axial mode operation and with vertical cavity lasers the reason is to obtain a very high value of reflectivity. Gratings consist of a periodic array of index variations. One of the issues here is to make transition between the active and passive waveguides without introducing an unwanted discontinuity. This is of little

concern for VCSEL case because the axial direction is the growth direction and switching materials is always done several times during growth. To manufacture edge emitting laser diodes with DBR mirror is relatively complex since a lot of structure must be created along the surface of the wafer which is because in-plane DBR lasers are only formed when their unique properties such as wavelength tunability are required.

Distributed Feedback Lasers

DFB lasers are very popular devices widely used in optical communication systems. A distributed feedback (DFB) laser also uses grating mirrors, but the gain is included in the gratings, Fig. 3.3 (b). Thus, it is possible to make a laser from a single grating, although it is desirable to have at least a fraction of a wavelength shift near the center to facilitate lasing at the Bragg frequency. DFB lasers are usually within the in-plane cavity types but vertical cavity versions are also possible, however there is no advantage over the DBR vertical cavity lasers and fabrication is not any easier.

The frequency selectivity of DFB lasers is due to the periodic grating which forms constructive interference between forward and counter propagating optical waves at certain wavelengths. Therefore, for resonance to happen, the wavelength has to match with the grating period, thus the resonant condition of a DFB laser is: $\lambda_g=2n\Lambda$ where λg is the Bragg wavelength and Λ is the grating period, and n is the effective refractive index of the optical waveguide.

In a simple DFB laser, there are two modes equally spaced on each side of the Bragg wavelength that reach threshold simultaneously if there is no additional perturbing reflections such as from uncoated cleaves at the end. The first method to avoid two-mode emission is by using additional reflections to destroy the unwanted degeneracy. In practice, at least one cleaved mirror will do the job if the gratings are not too long so the net reflection phase from one end is shifted from that of the grating. However, the phase relation between the facet reflectivity and grating reflectivity is difficult to control and the phase is random, so the yield of good DFB laser is limited. Another method is using anti-reflective coated facets and half/quarter-wave shifted configuration to improve the yield and phase adjustments.

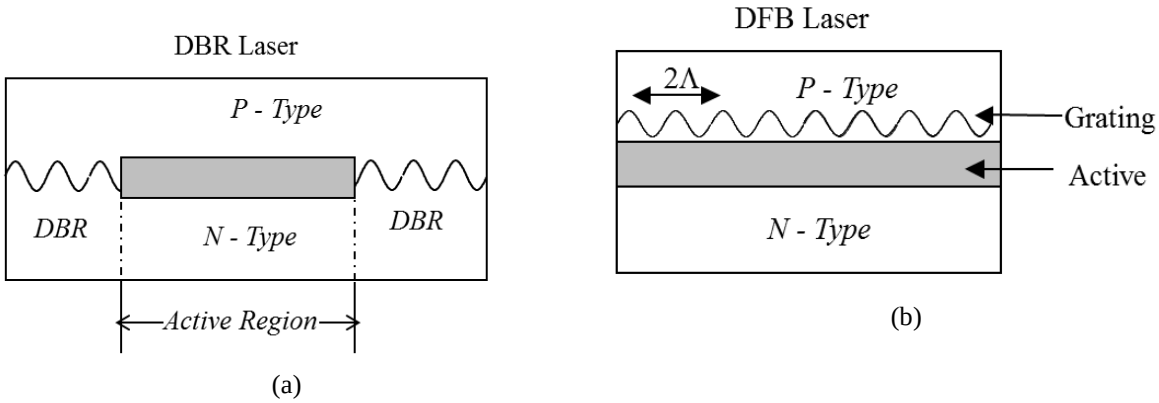

Fig. 3.3. Laser structures (a) DBR and (b) DFB.

External cavity lasers

Semiconductor lasers are very sensitive to external feedback, even a very small amount (order of -40 dB reflection) drive it from single mode operation to chaos. Therefore it is usual to put an isolator at the output of the laser to prevent an optical feedback from external optical interfaces. On the other hand, precisely controlled external optical feedback can be used to create wavelength tunable lasers with very narrow spectral linewidth.

An external-cavity diode laser is, therefore, a diode laser which typically has one end anti-reflection coated, and the laser resonator is completed with, a collimating lens and an external mirror as shown in Fig. 3.4. Another type of external-cavity laser uses a resonator based on an optical fiber rather than on free-space optics. Narrowband optical feedback can be obtained from a fiber Bragg grating. Longer resonator increases the damping time of the intra-cavity light and thus allows for lower phase noise and a smaller emission linewidth (in a single-frequency mode of operation). An intra-cavity filter such as the diffraction grating can further reduce the linewidth. Typical linewidths of external-cavity diode lasers are below 1MHz. One of the important advantages of external cavity lasers is its features for mode locking operation.

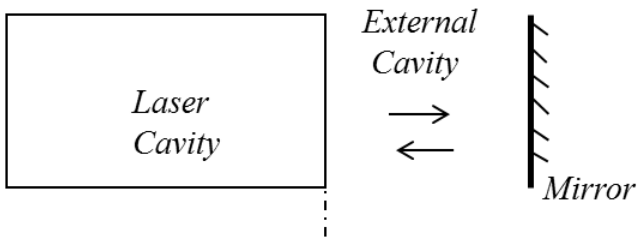

Fig. 3.4. External cavity laser.

Tunable semiconductor lasers

Modern WDM lightwave systems require single mode, narrow-linewidth lasers whose wavelength remains fixed over time. DFB lasers satisfy this requirement but their wavelength stability comes at the expense of tunability. A large number of DFB lasers used inside a WDM transmitter makes the design and maintenance of such a light-wave system expensive and impractical. The availability of semiconductor lasers whose wavelength can be tuned over a wide range would solve this problem. Typical tunable lasers are based on multi-section DFB and DBR structures. The current injected into the phase-control section is used to change the phase of the feedback from the DBR through carrier-induced index changes in that section. The laser wavelength can be tuned almost continuously over wide range of wavelength by controlling the currents in the phase and Bragg sections. Such lasers exhibited a tuning range of 17 nm and output powers of up to 100 mW with high reliability [79].

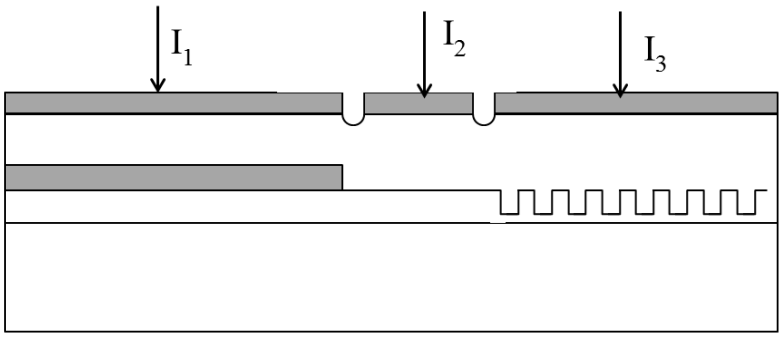

Fig. 3.5. Multi-section tunable laser.

3.2.2. Rate equations

The operating characteristics of semiconductor lasers are well described by a set of rate equations that govern the recombination effects of carriers inside the active region. Considering DFB lasers, the current injected to the active region is assumed to be uniform over the volume. Because of the diffusion of the charge carriers the amplification will then assume an approximately uniform value everywhere in the active region. In this section the single mode rate equations are used to discuss the steady-state characteristics, small-and large-signal modulation characteristics, and noise characteristics of a single-mode semiconductor lasers.

A rigorous derivation of the rate equations from Maxwell's equations together with a quantum-mechanical approach for the induced polarization can be performed to obtain the familiar equation that govern the physical phenomena in the active region [80]. However, they can also be obtained using intuitive approach by considering the phenomena that reduce and increase the carrier density, and photon density in the active region [78]. For standard double heterojunction semiconductors, the single mode rate equations for carriers, photons and optical phase in the active region can be written as follows:

$$\frac{dn}{dt} = \eta_i \frac{I_{bias}}{qV_{OL}} - \frac{n}{\tau_n} - v_g g\, p \tag{3.1}$$

$$\frac{dp}{dt} = \Gamma v_g g\, p + \Gamma\beta\frac{n}{\tau_n} - \frac{p}{\tau_p} \tag{3.2}$$

$$\frac{d\phi}{dt} = 2\pi\nu(t) = \frac{1}{2}\alpha\left(\Gamma v_g g - \frac{1}{\tau_p}\right) \tag{3.3}$$

where n and p are the carrier density and photon density in the active region respectively, η_i the internal quantum efficiency, I_{bias} bias current, q electron charge, V_{OL} the volume of the active region, τ_n carrier lifetime, v_g light group velocity in the active region, g stimulated emission gain, Γ confinement factor, β spontaneous emission factor, τ_p photon lifetime, ϕ the phase of the generated light, α the linewidth enhancement factor, and ν is the instantaneous optical frequency fluctuation.

Equation (3.1) indicates the rate at which electrons are created or destroyed inside the active region. The time rate of change of electrons is equal to the difference between total electrons injected to the active region and the electrons consumed to produce photon with stimulated emission and spontaneous emission. Other non-radiative recombination effects are assumed to be small compared to the spontaneous emission. While (3.2) defines the rate of change of photon density in the active region. In addition to the stimulated emission, a factor of the spontaneously emitted photons contributes to the lasing mode. In the phase equation (3.3) the instantaneous phase of the lasing mode is related to the change of carrier density. This phenomenon is known as the amplitude phase coupling effect represented by the linewidth enhancement factor. This means that whenever there is fluctuation of carrier density from the threshold value due to external modulation, the optical phase will be changed as well following the same profile as the change in the carrier density. This effect is known as the chirp effect. This is due to the fact that the refractive index, which is responsible for the change of propagation constant, depends on the carrier density.

The stimulated emission gain, *g*, is expressed as a function of both the carrier density and photon density. The relation between gain and carrier density can be well-approximated by a straight line, at least in the small-signal condition as $g = a(n - n_0)$ where n_0 is carrier density at transparency, and *a* is the differential gain. However better results could be obtained using logarithmic relation $g = a\ln(n/n_0)$ as shown in Fig. 3.6.

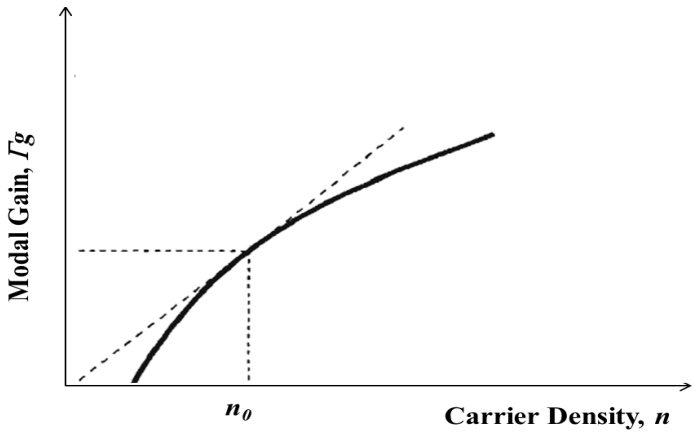

Fig. 3.6. Modal gain vs injected carrier density [78].

Different nonlinear gain models have been proposed for the relation between gain and photon density which is caused by different mechanisms such as spectral and spatial hole burning, two photons absorption [81] [82], and leakage current path [83]. Tucker *et al*. [84] introduced a multiplicative correction term $(1-\varepsilon p)$ based on phenomenological approach of two-level laser approximation, where ε is the gain compression factor. But in semiconductor lasers transitions could occur between various energy bands resulting in a large spread in transition frequencies. In [85], it is shown that the multiplicative factor gives multiple solutions. Channin [86] on the other hand proposed $(1+\varepsilon p)^{-1}$ which is positive for all values of the photon density. Another expression is also derived by Agrawal [82] using density matrix formalism yielding to correction term of $(1+\varepsilon p)^{-\frac{1}{2}}$ for the spectral hole burning effect

which is the dominant mechanism in most DFB lasers. In fact, the linear term is related to the first order Taylor series expansion of the others.

It must be stated that the contribution of gain compression should not be included in (3.3) because the index change associated with such nonlinear phenomena is expected to be much smaller than the carrier-induced index change, and hence doesn't have effect on the instantaneous phase or linewidth of the emitted optical signal unless in the case of very high power or non-cooled laser diode [80].

Although from theoretical point of view the three gain expressions show different behaviors, they give almost similar results in the laser dynamics at low photon density [87]. A comparison of the three gain expressions is shown in Fig. 3.7. At higher photon density level, the linear correction term compresses too much and hence gives an over estimation of the nonlinearity of the laser. However as can be seen from Fig. 3.8, the photon density for the entire bias current is within the region where the three nonlinear gains are almost equal. Therefore the linear gain compression term is used in this thesis since it has a good tradeoff between simplicity and accuracy.

$$g = a(n - n_0)(1 - \varepsilon p) \tag{3.4}$$

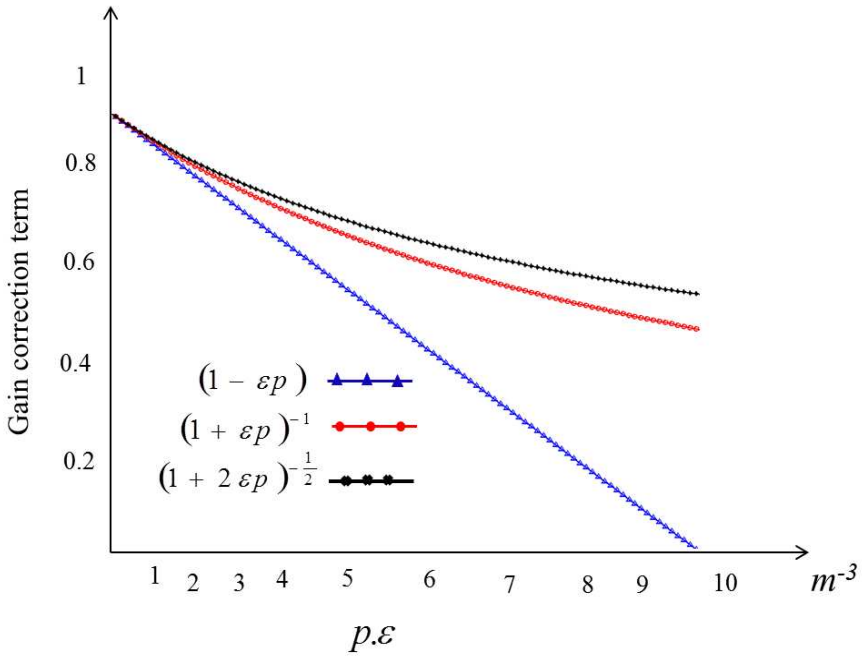

Fig. 3.7. Comparison of different gain expressions vs $p\varepsilon$.

In the following discussions, a DFB laser from EM4 Company is used to analyze the laser properties theoretically. The parameters used to obtain those properties are listed in Table 5 as follows:

Table 5. EM4 DFB laser parameters

Given parameters	Values
Central wavelength, λ	1550 nm
Threshold current, I_{th}	47mA
Slope efficiency, η_{LI}	0.29 mW/mA
Active region volume, V	$3.1\ 10^{-16}m^3$
Cavity length, L	1 mm
Linewidth enhancement factor, α	7.25
Spontaneous emission factor, β	$1.55\ 10^{-6}$
Differential gain, a	$4.323\ 10^{-21}m^2$
Carrier lifetime, τ_n	$2.9\ 10^{-9}s$
Photon lifetime, τ_p	$2.26\ 10^{-12}s$
Carrier density at transparency, n_0	$2.0\ 10^{24}m^{-3}$
Gain compression ratio, ε	$5.3\ 10^{-24}m^3$
Confinement factor, Γ	0.8

3.2.3. Steady-state characteristics

For the CW mode operation of the laser, the steady-state solution can be obtained by setting all time derivatives to zero. Two important features of steady-state are of general interest in characterizing laser performance, namely the light-current (L-I) curve which shows how the output power varies with the bias current; and the longitudinal-mode spectrum which indicates how the optical power is distributed among the various modes at a given current (for multimode lasers).

By setting *d/dt=0* in the rate equations, (3.1) and (3.2) can be simplified as

$$0 = \eta_i \frac{I_{bias}}{qV_{OL}} - \frac{n}{\tau_n} - v_g g p \tag{3.5}$$

$$0 = \Gamma v_g g\ p + \Gamma\beta \frac{n}{\tau_n} - \frac{p}{\tau_p} \tag{3.6}$$

With this simplification, the equations can be solved analytically, which will help us to understand some basic characteristics of semiconductor lasers. Considering (3.6), an expression for the photon density can be derived as

$$p = \frac{\beta \frac{n}{\tau_n}}{\frac{1}{\tau_p} - \Gamma v_g g} \tag{3.7}$$

This equation indicates that when the value of stimulated emission modal gain approaches $1/\tau_p$ (its threshold value), the photon density would approach infinite. The gain actually never reaches to its threshold value since carrier density will be clamped below its threshold value. At this point of operation, the laser is said to be reached at threshold. The threshold condition

can also be explained as follows: in order for a lasing mode to reach threshold, the gain in the active region must be increased to the point where all the propagation and mirror losses are compensated, so that the electric field of the photons exactly replicates itself after one round-trip in the cavity. Solving the round-trip equation of the photon by introducing the boundary conditions, we can get threshold conditions both for magnitude and phase. While the phase condition gives the modal wavelength, the threshold condition for magnitude can be given by

$$\Gamma v_g g_{th} = \frac{1}{\tau_p} \tag{3.8}$$

In the below threshold bias condition, solutions of (3.5) and (3.6) show that the total output optical power is negligible hence the injected current needs to supply carriers lost to radiative and non-radiative recombination. If the injection level is increased, the carrier density always stays below its threshold value (Fig. 3.8). So, the threshold current can be obtained from (3.5) and (3.8) under the below-threshold condition as

$$I_{th} = qV_{OL}\frac{n_{th}}{\eta_i \tau_n} = qV_{OL}\left(n_0 + \frac{1}{\Gamma v_g a \tau_p}\right) \tag{3.9}$$

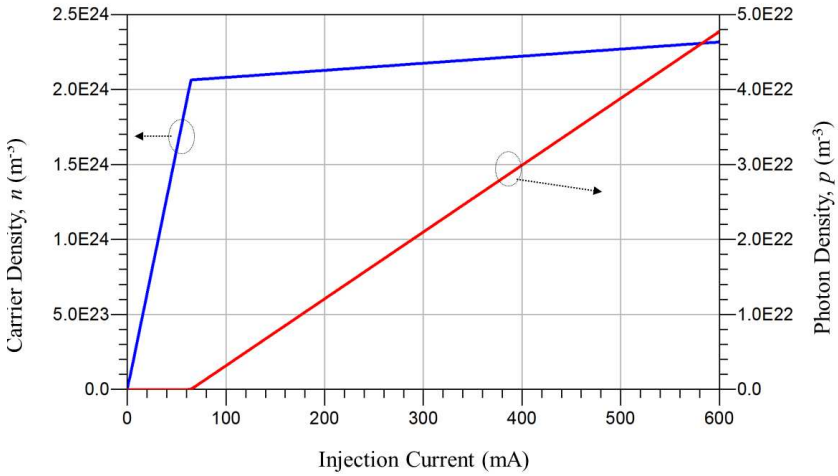

Fig. 3.8. Carrier and photon densities vs injection current of EM4 laser.

The laser output power can be obtained by considering the total number of photons that escape from the active region through the mirrors. The photon lifetime, τ_p, is related to the cavity loss by

$$\tau_p^{-1} = v_g \alpha_{cav} = v_g(\alpha_m + \alpha_i) \tag{3.10}$$

where α_i represents the intrinsic cavity losses and α_m refers to the amount of photons loss through the mirrors. For cleaved facet lasers (e.g. FP lasers), the equivalent mirror loss coefficient in the unit of [m^{-1}] can be defined as

$$\alpha_m = -\frac{1}{L}\ln(R) \tag{3.11}$$

where L is length of the active region, and R is the product of the mirrors' reflectivity. For DFB lasers the mirror loss should be adapted based on the structure of the laser and facet conditions.

In the above threshold case when the bias current increases, the carrier density and the actual gain approaches their respective threshold levels. The optical power output increases linearly with injection current and the total spontaneous emission saturates at a level found at threshold. The total output power emitted by the laser can be defined as the power that is emitted through the mirrors. If the laser has mirror of equal reflectivity, half of the total power will be emitted out of each sides. Considering that light is coming out from one of the mirrors, the total output power becomes

$$P_{opt} = \frac{1}{2} v_g \alpha_m h\nu P$$
$$= \frac{1}{2} \frac{h\nu}{q} \eta_d \left(I_{bias} - I_{th}\right) \tag{3.12}$$

where P is the photon number and η_d is defined as the differential quantum efficiency given by

$$\eta_d = \frac{\eta_i \alpha_m}{\alpha_i + \alpha_m} \tag{3.13}$$

The differential quantum efficiency η_d measures the efficiency of an increase in output light with an increase of the injected current while the internal quantum efficiency η_i indicates the fraction of terminal current that generates carriers in the active region.

Together with the mirror reflectivity, the differential quantum efficiency can be used to extract the intrinsic loss of the laser, α_m. The output optical power versus bias current plot (L–I curve) is given in Fig. 3.8. The slope of the curve which is usually referred as η_{LI} is therefore given by

$$\eta_{LI} = \frac{1}{2} \frac{h\nu}{q} \eta_d \tag{3.14}$$

The L–I curve indicates the threshold level and output power level for a given bias current. The linear relation holds true if the internal efficiency, confinement factor, and cavity losses remain constant at high injection levels.

Because of the temperature sensitivity of InGaAsP lasers, it is often necessary to control their temperature through a built-in thermoelectric cooler. As a result of the temperature, the slope of the light-current (L-I) curve decreases which can be attributed to junction heating occurring under CW operation. It can also result from an increase in internal losses or current leakage at high operating powers (Fig. 3.9). There is also a shift of the threshold current towards higher values. The relation between threshold current and temperature is given by [88]

$$I_{th}(T) = I(T_{ref})\exp\left(\frac{T - T_{ref}}{T_0}\right) \tag{3.15}$$

where $I(T_{ref})$ is the threshold current at a reference temperature and T_0 is a characteristic temperature often used to express the temperature sensitivity of threshold current. For InGaAsP lasers T_0 is typically in the range 50–70 K in contrast to 120 K for GaAs lasers. Therefore, InGaAsP lasers are temperature sensitive and it is often necessary to control their temperature through built-in thermoelectric cooler.

One important aspect of the DC characteristic (not indicated in Fig. 3.9) is that at very high bias current, the relation between bias current and output power is no more linear. The output power shows compression at high bias current.

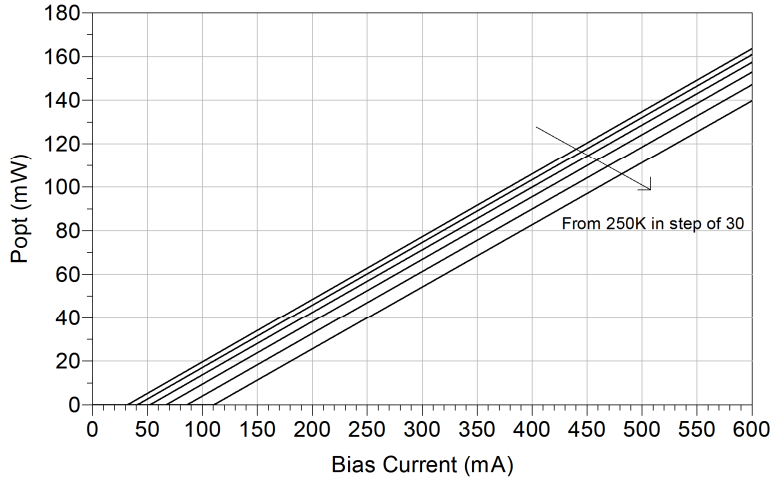

Fig. 3.9. L-I Characteristic curve of EM4 laser depending on temperature [79].

3.2.4. Intensity Modulation of semiconductor lasers

One of the very important features of semiconductor lasers is their ability to work in direct modulation operation. The DM scheme and the laser output power versus injection current of a typical semiconductor laser are shown in Fig. 3.10. Under direct modulation, the bias current causes not only the modulation of the output optical power but also modulation of the optical frequency/phase (chirp). In this section both intensity modulation and frequency modulation in the small and large-signal cases are covered.

The modulation response of the laser can be solved by assuming a time dependent modulation of the bias current above threshold $I(t) = I_{bias} + i_m(t)$ where i_m is the modulation current. For the analysis of small-signal modulation, the time varying term ($i_m(t)$) is small in magnitude and this helps us to linearize the rate equations simplifying the calculation to determine the modulation bandwidth.

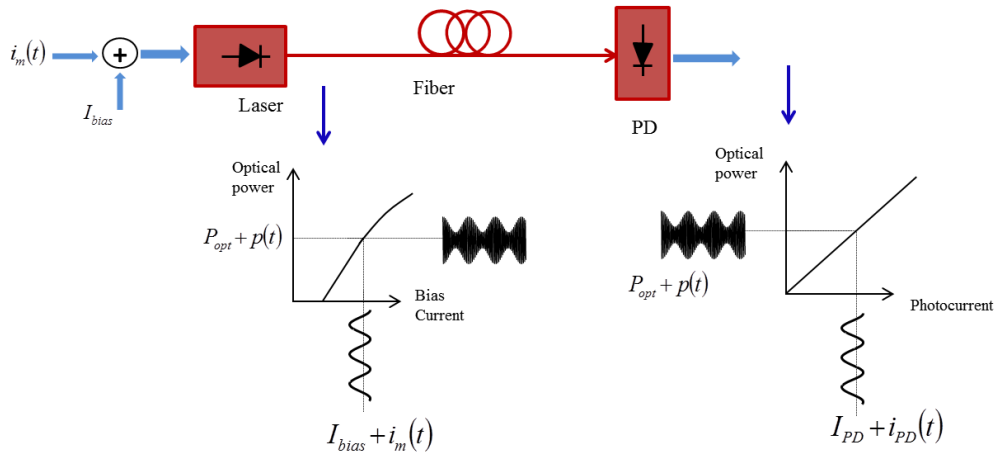

Fig. 3.10. Direct intensity modulation-direct detection RoF link.

*a). **Small-signal Intensity Modulation (IM)***

The small-signal analysis is based on the assumption that if the bias current varies periodically around its value, we can find useful analytic solution from the rate equation and the modulation bandwidth can be determined. The modulation current $i_m(t)$ introduces deviations on the carrier density, photon density and optical frequency/phase which are denoted as n_1, p_1, and ν_1. These deviations are periodic at a modulation frequency of ω. A criterion for the validity of small-signal approximation is generally expressed in terms of the modulation depth as $m<<1$ where m is given by

$$m = \frac{i_{m\_\max}}{I_{bias} - I_{th}} \tag{3.16}$$

Under small-signal modulation, the gain is dependent on carrier density and photon density (3.4); thus the gain will be affected by the two variations:

$$\partial g = a\, dn - a_p\, dp \tag{3.17}$$

The negative sign with a_p shows that gain decreases with increasing photon density. Relations for a_p and a can be derived from (3.4):

$$\begin{aligned} a &= \frac{\partial g}{dn} \\ a_p &= -\frac{\partial g}{dp} = -\varepsilon\, a\,(n - n_0) \end{aligned} \tag{3.18}$$

The differential gain coefficient, a, tends to decrease at higher photon densities, so it is assumed to be equal to g_0.

The rate equations for the small-signal fluctuations n_1 and p_1 can be linearized to obtain the solution in the frequency domain as follows

$$n_1 = \eta_i \frac{I_1}{qV_{OL}} . \frac{\Gamma v_g a_p p_a + j\omega}{\omega_R^2} H(\omega) \tag{3.19}$$

$$p_1 = \eta_i \frac{I_1}{qV_{OL}} . \frac{\Gamma v_g a\, p_a}{\omega_R^2} H(\omega) \tag{3.20}$$

with

$$H(\omega) = \frac{\omega_R^2}{\omega_R^2 - \omega^2 + j\omega\gamma} \tag{3.21}$$

Where, p_a is the steady state photon density at a particular bias current, I_1 is the magnitude of the modulation current in frequency domain, ω_R is the relaxation oscillation frequency and γ is the damping factor. Relaxation oscillation frequency and damping factor are the following expressions in the above threshold condition:

$$\omega_R^2 = \frac{v_g a\, p_a}{\tau_p} \tag{3.22}$$

$$\gamma = v_g a\, p_a + v_g a_p p_a + \frac{1}{\tau_n} \tag{3.23}$$

The relaxation oscillation frequency and the gain saturation phenomena can be explained from the rate equations as follows: when the gain in the active region is increased due to stimulated emission, photon density will increase which causes more carriers to be consumed and this causes the carrier density to be decreased creating gain saturation. As a result the photon density tends to be decreased due to the reduced optical gain. This saturation effect, in turn, will increase the carrier density; the process goes on this way. This whole phenomenon causes oscillation in the transient behavior of the light generation at an angular frequency of ω_R.

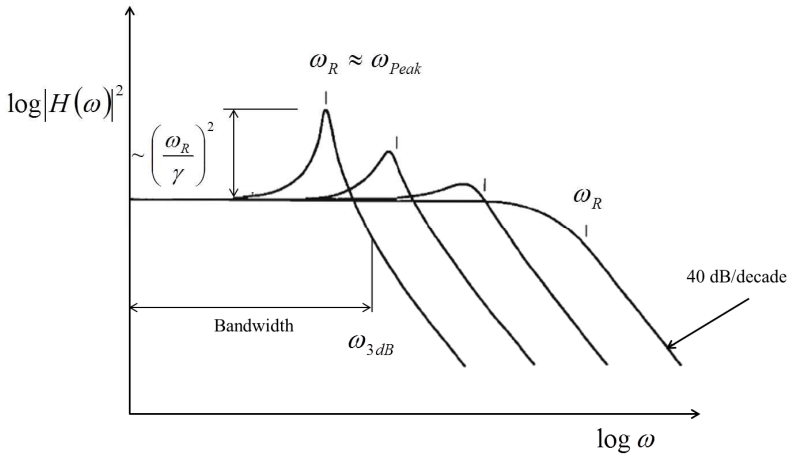

Fig. 3.11. Modulation transfer function of a semiconductor laser [78].

The parameter that is useful for practical systems that use DM of the light is the modulation bandwidth. It is defined as the frequency at which the modulation response has dropped by 3dB relative to its low-frequency or DC value. A sketch of the modulation transfer function of

a single mode semiconductor laser is given in Fig. 3.11. The response is flat at lower modulating frequencies and peaks around the relaxation oscillation frequency.

For the realistic evaluation of the modulation bandwidth, electrical parasitic effects associated with the packaging of the device should be considered as it may lead to a premature roll-off in the modulation response. However, it should be stated that for quantum well lasers with separate confinement heterostructure (SCH), the modulation bandwidth can be further reduced due to carrier transport effect. The transport effect introduces low-pass filter property on the intrinsic transfer function [89]. This effect can be eliminated by using narrower SCH region allowing a much larger modulation bandwidth.

*b). **Small-signal frequency modulation***

The amplitude modulation of the laser is always accompanied by frequency/phase modulation because of carrier-induced changes in the mode index. Any variation of the injection current yields a variation of the carrier density which in turn yields a variation of the refractive index and thus the optical emission frequency. This phenomenon of the dynamic shift of the emission frequency is referred to as frequency chirping. This frequency modulation effect may be desirable if we wish to dynamically tune the laser frequency, but for intensity modulation applications, the chirp limits the effectiveness of the optical link by broadening the modulated laser spectrum.

From (3.1) - (3.4), it is possible to relate the small-signal current modulation with the frequency modulation. The small-signal frequency modulation corresponding to the intensity modulation is obtained from (3.3), (3.19), and (3.20) as

$$\nu_1 = \frac{\alpha}{4\pi}\Gamma v_g a \eta_i \frac{I_1}{qV_{OL}} \frac{\Gamma v_g a_p p_a + j\omega}{\omega_R^2} H(\omega) \tag{3.24}$$

where ν_1 is the small-signal frequency fluctuation.

Equation (3.24) indicates that the amount of frequency modulation (FM) due to carrier fluctuation depends on the value of the linewidth enhancement factor. Just like the carrier density response, the FM response has a zero at $\Gamma v_g a_p p$ in the complex frequency plane and it follows the laser modulation transfer function.

By relating (3.20) and (3.24) we can obtain a simple result that relates the intensity modulation and frequency modulation (chirp) as follows:

$$\nu_1 = \frac{\alpha}{4\pi}\left(\Gamma v_g a_p p_a + j\omega\right)\frac{p_1}{p_a} \tag{3.25}$$

If we define $M=\nu_1/f$ as the frequency modulation index, we can relate the intensity modulation (IM) and FM modulation indices using (3.16) and magnitude of (3.25) as

$$\frac{M}{m} = \frac{\alpha}{2}\sqrt{\left(\frac{\Gamma v_g a_p p_a}{\omega}\right)^2 + 1} \tag{3.26}$$

It is shown in Fig. 3.12 that the normalized FM and IM responses have the same shape. Both responses exhibit peak around the relaxation oscillation frequency, but the IM response falls quickly after the resonance peak with 40dB/decade compared to 20dB/decade in the FM response.

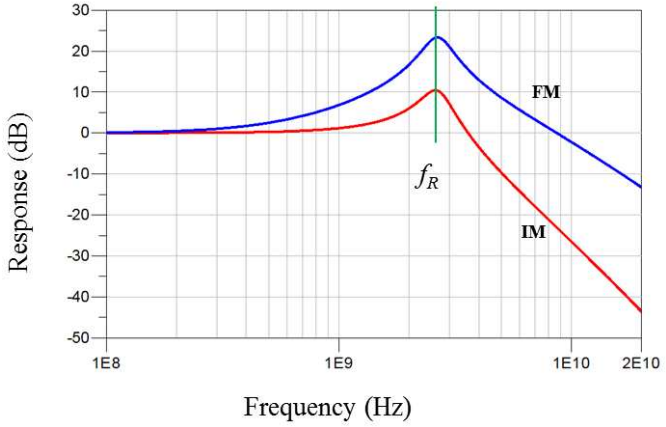

Fig. 3.12. Comparison of IM and FM modulation response of EM4 laser.

*c). **Large-signal modulation***

For practical purposes in communication applications, the modulation depth does not satisfy the small-signal approximation and therefore, the linearity applied for small-signal analysis will no more apply. Therefore, nonlinear effects will play an important role under large-signal condition. Large-signal intensity modulation is considered when the laser is typically biased close to threshold and modulated considerably above threshold. In this case, the rate equations cannot be solved analytically and therefore numerical analysis is necessary.

The FM response under large-signal can be estimated from the third rate equation (3.3) and the first order expansion of the gain around its threshold value which is written as

$$g = g_{th} + a(n - n_{th}) - a_p p \tag{3.27}$$

Substituting this gain expression and (3.8) into (3.3) we can relate the carrier variation to the change of photon density in the large-signal condition. This leads to an approximated relation between the frequency chirp and the optical power (P_{opt}) as [90]

$$\Delta\nu = \nu(t) - \nu_{th} = \frac{\alpha}{4\pi}\frac{1}{P_{opt}(t)}\frac{dP_{opt}}{dt} \tag{3.28}$$

This relation only assumes the frequency fluctuation as a function of carrier fluctuation. But at low modulation frequencies, the bias current also introduces modulation of the laser temperature which changes the index of the active material hence modulates the optical frequency [90]. This kind of chirp due to temperature is called adiabatic chirp and the total chirp is the sum of contributions from carrier variation and temperature effects.

3.2.5. Noise characteristics of semiconductor lasers

The optical signal emitted from semiconductor laser shows both intensity and phase fluctuations even at a fixed DC bias current. These variations are due to the random nature of photon generation where incoherent photons can be generated due to random electron-hole recombination and spontaneous emission. These phenomena introduce both instantaneous intensity and phase fluctuations (noise) on the emitted optical signal. The noises associated with semiconductor lasers can be manipulated using Langevin noise formulations where white noise sources are added to each rate equations to take into account random electron-hole recombination and spontaneous emission both for intensity and phase equations. Thus, by inserting the gain expression (3.4) to equations (3.1), (3.2) and (3.3), the rate equations with Langevin noise sources become

$$\frac{dn}{dt} = \eta_i \frac{I_{bias}}{q} - \frac{n}{\tau_n} - v_g a(n - n_0)(1 - \varepsilon\, p)p + F_n(t) \tag{3.29}$$

$$\frac{dp}{dt} = \Gamma v_g a(n - n_0)(1 - \varepsilon\, p)p + \beta \frac{n}{\tau_n} - \frac{p}{\tau_p} + F_p(t) \tag{3.30}$$

$$\frac{d\phi}{dt} = \frac{1}{2}\alpha\left(\Gamma v_g a(n - n_0) - \frac{1}{\tau_p}\right) + F_\phi(t) \tag{3.31}$$

where $F_n(t)$ is noise due to the nature of electron-hole recombination processes, $F_p(t)$ represents the intensity of spontaneously emitted photons, $F_\phi(t)$ represent the random phase of the photon generated by spontaneous emission. Langevin noise sources corresponding to the carrier density and photon density are in unit of $s^{-1}cm^{-3}$.

In the presence of Langevin noise sources, n, p, ϕ become random equations. Dealing with these random equations could be complex, so considering the system as memory-less (the correlation time of the noise sources is much smaller than the relaxation times) simplifies the solution considerably. Under this assumption, the Langevin sources satisfy the relations

$$\langle F_i(t)\rangle = 0 \quad , \quad \langle F_i(t)F_j(t)\rangle = 2D_{ij}\delta(t - t') \tag{3.32}$$

where the angle brackets denote ensemble average and D_{ij} is the correlation strength associated with the corresponding noise sources given by

$$\begin{aligned} D_{pp} &= \beta \frac{n_a}{\tau_n} p_a \\ D_{nn} &= \beta \frac{n_a}{\tau_n} p_a + \frac{n_a}{\tau_n} \\ D_{\phi\phi} &= \beta \frac{n_a}{4 p_a \tau_n} \\ \text{and } D_{pn} &= -\beta \frac{n_a}{\tau_n} p_a \quad , D_{p\phi} = D_{n\phi} = 0 \end{aligned} \tag{3.33}$$

where p_a, n_a represent the steady-state values of the carrier and photon densities.

*a). **Intensity noise***

Intensity noise is the fluctuation of the power emitted by a laser around its steady-state value. The spectrum of these fluctuations can be measured by detecting the laser output using a wide bandwidth photodiode and an electrical spectrum analyzer. Such a measurement yields the noise spectrum associated with the total power. Fig. 3.13 shows the intensity noise on the output power when it is modulated with an analog signal.

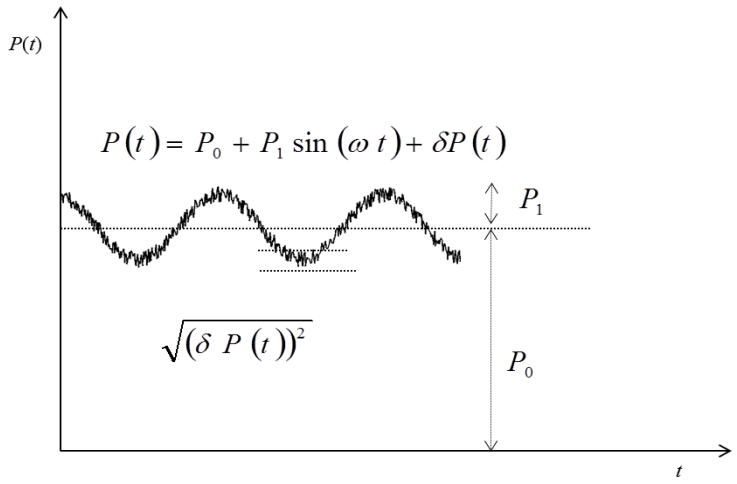

Fig. 3.13. Intensity noise on modulated laser signal for analog applications.

The intensity noise at a given angular frequency, ω, is characterized by the relative intensity noise (RIN, per unit measurement bandwidth) can be expressed as

$$\frac{RIN}{\Delta f} = 2\frac{S_{\delta P}(\omega)}{P_0^2} \tag{3.34}$$

where $S_{\delta P}$ is the double sideband spectrum of the power fluctuation, and is related to the mean-square power by

$$\left\langle \delta P(t)^2 \right\rangle \approx \mathrm{S}_{\delta P}(\omega).2\Delta f \tag{3.35}$$

and Δf is the spectral measurement filtering window.

Thus the intensity noise in a semiconductor laser can be related to laser parameters using small-signal analysis as [80]

$$\frac{RIN}{\Delta f} = \frac{\Gamma \beta n_a}{4\pi \tau_n p_a} \frac{\omega^2 + \gamma^2}{\left(\omega_R^2 - \omega^2\right)^2 + (\omega\gamma)^2} \tag{3.36}$$

Fig. 3.14 shows simulated RIN spectrum at three power levels of EM4 DFB laser with parameters given in Table 5. The RIN is considerably enhanced near the relaxation oscillation frequency ω_R but decreases rapidly for $\omega >> \omega_R$. At a given frequency, RIN decreases with an increase in the laser power.

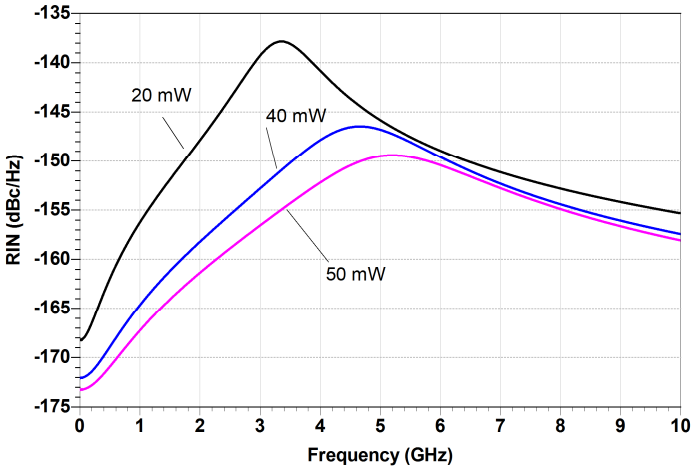

Fig. 3.14. RIN spectra at several power levels of EM4 laser.

b). ***Phase/Frequency noise***

The phase/frequency noise of the laser is related to the quantum fluctuations associated with the lasing process which affects both the intensity and phase of the optical signal. This noise is of interest in evaluating the performance of coherent and heterodyne optical communication systems. The third rate equation (3.31), shows mechanisms that contribute to phase fluctuations. The first term shows that fluctuations in the carrier populations lead to a phase change while the second term shows the spontaneous emission contribution. As discussed before, a small change in carrier density affects the optical gain, which in turn changes the refractive index and consequently the phase. The linewidth enhancement factor α provides a proportionality between the gain and index changes [91].

The frequency and phase noise power spectrums can be obtained from (3.31) in the frequency domain

$$S_\nu(\omega) = \frac{1}{2\pi}\frac{\Gamma\beta n_a}{4\pi\tau_n p_a}\left(1+\alpha^2\left|H(\omega)\right|^2\right) \tag{3.37}$$

$$S_\phi(\omega) = \frac{1}{f^2}S_\nu(\omega) \tag{3.38}$$

The frequency noise spectrum has similar qualitative behavior to that of the magnitude square of the laser transfer function. So a peak around the relaxation oscillation frequency is observed as shown in Fig. 3.15.

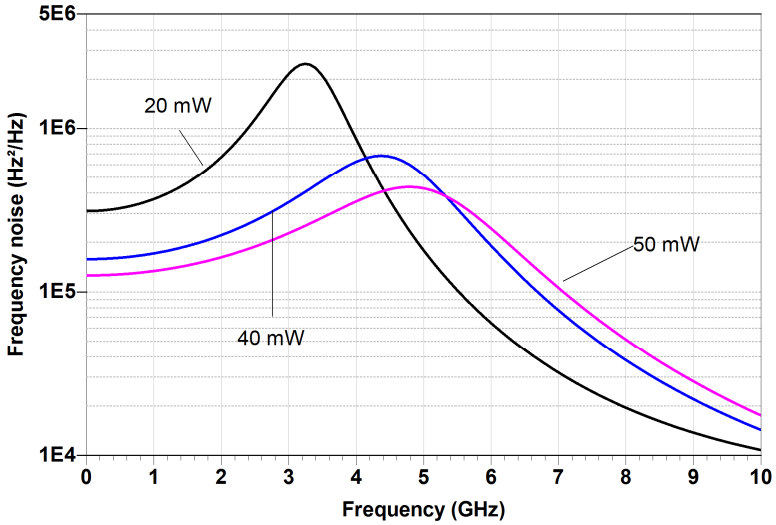

Fig. 3.15. Frequency noise spectrum of EM4 laser.

*c). **Spectral Linewidth***

The linewidth of a single longitudinal mode under CW operation is a manifestation of phase fluctuations occurring inside the laser which is usually few MHz. The linewidth of the laser emission ($\Delta\nu$) is defined as full-width half-maximum (FWHM) of the light spectrum. For semiconductor lasers, the linewidth can be derived from the autocorrelation function of the optical field which has Lorentzian shape as

$$\Delta\nu \cong 2\pi S_\nu(0) = \frac{1}{4\pi}\frac{\Gamma\beta n_a}{\tau_n p_a}\left(1+\alpha^2\left|H(0)\right|^2\right) \tag{3.39}$$

The frequency chirp is directly proportional to α while the linewidth depends on the square of α. The linewidth is inversely proportional to the optical power, but at very high power level, the linewidth starts to be independent of power due to additional terms that have to be included in (3.39) such as *1/f* noise [92].

It is experimentally demonstrated that the increase in residual spectral linewidth in a multiple quantum-well (MQW) distributed-feedback (DFB) laser is due to an increase in 1/*f* noise. Therefore, the FM noise spectrum of the laser is given by a sum of the white noise component and *l*/*f* noise component [92]. If the *1/f* noise is taken into account, the frequency noise spectral density is related to the linewidth as follows

$$S_\nu(f) = \frac{\Delta\nu}{2\pi} + \frac{k_f}{f} \tag{3.40}$$

where k_f is a constant related to the *1/f* noise. This makes the autocorrelation function to deviate from Lorentzian shape to Gaussian shape. This is the reason why linewidth measurements tend to show linewidth saturation at high power, there is even an increase in linewidth as the power is pushed further high as shown in Fig. 3.16.

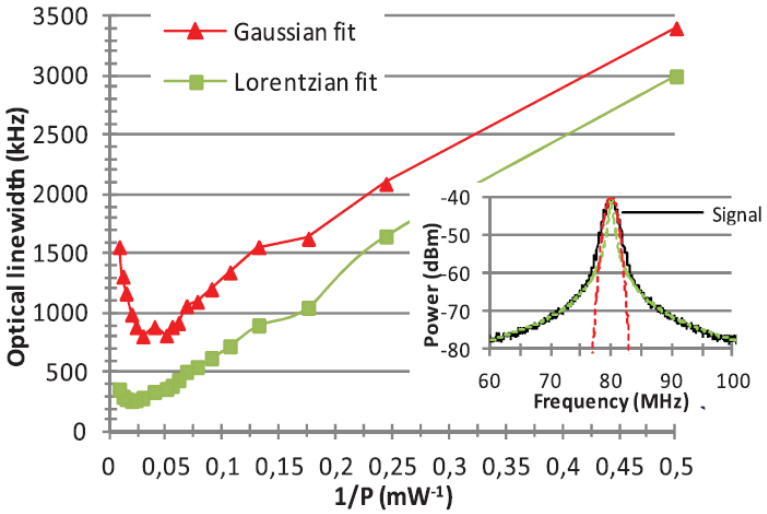

Fig. 3.16. Optical linewidth for two different fits at 25 °C [21].

*d). **Low-frequency noise (1/f RIN)***

The noise analysis based on the rate equations and Langevin noise sources exhibit a flat noise spectrum at lower frequencies and peaks at the relaxation oscillation frequency. However, experimental results of noise measurements of semiconductor lasers show that there is a 1/*f* component in the spectrum at low frequency ranges [93] [94]. This low-frequency noise is observed both in intensity noise spectrum and frequency noise spectrum. Studies show that the 1/*f* noise in semiconductor lasers could have an ultimate physical limit based upon similar factors to fundamental noise generated in other semiconductor and solid state devices.

There are two existing theories as to the origin of low-frequency fluctuations in the laser diode and how the low-frequency noise is affected by the injection current modulation. The first hypothesis argues that low-frequency intensity fluctuations are due to trapping of carriers in the semiconductor medium with a 1/*f* power low-frequency spectrum, while the other view holds that competitions between longitudinal modes of the laser diode causes an enhancement of low-frequency fluctuations.

If we assume that the low-frequency noise is caused by the modes competition in the active layer, then theoretically, the 1/*f* noise should disappear completely if mode-competition is completely suppressed by perfect mode-locking. And it should disappear in the case of a purely single mode laser. However, studies revealed that the residual level of 1/*f* noise is often observed even in the single mode DFB lasers. Therefore, for single model lasers such as DFB laser, the origin of low-frequency noise should be due to the trapping of carriers inducing additional behavior of carrier fluctuations. Trapping of carriers will cause the non-radiative recombination current to fluctuate and eventually introduces slow modulation of the injected carrier density.

For a single mode laser, the 1/*f* noise can be expressed in the rate equation as [95]

$$\frac{dn}{dt} = \eta_i \frac{I_{bias}}{q} - \frac{n}{\tau_n} - v_g a(n - n_0)(1 - \varepsilon p)p + F_n(t) + F_{n,1/f}(t) \qquad (3.41)$$

The spectrum of the low-frequency noise, $F_{n,1/f}$ is given by [96] [97]

$$\left\langle F_{n,1/f}^2(f)\right\rangle = \frac{\alpha_H n_{th}}{V_{OL}\tau_n^2 f} \tag{3.42}$$

where α_H is Hooge's parameter.

Equation (3.41) will not only introduce low-frequency noise on the output optical power but it will also have effect on the third rate equation and hence the linewidth of the optical signal increases since the frequency noise spectrum changes from (3.39) to (3.40).

3.2.6. Two level rate equations

The operating characteristics of high speed semiconductor lasers can be affected by the carrier transport effect due to the separate confinement heterostructure (SCH). This can be characterized by using current continuity equation for the carrier in the SCH (Fig. 3.17). Assuming the filling of electrons throughout the quantum-wells (QWs) is homogeneous, we can establish another rate equation that considers the drift of carriers across the SCH, the carrier capture by the QWs, and the carriers that escape from QWs. Therefore the rate equations for carrier and photon density become [98]:

$$\frac{dn_B}{dt} = \eta_i \frac{\Gamma_q I_{bias}}{qV_{OL}} - \frac{n_B}{\tau_s} + \frac{\Gamma_q n}{\tau_e} \tag{3.43}$$

$$\frac{dn}{dt} = \frac{n_B}{\Gamma_q \tau_s} - n\left(\frac{1}{\tau_n} + \frac{1}{\tau_e}\right) - v_g g\, p \tag{3.44}$$

$$\frac{dp}{dt} = \Gamma v_g g\, p + \Gamma\beta\frac{n}{\tau_n} - \frac{p}{\tau_p} \tag{3.45}$$

where n_B is the carrier density in the SCH, n_B/τ_s is the rate of carrier loss from the SCH region to the quantum-well active region, $\Gamma_q = V_{OL}/V_{SCH}$ is the fraction of SCH region filled by the QW active region, and n/τ_e is the rate of carrier loss from the QW to the SCH region.

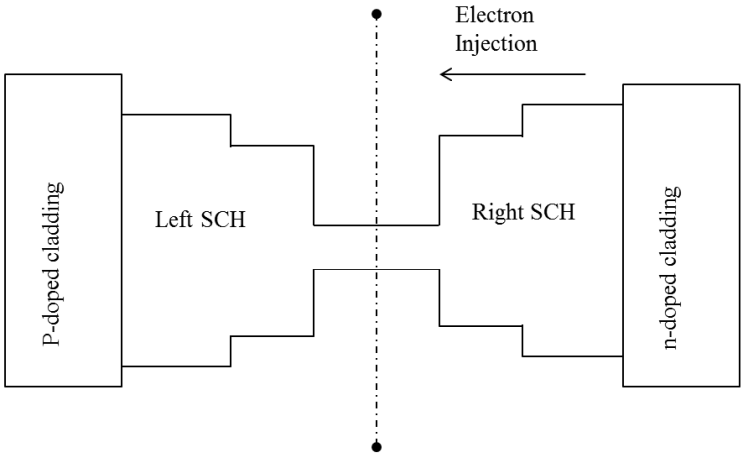

Fig. 3.17. Single quantum well structure with SCH.

Small-signal analysis performed to obtain the small-signal modulation response shows that the transport effect introduces parasitic like roll-off. The small-signal output power modulation response is given by

$$\frac{P_1}{I_1} = \eta_i \frac{h\nu}{q} \frac{1}{1 + j\omega\tau_s} \cdot \frac{\omega_{RT}^2}{\omega_{RT}^2 - \omega^2 + j\omega\gamma_T} \tag{3.46}$$

where the subscript '*T*' refers to parameters influenced by transport effect compared to the intrinsic transfer function without SCH in (3.21). The above expressions for the modulation response have low-pass filtering factor with cutoff at $\omega=1/\tau_e$, new relaxation frequency, and damping factor values. The SCH region reduces the differential gain from a to a/χ, where the factor $\chi=1+(\tau_s/\tau_e)$. But the gain compression factor remains unchanged. The reduced differential gain reduces the relaxation oscillation frequency and increases the damping factor. As a result, for high value of τ_s the modulation bandwidth of the device will be reduced.

The expression for the relative intensity noise can also be obtained using the small-signal analysis by making the Langevin noise sources as driving force [98] as shown in (3.47). It has been reported that the additional low frequency roll-off in the modulation response is absent in the RIN expression.

$$RIN \cong \frac{\Gamma\beta n_a}{4\pi\tau_n p_a} \frac{\omega^2 + \gamma_T{}^2}{\left(\omega_{RT}^2 - \omega^2\right)^2 + (\omega\gamma)^2} \tag{3.47}$$

This is an indication of the fact that in the presence of transport effect, the maximum possible bandwidth of the laser cannot be determined directly from the relaxation oscillation frequency reading of the RIN spectrum because of the additional low pass behavior of the modulation response. It is important to note that the transport effect (low pass behavior of the modulation response) is eliminated if the separate confinement heterostructure is narrow.

3.2.7. Electrical modeling of semiconductor lasers

As high-speed semiconductor lasers continue to be important in analog microwave and millimeter-wave optical links, detailed analysis of its operating characteristics is crucial to the design of those links. The equivalent circuit model of a packaged semiconductor laser can be developed based on the scheme suggested by [99] where parasitic circuit and intrinsic laser circuits form cascaded networks to obtain the complete laser model. The small signal, large-signal and noise models of the intrinsic laser for a general double heterojunction laser can be obtained from the single mode rate equations. The model can be used to represent different laser structures as long as they are represented by the single mode rate equations. The circuit parameter values for the different laser structures have to be determined from measurement values [100].

This section explains the general approach of circuit modeling of single mode semiconductor lasers from the rate equations for system simulation purposes. The large-signal equivalent circuit model of the laser is enhanced by introducing the laser phase noise into the model which will be used to investigate the phase noise influences on system performance in the next chapter.

*a). **Small-signal model***

The small-signal impedance characteristic of an intrinsic laser diode model was studied in [8]. The small-signal model is constructed from the impedance function obtained from the rate equations under small-signal modulation of the bias current and by arranging the circuit elements to have values of lumped RLC components. This model is then extended in [9] by including the effect of spontaneous emission which is coupled to the lasing mode. Laser noise is added by including Langevin noise sources formulation in [10]. The small-signal circuit model can be used to determine the modulation response, noise and parasitic circuit effects.

However, those previous models were based on the rate equations which did not include lateral carrier diffusion. In [11], the small-signal circuit of the laser that takes into account many factors such as space-charge capacitance, heterojunction I_V characteristics, carrier diffusion effects and parasitic circuits is presented. The non-uniform electron density in the lateral axis causes the carrier diffusion effect and it is modelled by gain compression term in the rate equations.

Fig. 3.18 shows a widely accepted small-signal equivalent circuit [11] where the input terminals represent the electrical contacts on the device chip. Contact capacitance and series resistance between the contacts and active layer, and space-charge capacitance are modeled by C_s, R_s and C_f respectively. The small-signal photon density is proportional to the current in the inductive branch of the model. Alternatively, the output voltage across R_{s2} can be used to represent optical intensity.

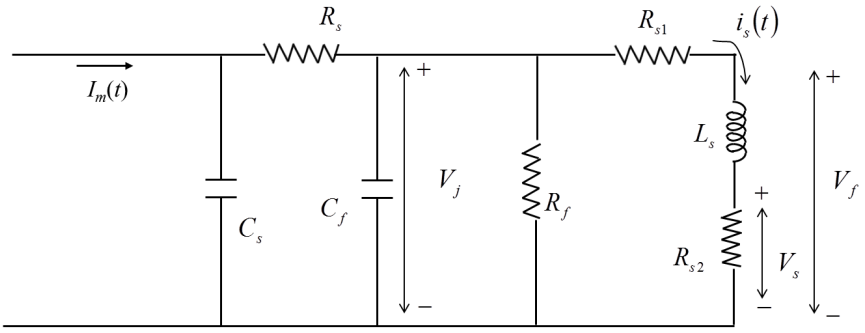

Fig. 3.18. Small-signal equivalent circuit of the laser diode.

*b). **Large-signal and noise circuit model***

Compared with small-signal equivalent circuit, the synthesis of a large-signal model is trivial. The advantage of large-signal electrical model is that it can represent the signal in the large-signal condition and also can be reduced to small-signal model under the small-signal condition. These kinds of models were first proposed by [12] where the laser junction is represented by the simple Shockley diode. The large-signal circuit model enables the simulation of laser characteristics by a general purpose nonlinear circuit analysis program.

The large signal model can be easily derived from the rate equations by writing (3.1) and (3.2) into manageable nodal circuit current equations. The node currents can be written as follows

$$\eta_i I_{bias} = I_{sp} + \tau_n \frac{dI_{sp}}{dt} + I_{st} \tag{3.48}$$

$$I_{st} + \beta I_{sp} = \frac{V_p}{R_p} + C_p \frac{dV_p}{dt} \tag{3.49}$$

where:

$$I_{st} = qV_{OL} v_g a(n - n_0)(1 - \varepsilon p) p \tag{3.50}$$

$$I_{sp} = qV_{OL} \frac{n}{\tau_n} \tag{3.51}$$

$$p = \Gamma S_n V_p \tag{3.52}$$

$$R_p = \frac{\tau_p}{qV_{OL} S_n} \quad \text{and} \quad C_p = qV_{OL} S_n \tag{3.53}$$

$S_n = (V_{OL})^{-1}$ $V^{-1}m^{-3}$ and V_p represents the number of photons but in unit of Volt. I_{st} is the stimulated current which includes the differential gain term, a, and the gain compression term ε. We can observe from (3.48) that the bias current is distributed into three branches: the diode junction current, instantaneous carrier fluctuation and stimulated emission. On the other hand (3.49) shows that the stimulated emission current and a portion of spontaneous emission current are dissipated in the resistor R_p and stored in the capacitor C_p. Therefore, R_p and C_p represent the photon loss and storage mechanism in the active region. Therefore, writing the equations as functions of input current I_{bias} and output voltage V_p will allow us to construct the equivalent circuit as shown in Fig. 3.19.

This two-port circuit model represents the intrinsic laser, and it can be cascaded with real driving microwave circuits and parasitic elements related to connectors, packaging effects and matching network for maximum RF power transfer during DM operation. Therefore, the model can be used for simulations from the circuit-level to the system-level performance analysis.

The voltage V_p at the output port is proportional to the optical power output of the laser which is obtained under steady state condition ($d/dt = 0$) as

$$P_{opt} = 0.5\eta_d \frac{h\nu}{\tau_p} V_p = \eta_{LI} (I_{bias} - I_{th}) \tag{3.54}$$

where h is Planck's constant, ν is the lasing frequency, and η_{LI} is laser slope efficiency (mW/mA). Note that the first equality is direct relation of the output voltage of the model and the optical power output.

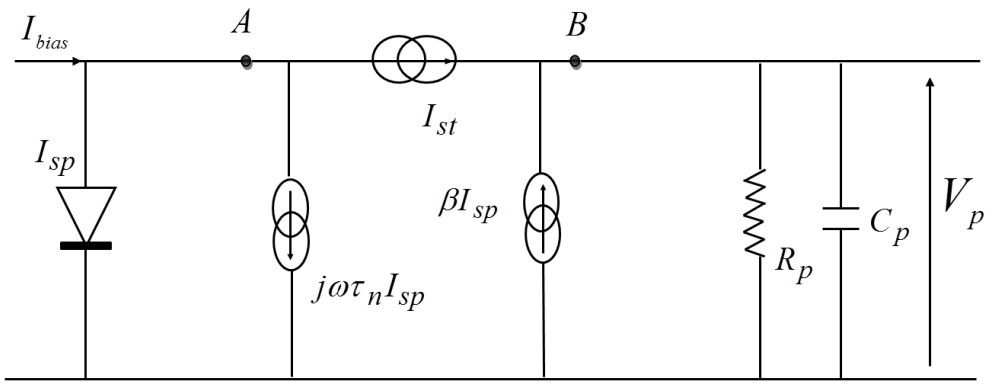

Fig. 3.19. Large-signal Equivalent circuit of QW laser based on one level rate equations.

It can be seen from the model that both the electrical and optical properties of the device are represented in the model. The electrical property of the laser is obtained from the left side (node A) of the model and it is used to evaluate the V-I characteristic of the laser diode junction, V_j. The input port of this model represents the electrical contact points where parasitic circuits and matching networks have to be cascaded. The right side of the model characterizes the optical cavity, denoting the rise and fall of the photon density in the active region. The optical power output is proportional to the voltage at B.

The junction current (I_{sp}) is represented by the diode current equation

$$I_{sp} = I_{sat} \exp\left(\frac{V_A}{\gamma k_B T/q}\right) \tag{3.55}$$

where I_{sat} is the saturation current, V is the hetero-junction voltage, γ is diode ideality factor, T is the ambient temperature and k_B is Boltzmann constant.

The modulation response of the laser diode can be obtained by simply evaluating the ratio of output voltage over input current in the frequency domain as

$$H(\omega) = \frac{V_s(\omega)}{I(\omega)} \tag{3.56}$$

where $V_s(\omega)$ is the output voltage and $I(\omega)$ is the input modulating current.

The effect of temperature on the threshold current and slope of the L-I curve is modeled by taking (3.15) into account. This can be achieved by modifying model parameters such as differential gain and carrier density at transparency that depend on temperature. The differential gain coefficient, a, is proportional to the exponential term $exp(-\Delta T/T_0)$ while the carrier density at transparency (n_0) is proportional to $exp(\Delta T/T_0)$. But the dependency of internal injection efficiency (η_i) [101] on temperature is not included.

c). Noise Model

The noise in semiconductor lasers is modelled by the white Langevin noise sources (3.29) and (3.30). The spectral densities of Langevin noise currents related to the laser cavity parameters are given by [78]

$$\left\langle {i_n}^2 \right\rangle = q^2 V_{OL}^2 \left\langle {F^2}_n(f) \right\rangle = q^2 V_{OL}^2 \left(\frac{n_a}{\tau_n} + 2\beta \frac{n_a}{\tau_n} \frac{p_a}{\Gamma} \right) \tag{3.57}$$

$$\left\langle {i_p}^2 \right\rangle = q^2 V_{OL}^2 \left\langle {F^2}_p(f) \right\rangle = q^2 V_{OL}^2 2\beta \frac{n_a}{\tau_n} \frac{p_a}{\Gamma} \tag{3.58}$$

These average values can be obtained from the DC response of the laser at the required bias level. By adding current noise sources i_n and i_p to the carrier density (3.48) and photon density (3.49) node current equation respectively, the large-signal equivalent circuit model can include the laser noise sources as shown in Fig. 3.20.

The low-frequency noise can be simply added to the carrier side of the large-signal model. Its spectral density is given in (3.42).

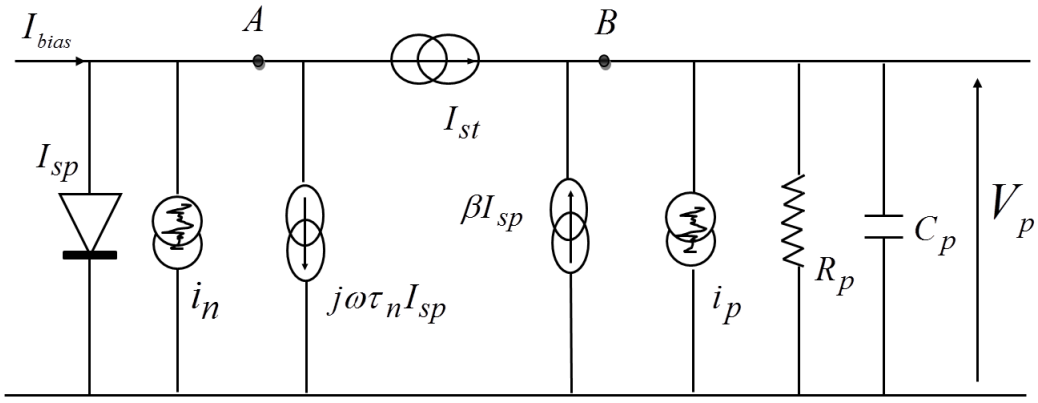

Fig. 3.20. Large-signal and noise model.

*d). **Including Transport effect***

To include the transport effect of carriers across the SCH, the rate equation that determines the dynamics of carriers in the SCH should be considered. The equivalent circuit model can be obtained by writing the two level rate equations (3.43) - (3.45) as current nodal equations as follows

$$\eta_i I_{bias} + qV_{OL} \frac{n}{\tau_e} = \frac{qV_{OL}}{\Gamma_q} \frac{n_B}{\tau_s} + \frac{qV_{OL}}{\Gamma_q} \frac{dn_B}{dt} \tag{3.59}$$

$$\frac{qV_{OL}}{\Gamma_q} \frac{n_B}{\tau_s} - qV_{OL} \frac{n}{\tau_e} = qV_{OL} \frac{n}{\tau_n} + qV_{OL} \frac{dn}{dt} + qV_{OL} v_g gp \tag{3.60}$$

$$\frac{dp}{dt} = \Gamma v_g g\ p + \Gamma\beta \frac{n}{\tau_n} - \frac{p}{\tau_p} \tag{3.61}$$

These equations can be reduced to:

$$\eta_i I_{bias} + \frac{\tau_n}{\tau_e} I_{sp} = \frac{V_B}{R_B} + C_B \frac{dV_B}{dt} \tag{3.62}$$

$$\frac{V_B}{R_B} - \frac{\tau_n}{\tau_e} I_{sp} = I_{sp} + \frac{dI_{sp}}{dt} + I_{st} \tag{3.63}$$

$$I_{st} + \beta I_{sp} = \frac{V_p}{R_p} + C_p \frac{dV_p}{dt} \tag{3.64}$$

where $V_B = \frac{n_B}{C_n}$

$$R_B = \frac{\Gamma_q \tau_s}{q V_{OL}} \frac{1}{C_n}$$

$$C_B = \frac{q V_{OL} C_n}{\Gamma_q} \tag{3.65}$$

$$C_n = \frac{1}{V_{SCH}}$$

I_{sp}, I_{st}, V_s are similar to the node currents in the quantum well model

The right hand side of (3.63) and (3.64) represent the intrinsic laser. The large-signal equivalent circuit of the laser can be developed using (3.62) and (3.64) is shown in Fig. 3.21. The intrinsic laser model is contained in separate block.

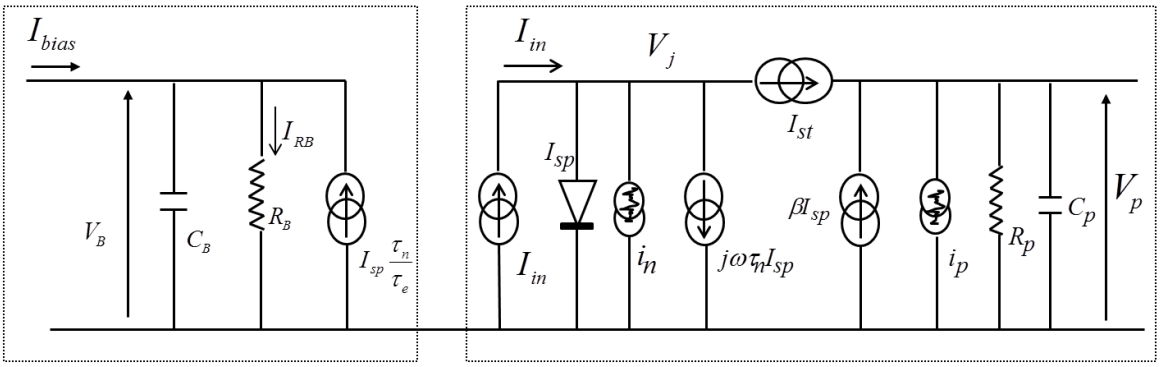

$$I_{in} = I_{RB} - I_{sp} \frac{\tau_n}{\tau_e}$$

Fig. 3.21. Large-signal equivalent circuit of quantum well lasers based on two level rate equations.

*e). **Complete DFB laser circuit model***

The equivalent circuit models discussed so far didn't include the laser phase noise. But it plays a very important role for system performance especially in system based on mixing of optical signals to generate the required RF signal such as optical heterodyne systems. The above models can be used to analyze IM-DD RoF systems mainly because the laser phase noise doesn't have considerable effect in the case of direct modulated laser systems for short range communications [102] [103]. But for coherent and heterodyne RoF systems the laser phase noise should be included in the model so that these systems can be studied using circuit analysis methods to predict their performances under different operating conditions.

The main sources of laser phase noise are represented by the third rate equation (3.31). By creating a link between phase noise and equations from (3.48) - (3.49), the laser phase noise can be integrated to the large-signal model. The instantaneous frequency (phase) fluctuation simplified by introducing the photon lifetime from the threshold carrier density using (3.8) is used to obtain the nodal current equation that can be integrated with the photon and carrier node currents.

$$\frac{d\phi}{dt} = 2\pi\nu(t) = \frac{1}{2}\alpha\Gamma a v_g (n - n_{th}) + F_\phi(t) \tag{3.66}$$

This can be changed into current equation by multiplying the equation by charge of an electron, *q*, as

$$I_{FN}(t) = q\frac{1}{4\pi}\alpha\Gamma a v_g (n - n_{th}) + \frac{1}{2\pi} i_\phi \tag{3.67}$$

where

$$i_\phi^2 = q^2 \left\langle F_\phi^2(t) \right\rangle = q^2 \beta \frac{\Gamma n_0}{\tau_n} \frac{1}{2 p_0} \tag{3.68}$$

Combining (3.51) and (3.67), the frequency fluctuation finally becomes

$$I_{FN}(t) = \frac{1}{4\pi}\alpha\Gamma a v_g \frac{\tau_n (I_{sp} - I_{th})}{V_{OL}} + \frac{1}{2\pi} i_\phi \tag{3.69}$$

The optical phase/frequency of the laser is integrated to the large-signal model by using a simplified approach which is depicted in Fig. 3.22. The output of the circuit model (Fig. 3.21), proportional to the optical power, is combined with an '*optical carrier*' whose phase is modulated by the laser phase equation (3.3). The phase modulation can be performed by using either a phase modulator or frequency modulator. In the complete laser model (Fig. 3.22), the instantaneous frequency fluctuation of the optical signal represented by I_{FN} modulates a single frequency RF signal which represents the optical carrier. At the mixer, the frequency modulated optical carrier is multiplied with the square root of the optical power (output of the large-signal model, V_S). At the end of the model, the signal represents an optical field which includes the intensity and phase/frequency properties of the laser.

In this approach the output of the complete laser model can be represented by the expression:

$$I_{OUT}(t) = \sqrt{P_{opt}(t) + p_n(t)} \exp\left(j\omega_{opt} t + \phi(t)\right) \tag{3.70}$$

$p_n(t)$ represents the laser intensity noise, $\phi(t)$ the laser phase noise.

This modeling approach enhances the capability of the conventional laser model to study different types of systems precisely predicting the laser properties under different working conditions. It should be noted that the instantaneous frequency fluctuation I_{FN}, represents both noise and small-signal modulation. During noise analysis, the current equation (3.69) represents the carrier noise and second term represents Langevin noise source for phase. For

small-signal analysis, only the first term will be used. As a result, the integration of (3.69) with the large-signal model parameters helps to include the frequency modulation (chirp) introduced by the laser into the analysis.

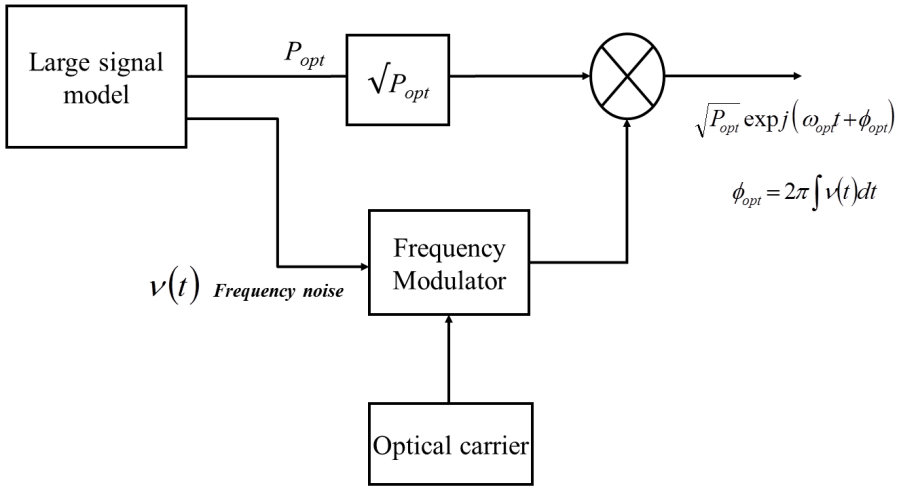

Fig. 3.22. Block diagram of semiconductor laser circuit model with phase modulator.

f). Model Implementation in ADS

Both the small-signal and large-signal equivalent circuit model of the laser can be implemented on general purpose circuit analysis softwares like ADS. The small-signal model consists of lumped circuit elements and can be simply implemented using the built-in libraries already available in ADS. For the large-signal model, the relation between the node currents (3.48), (3.49) and (3.69) are implemented using a four-port symbolically defined device (SDD) as shown in Fig. 3.23.

SDD is a component in ADS library with ports from 1 to 10 that permits writing equations to relate various other circuit parameters allowing the implementation of complex circuit systems. It is a very useful component to represent nonlinear devices. It can be used both in large-signal and small-signal simulations. A weighting function in this component is used to represent time derivative and integration of a voltage or current. For the noise generation, standard noise source with specified noise spectral density are used. Similarly for two level rate equation models (3.62) and (3.63) are implemented using SDD and lumped elements. ADS schematic of the large-signal model is shown in Fig. 3.23 where the parasitic circuit is inserted at the input of the model.

The optical carrier is modulated by the frequency/phase of the laser by using a frequency/phase modulator available in ADS library. One drawback of this method is that the modulators in ADS work only for baseband modulating signal.

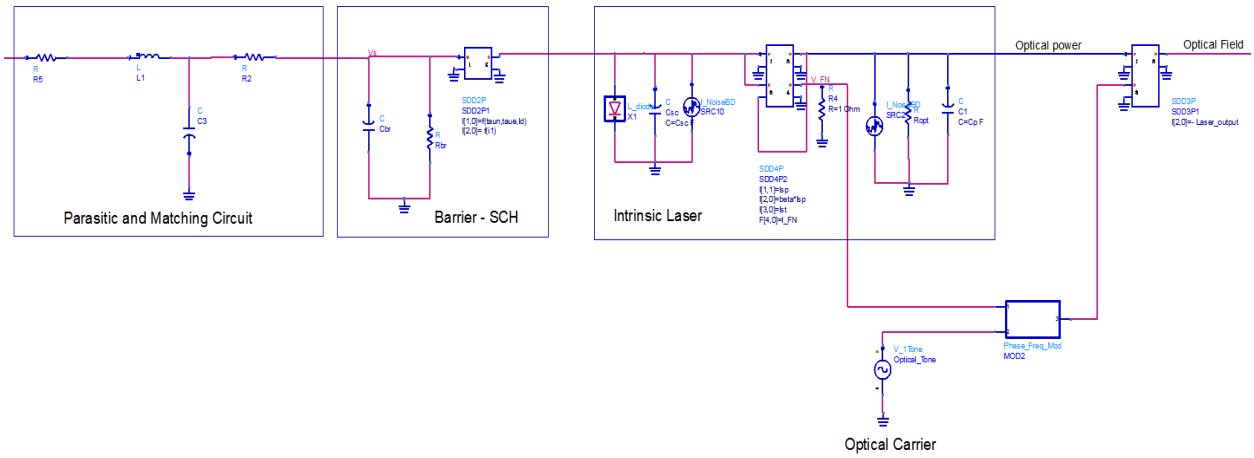

Fig. 3.23. ADS Schematic of complete electrical circuit model of the laser.

3.2.8. Parameter Extraction from measurements

In order to perform simulations, laser cavity parameters and physical parameters should be extracted from measurements of some of the laser characteristics. The static response of the laser, dynamic response and noise measurements are used to extract the parameters needed for the laser model simulation. The approach used in this work is firstly to estimate the cavity parameters initially from the expressions and measurement values. The second step is finely tuning the initial values until the best match between simulated and measured characteristics is achieved. These procedures lead to sets of laser cavity parameters which can represent the laser for system design purposes.

Assuming that the available measurement data at hand are the static response (L-I curve), RIN spectrum, and the optical phase noise power spectrum. Some of the expressions that are used to extract the intrinsic region parameters are given below.

Carrier and Photon lifetime

The saturation current and diode ideality factor of the Shockley diode (3.55) that represents spontaneous emission can be obtained from the V-I characteristic of the laser using I_{th} and V_{th} values. The slope of the L-I characteristic curve which is also called the steady state gain (η_{LI}) is crucial to calculate the photon lifetime in the active region. The expression that relates the steady state gain to the photon lifetime can be obtained from (3.10), (3.12), and (3.14) as:

$$\tau_{\mathrm{P}} = \frac{2\eta_{LI}}{\eta_i v_g \alpha_m} \frac{q}{h\nu} \tag{3.71}$$

To obtain the carrier lifetime, we can use the value of extrapolated threshold current value from the measured L-I curve and carrier density at threshold, n_{th}, using the expression:

$$\tau_n = \frac{qV_{OL}n_{th}}{I_{th}} \tag{3.72}$$

with

$$n_{th} = \frac{n_0}{1 - 1/n_{sp}} \tag{3.73}$$

n_{sp} is the population inversion factor which has value between 1 and 2 [104].

Gain compression ratio

The RIN curve can give information about the modulation characteristics and approximate values of important parameters such as the differential gain, relaxation oscillation frequency and damping factor.

The relaxation oscillation frequency and damping factor are fitting parameters at different bias currents. Knowledge of the relaxation oscillation frequency helps to obtain an estimation of the linear gain slope, *a*, through the expression

$$a = \frac{qV_{OL}\omega_R}{\Gamma v_g (I_{bias} - I_{th})} \tag{3.74}$$

where I_{bias} is the bias current at which the RIN measurement is taken.

The gain compression ratio of the laser is estimated from the damping factor through the approximated relation

$$\varepsilon = 2\pi\gamma \frac{qV_{OL}}{\Gamma(I_{bias} - I_{th})} \tag{3.75}$$

Similarly from the knowledge of gain damping factor and RIN value at low frequency, the spontaneous emission factor, β, is estimated from (3.36) as

$$\beta = \frac{v_g a}{\varepsilon} \tau_p (I_{bias} - I_{th}) 10^{\frac{RIN}{10}} \tag{3.76}$$

Linewidth enhancement factor

From equation (3.39), the linewidth measurement allows the calculation of the linewidth enhancement factor.

$$\alpha \cong \sqrt{\Delta\nu \cdot \left(\frac{1}{4\pi} \frac{\Gamma}{p_a} \frac{\beta n_a}{\tau_n} \right)^{-1} - 1} \tag{3.77}$$

3.2.9. Laser characterization

Characterization of laser is a requirement for any optical system design to have a good understanding of the device behavior. The most common of the diode laser characteristics is the L-I curve. It characterizes the relation between the optical output and the electrical input drive current. This curve is used to determine the laser operating point (drive current at the required optical power) and threshold current (current at which lasing begins). In addition to the L-I curve, the V-I curve of the laser is necessary to study the electrical properties of the laser.

Other important laser parameters such as wavelength, spectral linewidth, relative intensity noise, phase noise, modulation response, and modulation chirp can be measured with appropriate measurement setups. Some of these properties have relatively simple definitions and can be measured straightforwardly, while others properties of semiconductor lasers are defined rather non-intuitively and the measurements of these properties often require good understanding of their physical mechanisms and the limitations of various measurement techniques. This section presents some of the measurement setups to characterize the RIN and phase noise of the laser which are essential to obtain the parameters needed for the circuit model.

*a). **Relative intensity noise***

The fluctuation of the emitted optical power by the semiconductor laser can be measured by using a wide-bandwidth photodiode and a spectrum analyzer as shown in Fig. 3.24. This measurement yields the noise spectrum associated with the total power. In addition to the intensity noise from laser diodes, there are other phenomena that contribute to the total intensity fluctuation in an optical system. One such example is the result of noise conversion from frequency noise to intensity noise. Frequency instabilities in the laser source can be converted into intensity noise through a frequency-dependent transfer function as well as chromatic dispersion. When the laser frequency fluctuates, the transmission efficiency varies, thus causing intensity fluctuation. In addition, if the transmission system is dispersive, different frequency components will arrive at the detector at different times; interference between them also causes frequency noise to intensity noise conversion [105]. In general, the optical intensity noise in an optical system is linearly proportional to signal optical power; therefore, it is more convenient to normalize the measure of intensity noise by the total optical power as in (3.34). RIN is obtained after detection where the electrical power P_{ele} generated at the output of a photodiode is proportional to the square of the received optical power P_{opt}.

The RIN measurement setup (Fig. 3.24) consists of an optical attenuator, a wideband PD, an electrical preamplifier, and an RF spectrum analyzer. The optical attenuator is used to reduce the photo-detected optical power to avoid photodetector's saturation. A wideband photodiode is necessary because the RIN is usually measured from few tens of kHz up to 20 GHz. The electrical amplifiers must have pass-band spectrum which covers the desired spectrum and should possess low noise with the required gain. The amplified photocurrent is then measured with an electrical spectrum analyzer which has high bandwidth to display the required noise spectrum. For this measurement, laser diode is operated in a continuous wave.

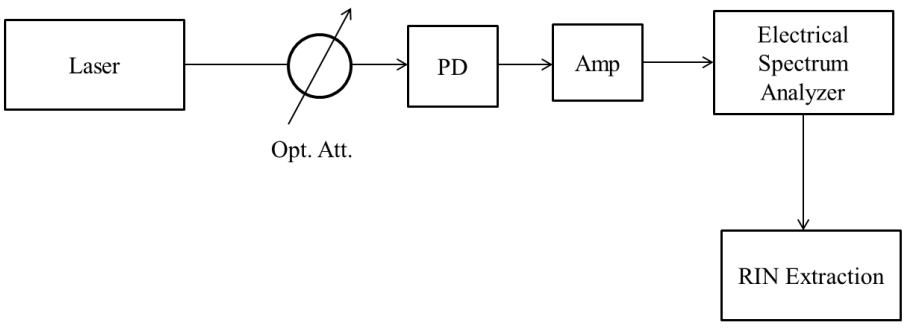

Fig. 3.24. RIN measurement setup.

Since the electrical noise power measured at the output of the photodiode is the sum of three contributions: thermal noise, shot noise and intensity noise in excess of the optical source, the measured electrical noise power spectrum is written as:

$$P_{Total} = K_{calib}(f)\left[\frac{k_B T}{R_L} + 2q\langle I_{ph}\rangle + RIN(f)\langle I_{ph}\rangle^2\right] \tag{3.78}$$

where k_B is the Boltzman constant, T is temperature in Kelvin, R_L is the load resistance of the photodiode, q is the charge of electron and $<I_{ph}>$ is the average photocurrent. The coefficient, K_{calib}, represents the frequency response of the photodiode, the microwave mismatching between the electrical components (the photodiode, amplifier and spectrum analyzer), gain and noise figure of the amplifier. It is important to mention that this factor depends on the level of the optical power detected by the photodiode. It is therefore necessary to know the electrical spectrum to the value of means photocurrent measurement.

There are different methods of calculating RIN spectrum from the noise power measured from the spectrum analyzer. The first method uses calibration techniques to calculate the coefficient K_{calib} while the second method uses direct measurement of (3.78) by turning the laser under study on and off.

Calibration

Calibration of the measurement setup allows obtaining the coefficient K_{calib} in order to extract the RIN spectrum using (3.78). For this purpose, we use a reference optical source whose intensity noise is negligible compared to the shot noise over the spectral range of interest. For instance, a solid-state (Nd:YAG) laser whose peak intensity noise is located at low frequencies (relaxation oscillation appears at low frequency) can be used for calibration. Its intensity noise is limited compared to the shot noise over a wide bandwidth, typically from 100MHz to 18 GHz. So with the low noise optical source connected to the photodiode, the noise power measured at the spectrum analyzer will be

$$N_{Total} = K_{calib}(f)\left[\frac{k_B T}{R_L} + 2q\langle I_{ph}\rangle\right] \tag{3.79}$$

If the incident optical input to the photodiode is removed, the measured electrical noise power will be only thermal noise

$$N_{therm} = K_{calib}(f)\left[\frac{k_B T}{R_L}\right] \tag{3.80}$$

This allows us to deduce the calibration coefficient using

$$K_{calib}(f) = \frac{N_{Total} - N_{therm}}{2q\langle I_{ph}\rangle} \tag{3.81}$$

This equation holds true as long as the contribution of shot noise is greater than that of thermal noise. For this, it is necessary to have a non-negligible mean photocurrent (of the order of mA) and use an electrical amplifier with low noise figure.

RIN Spectrum

Finally, replacing the reference laser by the laser under test, the RIN sepctrum can then be calculated from (3.78) - (3.81) as follows

$$RIN(f) = \frac{\frac{N_{Total} - N_{therm}}{K_{calib}(f)} - 2q\langle I_{ph}\rangle}{\langle I_{ph}\rangle^2} \tag{3.82}$$

The accuracy of the measurement depends mainly on the quality of the calibration factor and the detected value of the mean photocurrent.

Direct measurement

The second method of RIN evaluation is based on the same setup as in Fig. 3.24. Two measurements are performed: the first one with the laser under study turned-on measures the total noise contribution and a second measurement is made with the laser turned off. In the latter case, the noise power measured at the output of the system is composed of thermal noise of the photodiode and the electrical amplifier.

$$RIN(f) = 10\log\left(\frac{Difference\ \ of\ \ the\ measured\ noise\ \ powers}{G\langle I_{ph}\rangle^2 R_L}\right) \tag{3.83}$$

where – G is the link gain.

b). Phase noise characterization

Semiconductor lasers, like other electrical oscillators, are characterized by frequency instabilities which defines the degree to which an oscillating source produces the same frequency value throughout a specified time. Phase noise is a term mostly used to describe the characteristic randomness of frequency instabilities. The source of phase noise in semiconductor lasers is due to the carrier recombination phenomena in the laser cavity (section 3.2.5 b). The linewidth enhancement factor which relates the small variation of the real and imaginary parts of the refractive index due to the change in carrier density in the active region can be estimated from the phase noise or linewidth measurement. However, the fundamental broadening of the laser output spectrum is due to the spontaneous emission [91], the addition of the linewidth enhancement factor to the expression emphasizes the fact that the variations are due to the change of carrier concentration at constant carrier temperature. Therefore, linewidth enhancement factor is a critical parameter determining both the static linewidth of the laser and the instantaneous change in emission wavelength.

Theoretically, phase noise can be explained as follows: assuming an ideal sinusoidal source with nominal amplitude E_0 and nominal frequency f_0 described by

$$E(t) = E_0 \sin(2\pi f_0 t) \tag{3.84}$$

But the actual signal can be better modelled by:

$$E(t) = (E_0 + \delta(t))\sin(2\pi f_0 t + \Delta\phi(t)) \tag{3.85}$$

where $\delta(t)$ is amplitude fluctuation, and $\Delta\phi(t)$ is phase fluctuation.

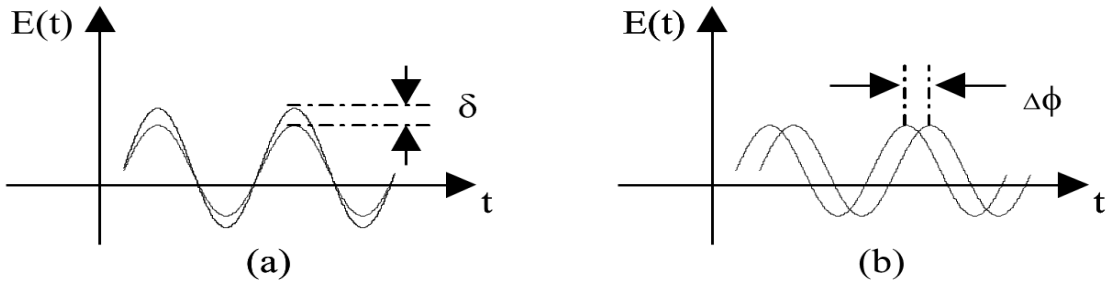

Fig. 3.25. Illustration of (a) amplitude and (b) phase noise.

The phase term could contain two terms: deterministic terms which are discrete signals appearing as distinct components in the spectrum, also called spurious components, and the second term is due to the random nature of the phase fluctuation and commonly called phase noise. The single sideband phase noise denoted by $L(f)$ is considered as the standard measure for characterizing frequency and phase instabilities in the frequency domain [106]. It is defined as one half of the double sideband spectral density of the phase fluctuation, $S_\phi(f)$, which is measured by the spectrum analyzer:

$$L(f) = \frac{1}{2} S_\phi(f) \tag{3.86}$$

$S_\phi(f)$ is related to the variance of the phase fluctuation by

$$S_\phi(f) = \frac{\Delta\phi_{rms}^2(f)}{BW} \tag{3.87}$$

where BW is the bandwidth used to measure the phase fluctuation.

$L(f)$ can also be defined as the ratio of power in one sideband due to phase noise (for 1 Hz bandwidth) to the total signal power (carrier plus sidebands) as in (3.88). Its unit is in *dBc/Hz* (dB with reference to the carrier power).

$$L(f) = \frac{Power\ \ density\ in\ one\ \ phase\ noise\ \ sideband, per\ Hz}{Total\ \ signal\ \ power} \tag{3.88}$$

Among the various techniques [107] [108] [109] to characterize the phase noise of semiconductor laser, homodyne and delayed self-heterodyne methods are some of the classical measurement setups. The linewidth of an optical source can also be determined from the same setup.

In the delayed self-heterodyne method (Fig. 3.26), the optical signal is split into two paths by an optical splitter. The central frequency of the optical signal in one arm is shifted by 80 MHz using an acousto-optic phase modulator. The other arm delays the optical signal to maintain or remove the correlation between the two optical signals. The two optical signals beat at the photodiode resulting in a photocurrent at 80MHz which is measured by an electrical spectrum analyzer.

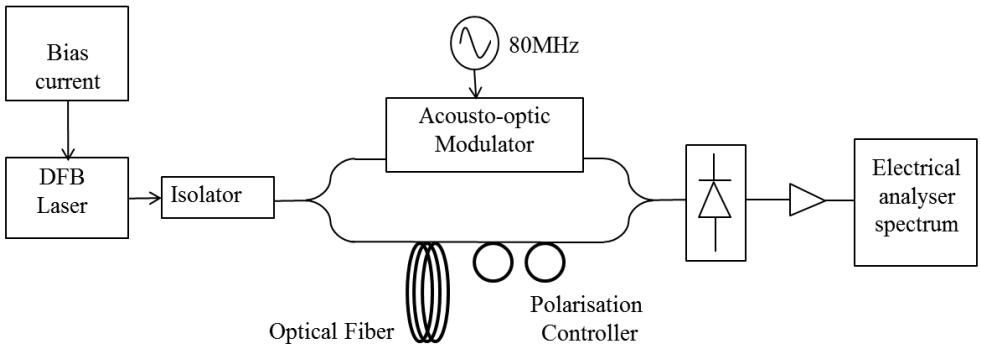

Fig. 3.26. Laser phase noise measurement setup.

The frequency shift is helpful to avoid inaccurate measurement because of the noise in low frequency noise region from the spectrum analyzer. If the delay introduced is longer than the coherence time, the phase noise spectrum of the signal measured by the electrical spectrum analyzer is twice the phase noise of the laser under test, similar to the analysis of heterodyne detection using two free running lasers in (2.8). However, if the delay line is shorter than the coherent length (shorter coherence time), the phase noise spectrum of the measured signal by the electrical spectrum is given by

$$S_{\phi}(f) = S_{\phi\_ESA}(f)\, 4\sin^2(\pi f \tau) \tag{3.89}$$

where S_{ϕ} and S_{ϕ_ESA} are phase noise spectrums of laser and the signal measured by the electrical spectrum analyzer, τ is the delay time, and f represents the offset frequency from the center frequency (80 MHz).

In this work we have extracted the linewidth enhancement factor using the linewidth measurement values obtained using delayed self-heterodyne method and Lorentzian fit. The laser under study is the high power 1.55 µm DFB laser realized by III-V lab [21]. Measurements of static response, dynamic response, RIN, linewidth are performed in collaboration with Frédéric Van Dijk and Mickaël Faugeron. Once the linewidth enhancement factor and other laser parameters are extracted, we can use (3.39) to compare simulation and measurement values versus bias current as shown in Fig. 3.27.

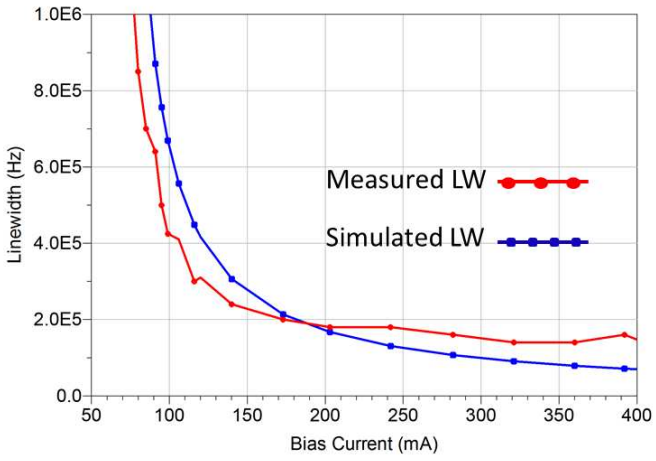

Fig. 3.27. Comparison of measurement and simulation of Linewidth of III-V lab laser.

3.2.10. Comparison of modeling results with measured laser responses

The first step to perform simulation is to calculate the initial model parameters using the expressions given in section 3.2.8. ADS simulation controllers that are used for laser simulation are the DC-simulator, Harmonic Balance and Envelope simulators. The nonlinear noise options in HB and Env simulators are used to calculate the RIN spectrum. The simulation setup in ADS to characterize the laser is shown in Fig. 3.28 where the complete laser model consists of matching circuit, SCH model and intrinsic large-signal model of the active region including the noise sources. The fiber and photodiode models will be discussed in the next sections. The phase noise simulation option using '*NoiseCon*' is used to obtain the single sideband phase noise. The controller uses noise simulation algorithm is based on small-signal mixing of noise [110]. The mixing analysis also computes the AM noise at offset frequencies from the any large-signal frequency.

The purpose of the comparison between measurement and simulation results is twofold: to demonstrate how accurate the equivalent circuit model of the laser to predict the laser properties, and to extract laser cavity parameters so as to perform system level simulations. Fig. 3.29 shows comparison of measurement and simulation of laser characteristics. The static response shows good agreement to measured data until 350mA beyond which the measured data has compression. The gain compression factor does not introduce this much compression even when large values are used. This phenomenon may be related to temperature dependency of the injection efficiency which is not included in our model. The RIN measurement and simulation results are in good agreement for the first few GHz frequencies. The little deviation of measurement and simulation at higher frequencies is attributed to the electronic noise floor due the measurement setup. Dynamic response simulation also shows good agreement for most of the practical modulation frequencies.

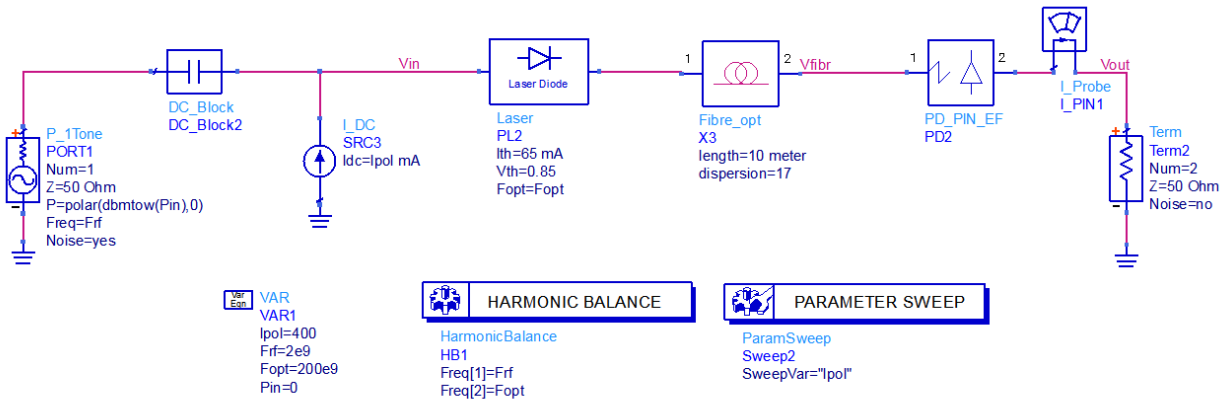

Fig. 3.28. ADS setup to characterize the laser.

Table 6. Extracted modeling parameters of III-V lab laser.

Given parameters	Values
I_{th}	65mA
η_{LI}	0.29 mW/mA
V	1.5 10^{-16}m^3
Linewidth	260kHz @150mA
Extracted parameters	Values
β	1.3 10^{-6}
a	2.08 10^{-22}m^2
τ_n	7.72 10^{-10}s
τ_p	4.8 10^{-12}s
n_0	2.23 10^{23}m^{-3}
ε	2.88 10^{-24}m^3
α	4
Γ	0.45

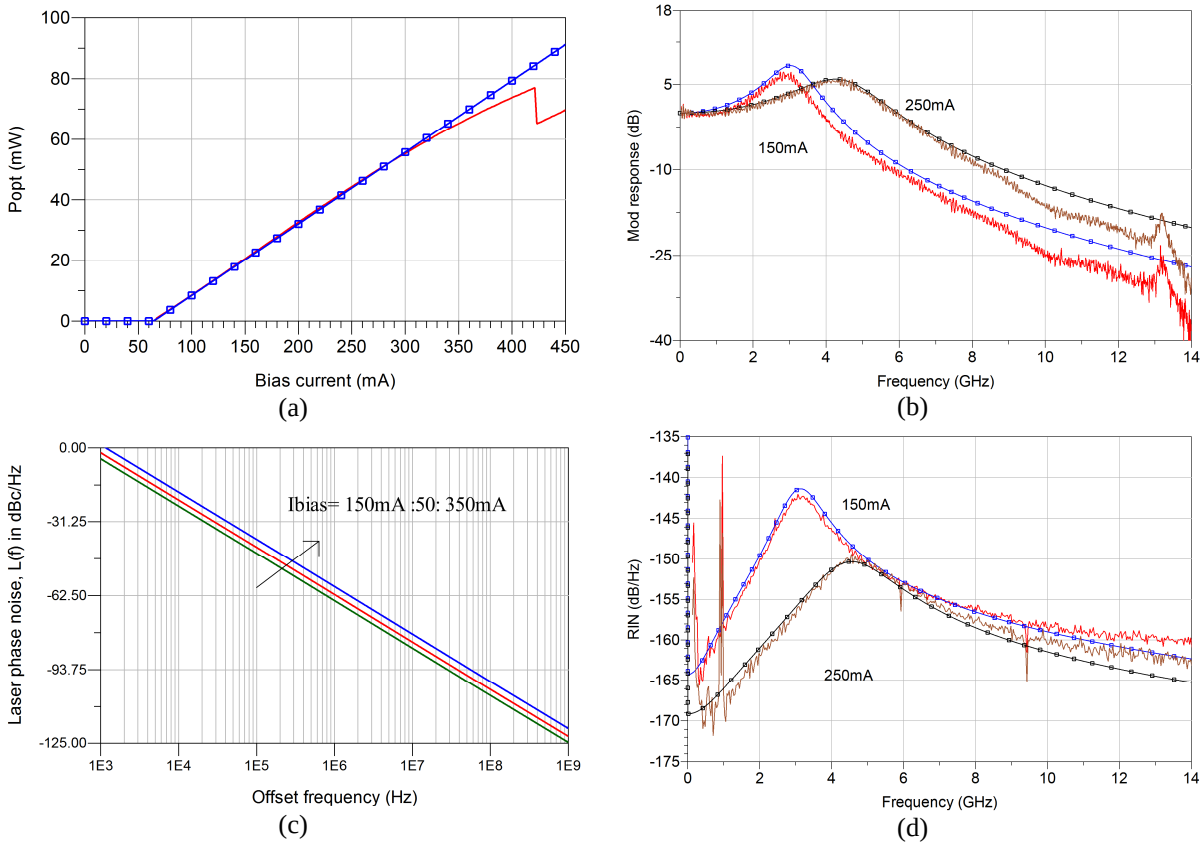

Fig. 3.29. Comparison of measurement and simulation of (a) static response and RIN (b) dynamic response (c) Phase noise (d) RIN.

3.3. Optical modulators

To transmit data across an optical fiber, the information must be first encoded, or modulated, onto the laser signal. Amplitude modulation (AM), frequency modulation (FM), and phase modulation (PM) are some of the techniques for analog transmission.

The limitations associated with DM of the laser are the chirp and modulation bandwidth. These problems can be solved by using optical external modulators. The two types of modulators widely used in communication system are electro-absorption Modulator (EAM) and electro-optic modulator (EOM). The type of optical modulators depends on the physical principle on how they operate to modulate the light to transmit information.

The working principle of EAM is based on the variation in the semiconductor optical absorption caused by an applied electric field. Integration with the laser source is a possible advantage of these kinds of modulators. In addition, the integration allows the modulator efficiency to be improved through the use of MQW structures.

On the other hand, in EOMs the modulation of the material refractive index changes in response to an electrical field, induced by an applied input voltage which has the information to be transmitted. Mach-Zhender modulator (MZM) is an electro-optic modulator that works based on the constructive and destructive interference of two phase-modulated optical beams each propagating in a separate waveguide (Fig. 3.30). With these kinds of modulators high bandwidth up to 40 GHz bandwidth is possible with different structures such as travelling wave. However, integration with the laser source is difficult because of their large size.

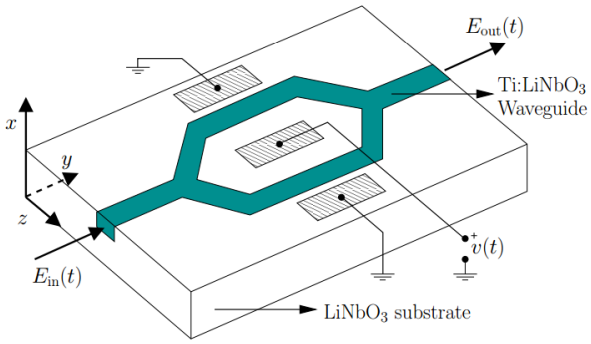

Fig. 3.30. Mach-Zehnder Modulator structure.

MZM works based on the interferometer effect between the two arms as shown in Fig. 3.30. Titanium-diffused Lithium Niobate (Ti:LiNbO3) is used as a wave guide and the phase of the light propagating through the arms can be modified by the applied voltage which changes the refractive index of the waveguide.

If the input optical field to the modulator is expressed as $E_{in} = \sqrt{P_{in}}.e^{j\omega_{opt}t}$, the optical field at the output of the modulator is $E_{out} = \frac{\sqrt{2}}{2}.[E_1(t) + E_2(t)]$ where $E_1(t)$ and $E_2(t)$ represent the optical fields propagating through each arms of the modulator with power P_1 and P_2.

When the light propagates through the arms of the MZM, the phase shift can be approximated according to the Pockels effect [111] as

$$\phi_1 = \phi_0 - \pi \frac{V_1(t)}{2V_\pi}$$
$$\phi_2 = \phi_0 - \pi \frac{V_2(t)}{2V_\pi} \quad (3.90)$$

$V_1(t)$, $V_1(t)$ are the voltages applied to each arm, V_π is the voltage required to bring a phase difference of π between the optical signals propagating through the two arms.

Assuming $\phi_0 = 2\pi$, the output of the modulator can be obtained by

$$E_{out} = \sqrt{P_1}.e^{j\omega_{opt}t} e^{j\frac{\pi}{2V_\pi}V_1(t)} + \sqrt{P_2}.e^{j\omega_{opt}t} e^{j\frac{\pi}{2V_\pi}V_2(t)} \quad (3.91)$$

After introducing the extinction ratio $ER = \frac{P_1 + P_2}{P_1 - P_2}$, the off-driving voltage (V_{off}), the insertion loss (α), the electro-optical transfer function can be written as [112]

$$\frac{E_{out}}{E_{in}} = \sqrt{\alpha}.e^{j\frac{\pi}{4V_\pi}(V_1(t)+V_2(t))} \left\{ \sin\left(\frac{\pi}{2} \frac{V_D - V_{off}}{V_\pi} \right) - j \frac{1}{\sqrt{ER}} \cos\left(\frac{\pi}{2V_\pi} \frac{V_D - V_{off}}{V_\pi} \right) \right\} \quad (3.92)$$

where $V_D = \frac{V_1 + V_2}{2}$. The chirp term $V_1(t) + V_2(t)$ can be set zero for push-pull configuration, $V_1(t) = -V_2(t) = V_{in}(t)$.

The static response of the modulator shows that the modulator is linear if the bias voltage is at the middle of the linear region ($V_\pi/2$). Therefore, the dynamic response of the modulator depends on the speed of the modulating signal and its amplitude.

A modulator model that is compatible with the laser model can be obtained by implementing (3.92) on an SDD and integrating the parasitic circuit is shown in Fig. 3.31. A 3dB power splitter is used to divide the input optical signal at the input and the two optical signals pass through the two arms of the modulator where their phase is modulated by the RF signal. The optical signals are then combined after a phase shift of 90° on the lower arm to create the interference effect needed for intensity modulation. The parameters such as insertion loss of 4dB, extinction ratio of 24, V_π of 6 V are taken from the data sheet [113]. The measurement data of S11 of the modulator is inserted to the model using S2P component of ADS. Since the modulator has bandwidth greater than 28 GHz, it has no influence on intermediate frequencies. The modulator characteristics such as static response and modulation response can be obtained using S-parameter simulation or harmonic balance simulation (3.35).

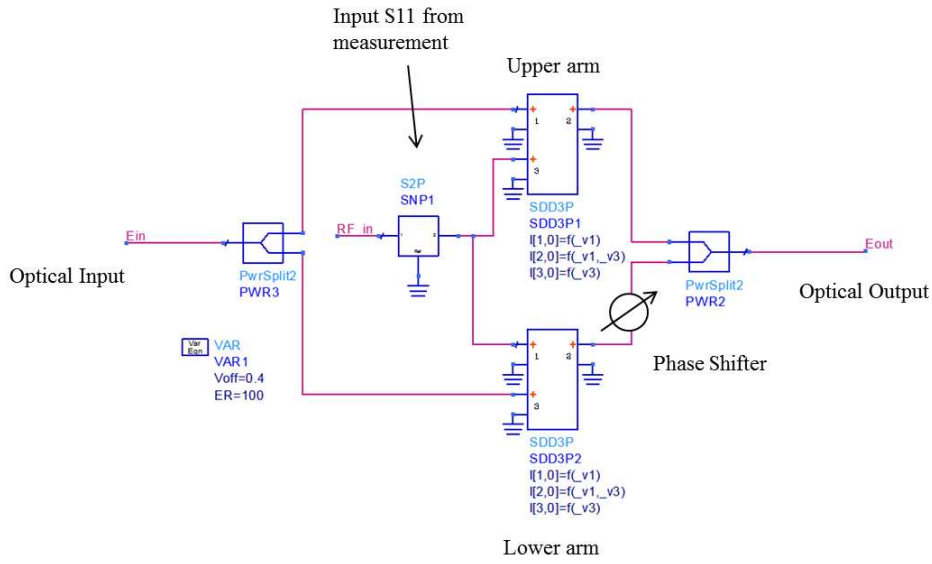

Fig. 3.31. MZM modulator model in ADS.

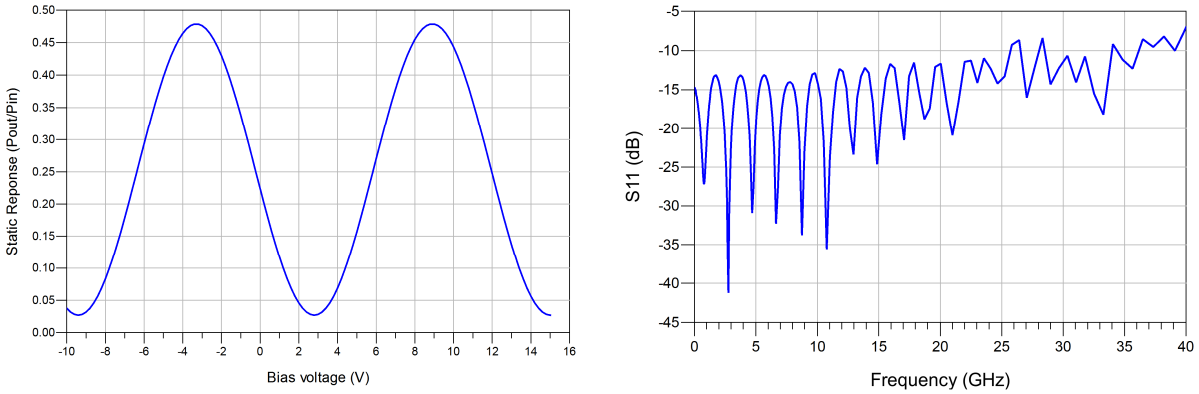

(a) (b)

Fig. 3.32. MZM characteristics (a) electro-static response (b) S11.

3.4. Photodiode

Photo-detectors (PDs) are the first component in the optical receiver chain. Their purpose is to convert an optical (analog or digital) signal to an electrical signal usually called the *photocurrent*. The physical mechanism at the basis of the semiconductor detectors is the optical generation of electron-hole pairs through the absorption of incident photons. The photo-generated electron-hole pairs are then separated and collected to the external circuit by an electrical field which can be induced by an external voltage in a reverse biased PN junction. The carrier generation is determined by the absorption threshold, the minimum energy photons must have to be absorbed. Hence, the energy of the photon must be higher than the bandgap energy of the intrinsic material of the PD. The photocurrent generated by the photodiode, typically PIN PD, is contribution of two currents: drift current associated with carriers generated inside the intrinsic depleted region and diffusion current caused by minority carriers generated from the edge of the intrinsic region. But the main contribution is from the drift current and diffusion currents are much slower and should be reduced for high speed operation.

The relation between the photocurrent and the input optical power is given by the relation

$$I_{ph} = r_{PD} P_{opt}(t) \tag{3.93}$$

where r_{PD} is given in A/W.

PIN and APD photodiodes are the main optical receivers used in many applications. PIN diodes consist of an intrinsic layer inserted between the p-type and n-type layers. This structure detects light and generates current when it is reverse biased. However, the responsivity is very small and it is often coupled with trans-impedance amplifier (TIA) in front of the PD. InGaAsP and Ge can be used for the 1.3 µm window (*Ge* can be used for longer wavelength since it has lower bandgap energy). For 1.55 µm window, the material used is usually InGaAs which has bandgap energy of 0.77eV.

The receiver sensitivity can be greatly improved by using avalanche photodiodes (APD). In this structure, additional p-type layer is added in between the intrinsic and n-type layer for the avalanche multiplication of carriers. It can generate high current under reverse bias but the problem is that it generates high noise and the gain is temperature dependent. PIN photodiodes are preferred for most of the optical fiber communication systems due to its cheaper price, less sensitive to temperature and requires lower reverse bias voltage than the APD. However, the APD is generally preferred when the system is loss limited, as occurs for long distance links.

The noise generated by the photodiode is as a result of the noise in the input light (RIN of laser), and the noise from the device itself (Fig. 3.33). But if we limit ourselves to the detector noise, the noise current can be added to the detector current as follows:

$$I_{PD} = r_{PD} P_{opt} + I_d + i_n \tag{3.94}$$

where I_d is the dark current and i_n is a zero-average random process having white power spectrum. This noise can be modelled as thermal noise in photoresistors, shot noise in photodiodes and phototransistors, multiplied shot noise in APDs.

For small-signal conditions, e. g. in analog links the photodiode operating with constant current I_{PD}, the shot noise model yields the power spectrum

$$S_{PD} = 2qI_{PD} = 2qI_{ph} + 2qI_d \approx 2qr_{PD}P_{opt} \tag{3.95}$$

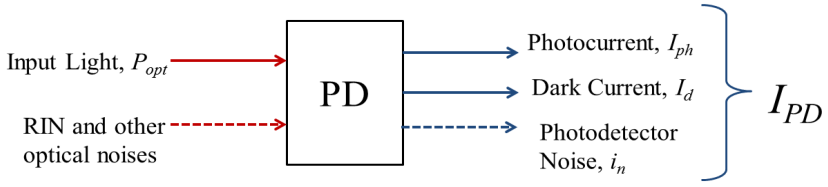

Fig. 3.33. Generation of noise from the photodetector

In analog optical systems, the shot noise floor (relative to the RF power) of the photodiode can be reduced by increasing the input optical power. However, increasing input optical power discloses the power-dependent noise conversion effect of the photodiode. In some RoF

applications, this power dependent noise conversion affects the phase noise of the generated microwave signal and can be a limiting factor [114]. This can be observed when the power level of the incident pulse train across the photodiode increases which will generate more carriers. The interaction between the carriers generates internal electric fields opposing the bias field of the diode. This causes the transit time of carriers to increase and results transmission delay, hence phase fluctuation of the RF signal. Increasing the bias voltage is one way of improving power-to-phase fluctuations; however, device failure due to the runaway of dark current occurs due to a bias voltage that gets too large. This effect is more pronounced at high modulation frequencies.

The other important characteristic of photodiodes RoF applications is the frequency response. The frequency response of a PIN photodiode is limited by four main mechanisms: transit time of the carrier drifting across the intrinsic layer, effect of diode capacitance and any other parasitic capacitance, charge trapping at hetero-junctions, diffusion time of carriers generated out of the un-depleted region. Carrier diffusion and heterojunction charge trapping can be made irrelevant technologically by reducing diffusion length and inserting a thin quaternary layer at the hetero-interface. Thus, the main bandwidth limiting factors of a standard PIN photodiode are transit time of the drift current and the RC constant due to the parasitic elements [115].

$$f_{-3dB} \cong \frac{1}{\sqrt{\frac{1}{f_{RC}^2} + \frac{1}{f_{tr}^2}}} \tag{3.96}$$

f_{RC} is the RC limited cutoff frequency and f_{tr} is the transit time limited cutoff frequency.

Therefore, the device modulation bandwidth can be maximized either by decreasing the transit time, or reducing the RC time constant. In Uni-travelling carrier (UTC) PDs the transit time is reduced by making only the fast moving carrier i.e electrons to move across the depleted region contrary to the standard PIN PD case where both electrons and holes transport contributes to the photocurrent. Hence the device speed in UTC structure is not dependent on the slower hole transport. UTC-PDs usually have a travelling wave PIN diode structure but with a separation between the optical waveguide section and the absorption section to help the absorption to take place in the separation region which reduces the transit time. This mechanism leads to a big improvement in the device speed. UTC photodiodes have also other advantage: they have high saturation power due to the fact that the optical power is absorbed in a distributed manner. These kinds of devices have been proposed for broadband wireless applications in the millimeter-wave broadband systems [116] [117] [118].

Like semiconductor lasers, equivalent circuit model photodiodes can be developed incorporating the rate equation for electrons and holes in the absorption region [119]. The equivalent circuit model including the nonlinear behavior is also presented in [114] [119] [120] [121].

In this work, the photodiode for RoF applications is represented by the simplified equivalent circuit model shown in Fig. 3.34 which consists of photocurrent source, junction capacitance and resistance, a noise source that models the shot noise, and parasitic resistance and

inductance. The model assumes that this photodiode is in the RC time limited case and the PD bandwidth is external circuit dependent. The photodiode's conductance R_d is very high of the order of 5kΩ. The matching resistance represented by R_{PD} in the circuit model is used to reduce the power reflection from the load.

In the coming chapters, two types of PDs will be considered for the two systems under study. For the IM-DD links, Emcore PIN photodiode [122] is used. The main parameters the Emcore PD are responsivity 0.65 A/W, bandwidth 20GHz, and RF return loss 12dB. For the heterodyne RoF link UTC PD is used to generate the millimeter wave signal. The parameters of for the equivalent circuit the UTC PD are obtained from [117].

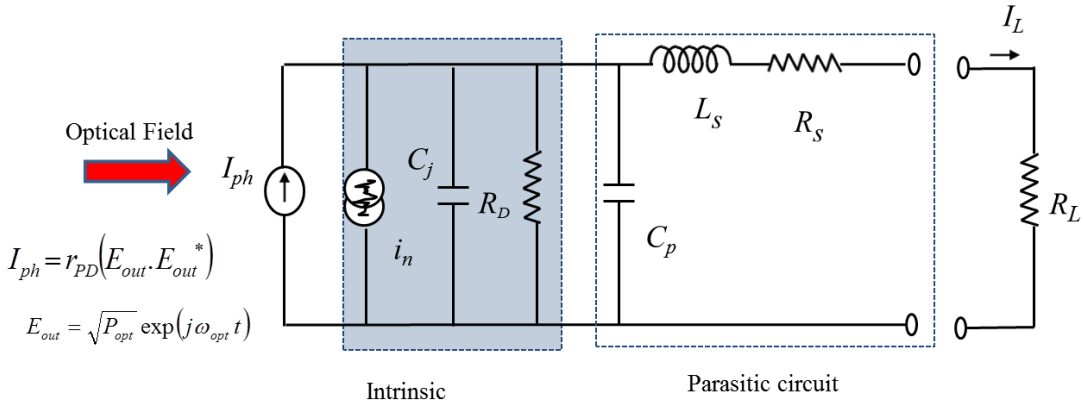

Fig. 3.34. Equivalent circuit of PIN photodiode.

The photocurrent I_{ph} is obtained by multiplying the responsivity of the photodiode with the optical power which is the magnitude square of the optical field. Since the laser diode output is optical field, a square root function should be used in the photodiode model to convert the optical field to optical power. This makes the photodiode model to have a non-linear transfer function between the input optical and the output electrical signal. This reassures the detection after the photodetector replicates the modulating signal for intensity modulation systems. It is important to note that the square detection dependence is not the source of nonlinear distortion due to the photodetector. The scattering parameters, (S_{21}) and (S_{22}), simulation of Emcore photodiode are given in Fig. 3.35.

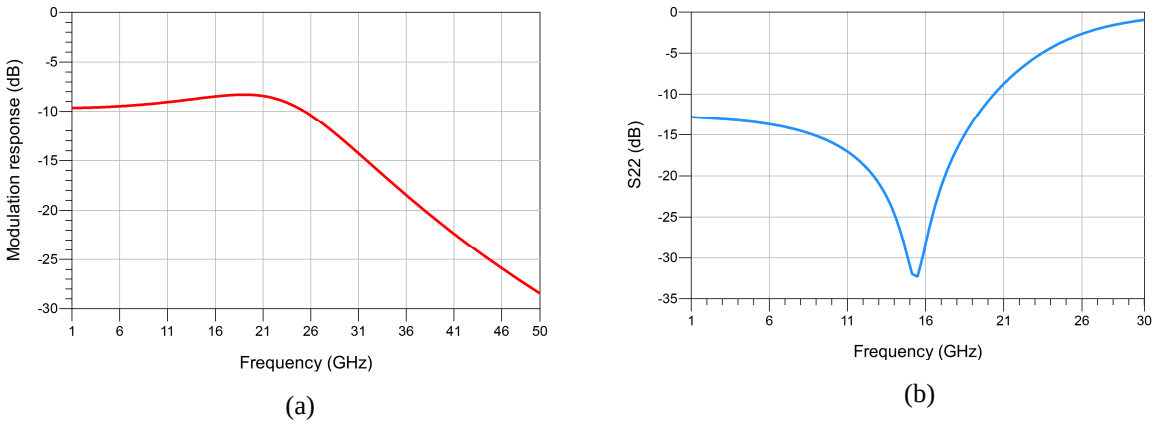

(a) (b)

Fig. 3.35. S-parameter simulation of the photodiode model.

3.5. Optical Fibers

Except for free space optical communication, optical fiber serves as a medium of communication for all light-wave systems by carrying information from one point to another in the form of light. Optical fiber is a very thin cylindrical dielectric medium that allows propagation of electromagnetic waves (light) and is made of glass usually SiO_2 since it has very low attenuation at optical frequencies. It consists of a central 'core' with high refractive index surrounded by a 'cladding' with lower refractive index. This helps the propagation of light within the fiber due to the physical phenomenon of total internal reflection.

There are two effects of fiber optic that should be studied to design optical communication systems. Fiber attenuation and dispersion are the most limiting factors for short and medium range communication systems.

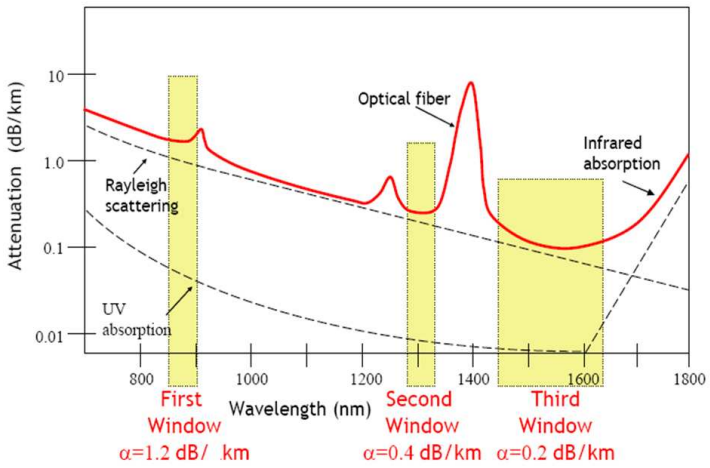

Fig. 3.36. Single mode fiber attenuation with respect to the optical spectrum.

As shown in Fig. 3.36, the single mode fiber attenuation is typically 0.4dB/km and 0.2dB/km for 1330 nm and 1550 nm windows, respectively. The attenuation decreases the signal to noise ratio at the optical receiver and limits the transmission distance of the optical fiber communication systems. In some optical systems, optical amplifiers such as erbium doped fiber amplifiers (EDFAs) which can easily provide gain of 20dB or more are used to increase the link length or provide distribution to a large number of users but this decreases the signal to noise ratio [48].

Fiber dispersion is another important issue which leads to the broadening of data pulses as the optical signal travels along the fiber causing inter-symbol interference (ISI) between bits. There are three types of dispersion in the fiber: chromatic dispersion, modal dispersion, polarization mode dispersion.

Chromatic dispersion is overall effect of two types of dispersion: material dispersion which is due to the refractive index of the fiber material dependency on the wavelength of the light passing through it and waveguide dispersion. Material dispersion causes each wavelength to travel with a different velocity in the fiber and arrives at the destination at different times. This dispersion occurs in all transmission systems since the light source and data signal has finite bandwidth. Waveguide dispersion results from the waveguide characteristics such as

fiber indices and the shape of the fiber core and cladding. This type of dispersion is very small and can be neglected in the transmission link.

Modal dispersion results from the modes of a multimode fiber propagating with different velocities. This kind of dispersion is null by definition in single mode fibers (a fiber which has very small radius comparable to the optical wavelength at 1550nm). Modal dispersion depends on the number of propagation modes that exist in the fiber which is determined by the fiber core size and the index difference between the core and the cladding.

Polarization mode dispersion is a special type of modal dispersion which exists in single mode fibers. This dispersion is due to the fact that there are two modes coexisting in single mode fibers. The two modes are orthogonally polarized and may travel through the fiber at different speed causing them to have group delay difference.

The effect of chromatic dispersion is more significant at higher modulation frequencies and severely limits the fiber transmission distance. In the conventional intensity modulated direct detection (IM-DD) RoF system, the information signal is generated on both sides of the optical carrier which is known as double sideband (DSB) modulation. When the optical carrier and the two sidebands are transmitted over fiber, the chromatic dispersion causes a phase change for each sideband depending on the fiber length, modulation frequency, and chromatic dispersion parameter. This results in the two RF signals generated by the two sidebands beating with the optical carrier, at the receiver, being out of phase, resulting in zero transmission in some cases.

There have been many solutions proposed to reduce the effect of fiber dispersions in the communication systems. Dispersion shift fiber (DSF) is one solution. This is important as single mode fibers operating in the 1550nm window are becoming important. The idea is to shift the dispersion zero of the fiber from the second window (1330 nm) to at the third window (1550 nm) in DSF. Another way to decrease the effects of dispersion is to use a compensating fiber with a strong negative dispersion known as dispersion compensation fiber (DCF). This is linked to the linear effect of dispersion which can be reversed.

Another important characteristic of optical fiber is its nonlinear effect. Since most RoF applications are limited to few tens or hundreds of meters [123] [124], only dispersion is of a major concern. However, for long-haul analog optical links like in cable-TV applications, other fiber impairments such as nonlinear effects (four-wave mixing, cross-phase modulation, self-phase modulation, stimulated Brillouin scattering, stimulated Raman scattering) influence the system performance [48].

In single mode optical fibers, neglecting nonlinearities and polarization related effects, the optical field modal amplitude propagates according to the following wave equation

$$E(\omega, z) = E(\omega, 0).H(\omega) \tag{3.97}$$

with E the optical field, z propagation distance, α the fiber attenuation, and β the propagation constant.

Thus the transfer function of the fiber, with locally flat attenuation, can be written as

$$H(\omega,z)=\exp(-\alpha z-j\beta(\omega)z) \tag{3.98}$$

The propagation constant expanded in Taylor series around the central optical frequency, ω_{opt} is given by

$$\beta(\omega)=\beta_0+\beta_1(\omega-\omega_{opt})+\frac{\beta_2}{2}(\omega-\omega_{opt})^2 \tag{3.99}$$

Considering the single frequency optical field is modulated by a sinusoidal signal of frequency $\cos(\omega_c t)$, the optical field (2.2) can be expressed as:

$$E(t)=E_0\left(\exp\left(j\left(\omega_{opt}\,t+\phi_{opt}\right)\right)+\frac{m}{2}\exp\left(j\left(\omega_{opt}\,t+\phi_{opt}\pm\omega_c t\right)\right)\right) \tag{3.100}$$

where *m* is the intensity modulation index.

Since the propagation constant of the fiber is not constant over frequency, the three frequency components will have different propagation constants, hence different phase. At the end of the fiber, the optical field can be written as

$$E_1(t)=E_1\left(\begin{array}{l}\exp\left(j\left(\omega_{opt}\,t+\phi_{opt}+\varphi_0\right)\right)+\frac{m}{2}\exp\left(j\left(\omega_{opt}\,t+\phi_{opt}-\omega_c t+\varphi_1\right)\right)\\ \\ \qquad\qquad\qquad\qquad+\frac{m}{2}\exp\left(j\left(\omega_{opt}\,t+\phi_{opt}+\omega_c t+\varphi_2\right)\right)\end{array}\right)$$

where φ_0, φ_1, φ_2 represent the different phase difference between the three optical frequencies because their propagation speed in the fiber is different. These phase differences are due to the β_2 term of (3.99). The other terms β_0 and β_1 introduce merely phase delay and group delay respectively which are the same for all the frequency components, hence they do not distort the signal. Therefore β_2 is responsible for the signal distortion by introducing group delay difference between the three frequency components. This effect is known as chromatic dispersion. It is usually denoted as "D" which is related to β_2 as follows

$$D=-\frac{2\pi c}{\lambda^2}\beta_2 \tag{3.101}$$

c is the speed of light, and λ is the central wavelength of the optical signal.

To include the fiber dispersion effect in our system, we have modelled the dispersion effect by implementing the last term of (3.99) on a current controlled current source (CCCS). The gain of CCCS is expressed in frequency domain which is equal to the transfer function of the fiber (including attenuation and chromatic dispersion). Thus the fiber model includes the dispersion and attenuation effects which are the most important parameters for most of RoF applications.

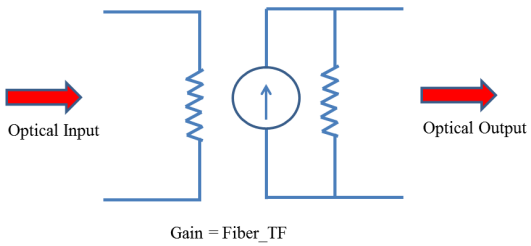

Fig. 3.37. Electrical circuit model of optical fiber.

Theoretically, the small-signal analysis [105] shows that the dispersion of the fiber optic introduces conversion factors for both the optical intensity and phase. If the optical spectral density at the fiber input and output are S_{in} and S_{out}, and the optical phase at the input and output of the fiber are ϕ_{in} and ϕ_{out} respectively, we can write the following relation:

$$S_{out} = \cos\left(\frac{LD\lambda^2}{4\pi c}\omega_c^{\,2}\right)S_{in} - \sin\left(\frac{LD\lambda^2}{4\pi c}\omega_c^{\,2}\right)\phi_{in} \tag{3.102}$$

$$\phi_{out} = \sin\left(\frac{LD\lambda^2}{4\pi c}\omega_c^{\,2}\right)S_{in} + \cos\left(\frac{LD\lambda^2}{4\pi c}\omega_c^{\,2}\right)\phi_{in} \tag{3.103}$$

From these equations, one can drive the transfer function of the fiber. They can help to estimate the dispersion-length effect on the RF signal due to PM-AM conversion. For instance in the presence of chirp, fiber dispersion introduces conversion factor of phase modulation to intensity modulation. During direct modulation of the laser, the relation between intensity modulation and phase/frequency modulation spectrum or chirp can be obtained from (3.25). If the ratio of frequency modulation response to intensity modulation response is represented by $H_{FM\text{-}IM}$, one can deduce the fiber transfer function in the presence of chirp using (3.102) as follows [105] [125]:

$$H_{FR} = \left|\cos\left(\frac{LD\lambda^2}{4\pi c}\omega_c^{\,2}\right) - \sin\left(\frac{LD\lambda^2}{4\pi c}\omega_c^{\,2}\right)H_{FM-IM}\right| \tag{3.104}$$

If we assume no chirp condition, the term $H_{FM\text{-}IM}$ vanishes, but the fiber dispersion still introduces a frequency selective transfer function due to the first term in (3.104). The length of the fiber and the RF signals frequency have to be chosen to avoid dip points (the dispersion induced power penalty) (Fig. 3.39).

To investigate the fiber effect for IM-DD systems, ADS project shown in Fig. 3.38 can be used. The laser is represented by pure RF source (no chirp is assumed) and the modulating signal is at a frequency of 40 GHz. This simulation assumes fiber dispersion of 17ps/nm/km, attenuation of 0.2dB/km, and UTC photodiode (bandwidth 100GHz). In Fig. 3.39 (a), the output RF power after detection at 40GHz is shown with respect to the length of the optical fiber. Comparison between theoretical expectation using the first term of (3.104) and the fiber model shows a good match. It is evident that dispersion creates transmission minimums at harmonics of products of length - RF frequency. In (b) the output RF power Vs length is shown for modulating frequencies of 40 GHz and 60 GHz. When the modulating frequency

increases, the period of minimum transmission increases putting limitation on the maximum transmission reach. This effect could be more pronounced in the presence of chirp. This is one of the limitations of direct modulation systems in the presence of chirp. Dispersion also affects double sideband modulation in external modulation systems. Therefore single sideband modulation technique is often used to battle dispersion [45].

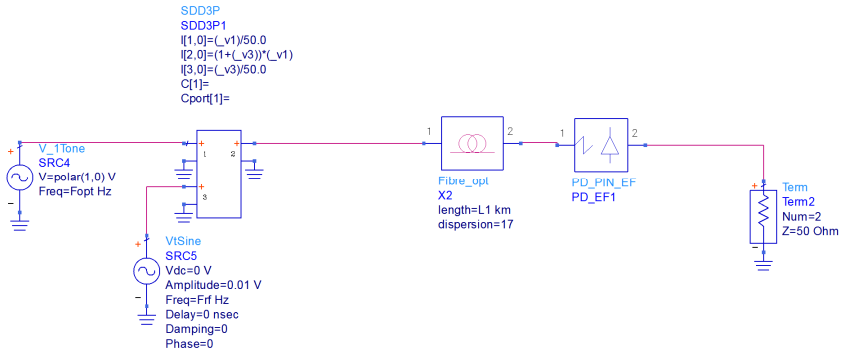

Fig. 3.38. ADS schematic to study fiber effects.

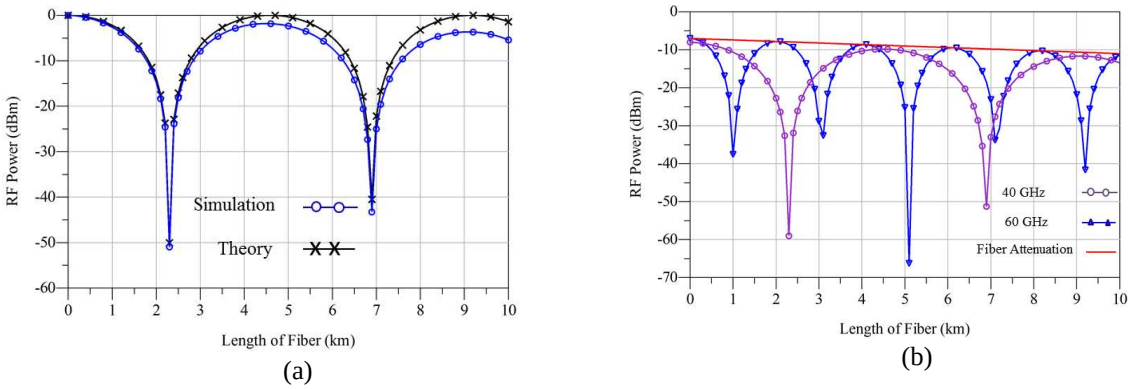

Fig. 3.39. Microwave signal transmitted over the fiber comparison of theory and simulation.

The other way to explain the effect of dispersion is by using its impact on the relative intensity noise. It has been demonstrated in [105] that the PM-IM conversion due to fiber dispersion can actually compensate the RIN if small amount of dispersion with proper sign is present. The compensation also appears to be effective even for extreme case where the laser is operated within the coherent collapse regime.

3.6. Summary

The first part of the chapter briefly explains the properties of single mode semiconductor lasers to lay ground for developing equivalent circuit model of the device for large signal system simulations. Important issues such as the static response, dynamic response and noise properties of the laser are the discussed using the rate equations.

The well-known large signal model of single mode semiconductor lasers is then derived from the rate equation and noise sources are integrated to fully represent the device. The inclusion of optical phase noise is of the main objective. Besides, the two level rate equations are used to further enhance the models capability to represent the carrier transport effect. The model is validated by comparing measurements of DFB laser properties with simulations.

The last part discusses circuit modeling of other RoF components: optical modulators, photodiodes, and optical fibers. The main properties of each of these components are modelled by using their respective functions. All of the RoF models are suitable to perform different system simulations in ADS.

4

Study of Radio over Fiber systems

4.1. Introduction

Like any other analog communication systems, RoF systems are influenced by nonlinear and noise effects that come from the various components. The optical source, semiconductor laser, is a fundamental component that affects the system performance in terms of its nonlinearity, intensity noise, and phase noise characteristics. The study of RoF links in circuit analysis software helps to precisely predict the influences of each component in the system while including other electronic effects like parasitic and driver circuits. In this chapter, the electrical equivalent circuit models of RoF components developed in the previous chapter will be used characterize both direct/external modulation and optical heterodyne links. This kind of system level simulation is important in order to evaluate the RF-to-RF performances of the RoF links.

4.2. Properties of RoF links

As shown in Fig. 4.1, an intensity modulation RoF link can be represented by a cascade of two-port simplified models of the RoF components. It shows that the RoF link acts like a simple microwave transducer from the point of view of the transmitted and received electrical signal. With this approach, the characteristics of a transducer such as noise figure and insertion loss/gain of the whole RF-to-RF link can be calculated easily. It allows optimization and design of RoF systems by applying basic circuit principles such as matching conditions. In this section, microwave properties of different RoF systems are defined based on the simplified two-port model of the RoF link indicated in Fig. 4.1. The definitions are based on the analysis performed in [126].

However, some of the optical components such as lasers, modulators and optical fibers have characteristics that cause performance degradation that cannot be deduced from noise figure or insertion loss. Phenomena like nonlinear distortion and phase noise fall under this category. Dynamic range can be used to evaluate the nonlinearity of the system. To evaluate transmission of digital signals with complex modulation formats such as OFDM, the measure of error vector magnitude (EVM) or bit error rate (BER) have to be used. The issue of EVM evaluation will be studied in Chapter 5. EVM is an important parameter that helps to get an idea of the nonlinear and noise distortions introduced by the link.

The models presented in Fig. 4.1 are simplified small-signal models of a directly modulated RoF link. Notations of inputs and outputs of the models which will be used in the coming discussions are defined as follows: the input RF signal which reaches the laser intrinsic equivalent circuit is represented by i_{LS}, the signal at the input to the fiber is referred as i_{opt_in}, it represents the amplitude of the optical field. The optical power can be obtained by simply squaring i_{opt_in}. The simple photodiode model squares the input current and multiplies it by its responsivity to obtain the small-signal photocurrent i_{ph}. The current that reaches to the load is denoted as i_L. Block letter I will be used to represent the signal in the DC case. The available power from the generator is denoted as p_{av} and the power delivered to the load is represented by p_L.

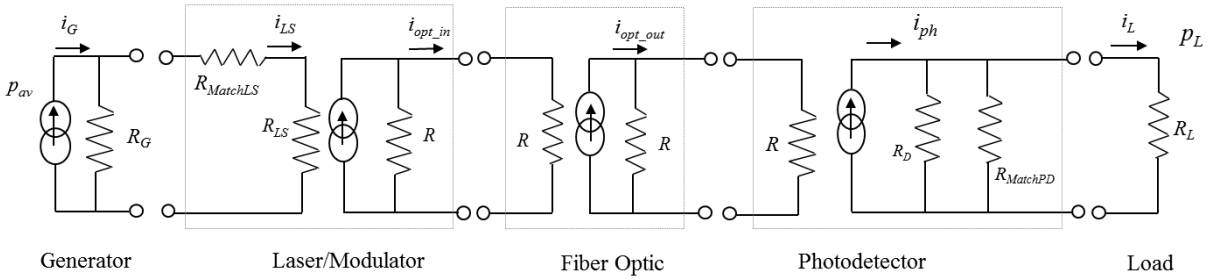

Fig. 4.1 Two-port network of a direct modulated laser RoF link.

The simplified RoF link model consists of a series resistor ($R_{MatchLS}$) at the input of the laser and a parallel resistor ($R_{MatchLS}$) at the output of the photodiode to satisfy the matching impedance condition which assures maximum power transfer and minimum reflection loss. This kind of matching may be insufficient if the load impedance is complex. Nevertheless, it can be used to enhance the gain at lower frequencies. In this section, resistive matching is considered to define the analog properties of the RoF link with matching condition.

In Fig. 4.1, R_G is the RF generator resistance, $R_{MatchLS}$ is the laser input resistance, R_{LS} is the laser input resistance, R_{LS} is the laser input resistance, R is the output resistance of the current controlled current sources (considered as infinite), R_D is the parallel conductance of the photodiode (about 5 kΩ), R_L is the load resistance. Therefore the relations between various current i_{LS}, i_{opt_in}, i_{ph}, and i_L can be written as follows

$$i_{LS} = \frac{R_G}{R_{LS} + R_{MatchLS} + R_G} i_G \tag{4.1}$$

$$i_{opt\_in} = \sqrt{\eta_{LI} i_{LS}} \tag{4.2}$$

$$i_{opt\_out} = \exp(-\alpha L) i_{opt\_in} \tag{4.3}$$

$$i_{ph} = r_{PD} \left(i_{opt\_out}\right)^2 \tag{4.4}$$

$$i_L \cong \frac{R_{PD}}{R_{PD} + R_L} i_{ph} \quad , \quad where\ R_D >> R_{PD} \tag{4.5}$$

4.2.1. Link Gain

Link gain is defined as the ratio of delivered power into a matched load, p_L, to the available power of the generator, p_a.

$$g_i = \frac{p_L}{p_a} \tag{4.6}$$

As the DM link consists of a modulated light source, fiber optic and photodetector, the expression for the link gain is obtained by multiplying the gain of each element and can be expressed as a function E/O, O/O and O/E conversion coefficients of individual components in the link. If the modulated output optical power is p_{opt}, the optical coupling losses and optical losses l_{opt}, the modulated optical power input to the photodetector p_d, the small-signal gain of an IM-DD link can be written as product of intrinsic RF gain of the RoF components: laser (g_L), gain of fiber optic (g_{OF}) and gain of photodetector (g_{PD}) as follows

$$\begin{aligned} g_i &= g_L g_{OF} g_{PD} \\ &= \frac{p_{opt}^{\ 2}}{p_a} \left(l_{opt}\right)^2 \frac{p_L}{p_d^2} \end{aligned} \tag{4.7}$$

Note that the square of the optical power in (4.7) is due to the fact that the optical power is equivalent to the photocurrent after the photodiode. So, the power delivered to the load is equivalent to the square of the optical power. To obtain the gain of a direct modulated RoF links shown in Fig. 4.1, we need to define intrinsic RF gain of each individual component.

During direct intensity modulation of the laser, the modulating current is added to the bias current which is translated modulation of the optical power. The current that enters to the laser model, i_{LS}, is related to the current from the generator using (4.1). The output of the laser is related to the input modulating signal by (4.2). Since the output of the laser model represents optical field, the optical power (intensity) can be obtained by squaring the laser model's output current ($p_{opt} = i_{opt\_in}^2$). Thus if the available RF power from the source is written as ($i_G^2 R_G/4$), the small-signal intrinsic gain of the laser can be written as

$$g_L = \frac{p_{opt}^{\ 2}}{p_a} = \frac{\left(\eta_{LI} i_{LS}\right)^2}{i_G^{\ 2} \frac{R_G}{4}} = \left(\eta_{LI}\right)^2 \frac{4}{R_G} \left(\frac{R_G}{R_{LS} + R_{MatchLS} + R_G} \right)^2 \tag{4.8}$$

η_{LI} is the slope efficiency of the laser defined in (3.14). If we assume that the circuit satisfies impedance matching condition at the input, $R_G = R_{MatchLS} + R_{LS}$, the laser gain can be simplified as

$$g_L = \eta_{LI}^{\ 2} \frac{1}{R_G} \tag{4.9}$$

The simplified fiber optic model represents the optical loss associated with optical attenuation due to the fiber optic. It can be defined as the ratio of optical power at the output

of the fiber (p_{opt_out}) to the optical power at the input (p_{opt_in}). Therefore from (4.3), the conversion gain of the fiber optic can be obtained as follows

$$g_{OF} = \left(l_{opt}\right)^2 = \left(\frac{p_{opt\_out}}{p_{opt\_in}}\right)^2 = \left(\frac{i_{opt\_out}}{i_{opt\_in}}\right)^4 = \exp\left(-4\alpha L\right) \tag{4.10}$$

where α and L are the fiber attenuation (in linear unit) and length respectively.

The PD model performs square detection before it delivers the photocurrent to the load. Assuming the optical power input to the photodiode is $p_d=(i_{opt\_out})^2$ and using the relations (4.4) and (4.5), the gain efficiency of the PD can be obtained as

$$g_{PD} = \frac{p_L}{{p_d}^2} = \frac{{i_L}^2 R_L}{\left(i_{opt\_out}\right)^4} = \left(r_{PD}\right)^2 \left(\frac{R_{PD}}{R_{PD}+R_L}\right)^2 R_L \tag{4.11}$$

If $R_{PD}= R_L$, the conversion coefficient of the PD can be simplified as

$$g_{PD} = {r_{PD}}^2 \frac{R_L}{4} \tag{4.12}$$

From (4.9), (4.10) and (4.12), the intrinsic gain of the direct modulated RoF link can be obtained using

$$g_i = {\eta_{LI}}^2 \frac{1}{R_G} \exp\left(-4\alpha L\right) {r_{PD}}^2 \frac{R_L}{4} \tag{4.13}$$

If the source and load resistances are equal and optical loss is assumed to be negligible, (4.13) can take a more simplified form as follows

$$g_i = \frac{1}{4}\left(\eta_{LI} r_{PD}\right)^2 \tag{4.14}$$

If there is no matching resistor in parallel to the load resistor, the ¼ term in (4.14) disappears.

The gain of external modulated links can be obtained with a similar manner. In this case, the modulation efficiency of laser is replaced by the modulation efficiency of the modulator. Considering resistive matching at the RF input of a MZM modulator and at output of the PD as in Fig. 4.1, the intrinsic gain of an external modulated RoF link (with negligible optical loss) is given by

$$g_i = \frac{1}{4}\left(\eta_{MZ} r_{PD}\right)^2 \tag{4.15}$$

where η_{MZ} is the modulator slope efficiency given by [127]

$$\eta_{MZ} = \frac{1}{2}\frac{\pi P_{opt} R_G}{V_\pi} \tag{4.16}$$

P_{opt} is the constant input optical power to the modulator which can be obtained from the static response of the laser for a corresponding bias current. From (4.14) and (4.15) we can reach to an important conclusion: in DM the intrinsic gain is constant with respect to the bias current in the small-signal regime, while in the external modulation, the gain increases with the square of the optical power. The link gain in the DM case is less than one, but the intrinsic gain of the external modulation link can be greater than one. However, by choosing the right matching circuit at a frequency band of interest, the gain of a directly modulated RoF link could be made higher one as reported by in [128] where authors have demonstrated gain of greater than one for more than 10 MHz bandwidth in the S-band.

Equation (4.14) seems to show that the intrinsic is independent on the RF input power. But if the power of the modulating RF signal continues to increase, the gain starts to decrease as a result of nonlinear behavior of the RoF link. The main nonlinear component in the RoF system is the laser diode in which the nonlinear effect is taken into account using the gain compression ratio of the laser diode (ε). Thus the laser modulation efficiency (η_{LI}) decreases at high RF power. Therefore, (4.14) holds true only in the linear region for small-signal modulation around the bias point. This leads to a conclusion that there exists a maximum input power after which the link output power saturates at a level (P_{sat}) as shown in Fig. 4.2. The other nonlinear behavior arises from the clipping effect if the laser is biased close to the threshold current. An important figure of merit to evaluate the gain compression is 1dB compression point (Fig. 4.2). It is defined as the input signal which causes the intrinsic gain to be reduced by 1dB.

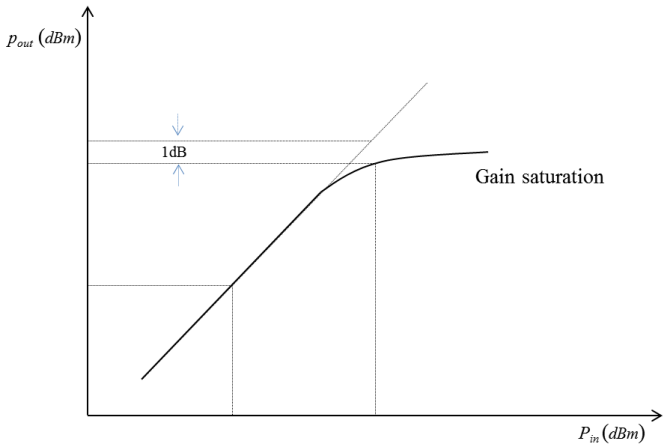

Fig. 4.2 Gain compression curve include dynamic range.

4.2.2. Noise Figure

Noise figure (*NF*) is a measure of degradation of the signal-to-noise ratio due to the device, the circuit or the system. NF for any two-port network or device is defined as the ratio of SNR at the input to the SNR at the output in logarithmic unit:

$$NF = 10\log\left(\frac{s_{in}/n_{in}}{s_{out}/n_{out}}\right) \tag{4.17}$$

Alternatively, NF can be written in terms of gain, input signal and noise. If the system or device adds noise n_{add}, the output signal and output noise are related to the input signal and noise as $s_{out}=g_i s_{in}$ and $n_{out}=g_i n_{in} + n_{add}$ respectively. Substituting those relations to (4.17), we can obtain another simplified expression

$$NF = 10\log\left(1+\frac{n_{add}}{g_i n_{in}}\right) \tag{4.18}$$

n_{in} is the thermal noise from the generator and its power is given in frequency domain as

$$n_{in} = k_B T\Delta f \tag{4.19}$$

where Δf is the measurement noise bandwidth, k_B is Boltzmann's constant, and T is temperature. It is measured at a temperature of 290 K, which is the standard temperature for noise figure measurement as defined by the IEEE.

Equation (4.18) shows that the noise figure is independent of the signal itself. The additional noise n_{add} could be caused by different components in the system. In IM-DD optical links, it includes the thermal noise from the laser, RIN, photodiode shot noise, and thermal noise from the electronic circuit. If we consider the simplified circuit in Fig. 4.1, the matching and laser resistances at the laser input contribute to the noise figure. When it is translated to the output of the system/device, the noise power is given by $g_i k_B T\Delta f$. As a result the total noise added by the system/device seen at the output can be written as

$$n_{add} = g_i k_B T\Delta f + k_B T\Delta f + n_{shot} + n_{RIN} \tag{4.20}$$

The second term ($k_B T\Delta f$) is thermal noise due to the load resistor.

n_{shot} is the shot noise power at the load. Shot noise is the photodiode noise which comes from the random behavior of the photodetection. Shot noise power is given by

$$n_{shot} = q\langle I_L\rangle\Delta f\ R_L \tag{4.21}$$

$<I_L>$ is the average load current which is related to the photocurrent I_{ph} by (4.5).

As for n_{RIN}, it represents noise power at the output due to the intensity noise of the laser. It is obtained by using

$$n_{RIN} = \langle I_L\rangle^2\ RIN\ R_L\Delta f \tag{4.22}$$

where *RIN* is the single sideband laser relative intensity noise at the RF signal frequency in linear unit. If the relative intensity noise spectrum is given in double sideband, there should be a factor of ½ in (4.22). From (4.21) and (4.22), we can observe that the shot noise power decreases linearly with the photocurrent but the noise power due to RIN decreases as a square of the photocurrent.

Assuming Δf = 1Hz, the noise figure at the output of the link can be calculated by substituting all additional noise sources (4.20) - (4.22) into (4.18) as follows

$$NF = 10\log\left(2 + \frac{\left(\frac{k_B T}{R_L} + q\langle I_L\rangle + \langle I_L\rangle^2 RIN\right)R_L}{(\eta_{LI} r_{PD})^2 n_{in}}\right) \tag{4.23}$$

From this expression, we can drive specific cases according to the dominant noise. It is valid for the simplified cascaded circuit shown in Fig. 4.1 where a lossy resistive matching is used.

The noise figure of an external modulated link is quite similar to that of direct modulated links except the modulation efficiency term which is related to the optical power, half-wave voltage and load resistance:

$$NF = 10\log\left(2 + \frac{\left(\frac{k_B T}{R_L} + q\langle I_L\rangle + \langle I_L\rangle^2 RIN\right)R_L}{(\eta_{MZ} r_{PD})^2 n_{in}}\right) \tag{4.24}$$

For optical heterodyne links, the noise figure calculation has to include passband intensity noises from the two lasers and baseband intensity noise at the millimeter-wave band and shot noise. Besides the phase noise conversion to intensity noise should be included. Because of the high phase noise levels from the two lasers, the intensity noise converted from phase noise is usually dominant. Considering the photocurrent for a heterodyne system given in (2.4), the noise figure of the heterodyne link can be written as follows [65] [129] and [130]:

$$NF = 10\log\left(2 + \frac{\left(\frac{2k_B T}{R_L} + q\langle I_L\rangle + RIN_{H1} I_{L1}^2 + RIN_{H2} I_{L2}^2 + I_{L\_mm}^2 \left(RIN_{L1} + RIN_{L2} + RIN_{\phi}\right)\right)R_L}{(\eta_{MZ} r_{PD})^2 n_{in}}\right) \tag{4.25}$$

where RIN_{H1} and RIN_{H2} are the relative intensity noise evaluated at millimeter wave, RIN_{L1} and RIN_{L2} are RIN from the first and second lasers respectively evaluated at the modulating RF frequency, and RIN_{ϕ} is the phase to intensity noise conversion. I_{L1} and I_{L2} are the DC photocurrents of individual lasers at the load, I_{L_mm} is the power of the millimeter-wave carrier.

4.2.3. Dynamic Range

The dynamic range (DR) is defined as the ratio of the maximum input RF power, $p_{in,max}$, to the minimum input RF power, $p_{in,min}$, that can be carried by the optical link [131] [132].

$$DR = 10\log\left(\frac{p_{in,\max}}{p_{in,\min}}\right) = 10\log\left(\frac{m_{\max}^2}{m_{\min}^2}\right) \tag{4.26}$$

where m_{min} is the modulation index of the input signal that results in equal signal and noise powers at the output (SNR=1), and m_{max} is the modulation index where the 1dB compression point occurs. If m_{max} represents the modulation index that makes the third order intermodulation distortion power equal to the noise power, the ratio (4.26) becomes the spurious-free dynamic range (SFDR). This is the case when the modulating RF signal is composed of two tones f_1 and f_2. The concept of DR, SFDR, and noise figure can be well understood from the diagram shown in Fig. 4.3.

The point where the power of the fundamental harmonic and the third order intermodulation product meet, which is known as the third order intercept (IP3) point, is another indicator of the nonlinearity of a link. IIP3 is corresponds to the input RF power and OIP3 refers to the output third order intercept points. SFDR can be obtained from OIP3 as follows:

$$SFDR_{dB} = \frac{2}{3}\left(OIP3_{dB} - N_{total}\right) \tag{4.27}$$

where N_{total} is the total noise of the link at the output.

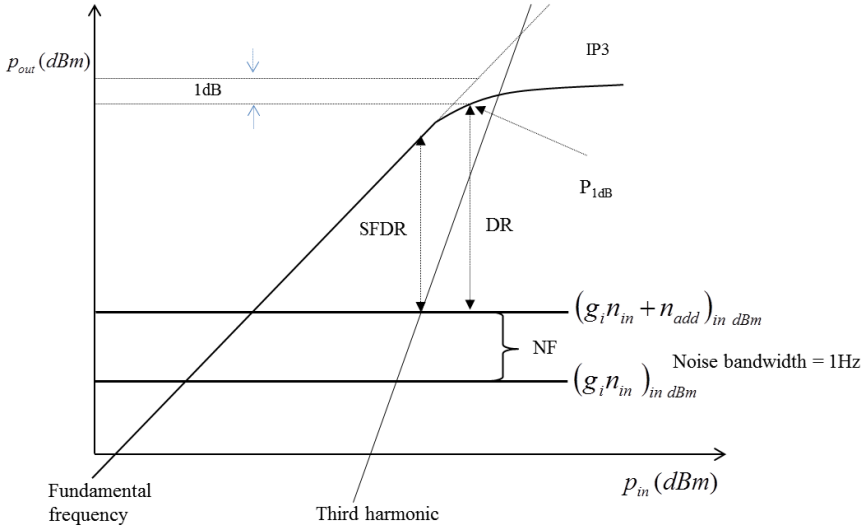

Fig. 4.3 Power of the fundamental frequency and third-order harmonic at the output of a nonlinear system versus input RF transmitted power showing dynamic range, SFDR and noise figure.

4.3. IM-DD RoF links

In this section, the performance of optical links are studied with simulation using ADS schematics of a direct modulated and external modulated RoF links which are shown in Fig. 3.28 and Fig. 4.7 respectively. These systems consist of sub-circuits representing DFB laser, MZM and photodiode include corresponding parasitic and matching circuits. The laser model in this simulation represents the DFB laser from III-V lab whose physical parameters are given in Table 6 (in section 3.2.10). The modulator model represents the MZM from Photline technologies with parameters given in section 3.3. The photodetector model represents PIN photodiode from Emcore, and the fiber model is the standard SMF with attenuation 0.2 dB/km attenuation and 17ps/nm/km dispersion.

The system parameters used for this simulation are as follows: the laser bias current is 400 mA, and bias voltage of modulator is at half of V_π. For simulations of direct modulated links

in this thesis, the RF frequency transmitted over the fiber link is chosen to be 2 GHz to avoid the relaxation oscillation. Comparison of intrinsic gain of direct and external modulation links is shown in Fig. 4.4. The EM link has higher gain compared to the DM link. The external modulator considered for this study has -3dB bandwidth of 28 GHz. Since the modulation frequency is chosen at 2 GHz and the absence of chirp effect, the influence of dispersion is very limited. Besides, the attenuation of 0.2dB/km is negligible for short distance communications.

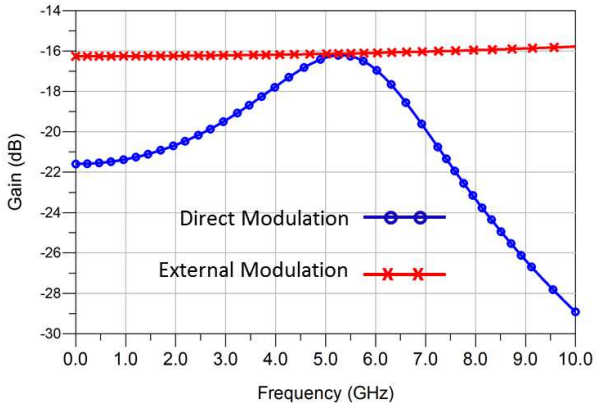

Fig. 4.4 RoF gain for IM-DD links.

4.3.1. RF power compression

Under large signal modulation, RoF links introduce distortion to the RF power due to the nonlinear behaviors of the modulation devices (laser or modulators). The gain compression point of RoF links can be obtained using harmonic balance simulation by taking the ratio of the RF signal powers at the output and the input. In Fig. 4.5, the gain compression and the SFDR levels of both DM and EM RoF links are given. The DM system has high 1dB compression point at RF input power of 31dBm compared to the EM link which is around the input RF power of 17dBm. The source of the compression in DM links is related to clipping effect due the threshold current. The slope of the static response of the laser (η_{LI}) is constant for bias currents above the threshold as shown in Fig. 3.29(a). In the EM case, the source of the nonlinear compression is due to the static characteristics of the modulator as shown in Fig. 3.32.

To evaluate the SFDR of the links, two tones of RF signals (2 GHz and 2.01 GHz) modulate the RoF links. The power of the fundamental frequency and third-order intermodulation product is shown in Fig. 4.5. The DM link is shown to have higher SFDR compared to the EM link. But in both cases, higher level of dynamic range is obtained since no amplifiers are employed in the system.

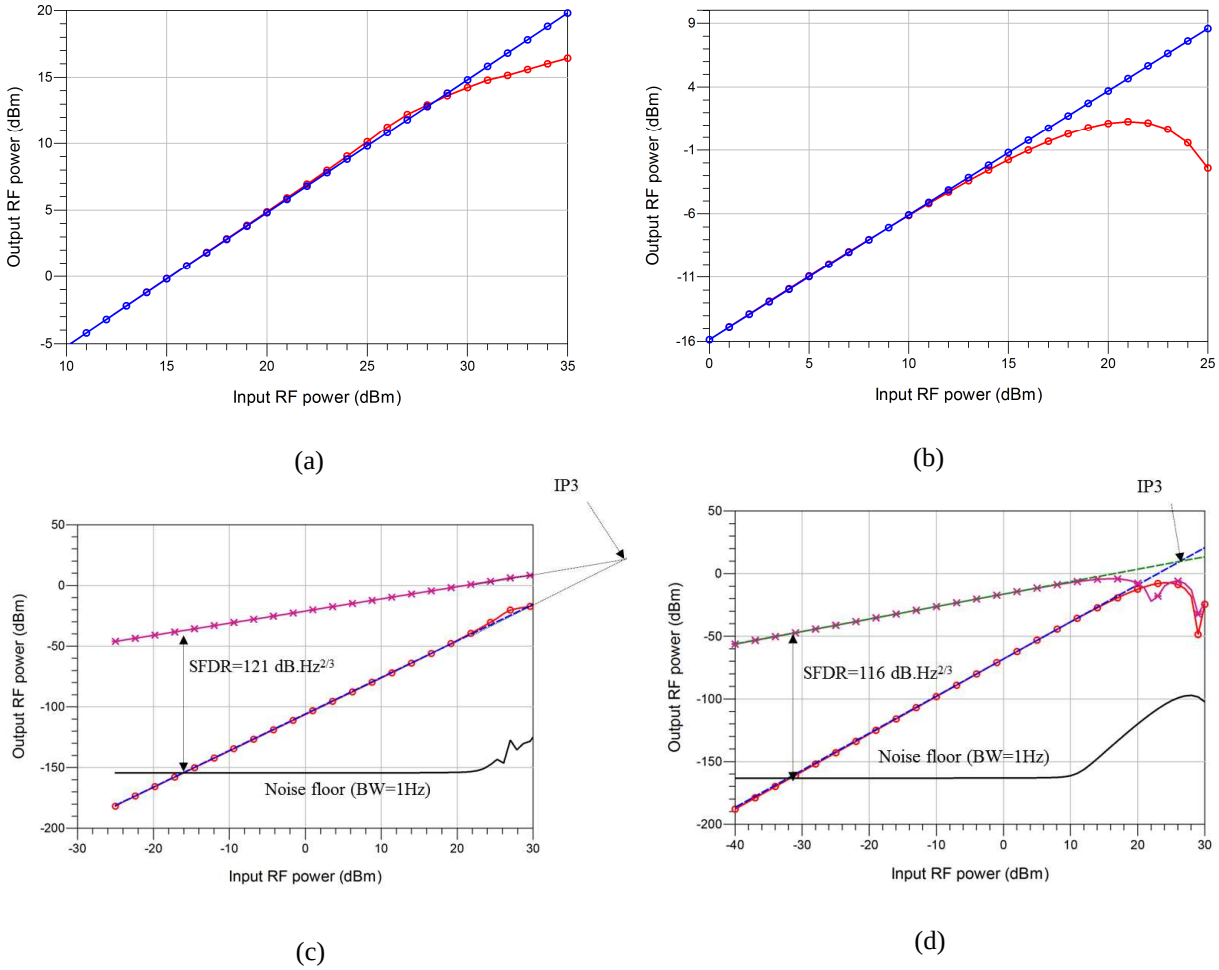

Fig. 4.5 (a) Gain compression of DM link (b) Gain compression of EM link (c) SFDR of DM link (d) SFDR of EM link.

4.3.2. Noise figure

In ADS, noise figure can be simulated using various controller tools: S-parameter, harmonic balance, envelope and AC simulators. The S-parameter and AC simulators are only used for linear systems. Therefore for precise evaluation of noise figure harmonic balance simulator has to be used using either its nonlinear noise option or using Noiscons component which can calculate noise figure using the standard noise figure configuration. Both single sideband and double sideband noise figures are calculated using ADS simulators. But for the RoF systems, when we say noise figure, it refers to the single sideband noise figure.

Noise figure versus bias current of a direct modulated laser link is presented in Fig. 4.6 by comparing simulation and calculation based on the definitions given above. In (a), the contributions of different types of noises from the RoF components to the load are presented to analyze the dominant noise source according to the bias point. The noise power at the load due to the laser RIN decreases when the laser bias current increases. This can be understood by looking at the expression (3.36) where we can observe that the RIN spectrum is proportional to the inverse of the average optical power at low frequencies. But moving close to the relaxation oscillation frequency, the RIN spectrum begins to be proportional to the inverse of the cube of the average photon density or average optical power ($1/p_a^3$). Since the RoF link being investigated here is at 2GHz which is close to the relaxation oscillation

frequency of the laser under study, we expect that the RIN power is inversely proportional to the cube of the power. And in (4.22), the RIN contribution to the total noise at the load is proportional to the square of the photocurrent which is related directly to the laser bias current. Therefore the overall RIN contribution to the total noise at the load is inversely proportional to the average optical power hence the laser bias current. This relation, however, is valid only at low power levels. According to [90], at high injection levels, the RIN spectrum starts to converge to the shot noise level of the RIN spectrum and becomes proportional to $1/p_a$. That is why the RIN noise power at the load drops quickly at low bias current and starts to slow down at higher bias currents. On the other hand, the shot noise power at the load increases with the bias current as we would expect it from the relation (4.21).

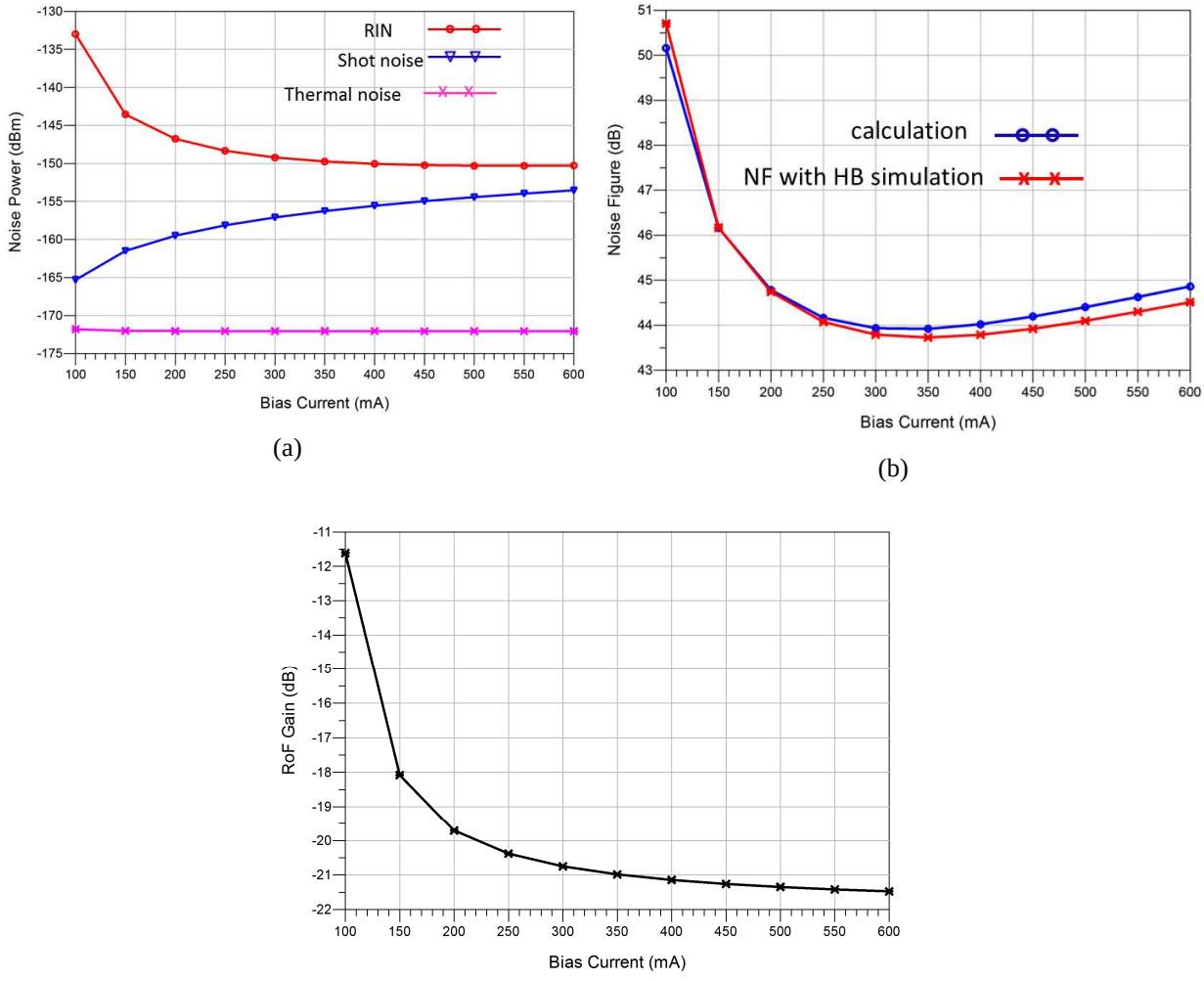

Fig. 4.6 HB noise simulation of DM IM-DD RoF link (a) individual noise powers at the output (b) noise figure (c) Gain of the link.

Fig. 4.6(b) illustrates the noise figure of the direct modulated link where NF simulation using harmonic balance simulator is compared with calculations made using (4.23). The noise figure obtained using HB simulation is the single sideband NF and it is about 0.4dB lower than that obtained using calculation from individual noise powers as in (4.23) in the shot noise dominant region.

In general, the result shows that there exists an optimum bias point where the NF of a directly modulated RoF link is minimum contrary to what one would expect from (4.23) which shows NF is directly proportional to the photocurrent (bias current). But this is logical because the system is being changed from RIN dominated to shot noise dominated when the bias current increases.

For external modulated links, NF can be studied with respect to the modulator bias voltage. This study is made using the ADS schematic shown in Fig. 4.7 when the modulator is biased at 6 V (half of V_π) and the laser is biased at constant current of 400mA. Since the bias current is constant, the RIN contribution to the total noise power is governed its relation with the photocurrent as in (4.22). As a result, the RIN noise contribution to the total noise power at the output increases with the photocurrent faster than shot noise. At low bias, shot noise and thermal noise are dominant but as the bias voltage increases the link becomes dominated by shot noise and RIN. The overall characteristic of NF versus bias voltage of the modulator is given in Fig. 4.8 (b) where the NF increases when the bias voltage increases from the minimum transmission bias point (V_{off}) to the maximum transmission bias point (V_{on}) of the modulator.

Compared to the noise figure of the direct modulated laser (Fig. 4.6 (b)), the noise figure of the EM link (Fig. 4.8 (b)) is lower. This is because the modulation efficiency of the external modulator (η_{MZM}) is higher than that of the laser diode resulting higher intrinsic gain. At 2 GHz, the intrinsic gain of the DM link is -20dB compared to -16dB for the external modulated link.

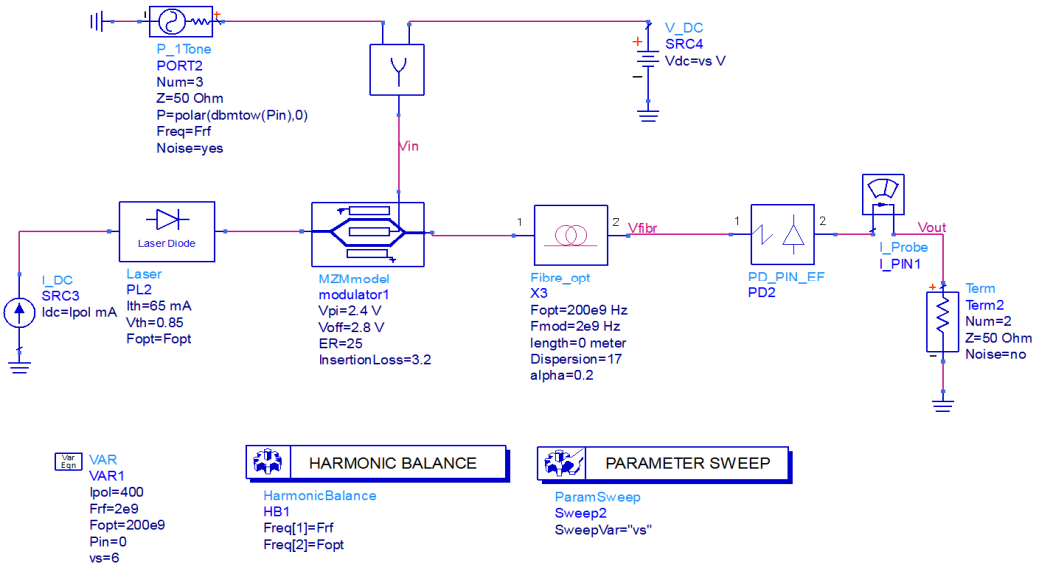

Fig. 4.7 ADS schematic for External modulated IM-DD RoF link.

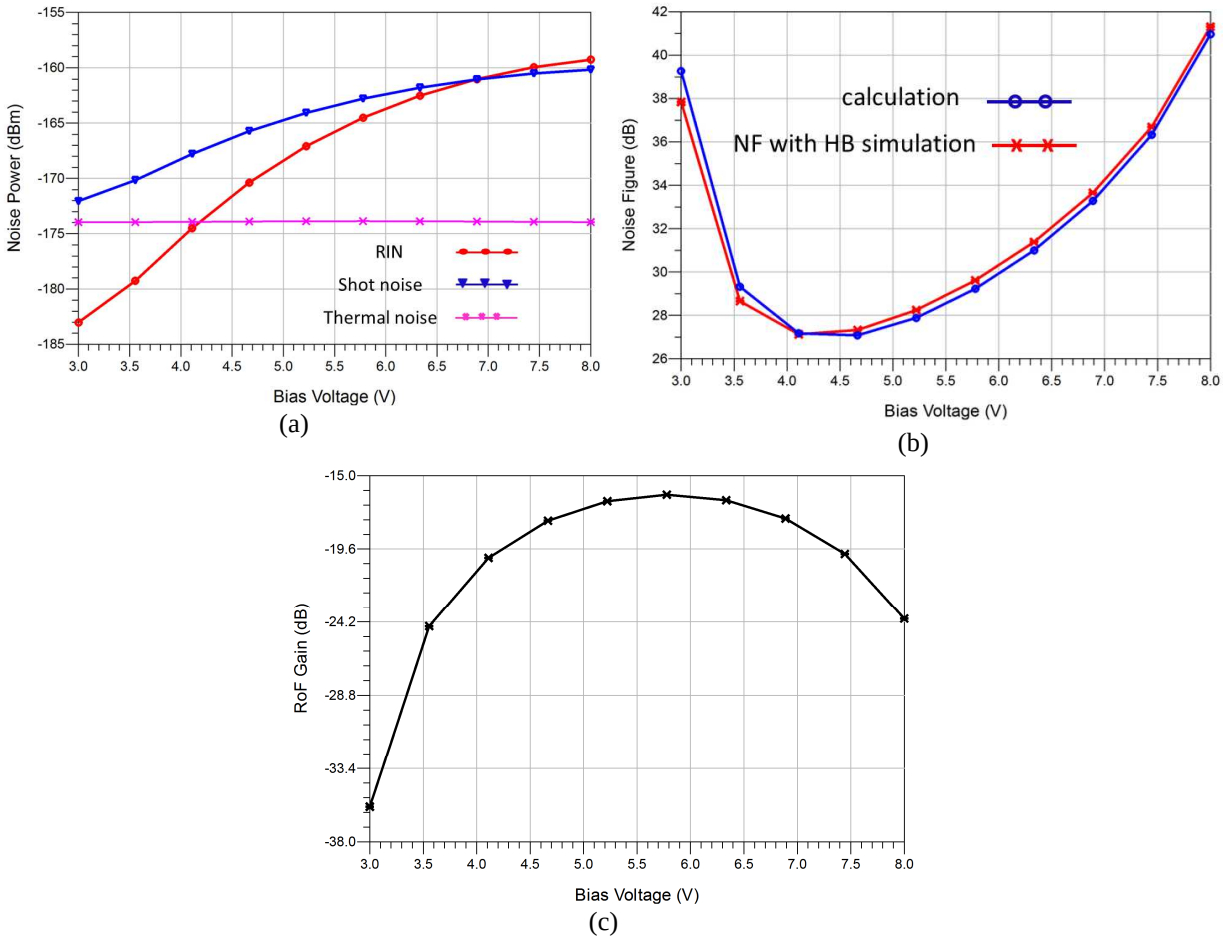

Fig. 4.8 HB noise simulation of EM IM-DD RoF link (a) individual noise powers at the output (b) Noise figure (c) Gain of the link.

4.3.3. Spectral purity

For some systems with stringent spectral purity requirements, the intrinsic gain and noise figure are not enough to characterize the link. The phase noise of the RF signal generated after the photodiode gives a measure of the spectral purity of the signal. One of the reasons of phase noise degradation of RF signal in IM-DD RoF links is the low-frequency intensity noise of the laser up-conversion during DM of the laser. This phenomenon is investigated in [133] where up-conversion factor is derived for a directly modulated laser. The up-conversion factor determines the amount of low-frequency noise transposed to the microwave frequency as illustrated in Fig. 4.9.

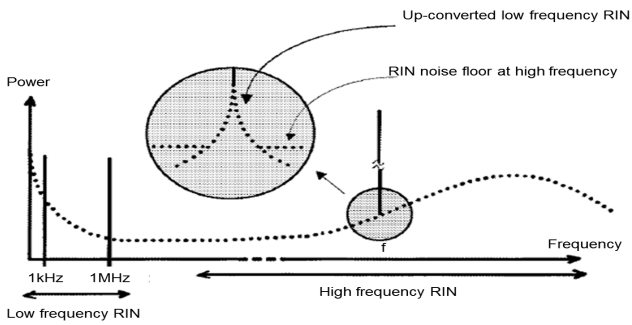

Fig. 4.9 Low-frequency noise conversion to the microwave signal [133].

The low-frequency noise can be included in the large-signal model of the laser by simply inserting the low-frequency noise source with spectrum given in (3.42). This noise is independent on bias current. The parameter that characterizes the low-frequency noise is Hooge's parameter which is between 10^{-3} to 10^{-4} for III-V semiconductor materials. The noise conversion and the intensity noise floor contribution to the microwave phase noise can be explained by the following expression [133]:

$$P_{\phi}(f_{RF}) = \frac{1}{2} R_L \left(2qI_{ph}^2 + RIN(f_{RF}) I_{ph}^2 + \frac{kT}{R_L} \right) + \frac{b_{\text{det}}^2}{R_L} |K_{PM}|^2 (f_{RF}) RIN_{1/f} \qquad (4.28)$$

where P_{ϕ} is the total phase noise power, $RIN(f_{RF})$ is the relative intensity noise of the laser at the modulation frequency, $K_{PM}(F)$ is the PM/AM noise conversion factor, $RIN_{1/f}$ is the low-frequency intensity noise of the laser (low-frequency RIN).

Equation (4.28) shows that the microwave phase noise is composed of two components: the phase noise close to the modulation frequency, f_{RF}, and the phase noise far from the carrier. The *1/f* noise up-converted to the f_{RF} is dominates at very low frequencies with *1/f* characteristics. With the increasing offset, it is merged with the phase noise floor which is determined by the sum of other noise sources in the link. If the fiber dispersion is taken into consideration, the laser phase noise is converted to amplitude noise which results in close-in phase noise around the microwave frequency of interest.

The directly modulated RoF link shown in Fig. 3.28 is used to simulate the low-frequency noise level and its contribution to the phase noise of the RF frequency after the photodiode. For this simulation, the III-V lab laser biased at 400 mA, and Emcore photodiode are used. If all the noise sources including laser phase noise are turned off except the *1/f* noise in the system, the phase noise of the RF signal after the photodiode will have the spectrum shown in Fig. 4.10 (a), assuming no fiber dispersion. The *1/f* noise appears at very low frequency and its magnitude is be very small.

Fig. 4.10 (b) shows the phase noise of the RF signal after the fiber of different lengths. These simulations show that the close-in phase noise is negligible compared to the noise floor and chromatic dispersion doesn't have pronounced effect on the spectral purity of the RF signal.

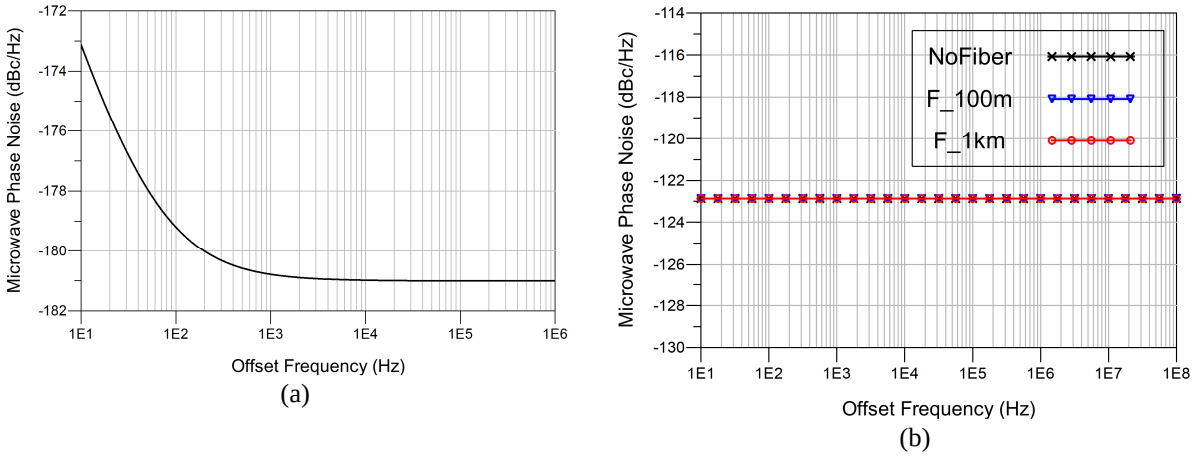

Fig. 4.10 Simulation of RF phase noise after RoF link (a) only *1/f* noise (b) laser phase noise conversion to microwave phase noise due to chromatic dispersion.

4.4. Heterodyne RoF links

Typical optical heterodyne system consists of two free running lasers, an optical combiner, and a photodiode. An example of an analog optical link with remote heterodyne detection is depicted in Fig. 2.9. In this section the properties of these systems are studied by simulation using the equivalent circuit models of the O/E and E/O components developed in chapter 3 which are suited for these kinds of systems since both the intensity and optical phase noises are included. ADS schematic of a heterodyne system is given in Fig. 4.11. The output of the laser models at '*optical*' frequencies are coupled together before the photodiode. The two heterodyning lasers represent the III-V lab DFB laser and EM4 DFB laser. The photodiode represents UTC photodiode with parameters given in section 3.4. The first laser is biased at 400 mA and the second laser is biased at 180 mA. The RF signal that modulates the MZM is 2 GHz.

The intrinsic gain analysis for these systems is identical to that of IM-DD systems. But here the noise figure includes the shot noise and RIN contribution from the second laser. However, the performance of heterodyne system for analog communication is largely dependent on the laser phase noise. Since the RF signal after the photodiode is the result of beating between the optical signals from the two uncorrelated lasers, chirp has a direct impact to the wanted signal even when there is no fiber dispersion effect.

4.4.1. Noise Figure

Noise simulation of an external modulated heterodyne link shows that the system is shot thermal noise limited. The contributions of RIN noise from both of the lasers, shot noise and thermal noise have the same behavior as the EM IM-DD link as shown Fig. 4.8(a), but with higher noise power level because of the high photocurrent in the heterodyne system. But the noise figure of heterodyne systems is higher than IM-DD links because of the additional noise from the second laser. Since the heterodyne link is based on external modulation, the individual noise components present in EM IM-DD links will still be here. However, the heterodyne links is dominated by the high phase noise from the two lasers. As shown in Fig. 4.12, the noise figure obtained from HB NF simulation coincides with noise figure calculation using (4.25). The reason for this problem is not fully understood up until now.

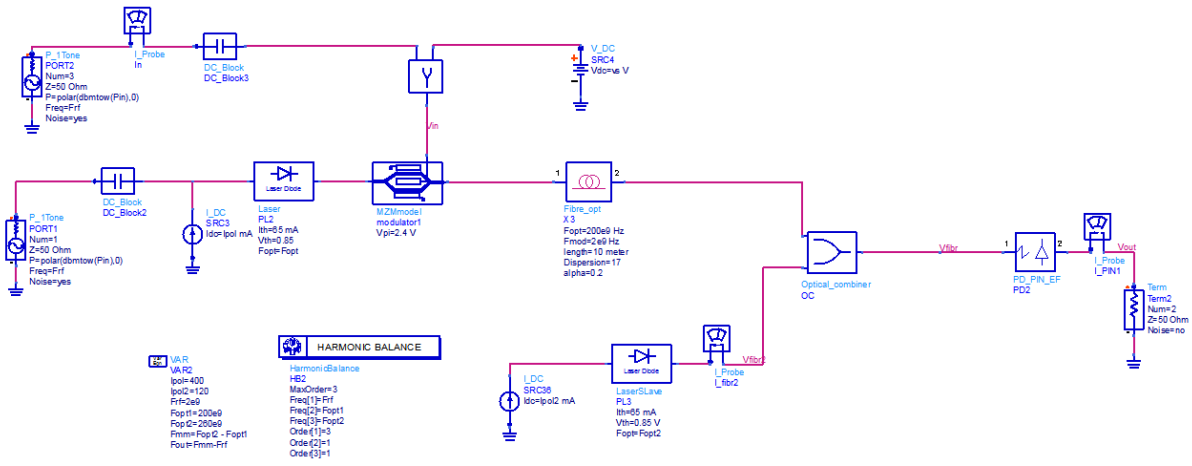

Fig. 4.11 ADS schematic of external modulated heterodyne RoF link.

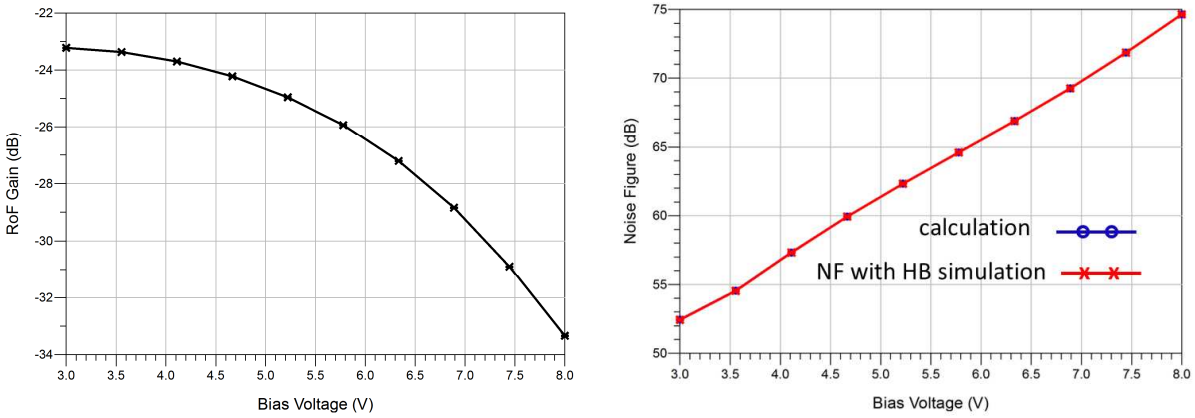

(a) (b)

Fig. 4.12 HB simulation noise simulation of EM heterodyne RoF link (a) gain of the optical link (b) noise figure.

4.4.2. Laser phase noise influence

As it has been explained in section 2.5.2, the laser phase noise has direct impact on the signal generated using optical heterodyne systems. The optical phase noise contribution to the wanted signals which are the sidebands of the beating signal (ω_{mm}= ω_{opt1} - ω_{opt2}) can be explained by exploiting the trigonometric relations similar to those carried out in section 2.5.2. Assuming the microwave signal that modulates the laser or MZM is $cos(\omega_c\, t)$, at a frequency f_c, the modulated optical signal after Taylor series expansion can be expressed as

$$E_1(t) = E_1\, e^{\left(j\left(\omega_{opt1}\, t + \phi_{opt1}\right)\right)} \left[1 + m\cos\left(\omega_c t\right)\right]$$

$$= E_1\, e^{\left(j\left(\omega_{opt1}\, t + \phi_{opt\,1}\right)\right)} \left[1 + \frac{m}{2}\left(e^{\left(j\omega_c t\right)} + e^{\left(-j\omega_c t\right)}\right)\right] \qquad (4.29)$$

$$= E_1 \left(e^{\left(j\left(\omega_{opt1}\, t + \phi_{opt\,1}\right)\right)} + \frac{m}{2} e^{\left(j\left(\omega_{opt1}\, t \pm \omega_c t + \phi_{opt1}\right)\right)} \right)$$

After transmission over the fiber, the three frequency components travel at different speed through the fiber due to chromatic dispersion. Therefore, at the output of the fiber, the three frequency components will have different phase delay components as follows

$$E_1(t) = E_1 \left(\begin{array}{l} e^{\left(j\left(\omega_{opt1}\, t + \phi_{opt1} + \varphi_0\right)\right)} + \frac{m}{2} e^{\left(j\left(\omega_{opt1}\, t + \phi_{opt1} - \omega_c t + \varphi_1\right)\right)} \\ \\ \qquad\qquad + \frac{m}{2} e^{\left(j\left(\omega_{opt1}\, t + \phi_{opt1} + \omega_c t + \varphi_2\right)\right)} \end{array} \right) \qquad (4.30)$$

φ_0, φ_1, φ_2, correspond to the group delay introduced by the chromatic dispersion of the fiber as discussed in section 3.5. For small modulating microwave frequency (ω_c) these phase differences can be neglected.

The second laser output can be expressed as

$$E_2(t) = E_2\, e^{\left(j\left(\omega_{opt2}\, t + \phi_{opt2}\right)\right)} \tag{4.31}$$

If we suppose that polarization alignment is achieved between the two optical signals, the resulting photocurrent becomes

$$I_{RF} = R\ \left(E_1(t) + E_2(t)\right)^2 = R \left[\begin{array}{l} E_1^{\,2} + E_2^{\,2} + E_1^{\,2}\dfrac{m^2}{2} + E_1^{\,2}\dfrac{m}{2}\cos\left\{\omega_c t + (\varphi_1 - \varphi_0)\right\} \\ \qquad\qquad + E_1^{\,2}\dfrac{m}{2}\cos\left\{\omega_c t + (\varphi_0 - \varphi_2)\right\} \\ + E_1^{\,2}\dfrac{m^2}{4}\cos\left\{2\omega_c t + (\varphi_1 - \varphi_2)\right\} \\ + E_1 E_2 \cos\left\{\omega_{mm} t + (\phi_1 - \phi_2) + \varphi_0\right\} \\ + E_1 E_2 \dfrac{m}{2}\cos\left\{(\omega_{mm} - \omega_c)t + (\phi_1 - \phi_2) + \varphi_1\right\} \\ + E_1 E_2 \dfrac{m}{2}\cos\left\{(\omega_{mm} + \omega_c)t + (\phi_1 - \phi_2) + \varphi_2\right\} \end{array}\right] \tag{4.32}$$

The desired signal can be found from the last two terms of (4.32) i.e. sidebands of the beat signal ω_{mm} which can be separated from the other components by using suitable band pass filter. It contains the phase noise from the two uncorrelated laser sources. The linewidth of the millimeter-wave signals is equal to the sum of linewidths of the two lasers. If the modulating microwave signal carries phase sensitive digital signals such as OFDM signals, the received signal would be severely degraded by the optical phase noise.

This can observed using phase noise simulation techniques available in ADS using the schematic shown in Fig. 4.11. The two lasers represent III-V lab laser biased at 400mA, and EM4 laser biased at 180 mA. The phase noise simulation technique in ADS is based on small-signal mixing of noise [134]. The tools are dedicated to oscillator phase noise simulation in frequency domain, but the technique can be used to study phase noise around any large-signal frequency such as optical frequency in our case because the phase noise of a large-signal carrier can be analyzed from small-signal mixing of noise. The mixing analysis additionally computes the AM noise as well at offset frequencies from the any large-signal frequency. The phase noise simulation method in ADS calculates the single sideband phase noise by the same way as the standard phase noise notation which is often denoted as $L(f)$. This spectrum can be computed from the phase noise spectral density as in (16) and is expressed in dBc/Hz.

Fig. 4.13 shows the phase noise spectrums of the millimeter-wave signal (ω_{mm}- ω_c). Since the EM4 laser has very high phase noise at 180 mA, the millimeter-wave signal has exactly the same phase noise as the EM4 laser.

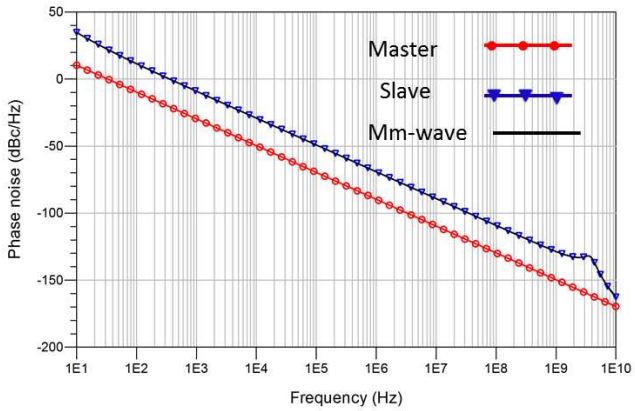

Fig. 4.13 Simulation of phase noise of lasers and millimeter-wave signal.

The level of phase noise in optical heterodyne systems is unacceptable for many applications. Consequently, some techniques have to be employed to reduce the phase noise level. As it has been discussed briefly in chapter 2, the methods used to mitigate the effect of laser phase noise from the two laser sources can be divided into two categories: the first one is by using two free running lasers and electrical self-homodyne method [65] or using phase noise cancelling circuits as in [135], and the second method is by creating correlation between the two sources through an optical or electrical feedback mechanism [41] [42].

Optical phase locked loop (OPLL) method is one of the methods that create correlation between the sources using electrical feedback. OPLL is of interest because of its potential to significantly reduce the relative phase noise of a pair of frequency-locked lasers, resulting in the optical generation of high spectral purity signal, mainly for millimeter-wave applications. This following section will briefly discuss some theoretical background about OPLL.

4.4.3. Optical phase locked loop

The theory behind OPLL is based on the classical control theory of negative feedback which consists of a forward-gain element with transfer function $A(\omega)$ and feedback element $B(\omega)$ as in Fig. 4.14.

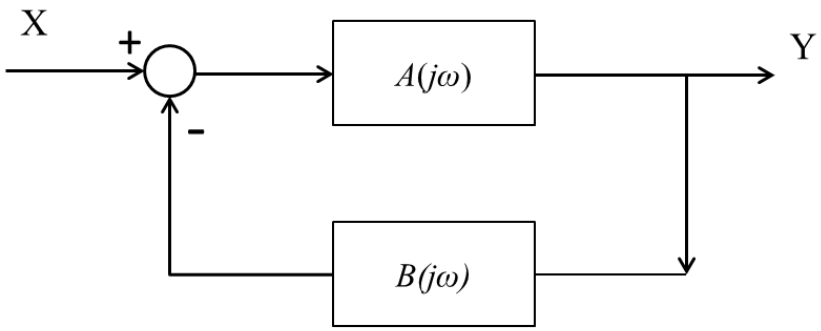

Fig. 4.14 Negative feedback loop.

In the case of OPLL, A represents the laser frequency modulation (FM) response, and B represents the loop transfer function. A heterodyne system with OPLL is represented in block diagrams in Fig. 2.9. The phase difference between the local oscillator and the optically generated RF signal is feedbacked to the slave laser to force it to follow the master laser phase profile.

The closed loop transfer function of such systems is given by:

$$TF(\omega) = \frac{Y}{X} = \frac{A(\omega)}{1 + A(\omega) \times B(\omega)} \tag{4.33}$$

The millimeter-wave signal which is filtered from the photocurrent given in (4.32) is mixed with the LO, which is represented by $a_{LO}cos(\omega_{LO}+\phi_{LO})$, to give a phase error signal:

$$I_{err} = K_m \, a_{LO} \, R \, E_1 E_2 \sin\left(\left(\omega_{LO} - \omega_{mm}\right) t + \left(\phi_m - \phi_s\right) - \phi_{LO}\right) \tag{4.34}$$

where K_m is related to the gain conversion factor of the mixer, a_{LO} is the LO current amplitude, ω_{OL} is the LO angular frequency and ϕ_{OL} is the LO phase noise. ϕ_m and ϕ_s represent the phase of the master and slave lasers respectively.

The feedback loop at the receiver consists of high speed photodiode (e.g. UTC PD), electrical low pass filter, LO at the millimeter-wave band, and slave laser. The delay component in Fig. 2.9 is used to take into account the propagation delay in the optical connection and electrical circuits for the loop. Time delay is one of the most important issues for the OPLL stability condition. In free space optics, it is much higher but it can be reduced as much as in order of picoseconds in integrated OPLL structures [136].

Since the slave laser at the receiver usually has high spectral width, the aim is to reduce the phase noise by using OPLL. This can be achieved by adding the phase error signal (4.34) to the bias current of the slave laser to force it to follow the profile of the master laser. The error signal has to pass through the low pass filter to reduce the noise bandwidth. The OPLL architecture can be improved with a balanced detection which could be used to reduce unwanted intensity noise (from both lasers) in the loop.

The effect of the feedback on the properties of the slave laser can be investigated by considering the rate equations. Since the feedback is added to the bias current of the laser, the loop has some influence on the laser internal parameters. These influences can be modelled by adding the feedback term to the rate equations that represent carrier density. The coupling of carrier density and photon densities will introduce changes in the behavior of the laser characteristics such as relaxation oscillation frequency, RIN, and phase noise. The modified carrier density rate equation can be written as [137]

$$\frac{dn}{dt} = \frac{\eta_i I_{bias}}{qV_{OL}} - \frac{n}{\tau_n} - a v_g \, p(n - n_0)(1 - \varepsilon p) + k \, p(t - \tau) + F_n(t) \tag{4.35}$$

where k is a constant representing the laser FM response, τ is the loop propagation delay.

4.4.4. Optical phase locked loop properties

Simplified small-signal model of an OPLL for phase propagation in the loop is shown in Fig. 4.15. The slave laser acts as a current controlled oscillator which has a phase equal to the integral of the input current fluctuation. Its transfer function for the phase propagation in the loop is $1/\omega$. The open loop transfer function of the feedback circuit is defined by the product of frequency responses of all the components and is used to state the loop bandwidth and loop gain. It can be expressed as:

$$G_{op} = \frac{K_{dc}\, H_F(\omega) H_{FM}(\omega) \mathrm{e}^{(\omega\tau)}}{\omega} \tag{4.36}$$

where K_{dc} is the feedback loop gain which is given by the magnitude of (4.34), the low frequency values of the loop filter response and the FM response (FM sensitivity) of the slave laser. $H_F(\omega)$ is the frequency response of the filter, and $H_{FM}(\omega)$ is the frequency response of the slave laser normalized with FM sensitivity. The time delay caused by the feedback is taken into account by the exponential term.

The open loop transfer function is used to define some important performance metrics such as loop bandwidth and stability. The loop bandwidth is defined as the largest frequency for which the open loop transfer function is larger than unity. However, it is usually limited by the loop stability condition which states that the magnitude of the open loop function should be less than unity when its phase is $-\pi$. Therefore, the frequency at which the phase of G_{op} equals $-\pi$ represents the maximum possible value of the loop bandwidth.

Generally speaking, the closed loop bandwidth is determined by the requirements for loop stability, the sum of slave and master laser linewidths, and phase noise level of the mm-wave signal required by the system. Since semiconductor lasers have a large amount of phase noise, a wide feedback bandwidth is necessary. In order to achieve the wide feedback bandwidth, the loop-propagation delay must be small and the bandwidths of the electrical components together with the slave laser FM response must be wide and uniform in both magnitude and phase [61].

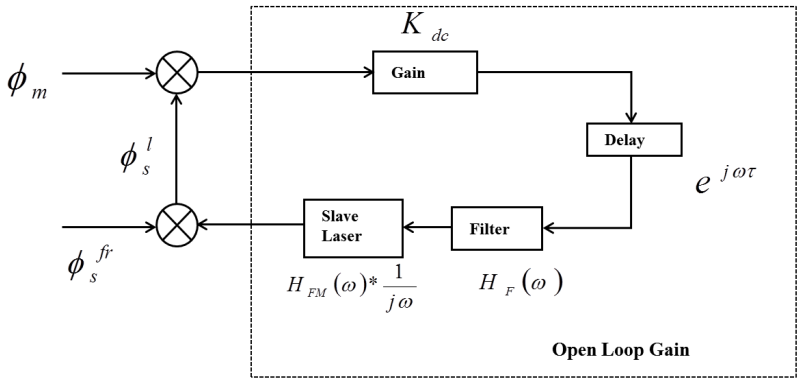

Fig. 4.15 Simplified small-signal schematic of an OPLL [138].

From the simplified small-signal model of the loop (which neglects the amplitude noise in the loop), we can obtain the phase of the slave laser after locking as

$$\phi_s^l = \phi_m \frac{G_o}{1+G_o} + \phi_s^{fr} \frac{1}{1+G_o} \tag{4.37}$$

ϕ_s^l is the phase of the locked slave laser, and ϕ_s^{fr} is the phase of free running slave laser. This equation shows a very important relation between the slave laser and master laser phase noise. The locked laser phase follows the master when the open loop gain is greater than one. For very low values of the open loop gain the slave laser phase noise is independent of the master laser phase noise and it will be equal to the ϕ_s^{fr}.

The residual phase error of the loop is also another important parameter to evaluate OPLL performance. It is defined as the variance of phase deviation of the locked laser from the ideal case where it follows the master laser. For stable OPLL, the standard deviation of the phase error should be much lower than 1 rad² [61]. The phase error variance is given by:

$$\sigma_\phi^2 = \left\langle \left(\phi_s^l(t) - \phi_m(t)\right)^2 \right\rangle \tag{4.38}$$

In frequency domain this can be related to the spectral density of the phase error by using Wiener-Khintchine theorem

$$\sigma_\phi^2 = \int_{-\infty}^{+\infty} S_\phi^e(f)\,df \tag{4.39}$$

S_ϕ^e is the spectral density the phase of the beat signal, (ϕ_m - ϕ_s) and it can be obtained from (4.37) as follows

$$S_\phi^e(f) = \left|\frac{1}{1+G_o}\right|^2 \left(S_\phi^m(f) + S_\phi^{s,fr}(f)\right) \tag{4.40}$$

where S^{m}, $S^{s,fr}$ are the spectral densities of the phase of master laser and free running slave laser respectively.

To link the residual phase error to the spectral linewidths of the two lasers, we can use (3.38) and (3.39). So, the phase noise spectral densities of the two lasers in terms of the spectral linewidth of the lasers can be written as

$$\begin{aligned} S_\phi^{s,fr}(f) &= \frac{\Delta\nu_m}{2\pi f^2} \\ S_\phi^m(f) &= \frac{\Delta\nu_s}{2\pi f^2} \end{aligned} \tag{4.41}$$

Finally, using (4.38) and (4.41) the residual phase error variance will be

$$\sigma_\phi^2 = \frac{\Delta\nu_m + \Delta\nu_s}{2\pi} \int_{-\infty}^{+\infty} \left|\frac{1}{1+G_o}\right|^2 \frac{1}{f^2}\,df \tag{4.42}$$

4.4.5. OPLL Simulation

ADS schematic for OPLL simulation is shown in Fig. 4.16. The setting of this simulation is as follows: master laser is biased at 400 mA, and slave laser is biased at 180 mA. The corresponding free running mode linewidths are 13.3 kHz and 1 MHz for the master and slave lasers respectively. The photodiode is UTC PD with similar parameters as in the previous simulations. Phase noise spectrums of the slave and master lasers are shown in Fig. 4.13 where the slave laser phase noise is the dominant contributor to the millimeter-wave phase noise. Local oscillator is used with appropriate sign to obtain the phase error signal for the loop. The loop filter is a first order low-pass filter with bandwidth of 6 MHz with stopband

attenuation of -15dB. This loop filter is chosen to obtain high performance loop which is shown to be less sensitive for time delay compared to higher order loops [64].

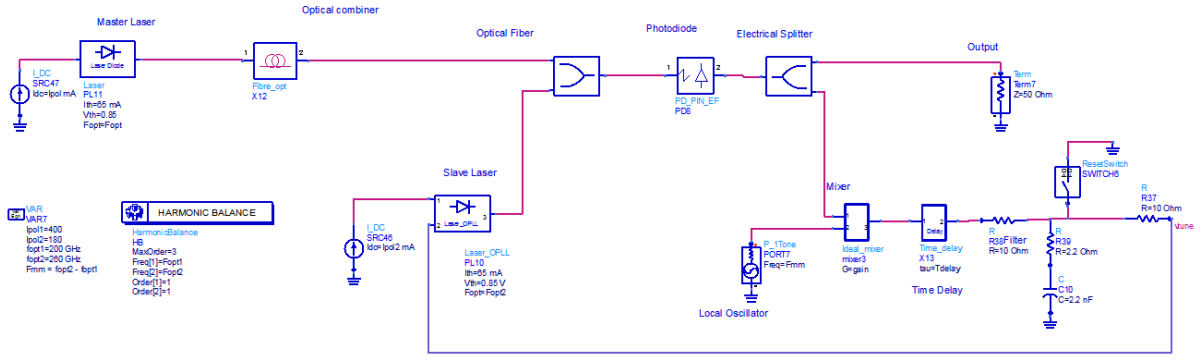

Fig. 4.16 Schematic of heterodyne system with OPLL simulation in ADS.

As a first step for OPLL simulation, the open loop transfer function should be studied separately to determine the bandwidth of the feedback loop. It is important to make sure that the open loop gain and bandwidth satisfy the stability requirements. The transfer function of the OPLL can be obtained by using small-signal analysis around the steady-state operating point. AC simulation can be used to evaluate the open loop transfer function which is shown in Fig. 4.17. The feedback bandwidth is estimated to 10MHz and the requirement for stability is achieved for time delay of 1 and 10ns but not for 100ns. The total phase error variance estimated to be 0.027 rad² in infinite bandwidth and 0.013 rad² in 12 MHz loop bandwidth.

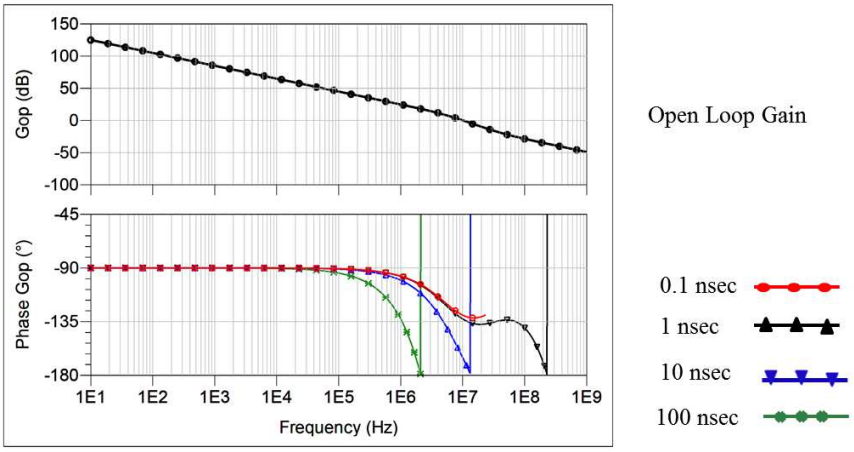

Fig. 4.17 Open loop transfer function (magnitude and phase) for different time delays.

The OPLL simulation can be performed by using HB or Env simulators. With the loop parameters in Table 7, the phase noise simulation result is shown in Fig. 4.18. The slave laser phase noise is locked to the master laser for lower offset frequencies (below f_{BW}) and causes significant reduction of the mm-wave phase noise to a level of -97 dBc/Hz. This is due to the correlation created between the master and slave lasers. But at higher offset frequencies (above f_{BW}), the slave laser phase noise becomes equal to the free running phase noise since the two lasers will become uncorrelated at high offset frequencies. The oscillation observed at higher offset frequencies is due to the loop delay effect. The result shown in Fig. 4.18 is obtained using loop delay of 10 nsec.

Table 7. OPLL Key parameters.

Parameters	Values
Loop bandwidth, f_{BW}	10 MHz
Loop gain, Kdc	0.07 GHz
Loop propagation delay, τ	10 ns
PD responsivity	0.45 mA/mW
Local oscillator power (f_{LO} = 60 GHz)	-3dBm
Mixer conversion loss	6dB

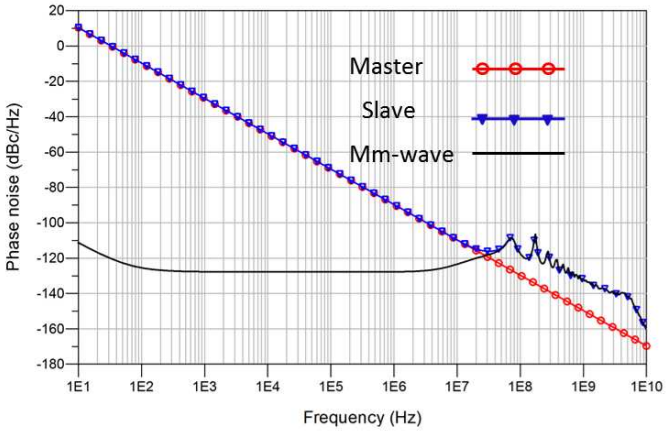

Fig. 4.18 Phase noise of slave laser, master laser and mm-wave signal with OPLL.

4.5. Summary

In this chapter, the analog properties of a RoF link mainly the intrinsic gain and noise figure are defined and simulation results are discussed for different system configurations. The equivalent circuit models of RoF components are used to obtain results in consistent with the theory. Assuming simple resistive matching at the laser input and photodiode output, it is shown that the intrinsic gain direct and MZM based EM links are mainly dependent on the conversion efficiencies of the modulating devices (laser or modulator) and photodiode. In external modulated link, it is possible to increase the gain by increasing the optical power because the conversion efficiency of the modulator is power dependent. As a result, the noise figure of an external modulated link is shown to have much lower level than direct modulated links.

The last part of this chapter deals with effect of laser phase noise in optical heterodyne system. Laser phase noise is of great concern in the case of complex modulated RF signal transmission over the fiber. To reduce the effect of laser phase noise, we have introduced OPLL to the heterodyne link. With careful consideration of loop parameters, the millimeter-wave signal generated by the heterodyne link is shown to have lower phase noise compared to the open loop case. These studies are made to demonstrate the effectiveness of the equivalent circuit models to analyze variety of systems even when negative feedback loop is included. In the next chapter, the OPLL system will be used for transmission of high data rate signal based on OFDM modulation.

5

60-GHz Wireless signal (OFDM) transmission over RoF links

5.1. Introduction

Despite the nonlinear and noise distortions of radio over fiber systems, their performance is generally accepted for current wireless communication systems such as 2nd generation (2G), and 3rd generation (3G) systems even when using low cost semiconductor lasers and photodiodes [139] [140]. Signal distortion and attenuation could be compensated by the receiver amplifiers and digital signal processing functionalities of the data recovery. However to achieve higher data throughput, next generation wireless systems will need more demanding requirements for RoF links. These systems will use OFDM technology which provides robust performance on a wireless channel. The high spectral efficiency, resilient to inter-symbol interference and flexibility of OFDM makes it attractive for wireless communications in the 60 GHz band. However, OFDM signals are sensitive to phase noise which causes the loss of orthogonality among subcarriers because of phase rotation on each subcarrier and inter-carrier interference between subcarriers.

In this chapter, we use the equivalent circuit models of RoF components to study the transmission of OFDM signal over heterodyne RoF links. The OFDM signal complying IEEE standards for the 60 GHz band is generated using MATLAB and circuit analysis is performed in ADS using co-simulation techniques. We demonstrate that the effects of noise and nonlinearity can be evaluated using circuit simulation techniques. This analysis has benefited from the simulation the RoF characteristics explained in the previous chapters to evaluate the influences of component level impairments over system performance. Performance of the system is evaluated using EVM simulation. It is shown that optical heterodyne systems are highly influenced by the optical phase noise from the optical sources and the performance of such systems can be considerably improved by using an optical phase locked loop.

5.2. 60 GHz wireless transmission characteristics

5.2.1. Attenuation

The 60 GHz signal is impacted by different phenomena such as oxygen absorption, different obstacles, material attenuation, path loss etc. At 60 GHz, the signal is absorbed by oxygen molecules to much higher extent compared to other frequencies. The oxygen absorption at 60 GHz leads to significant signal attenuation of up to 17 dB/km [141]. Signal attenuation at 60 GHz due to dry wall, white board, wall studs is also observed to be higher compared to other frequencies such as 2.5 GHz [142]. The main mechanisms of signal propagation at 60 GHz are line of sight (LOS), first-order and second-order reflection paths [143]. There is little diffraction since the signal wavelength is smaller than most of the objects. As a consequence of the aforementioned attenuation factors, 60 GHz signal does not travel far distance and these systems are suitable for high throughput indoor data delivery requiring lots of BSs of very small size to extend the network coverage.

5.2.2. Modulation options

There are few modulation classes that can be considered for millimeter-wave wireless transmission. These options include multi-carrier (OFDM), single carrier (SC), and constant envelope modulation [34].

OFDM modulation is well suited for multipath channels as the frequency selective fading is divided into a number of flat-faded channels. This help the equalization function to be efficient compared to other modulation options. The other advantage of OFDM modulation is its high spectral efficiency compared to others. However, OFDM systems are complex. The peak-to-average ratio (PAPR) of OFDM signals is much higher than other systems limiting the efficient use of amplifiers. Moreover, it is more sensitive to frequency offset and phase noise.

Generally, each modulation type offers its own advantage and disadvantage. For a given application, one can find the best choice. For instance, if an application requires the most resilient performance in multipath channels and transmitter power efficiency is not critical, OFDM could be the best solution. But if both battery life and support of higher data rates are equally important (for line of sight (LOS) or non LOS channels), single carrier modulation is preferred solution.

5.2.3. Wireless standards in the 60 GHz band

Standardizations targeting the 60 GHz band include IEEE 802.15.3c, WirelessHD, ECMA-387, Wireless Gigabit Alliance, and IEEE 802.11.ad. These standards are meant to address the market which is moving to the widely available millimeter-wave band to support multi-gigabit transmission as new wireless usages are demanding high data throughput.

The IEEE 802.11.ad is a family of IEEE.802.11 family and it is started as a new generation Wi-Fi system in the 60GHz allowing it to maintain the current Wi-Fi user experience. It is expected that this standard will be the most widely deployed technology. Below are the physical layer specifications of OFDM signals according to the three standards.

Table 8. OFDM PHY layer specification for the 60GHz standards.

Parameters	IEEE 802.15.3c HSI mode	ECMA-387 Type A	IEEE 802.11.ad OFDM PHY
Occupied bandwidth	1.815 GHz	~1.904 GHz	1.815 GHz
Sampling rate	2.640 GSa/s	2.592 GSa/s	2.640 GSa/s
Number of subcarriers	512	512	512
FFT period	193.9 ns	197.53 ns	193.9 ns
Cyclic Prefix duration	24.24 ns	24.7 ns	48.5 ns
Cyclic Prefix length	64	64	128
OFDM symbol duration	218.18 ns	222.23 ns	242.4 ns
Number of data subcarriers	336	360	336
Number of pilots subcarrier	16	16	16
Number of DC subcarriers	3	3	3
Number of null subcarriers	141	133	0
Number of unused subcarriers	16	0	157
Modulation	QPSK 16-QAM, 64-QAM	QPSK 16-QAM	SQPSK, QPSK 16-QAM, 64-QAM

5.2.4. OFDM signal

Orthogonal frequency division multiplexing is one of the best alternatives to tackle multipath propagation effects in wireless communication systems while maintaining several advantages such as high spectral efficiency, reduced inter-symbol interference, robustness to the impulsive noise. However, it has also some drawbacks such as sensitivity to carrier frequency offset and phase noise, sensitivity to I and Q imbalance, high peak-to-average ratio (PAPR), requires high speed digital to analog converter (DAC) and analog to digital converters (ADC) and high energy consumption.

OFDM building blocks are shown in Fig 5.1. At the transmitter, the IFFT block is used to map the bit stream of data to each sub-carrier. After the parallel to serial converter, cyclic prefix is added and the signal is up-converted to an intermediate frequency. At the receiver, the signal is down-converted and passed through the FFT block to demodulate the output bit stream. Mathematically, the transmitted signal can be written as:

$$s_{RF} = \mathrm{Re}\left\{\sum_{n=0}^{N-1} s_n\left(t - nT_{sys}\right)e^{(j2\pi f_c t)}\right\} \tag{5.1}$$

where Re{.} represents the real part of the signal, T_{sys} is the symbol length, N is the number of OFDM symbols, f_c is the center frequency, and $s_n(t)$ is the complex baseband signal representation for the n^{th} OFDM symbol.

In OFDM systems, when many subcarriers combine constructively, they create high peak signal in time domain. This peak is one of the disadvantages of OFDM modulation format since it causes clipping or distortion effects. It is characterized by the PAPR parameter which can be calculated as the ratio of maximum power to the mean power:

$$PAPR_{dB} = 10\log\left(\frac{power_{\max}}{power_{mean}}\right) \tag{5.2}$$

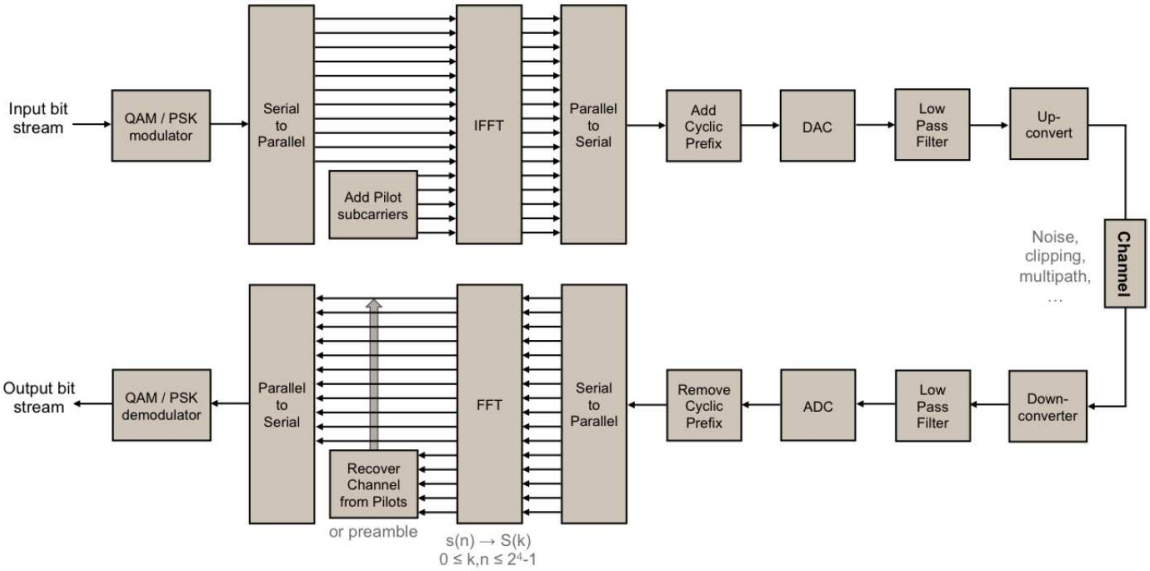

Fig 5.1. OFDM building blocks.

5.2.5. Phase noise in OFDM signals

The performance of OFDM systems are highly dependent on the frequency offset and phase noise of the system. The effect of frequency offset has been thoroughly analyzed in the literature and many methods have been proposed for its estimation and correction. For instance in [144], maximum likelihood estimation (MLE) algorithm is used to estimate and compensate the frequency offset. Phase noise on the other hand is a random process and it is difficult to compensate. Phase noise is caused by many components mainly transmitter and receiver oscillators. But if optical heterodyne RoF links are used for transmission of wireless OFDM signals, the large laser linewidth is the main cause of system phase noise. Several works have been done to investigate and quantify the effect of phase noise in OFDM signals [145] [146].

The effect of phase noise on each OFDM sub-carriers can be observed by writing the complex envelop of the transmitted signal, $s_n(t)$ as

$$s(n) = \frac{1}{N}\sum_{k=0}^{N-1} s_k \exp\left(j2\pi n \frac{k}{N} \right) \tag{5.3}$$

where s_k is the sampled signal in the frequency domain, N is the total number of OFDM symbols.

Assuming the channel in Fig 5.1 is linear and the only effect is phase noise, the received signal after the FFT block can be expressed as

$$r(k) = s(n)\, e^{j\phi(n)} \tag{5.4}$$

Using small-signal approximation on the phase fluctuation, we can write

$$e^{j\phi(n)} = \cos(\phi(n)) + j\sin(\phi(n)) \\ = 1 + j\phi(n), \text{if } \phi(\text{n}) \text{is small} \tag{5.5}$$

This approximation is important to separate the signal and noise parts as follows

$$r(k) = s(n)(1 + j\phi(n)) \tag{5.6}$$

Therefore, the demodulated bit stream of data will be

$$y(k) \approx s_k + \frac{j}{N}\sum_{r=0}^{N-1} s_k \sum_{n=0}^{N-1} \phi(n) \exp\left(j2\pi n \frac{k}{N}(r-k) \right) \\ = s_k + e_k \tag{5.7}$$

Equation (5.7) shows the error introduced on the received signal is merely due to phase noise. This effect can be analyzed in two ways. The first is when $r=k$: this is a cause of the common phase error (CPE) and it manifests itself by introducing phase rotation in the constellation map. The second effect is when $r \neq k$ causing inter-carrier interference. This is normally the cause of loss of orthogonality in the OFDM signal which is essential to the proper functioning of the system.

Some of the subcarriers in the OFDM signal are pilot subcarriers which are used for time and frequency synchronization, and phase noise correction. The OFDM demodulator, therefore, continuously track the known pilot subcarriers in the transmitted signals to compensate for the phase noise rotation. However, the amount of phase noise that can be compensated at the demodulator is limited. To evaluate and optimize the level of phase noise for phase noise dominated systems, it is useful to use the rule-of-thumb that the pilot tracking by the demodulator effectively compensates the phase noise at offsets up to about 10% of the OFDM subcarrier spacing [147].

5.2.6. Error Vector Magnitude

Signal to noise ratio (SNR), bit error rate (BER), and error vector magnitude (EVM) are common performance metrics for the performance evaluation of digital signal transmission in many wireless applications. But EVM provides fast and efficient method to measure and evaluate multi-level, multi-phase modulation signals [148]. EVM considers all of the potential phase and amplitude distortions as well as noise and provides a single comprehensive measurement figure for determining the performance of the system. It is defined as the average constellation error power with reference to the point of a highest constellation point of the modulation scheme, so it measures the rotation of the signal in the constellation as shown in Fig 5.2.

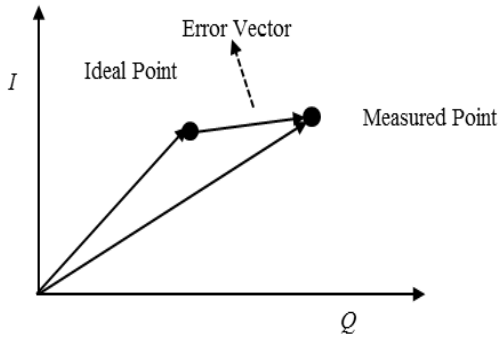

Fig 5.2. Diagram illustrating EVM calculation for a constellation point.

Mathematically, EVM is expressed as [149]:

$$EVM = \frac{\sqrt{\frac{1}{N}\sum_{1}^{N}\left(\Delta I_i^2 + \Delta Q_i^2\right)}}{R_{\max}} \tag{5.8}$$

where N is the number of symbols used in the measurement, ΔI and ΔQ are error vectors, and R_{max} is the magnitude of the ideal transmitted symbol for the chosen modulation.

A common problem with EVM measurements is the choice of the correct reference point. This is because the receiver does not have knowledge of the transmitted data, and EVM is measured by comparing the received signal with the closest reference point on the constellation plane. If the transmitted signal is highly degraded by the noise and other imperfections, a received signal point may be compared to the wrong reference point. When the signal degradation is very high, the calculated EVM value could even be lower than the real EVM value with reference to the correct reference point. This effect is shown in Fig 5.3 where the deviation of the EVM calculation based on the closest reference point and the real EVM [148]. The problem is even worse for higher level modulations such as 1*6-QAM* and *64-QAM*.

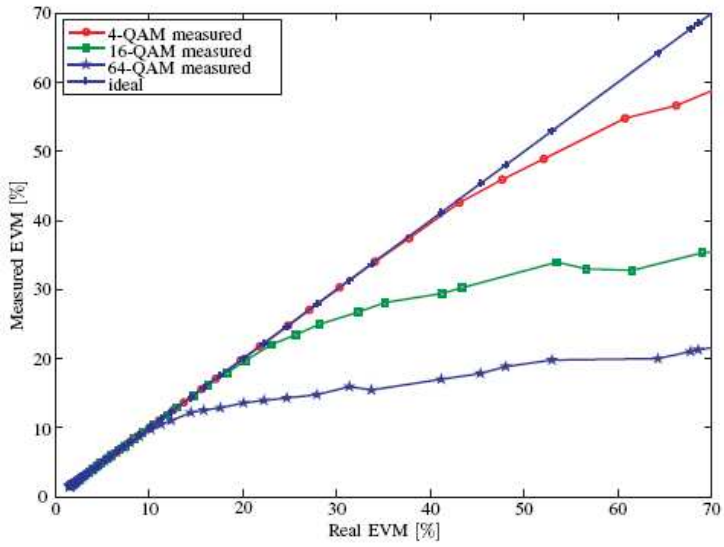

Fig 5.3. Measured EVM and Real EVM [148].

EVM measures combined effects of different impairments mainly nonlinearity, noise, gain and phase imbalance of IQ modulator. In OFDM signals the effect of non-linearity on the EVM performance is either compression or symbol dispersion. The intermodulation between subcarriers distorts the symbol on another carrier causing inter-carrier interference (ICI). These two phenomena make the effect of nonlinearity to appear as a random noise. However, nonlinearity cannot be treated as a random noise.

The effect of phase noise on the EVM can be studied using the variance of different noise sources because the noises are uncorrelated. In the context of RoF links, the noise sources are RIN from the laser, phase noise of the laser, photodiode shot noise, and thermal noises.

For a system noise modelled by a Gaussian noise model, EVM can be related to SNR by assuming that the error vector powers in (5.8) are equal to the noise powers [150] as:

$$EVM = \sqrt{\frac{1}{SNR}} \tag{5.9}$$

However, this formula is to be used with caution because the assumption is invalid if signal degradation is caused by nonlinearity and phase noise. In single-carrier, linear and memoryless systems, the relation between EVM and SNR is given by [151]

$$EVM = \sqrt{\frac{1}{SNR} + 2 - 2\exp\left(-\frac{\delta_\phi^2}{2}\right)} \tag{5.10}$$

where δ_ϕ is the total phase jitter of the system at the receiver and SNR is the output signal to noise ratio. For OFDM/QAM based systems, detailed analysis of EVM considering contribution of individual effects (noise, nonlinearity, and IQ imbalance) is given in [152]. The analytic EVM evaluation gives comparable results according to the general definition of EVM.

If IQ imbalance is neglected, EVM of an OFDM signal can be estimated from the phase noise spectrum, $L(f)$, and SNR as follows If the system is phase noise dominant, EVM can be related to the phase noise spectrum [153] [147] as

$$EVM = \sqrt{2 * \int L(f) df + \frac{1}{SNR}} \tag{5.11}$$

where $L(f)$ is the single sideband phase noise spectrum.

5.3. OFDM signal transmission over RoF links

In this study, RF signal carrying OFDM modulated digital signal is transmitted over different architectures of RoF links to investigate the effects of noise and nonlinear distortions by simulation. Since all of the system components are represented by equivalent circuit models, this study can be performed in ADS where co-simulation option can be used to analyze the influence of analog circuits over the digital signal.

ADS library offers various components to generate MB-OFDM signals. But those components are specifically designed for UWB standards in the centimeter wave band

according to the specification given in [154]. Therefore OFDM signal with the 60 GHz standard is generated using MATLAB and the baseband data is loaded to ADS. The simulation set-up is shown in Fig 5.4 where the EVM calculation is done after exporting the baseband data to MATLAB. Up-conversion and down-conversion of the baseband signals is performed using QAM modulator and demodulators available in ADS library components. Dataflow and envelop simulations are performed to evaluate the analog link on the digital signal.

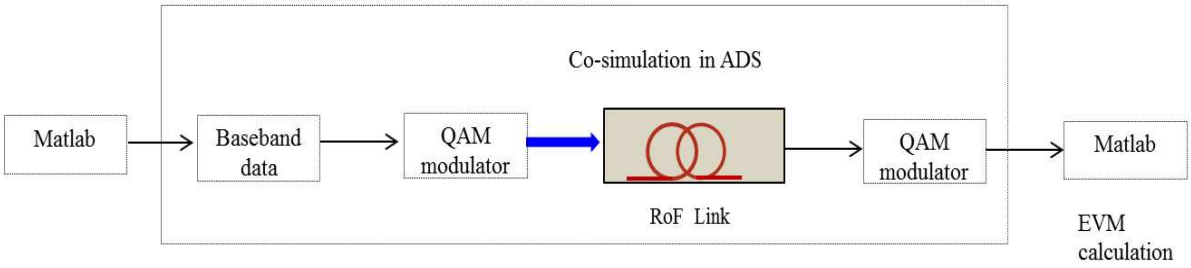

Fig 5.4. Simulation technique set-up OFDM signal transmission over the fiber links.

For this study, quadrature phase shift keying (QPSK) signal is generated using MATLAB [4] using the IEEE 802.15.3c specifications listed in Table 8. The QAM modulator considered is ideal to avoid I-Q imbalance. The baseband signal constellation and the up-converted signal at IF frequency are shown in Fig 5.5 when the total power of the OFDM signal 0dBm. Null and pilot subcarriers are plotted in red and the data subcarriers are in blue. Since the electrical components are ideal, the SNR in the back-to-back case about 30dB and the EVM is around 0.29% for almost all of range of usable power levels. The PAPR of the OFDM signal is calculated to be 13dB.

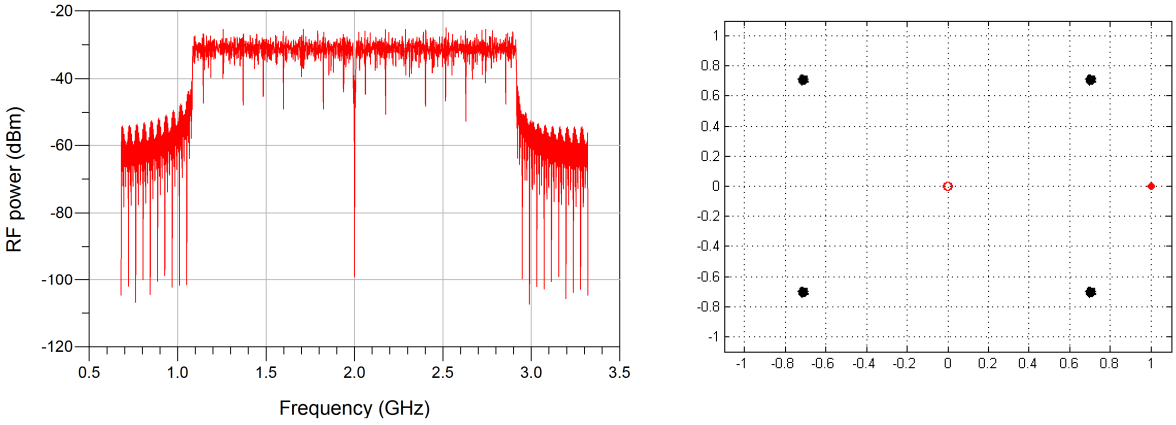

Fig 5.5. (a) Spectrum of transmitted RF signal and (b) constellation of the pure baseband signal.

5.3.1. IM-DD links for 60 GHz communication

IM-DD links with DM and EM links are characterized in section 4.3. For the transmission of the OFDM wireless signal, the setting for the optical link will be as follows: the III-V lab laser is biased at 400mA, fiber length is set to zero, and the photodiode is Emcore PIN photodiode. The photodetected IF signal is up-converted to millimeter-wave by using a mixer with gain of -6dB and noise free local oscillator. The schematic of the simulation setup of the

DM link is shown Fig 5.6. It should be noted that this study is made in the absence of laser chirp. Therefore single mode fiber has very limited effect on the RF signal (2GHz) for short distances. Thus the fiber length is assumed zero to reduce complexity.

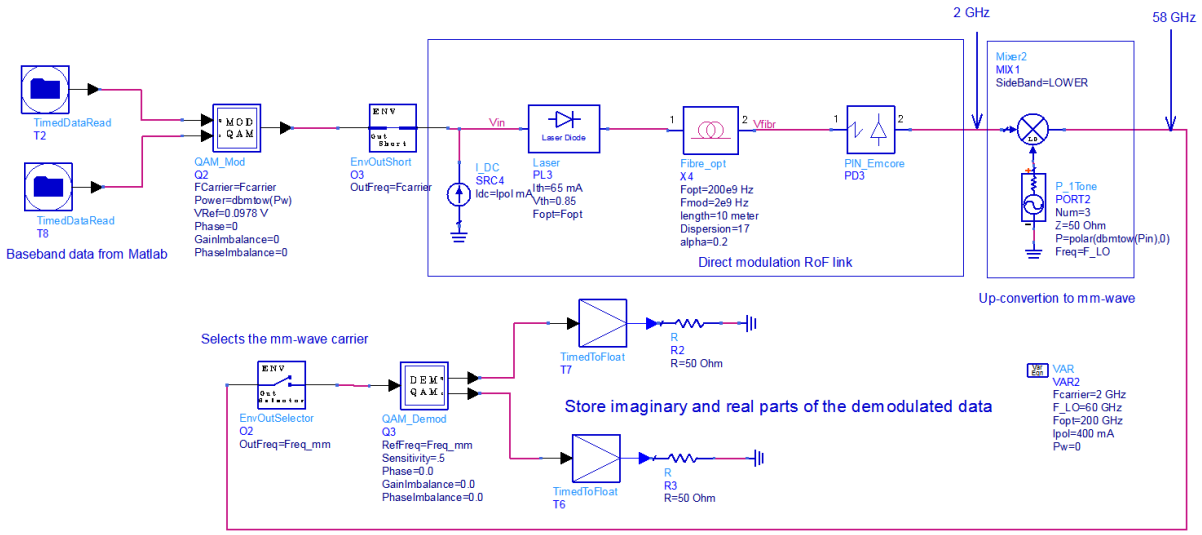

Fig 5.6. DM IM-DD simulation setup.

The spectrum of the received OFDM signal after transmission over the IM-DD link is shown in Fig 5.7. Because of the RoF link loss and mixer loss, the level of the received spectrum is around -65dBm compared to -30dBm in the back-to-back case. As we can see from the spectrum, the optical link has attenuated the signal but there is not considerable degradation on the constellation. This spectrum is obtained when total emission power is 0dBm which is close the optimum point where the effects of noise and nonlinear distortion are minimum. EVM calculation at this power level is about 1.74 %. Nevertheless, there is still an increase in EVM compared to the back-to-back case due to the unavoidable intensity noise of the optical components.

Considering the extreme cases when the input total OFDM power is -30dBm and 30dBm, we can observe the effects of intensity noise and nonlinear distortion in Fig 5.8 and Fig 5.9. In Fig 5.8, the SNR is very small (around 15dB) and the constellation is extremely distorted due to the noise from the RoF link. The EVM calculation shows around 40 %.

In Fig 5.9, the total power of the OFDM signal is increased to 30dBm to show the nonlinear distortion due to the RoF link. The constellation of the demodulated signal shows the signal distortion but it is hard to say whether the effect is noise or nonlinear distortion from the constellation since the nonlinear distortion effect appears as noise. As shown in Fig. 4.5, the input power level where 1dB compression point of the DM IM-DD link occurs is around 29dBm. Since the PAPR is 13dB, the system is in the saturation region if the input power is above 16dBm. This nonlinear distortion originates from the clipping effect due to the threshold current of the laser diode.

On the other hand, the external modulated RoF link characterized in section 4.3 shows that its noise figure is better than DM links. However, the 1dB compression point is around input power level of 17dBm (lower than the DM case) even if the MZM is biased at the linear region (6V). The noise and nonlinear effects in EM IM-DD links are shown on the OFDM

spectrum and constellation diagram of the received signal after the optical link in Fig 5.10 and Fig 5.11. Since the PAPR of the OFDM signal is 13dB, IP3 point is decreased by 13dB, thus the compression starts to occur when the total mean power of the OFDM signal is about 8dBm.

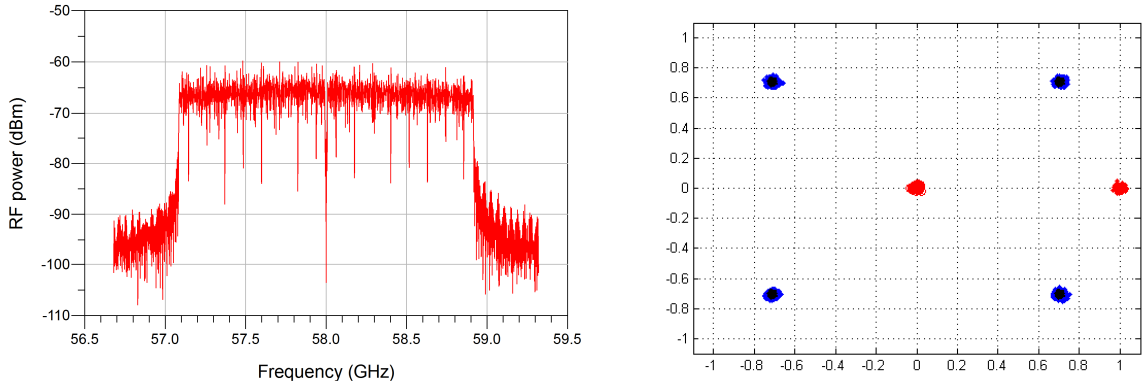

(a) (b)

Fig 5.7. DM IM-DD link (a) Received OFDM signal at millimeter-wave (b) constellation of demodulated baseband signal, P_{OFDM} = 0dBm.

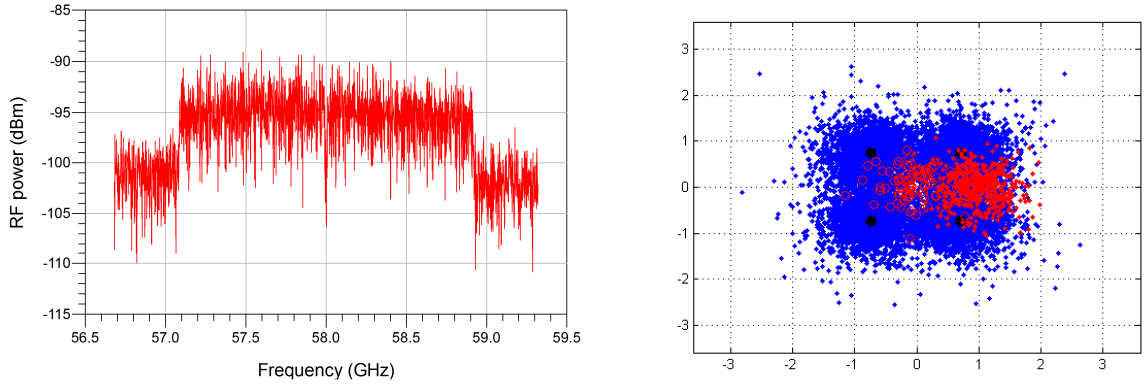

(a) (b)

Fig 5.8. DM IM-DD link (a) Received OFDM signal at millimeter-wave (b) constellation of demodulated baseband signal, P_{OFDM} = -30dBm.

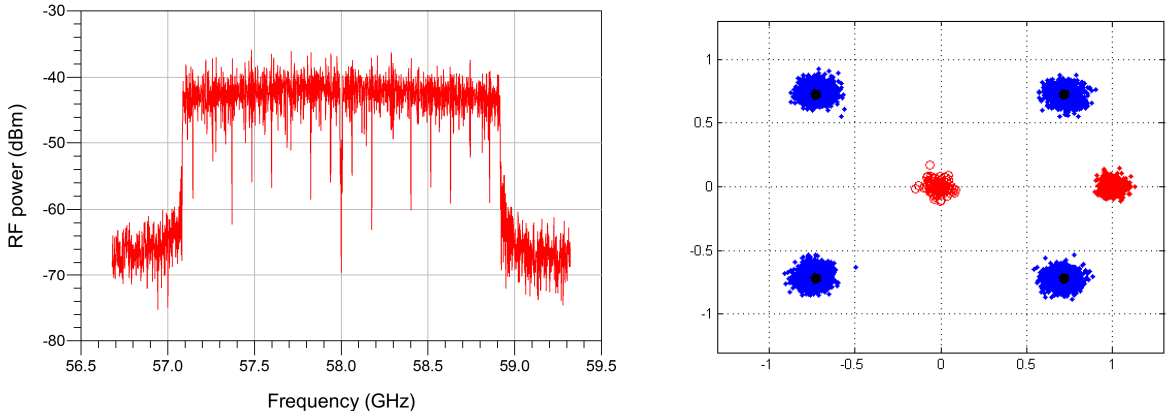

(a) (b)

Fig 5.9. DM IM-DD link (a) Received OFDM signal at millimeter-wave (b) constellation of demodulated baseband signal, P_{OFDM} = 30dBm.

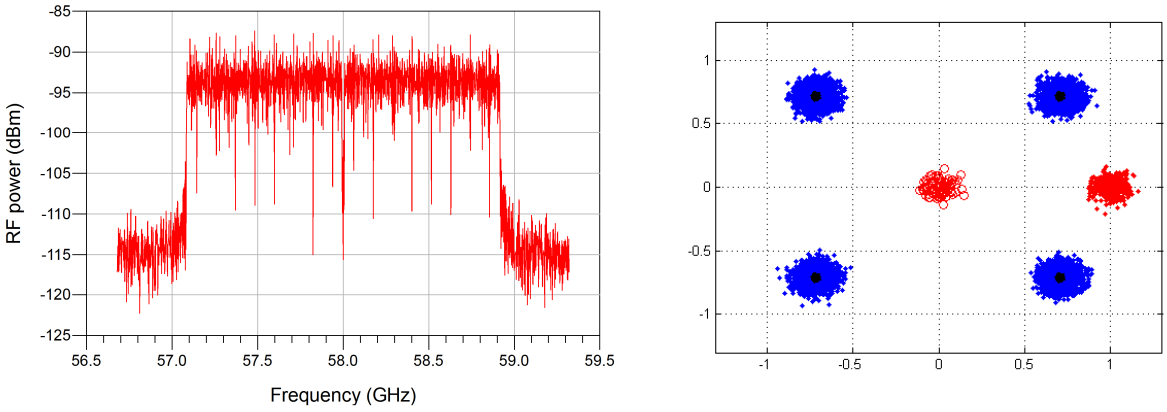

(a) (b)

Fig 5.10.EM IM-DD link (a) Received OFDM signal at millimeter-wave (b) constellation of demodulated baseband signal, P_{OFDM} = -30dBm.

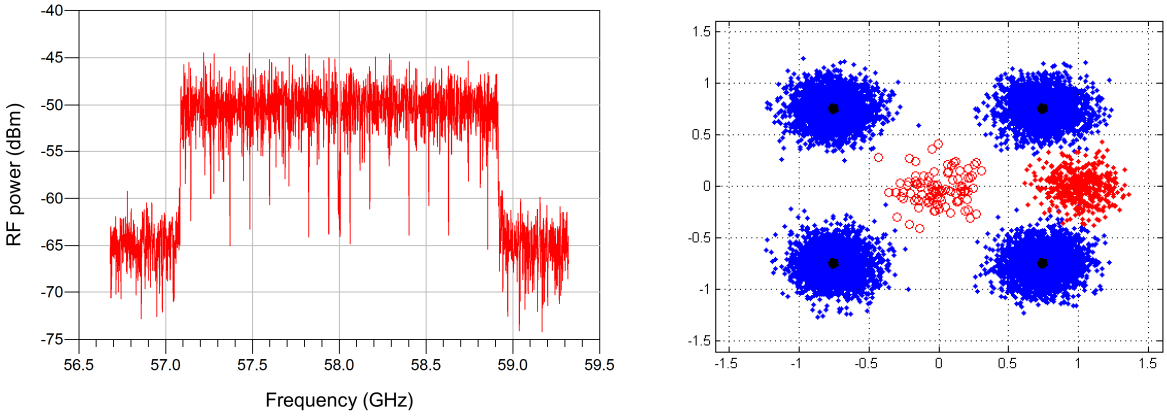

(a) (b)

Fig 5.11.EM IM-DD link (a) Received OFDM signal at millimeter-wave (b) constellation of demodulated baseband signal, P_{OFDM} = 20dBm.

EVM versus OFDM mean power at the input of the RoF link is given in Fig 5.12 for both DM and EM IM-DD links. For low emission power levels, the DM link offers poor performance compared to EM IM-DD links because of the high noise figure (44dB at bias current of 400mA compared to 30dB of EM at 6V bias voltage) as shown in Fig. 4.6. However, at high power levels, DM links offer better performance with EVM values less than 20% until power level of 30dB. Note that the 1dB compression point of the link at 400mA bias current is about 31dB. EVM simulation including a fiber length of until 10km doesn't change the result.

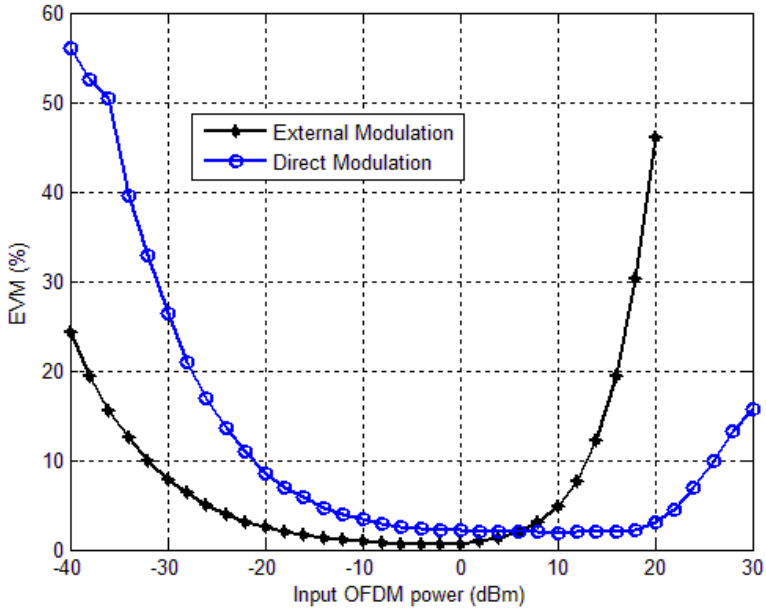

Fig 5.12.EVM vs input RF power.

5.3.2. Heterodyne using two lasers for 60 GHz communication

As it has been discussed up until now, optical heterodyne systems using two independent laser semiconductor laser diodes is highly influenced by the laser phase noise. In this section, the phase noise influence on the OFDM signals is investigated by simulation. The heterodyne link used for this study has the same setting as the setup shown in Fig. 4.11. Master laser (III-V laser) is biased at 400mA and slave laser (EM4 laser) is biased at 180 mA, MZM is biased at half of $V\pi$ (at 6V) and UTC-PD generates the millimeter-wave signal. The loop parameters are the same as before. Since the fiber dispersion effect for this configuration is negligible, fiber length is set zero for this simulation to reduce complexity.

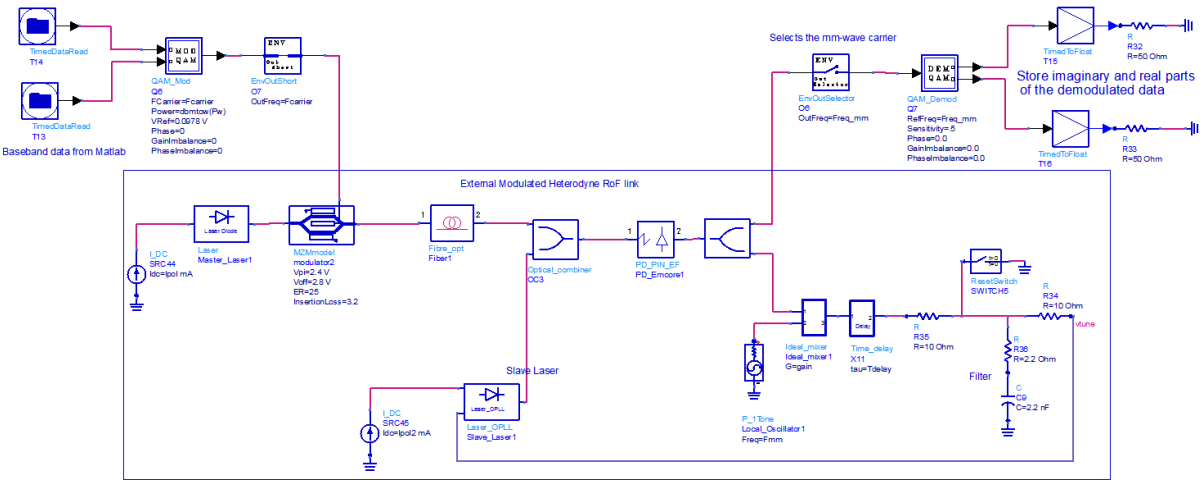

Fig 5.13.ADS schematic for co-simulation of externally modulated optical heterodyne RoF system with OPLL.

To investigate the effect of phase noise on the OFDM signals, co-simulation is performed by first removing all the intensity noise sources from the system. This allows us to differentiate

the different noise contribution. The phase noise spectrums of master laser, slave lasers are shown in Fig. 4.13.

The constellations of the demodulated signal with and without employing OPLL the loop are shown in Fig 5.14 where the impact of phase noise is evident as a circular distortion of the signal points about the center of the constellation. The OFDM demodulator can track and compensate phase variations of the signal by using the pilot tones, as long as the phase variations are relatively slow with respect to the symbol rate. However in the heterodyne system, the high level of phase noise makes it impossible for the demodulator to track the phase error, as a result EVM is about 40%.By injecting the phase error back to the slave laser (Fig 5.13), it is possible to effectively remove the phase rotation. With the OPLL the EVM value is reduced from 40% to about 1.4% when only phase noise is simulated. When all of the noise sources in the system are activated, the EVM value is reduced from over 40% to 2.5%. A plot of the received OFDM spectrum considering the only phase noise is shown Fig 5.15 where the signal level and SNR looks unaffected. Thus it is not possible to qualify the signal quality using only SNR.

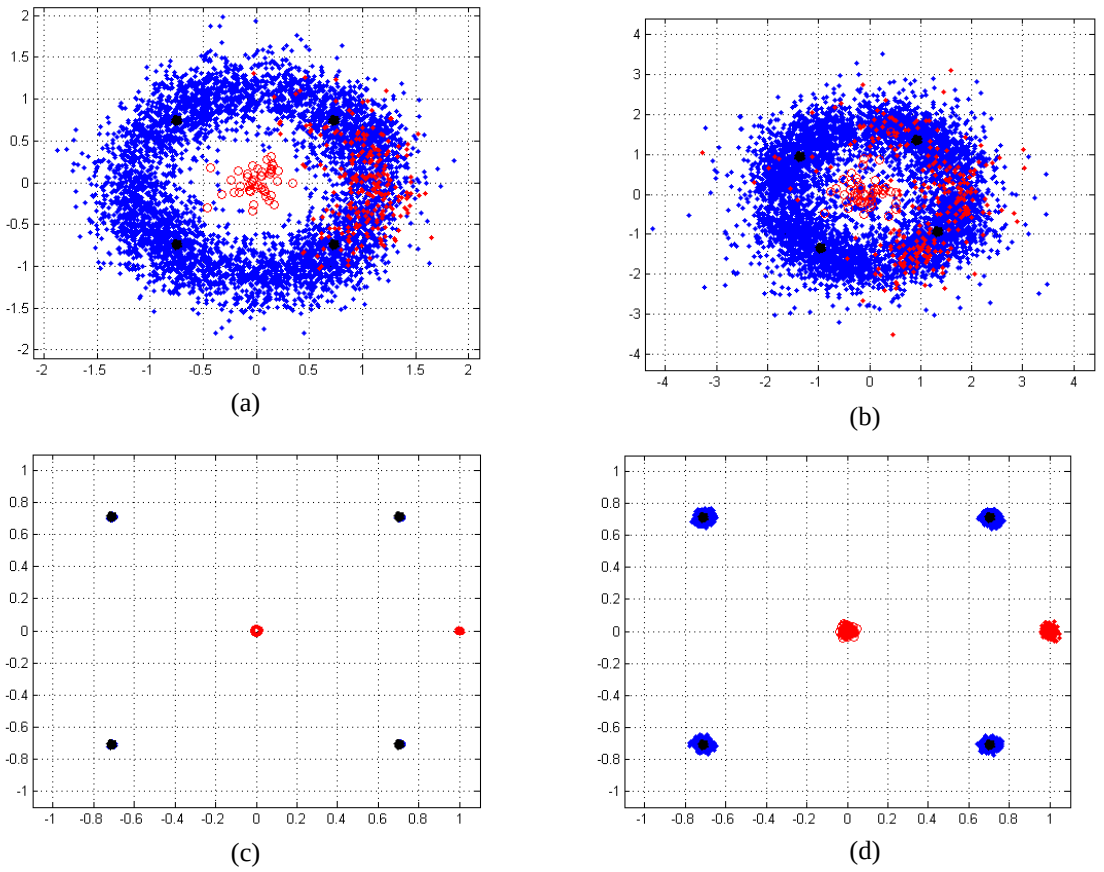

Fig 5.14.Constellation of the received signal, P_{OFDM} = 0dBm (a) free running lasers and only phase noise is activated (b) free running lasers with phase noise and intensity noise activated (c) locked lasers when only phase noise is activated (d) locked lasers with all noises activated.

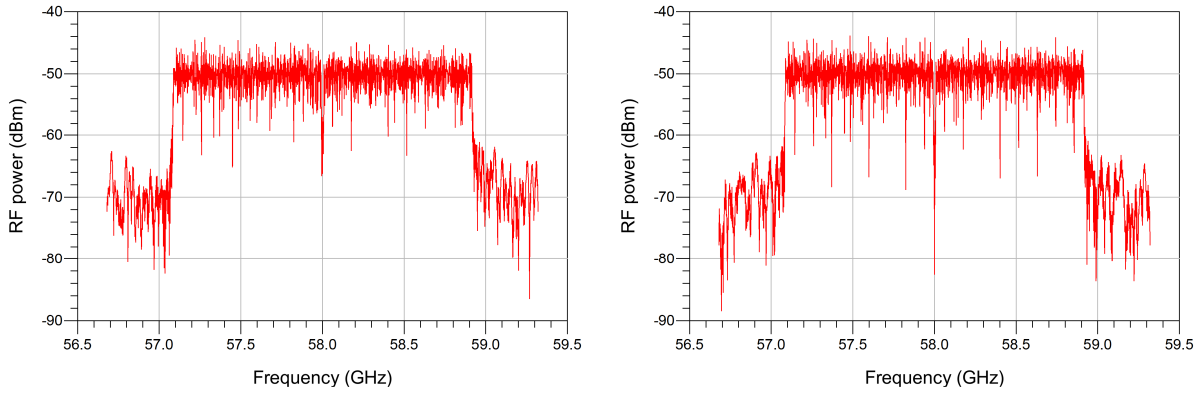

(a) (b)

Fig 5.15.Spectrums of received signal after transmission over the heterodyne RoF link (a) free running lasers (b) locked lasers, P_{OFDM} = 0dBm.

To examine the noise and nonlinear effect on the constellation, we can consider very small and high emission powers. For the case when the mean OFDM power (P_{OFDM}) is very small (-30dBm), the constellation is not very much improved when OPLL is used because the dominant effect at low emission level is the intensity noise which is not corrected by the feedback mechanism. Nevertheless, EVM is reduced from 24% to 16% using OPLL.

In the other extreme case when the mean OFDM power is very high (P_{OFDM} = 20 dBm), the RoF system performance is limited by the nonlinear distortion due to the MZM. The constellation is shown in Fig 5.17. The nonlinear effect presents itself as noise in the constellation, but the OPLL only correct the phase noise rotation and the nonlinear distortion persists at high power levels.

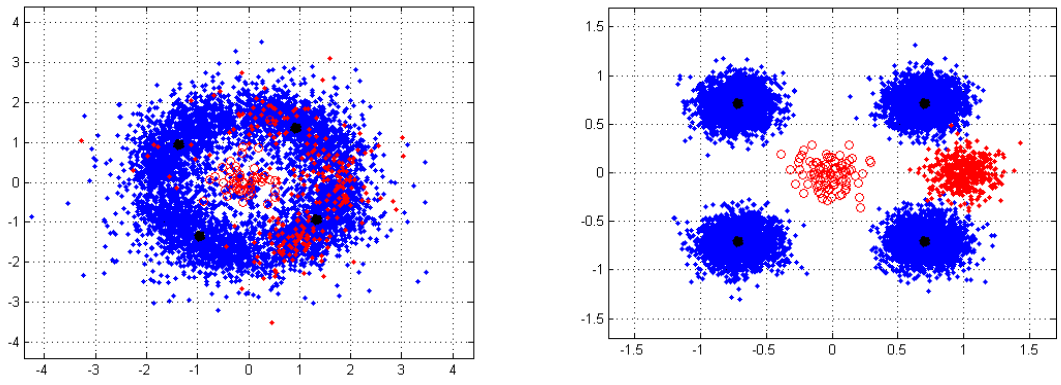

(a) (b)

Fig 5.16.Constellation of the received signal, P_{OFDM} = -30dBm (a) free running lasers (b) locked lasers.

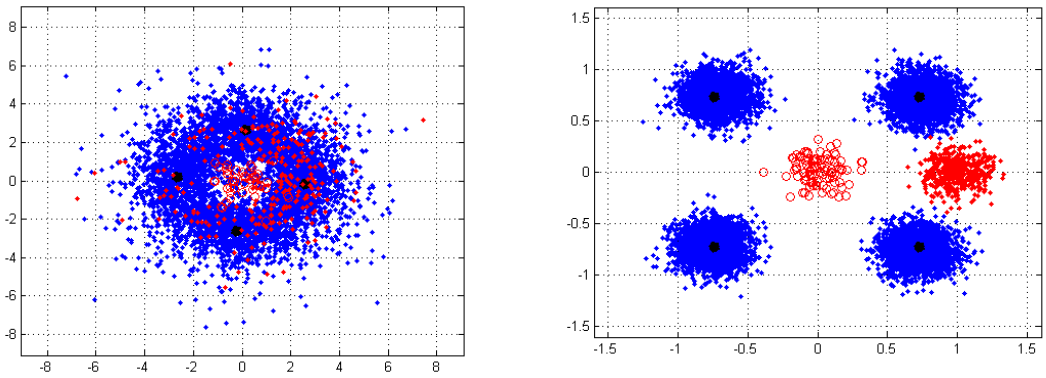

(a) (b)

Fig 5.17.Constellation of the received signal, P_{OFDM} = 20dBm, (a) free running lasers (b) locked lasers.

EVM simulation result of the EM optical heterodyne system for a sweep of input OFDM mean power is given in Fig 5.18. EVM curve for the heterodyne system with free running is not displayed since the values at its best is above 40%. The heterodyne link including OPLL performs better than the DM IM-DD at low power levels and better than the EM IM-DD link at high power levels. However, if realistic components such as mixers and local oscillators are used for the three systems, the EVM values would be higher than estimated in this study.

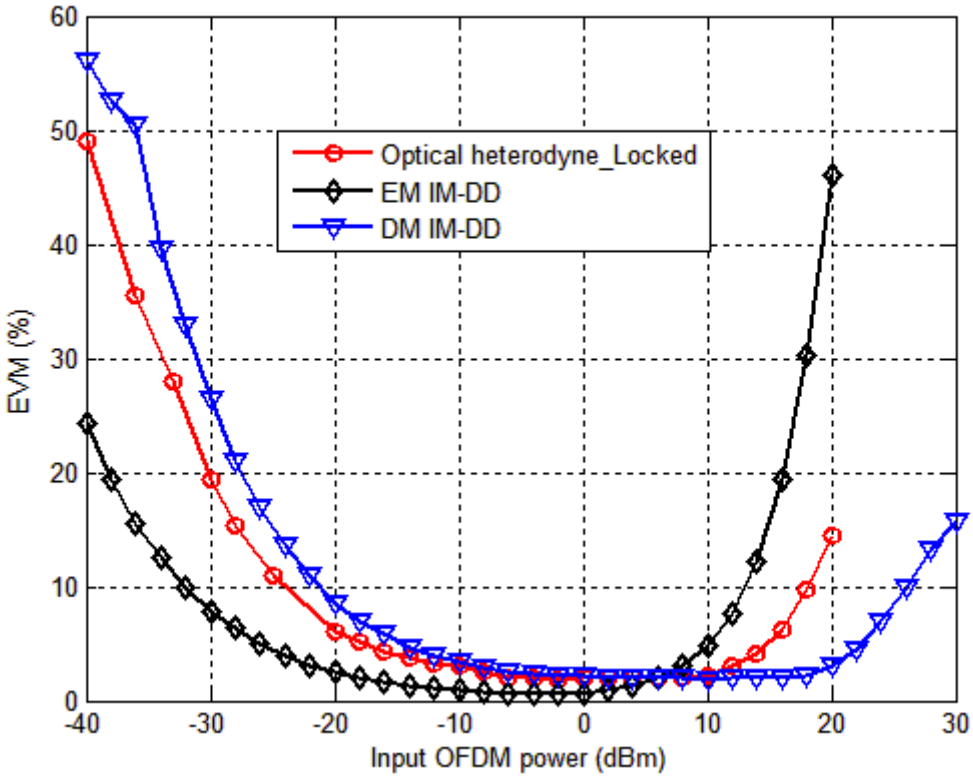

Fig 5.18.EVM vs input RF signal power.

5.4. Summary

In this chapter, transmission of wireless signals over three RoF systems in the millimeter-wave band complying with IEEE 802.15.3c standard is demonstrated. The RoF components are represented by the equivalent circuit models. The effects of noise and nonlinearity on the OFDM signal are presented using EVM simulation. In this study, the mixers and local oscillators are ideal. But it is known that real components especially in the millimeter band have many constraints. Besides, the wireless channel effects are not included. Hence, the analysis solely investigates impairments that come from the optical link. In this scenario the best EVM obtained considering the optical link imperfections is 0.47% compared to the BB EVM of 0.29%.

The EVM simulation in Fig 5.18 shows that the DM IM-DD link show high linearity and the EM IM-DD link performs well at low emission powers. It is evident that the performance of optical heterodyne systems would be better than IM-DD systems if electronic impairments are included. In conclusion, optical heterodyne systems with OPLL achieve higher performance than corresponding IM-DD system for high data rate transmission in the millimeter-wave band. However, complexity and cost are the main limitations to apply these systems in home area networks.

6

Conclusion and Perspectives

In this thesis, some of the most important issues of electrical equivalent circuit modeling microwave photonic devices are studied with particular attention given to single mode semiconductor laser which is the main limiting factor of microwave/millimeter-wave photonic systems. In chapter one, the importance of equivalent circuit model compared to numerical device simulations is explained. Even though there has been a shift towards numerical simulations driven by the rapid increase of computing power, equivalent circuit models will play more important role in the foreseeable future for system simulation purposes. Besides, equivalent circuit models are preferably used by circuit engineers who are familiar with circuit concepts for system evaluation. The main issue is therefore to develop accurate equivalent circuit models of photonic components that can represent devices properties and influences on the system performance.

Chapter two gives the general background study about the convergence of wireless technologies towards optical solutions for network coverage mainly in the millimeter-wave band. The main constraints in choosing the system architectures being system simplicity and cost, both optical and electrical solutions exist to generate millimeter-wave signals at the BS. Nevertheless, optical solutions are emerging to be one of the main candidates in terms of transmission performance, energy consumption and transparency. Since the wireless signal transmission in the millimeter-wave band is very short, the BSs are naturally ‘pico-cells’. Network coverage extension is achieved by deploying many BSs which are expected to be cheap and compact.

Semiconductor lasers are the integral parts of optical communication systems in general. The noise and nonlinearity of semiconductor lasers are often the main system impairments in communication systems. In chapter three, theoretical analysis is given about the properties of single mode semiconductor lasers from the rate equations point of view. The electrical equivalent circuit model of the laser is expected to precisely represent the device by integrating all the important properties in the model. To this end, the electrical equivalent circuit model of the laser is proposed using the rate equations based large signal model of the laser with intensity and phase noise of the laser. This modeling approach allowed us to simulate different properties of the laser including static response, dynamic response, noise

characteristics and spectral linewidth. The model is validated by comparing simulation and measurement of laser characteristics which are found to have a good match.

As complement to the laser model, equivalent circuit models of other photonic components such as photodiode, MZM, and optical fiber are also developed. These models also include some of the main properties of the devices such as the RC property and shot noise of the photodiode, the static and dynamic behavior of the MZM, attenuation and chromatic dispersion of the fiber optic. These models together with the laser model are essential to effectively study and analyze different RoF systems.

Chapter four deals with characterization of different RoF architectures using the equivalent circuit models developed in chapter three. As an analog system, a RoF link can be evaluated in terms of link gain, noise figure and dynamic range. The different RoF systems studied are DM and EM – direct detection (IM-DD) and external modulation – heterodyne detection systems. The laser RIN has dominant influence in DM system and shot noise is the limiting factor in external modulated IM-DD systems. External modulated IM-DD links have slightly lower dynamic range in terms of input RF power. While in heterodyne detection systems, the optical phase noise is the main limiting factor. The phase noise level is reduced considerably using OPLL. Considering a master laser with linewidth of 13.3 kHz and slave laser with linewidth of 1 MHz, the OPLL is able to obtain the total phase error variance of 0.044 rad^2 in a 12 MHz loop bandwidth.

In chapter five issues concerning about the transmission of digital signals with complex modulation scheme over analog circuit link are investigated. The digital signal is generated based on the current standard in the millimeter-wave band which OFDM format to enhance capacity of transmission. Based on the common performance metric such as SNR and EVM, IM-DD and optical heterodyne systems are studied for transmission of the OFDM signal. For the data rate of 3.08 Gb/s, in the ideal electronic condition all of the three systems achieve EVM values lower than 30 % for a range of input RF powers from about -30 to 20 dBm. But these simulation results are rather optimistic since electrical circuit effects such as mixer and local oscillator noises are not included.

In conclusion, the results and findings demonstrated in this thesis have two purposes. The first objective is to demonstrate the possibility of analyzing and designing RoF systems efficiently by developing precise circuit models of RoF components. The second objective is the system analysis itself. Among the three RoF systems studied, the DM IM-DD link shows the best in terms of linearity but at low emission power, the EM IM-DD link performs well. Compared to optical heterodyne systems, IM-DD systems show slightly good result in the ideal case but in reality regardless of their complexity, optical heterodyne systems with OPLL could achieve the best performance compared to IM-DD systems for wireless OFDM transmission in the millimeter-wave band.

In general, this thesis explores the equivalent circuit modeling approach of modeling microwave/millimeter-wave systems. This work could be further validated by using different measurement setups similar to the simulation setups shown in Fig 5.6 and Fig 5.13. This approach could also be used to investigate different proof-of-concept experiments e.g. to compare the performances of different millimeter-wave generation techniques such as those

discussed in chapter 2. The other potential usage of the equivalent circuit models would be in integrated photonic components and systems.

The tools developed in this thesis could also be used for the design of optical electronic integrated circuits (OEIC) to predict high-speed digital signal parasitic (crosstalk, ground-bonce, jitter) or broadband signal distortion using electrical domain CAD tools. Other advantages offered by electrical simulation such as the consideration of dispersion effects and high frequency losses (substrate, transmission lines, and components) can also be investigated.

A further extension of this work would be to develop equivalent circuit of multimode lasers using the multimode rate equations with a similar approach as the technique used for single mode semiconductor lasers. Similarly, multimode fiber effects such as modal dispersion can be included in the fiber model. Modeling high speed photodetectors is another area of extension. The equivalent circuit model of UTC-PD could be developed in detail as the importance of high speed photodetectors is evident to generate millimeter-wave signals.

RESUME EN FRANÇAIS

Les avancées en communication numérique optique dans les réseaux longue distance et les réseaux d'accès font apparaître des technologies émergentes dans les domaines micro-ondes et millimétriques. Ces systèmes hybrides sont fortement influencés non seulement par les performances des liens optiques mais aussi par celles des circuits électriques. Les effets des composant optiques et électriques peuvent être ainsi étudiés simultanément en utilisant des outils assistés par ordinateur et en développant des modèles de circuit électrique équivalent de chacun des composants de la liaison tels que les lasers à semi-conducteurs, modulateurs, photo-détecteurs et fibre optique.

Dans cette thèse, les modèles électriques des composants de la liaison photonique sont développés pour étudier des architectures différentes. La source de lumière optique étant le principal facteur limitant de la liaison optique, une attention particulière est accordée aux caractéristiques des lasers à semi-conducteurs. Le modèle de circuit équivalent de laser représentant intialement l'enveloppe du signal optique est modifié pour inclure les propriétés en bruit de phase du laser. Cette modification est particulièrement nécessaire afin d'étudier les systèmes où le bruit de phase optique ne peut être négligé : les systèmes de récepteurs hétérodynes optiques et les systèmes auto-hétérodynes optiques. Les résultats de mesures des caractéristiques statique et dynamique de laser sont comparés aux résultats de simulation afin de valider le modèle de circuit équivalent, et ce pour différentes conditions de fonctionnement. Il est démontré que le modèle de circuit équivalent peut prédire avec précision les comportements des composants pour les simulations au niveau système.

Pour démontrer la capacité de cette modélisation de la liaison photonique permettant d'analyser la dégradation des signaux micro-ondes/millimétriques transmis, le nouveau modèle de circuit du laser est utilisé avec les modèles électriques des autres composants afin de caractériser différents liens radio sur fibre (RoF) tels que la modulation d'intensité - détection directe (IM-DD) et les systèmes RoF hétérodynes optiques. Un signal de modulation complexe large bande avec des spécifications conformes à la norme IEEE pour la bande de fréquence à 60 GHz est transmis sur les liens RoF. La performance du système est analysée sur la base de l'évaluation de l'EVM. Cette étude montre l'intérêt des modèles des circuits qui nous permettent de prendre en compte les comportements à la fois électrique et optique simultanément pour l'analyse efficace des systèmes photonique micro-ondes/millimétriques.

BREF SOMMAIRE EN FRANÇAIS

Le déploiement de réseau d'accès haut débit qui peut offrir une vitesse de plus de 1 Gbit/s à la maison permet d'entrevoir des technologies et des normes émergentes à des débits de plusieurs Gbit/s. Les nouvelles normes pour la communication à ultra haut débit de données ne peuvent pas être prises en charge par les systèmes de transmission traditionnels en espace libre et sur des lignes de transmission (câble coaxial, ligne bifilaire) du fait d'une trop forte atténuation du signal millimétrique sur ces média, fréquences permettant un débit élevé. En espace libre, les pertes augmentent avec la fréquence et atteignent des pics à certaines fréquences, correspondant à l'absorption de certaines molécules atmosphériques. Dans un câble coaxial traditionnel, les pertes augmentent drastiquement avec la fréquence. La transmission à longue distance en utilisant ces méthodes s'avère impossible sans l'aide d'équipement de régénération. Les liaisons optiques offrent la meilleure alternative pour transmettre des signaux radio avec un bon rapport qualité/prix du coût de l'installation par rapport aux autres méthodes [4] [5]. Le procédé pour transmettre des signaux radio sur une liaison optique est généralement désigné comme système radio sur fibre (RoF) (Fig. 1).

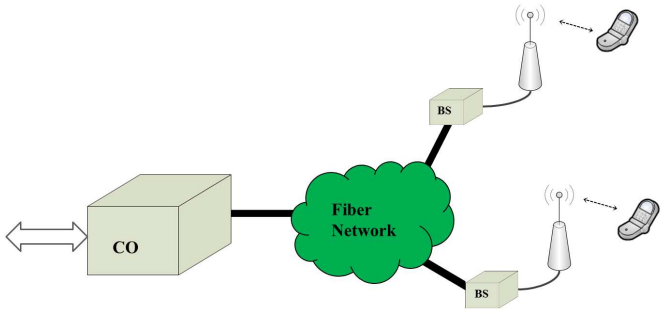

Fig. 1. Système de Radio sur fibre.

La figure ci-dessus est le système RoF typique intégré aux infrastructures de télécommunications existantes. Au cœur de ce système optique-sans fil hybride est la communication à fibre optique qui sert de colonne vertébrale pour l'interconnexion large bande entre le bureau central (CO) et l'antenne, via la station de base (BS). L'étude de technologie WDM sur ce réseau hybride, intégrant un accès sans fil, et fonctionnant en bande millimétrique se poursuit activement pour fournir une connectivité mobile à ultra haut débit à l'utilisateur. L'architecture des réseaux uniquement radio nécessite un grand nombre d'antennes et de stations de base à déployer afin de maximiser la couverture géographique. Les principales fonctionnalités de commutation et de routage doivent être situées dans un emplacement centralisé. Par conséquent, la complexité de l'antenne reliée à la station de base doit être réduite, tout en offrant un débit élevé.

Bien que l'intégration optique sans fil est en mesure de simplifier ce type d'infrastructure "backhauling" tout en offrant des avantages certains aux opérateurs et fournisseurs d'accès, la mise en œuvre d'un réseau hybride est délicate du fait des dégradations du signal RF haute fréquence transmis. Les fréquences considérées et les performances attendues sont les points à considérer pour l'intégration et l'optimisation de tels systèmes dans l'infrastructure existante. L'un des principaux défis techniques de ces réseaux réside dans la distorsion des signaux transmis sur la liaison optique dans un réseau hybride.

L'autre thématique qui est activement menée dans de nombreux centres de recherche est l'utilisation de liaisons à fibres optiques pour les communications à courte portée dans le réseau de la maison (HAN). Pour y faire face, de nouvelles normes dans la bande millimétrique sont apparues de capacité de plusieurs Gbit/s, mais à fortes pertes en espace libre. La fibre optique permet alors d'étendre la couverture radio. Ce réseau optique transparent à l'intérieur de l'habitat serait le prolongement naturel du réseau FTTH, il en devient idéal pour étendre les connexions et assurer une parfaite mobilité à l'aide des futurs standards de communication sans fil.

* * * *

Depuis le développement de la fibre optique à faible perte à la fin des années 1960, différentes méthodes de génération et de détection de la lumière ont été développés rendant les technologies matures et les communications optiques possibles. L'idée des liens optiques transmettant des signaux micro-ondes / RF est de profiter de tous les avantages de la fibre optique. Avec le temps, les liaisons optiques analogiques ont incorporé différentes techniques pour améliorer les performances de la liaison optique de transmission de tels signaux.

La conception d'une liaison optique est possible grâce au choix des différents composants opto-électriques (O/E) et électro-optiques (E/O) pour répondre aux exigences du système. De tels dispositifs doivent offrir une modulation, le contrôle et la détection de signaux RF comme représenté sur la Fig. 2. En général, la liaison radio sur fibre peut être constituée de composants optiques et de dispositifs optoélectroniques tels que des lasers à semiconducteurs, modulateur optique, amplificateur optique, fibre optique, photodétecteur. Les lasers à semi-conducteurs sont les plus largement utilisés comme source optique grâce à leur possibilité d'être directement modulé par des fréquences micro-ondes. La fréquence de modulation est toutefois limitée par la fréquence d'oscillation de relaxation du dispositif, qui dépend d'un certain nombre de facteurs : la durée de vie des photons, le gain différentiel, le temps de recombinaison des porteurs et la puissance de sortie optique. L'utilisation de largeurs de bande de modulation directe élevées nécessite à la fois une optimisation de la structure interne du laser à semi-conducteur et la conception de l'ensemble de laser afin de minimiser les effets parasites électriques externes. Une autre alternative pour élargir la largeur de bande de modulation est de moduler la lumière en utilisant des modulateurs optiques externes tels que les modulateurs électro-optique (EOM) de type Mach-Zehnder (MZM) et des modulateurs à électro-absorption (EAM). Quant à la fibre optique, il existe différents types de fibres ayant des caractéristiques différentes selon ses dimensions géométriques, sa structure, et le matériau utilisé. Le choix du type de fibre dépend de la distance de la liaison, Le détecteur optique est également un élément important qui doit être judicieusement choisi en fonction de la configuration système requise.

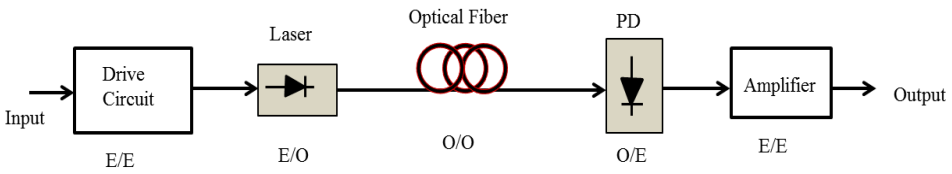

Fig. 2 Schéma de principe d'un système RoF.

Les composants E/O et O/E sont des transducteurs permettant de transmettre un signal hyperfréquence de l'entrée à la sortie avec peu de dégradation, agissant ainsi de manière transparente. Cependant, la liaison optique peut altérer les performances du système en raison de distorsions apportées par les composants RoF tels que les bruits d'intensité et de phase, les non-linéarités, la dispersion des fibres, l'atténuation de la fibre, la saturation et les sources de bruit du photodétecteur. Ce sont les paramètres les plus cruciaux dans la détermination de la dégradation du signal. Cela montre l'importance du choix de la technique de modulation utilisée, pour améliorer les performances de la liaison, mais aussi la conception et la fabrication des transducteurs.

La conception d'un lien optique-microondes commence toujours par la définition de ses spécifications. Le système doit être vérifié et analysé en fonction de divers paramètres. Ces systèmes bénéficient grandement de la conception assistée par ordinateur (CAO) et des outils qui permettent l'optimisation et la vérification d'un système particulier avant sa réalisation effective, réduisant ainsi de manière significative le cycle de conception et le coût. Cette conception dépend alors de la modélisation précise des dispositifs optoélectroniques. Ces modèles doivent être conformes aux caractéristiques mesurées tout en prédisant les performances au niveau système que ce soit en régimes petit ou grand signal.

Au niveau du composant, il existe deux types de modèles : le modèle physique et le modèle circuit. Bien que les modèles physiques des composants optoélectroniques soient utilisés pour l'optimisation des couches technologiques, les modèles de circuits équivalents sont quant à eux dédiés à l'analyse de circuits et aux procédures de conception. Un avantage du modèle "circuit équivalent" est qu'il peut être utilisé sur un logiciel de conception de circuit. Le modèle de "circuit équivalent" facilite également la conception de circuits intégrés monolithiques parce qu'il permet la simulation précise des caractéristiques de chaque composant dans un environnement de simulation circuit. Un autre avantage de cette modélisation est qu'il est possible d'étudier l'influence de différents paramètres indépendamment les uns des autres et de leur interaction sur les composants et circuits associés. L'objectif de cette thèse repose sur le développement d'un modèle de circuit équivalent approprié de lasers à semi-conducteurs simples pour différentes configurations de systèmes RoF.

Le choix du logiciel de conception est également une question importante pour étudier les performances du système. Ainsi des logiciels dans les domaines optique ou électrique existent. Ce choix doit dépendre du type de système qui doit être analysé. Les systèmes et réseaux optiques de grande dimension à multiplexage par longueurs d'ondes (WDM) peuvent être étudiés à l'aide de logiciels commerciaux du domaine optique (Rsoft, Optiwave, VPIsystems etc…). Ces logiciels offrent des modèles de lasers basés sur les équations de continuité, des modèles de fibres (monomode et multi-modes) et de photodétecteurs. Cependant, pour étudier le signal radio qui se propage sur les systèmes à fibre, il est souhaitable d'utiliser des simulateurs du domaine électrique de manière à tirer parti des outils déjà matures dans le domaine et de pouvoir y inclure les circuits de commande électrique et les composants parasites de la mise en boitier. Comme ces logiciels commerciaux ne disposent pas de bibliothèque de composants optiques et opto-électriques, il reste donc à les développer. A cet effet, nous avons besoin de circuits électriques équivalents de dispositifs

tels que les lasers à semi-conducteur, photodétecteurs et modulateurs pour évaluer le lien RoF complet. L'analyse circuit peut ainsi être autorisée pour évaluer les propriétés d'un système hybride optique-microondes.

La majorité des outils CAO du domaine électrique sont commerciaux : Advanced Design System (ADS), MWOFFICE (AWR), APLAC (Université Helsinkji). Ils comportent de nombreuses fonctionnalités telles que des algorithmes rapides pour calculer la réponse d'un circuit en régime non linéaire, des bibliothèques complètes de composants électriques actifs et passifs, la description du circuit à travers une schématique et l'optimisation. Les outils disponibles peuvent être utilisés pour la conception de systèmes optiques - analogiques réels, ce qui dépend de la précision des modèles développés. Dans ce travail, ADS de Keysight Technologies est utilisé pour étudier les systèmes RoF. Ce logiciel fournit des bibliothèques complètes de composants pour les standards de communication sans fil et la co-simulation sur une seule plate-forme [6]. Au niveau circuit RF, les outils de simulation peuvent être opérés en régimes linéaire et non linéaire : S-parameters, AC dans le domaine fréquentiel et en régime linéaire; l'Harmonic Balance (HB), DC et la simulation d'enveloppe (Env) en régime non linéaire. Les simulateurs HB et Env sont des outils essentiels pour effectuer une analyse à la fois dans les domaines temporel et fréquentiel. En outre, les caractéristiques de simulation de bruit basé sur le mélange des algorithmes pour l'intensité et la phase rendent ces outils préférables pour la prise en compte du mélange de bruit AM/PM. La fonction de co-simulation Ptolémée peut également être utilisée pour effectuer une simulation de transmission de signaux numériques à travers le système complet. Ceci nous permet d'examiner les effets des liaisons optiques sur la performance de la communication numérique de bout en bout d'un système RoF.

Dans cette thèse, la modélisation de composants RoF est développée dans le but d'analyser les différents types de liens RoF. Ces outils peuvent aider à la définition de spécifications d'une liaison et la sélection des dispositifs appropriés de transceivers E/O et O/E en vue de l'optimisation du système. L'accent est mis sur le modèle de circuit équivalent de simples lasers à semi-conducteurs à partir des équations de continuité et des éléments parasites de connexion.

L'intérêt pour la modélisation de diodes laser est directement lié aux progrès qui ont été accomplis pour moduler la lumière à des fréquences microondes, voire millimétriques. Comme les diodes lasers présentent à la fois des performances électroniques et photoniques, en temporel et en fréquence, il est nécessaire de prendre en compte les deux domaines, ce qui augmente la complexité de la modélisation qui doit combiner tous les mécanismes physiques internes au composant. Des logiciels de simulation du comportement physique 2D ou 3D sont utilisés au niveau composant : MINILASE, CLASID [7]. Ce type de simulations est lourd à mettre en œuvre et gourmand en ressources informatiques et temps de calcul. Des schémas électriques simplifiés sont ainsi privilégiés pour la conception et l'analyse de la radio sur fibre. De plus, de tels modèles facilitent la conception de circuits optoélectroniques intégrés monolithiques et permettent la simulation précise de leurs principales caractéristiques dans un environnement standard de simulation.

Plusieurs travaux réalisés dans la littérature montrent l'intérêt de développer le modèle de circuit de lasers à semi-conducteurs en régimes faible signal et grand signal. Un modèle petit signal de laser a été étudié dans [8] [9] [10] [11] basé sur les équations de continuité. Une représentation réaliste doit considérer le régime grand signal. En effet, les modèles petits signaux ne sont que des dérivées de modèles grand signal à un point de fonctionnement fixé.

Le modèle de circuit équivalent grands signaux de laser unique à semi-conducteur a été développé par Tucker [12]. Ce modèle utilise des éléments de circuit à constantes localisées et des sources de courant représentant les porteurs et les photons. Un modèle de circuit équivalent complet de diode laser doit intégrer à la fois le comportement intrinsèque et les circuits parasites externes pour évaluer les performances électriques et optiques avec le même simulateur.

On trouve dans la littérature un assez grand nombre de références sur la modélisation de laser et sa mise en œuvre sur des simulateurs circuits [12] [13] [14] [15] [16] [17]. Ces modèles ont une importance particulière pour étudier les liaisons optiques analogiques et évaluer les limites de la diode laser introduites par les distorsions dues aux non linéarités et au bruit. Un inconvénient majeur des modèles de circuits développés est l'absence de représentation de la phase optique du laser qui est particulièrement importante pour la détection cohérente et les systèmes RoF hétérodynes. L'introduction de la phase dans un modèle de laser permet également d'étudier l'interaction du bruit de phase avec la dispersion de la fibre qui pourrait conduire à une absence de transmission du signal. Dans ce travail, nous avons proposé un procédé pour inclure le bruit de phase optique dans le modèle précédemment développé [15] en utilisant une approche par simulation système. C'est une extension directe des travaux antérieurs réalisés au laboratoire ESYCOM-Le Cnam qui intègre le modèle du laser grand signal intégrant le bruit et les éléments parasites externes. Le modèle de laser précédent [15] a été utilisé pour réaliser des simulations de diodes laser à semi-conducteur en régime non-linéaire et étudier les distorsions harmoniques et l'intermodulation de signaux radio complexes modulant le laser [18] [19] [20].

Ce nouveau modèle de laser est représenté par un quadripôle dont le port d'entrée représente la commande électrique (polarisation et modulation RF) et dont le port de sortie représente le signal optique. Désormais, le signal de sortie de ce modèle intégrant la phase optique est proportionnel au vecteur "champ électrique" optique et non plus à la puissance optique. Cette méthode permet une simulation des effets du bruit de phase sur les performances du système pour les systèmes micro-ondes photoniques. Il est démontré que le modèle de phase est efficacement intégré au modèle du laser grand signal et bruité. Ce nouveau modèle de laser peut donc estimer le bruit d'intensité, le bruit de phase, la distorsion non linéaire et d'autres caractéristiques de la diode laser en régimes petit signal et grand signal. Le laser a été utilisé dans des systèmes plus complexes tels que les boucles à verrouillage de phase optique. Il a été validé en effectuant la comparaison entre les résultats de simulation du modèle de circuit et de mesure. Sur un laser DFB réalisé au III-V Lab [21] nous avons obtenu un très bon accord entre la simulation et les mesures confirmant ainsi la précision du modèle et son intégration dans des systèmes complexes en simulation.

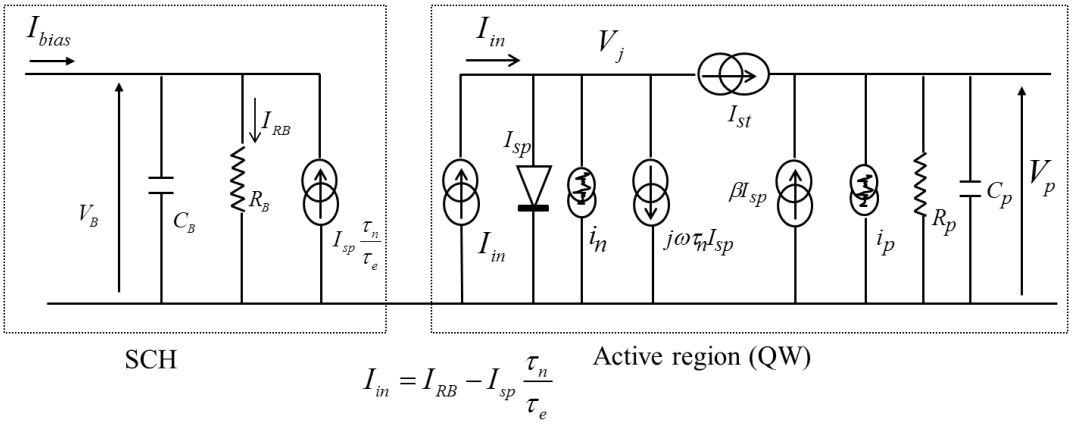

Fig.3 modèle initial grand signal en amplitude intrinsèque et éléments parasites.

Le modèle grand signal d'un laser monomode est donné sur la figure 3. Les éléments d'interconnexion sont situés à l'entrée du modèle intrinsèque initial développé à partir des 2 équations de continuité (porteurs et photons). Les sources de bruit en courant sont exprimées à l'aide des forces de Langevin. L'entrée de ce modèle est électrique et la sortie est optique, proportionnelle à l'enveloppe de la puissance optique. L'introduction du bruit de phase dans le modèle du laser initial est représentée sur la figure 4. Ce nouveau modèle complet permet de simuler les bruits de phase et de fréquence du laser. De même les effets introduits en modulation de fréquence sont simulables. En revanche, les effets de chirp du laser ne sont pas considérés dans le cadre de ce travail.

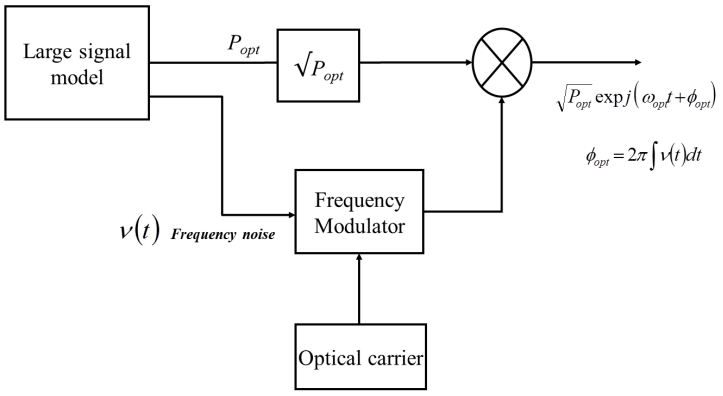

Fig. 4 Modèle grand signal et bruit de phase optique intégré.

* * * *

En conclusion, cette thèse explore la modélisation complète électrique de dispositifs photoniques et plus particulièrement celle du laser semi-conducteur qui est le principal facteur limitant des systèmes photoniques- micro-ondes. Dans le premier chapitre, l'importance de la modèlisation électrique, par rapport à des simulations numériques, de la physique des composants est expliquée. Bien que les simulations numériques soient plus aisées du fait de l'augmentation rapide de la puissance de calcul des ordinateurs, les modèles de circuits équivalents sont les seuls qui permettent des simulations au niveau système. En outre, les modèles électriques sont de préférence utilisés par les ingénieurs qui sont familiers des concepts de simulation circuit pour l'évaluation du système. La question principale est donc

de développer des modèles de circuits équivalents exacts simulant le comportement des composants photoniques qui influencent la performance d'un système complexe.

Le second chapitre introduit la convergence des technologies sans fil à des solutions optiques pour faciliter la couverture réseau, principalement dans la bande millimétrique. Des contraintes existent dans le choix des architectures système : la simplicité du système et son coût, des solutions à la fois optiques et électriques existent pour générer des signaux millimétriques à la Station de Base (BS). Néanmoins, les solutions optiques apparaissent comme l'un des candidats potentiels en termes de performances de transmission, de consommation énergétique et de transparence du réseau. Comme la transmission des ondes millimétriques en espace libre est courte, les stations de base sont de type «pico-cellule» et doivent être nombreuses. La couverture du réseau est assurée par le déploiement de nombreuses stations de base qui doivent être compactes et de faible coût. L'association d'un réseau filaire optique aux communications sans fil permet d'étendre la couverture.

Des lasers à semi-conducteurs sont des parties intégrantes de systèmes de communication optiques. Le bruit et la non-linéarité des composants sont souvent les principales déficiences du système dans les systèmes de communication. Dans le chapitre trois, une analyse théorique est menée sur les propriétés des lasers à semi-conducteurs et les équations de continuité qui les régissent. Le modèle électrique équivalent du laser est proposé à partir de cette étude, intégrant les non-linéarités et les bruits d'amplitude et de phase optique. Cette approche de modélisation nous a permis de simuler différentes caractéristiques du laser : les réponses statique et dynamique, les caractéristiques de bruit et de largeur spectrale. Le modèle est validé en comparant les résultats de simulation et de mesure des caractéristiques, un très bon accord est trouvé.

En complément du modèle de laser, les modèles de circuits équivalents des autres composants photoniques tels que la photodiode, le MZM et la fibre optique sont également développés. Ces modèles prennent en compte certaines des principales propriétés des dispositifs telles la fréquence de coupure et le bruit de la photodiode, les comportements statique et dynamique du MZM, l'atténuation et la dispersion chromatique de la fibre optique. Ces modèles conjointement avec le modèle laser sont essentiels pour étudier et analyser des systèmes RoF différents de manière efficace.

Comme pour un système analogique, les systèmes RoF peuvent être évalués en termes de gain de liaison, de bruit et de dynamique. Les différents systèmes RoF étudiés sont la modulation directe (DM) et la modulation externe (EM) - détection directe (DD) et des systèmes de détection hétérodynes.

Les facteurs de bruit des trois systèmes sont représentés sur la figure 5. Les principales contributions de bruit dans les liens RoF sont le RIN, le bruit de grenaille, le bruit thermique et le bruit de phase. Le bruit dominant qui limite les performances du système est différent selon l'architecture système. Le RIN du laser a une influence dominante dans le système de DM IM-DD, tandis que dans les systèmes EM IM-DD, le bruit de grenaille est le bruit dominant. La dynamique en puissance de bruit d'entrée RF est légèrement plus faible pour le lien EM IM-DD. Dans les systèmes de détection hétérodynes, le bruit de phase optique en conversion de bruit d'intensité est le bruit dominant, du fait du niveau élevé de bruit de phase

des lasers à semi-conducteurs. Les liens RoF EM IM-DD ont le plus faible facteur de bruit tandis que les systèmes hétérodynes présentent le facteur de bruit le plus élevé.

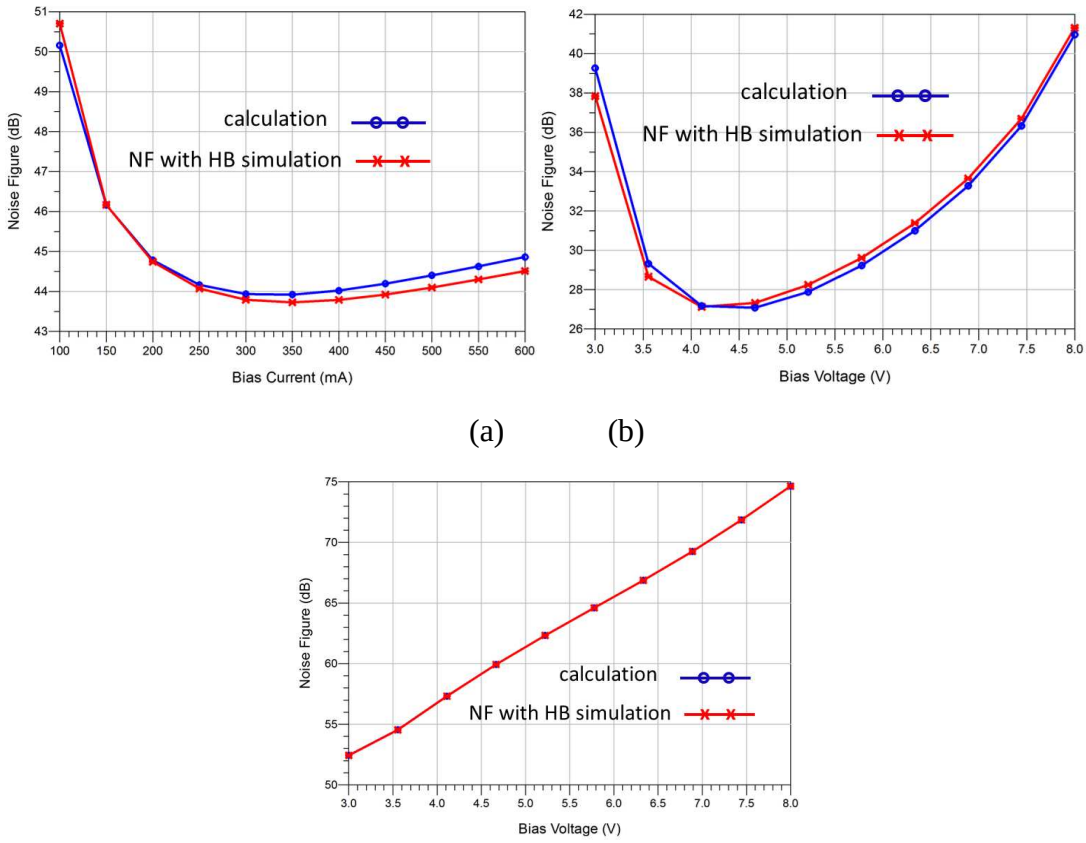

Fig. 5 Facteur de bruit de systèmes RoF (a) DM IM-DD (b) EM IM-DD (c) EM système hétérodyne.

Pour limiter la conversion du bruit de phase en bruit d'intensité, une boucle à verrouillage de phase optique peut être utilisée pour verrouiller le laser esclave bruyant sur le laser maître qui a généralement une largeur de raie plus faible. Le niveau de bruit de phase est réduit en utilisant une OPLL, comme les simulations le confirment. La schématique d'un système hétérodyne en modulation externe est représentée sur la figure 6.

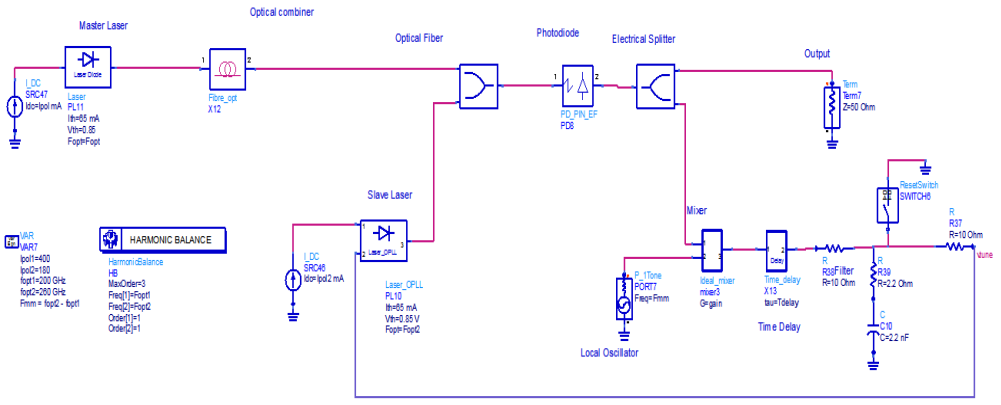

Fig. 6. système hétérodyne optique.

Les niveaux de bruit de phase du laser maître, du laser esclave et du signal millimétrique généré après détection sont représentés sur la figure 7. Pour cette simulation, le laser maître a une largeur de raie de 13,3 kHz et le laser esclave a une largeur de raie de 1 MHz en fonctionnement libre. Le signal millimétrique récupère alors le bruit de phase du laser esclave. L'utilisation de l'OPLL fixe la largeur de raie du laser esclave sur celle du laser maitre, réduisant ainsi fortement le bruit de phase du signal millimétrique généré. Il a variance de l'erreur est estimée à 0,013 rad² si la bande de verrouillage de la boucle est de 12 MHz.

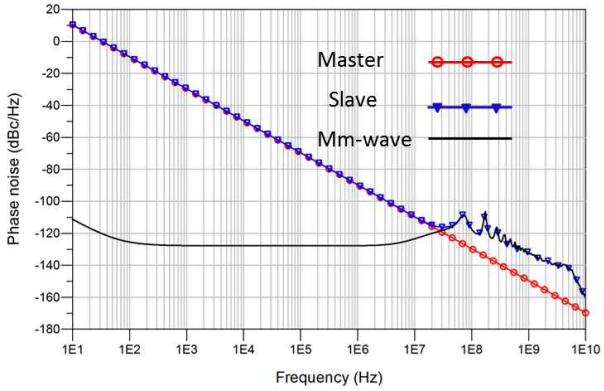

Fig. 7 Bruits de phase du laser maître, du laser esclave et du signal millimétrique généré après détection.

Enfin, les liens RoF sont utilisés pour transmettre des signaux numériques avec un schéma de modulation complexe autour d'une porteuse RF. Le signal numérique OFDM est généré selon la norme actuelle en bande millimétrique. Les performances en termes de SNR et EVM des systèmes optiques hétérodynes et IM-DD sont étudiés pour ce signal OFDM. Pour un débit de donnés de 3,08 Go/s, l'EVM n'excède pas 30% pour un puissance d'entrée RF située entre -30 à 20 dBm. Toutefois ces résultats de simulation sont plutôt optimistes car les effets de circuits électriques tels que les mélangeur et oscillateur local ne sont pas inclus. La comparaison entre les trois systèmes RoF est représentée sur la figure 8.

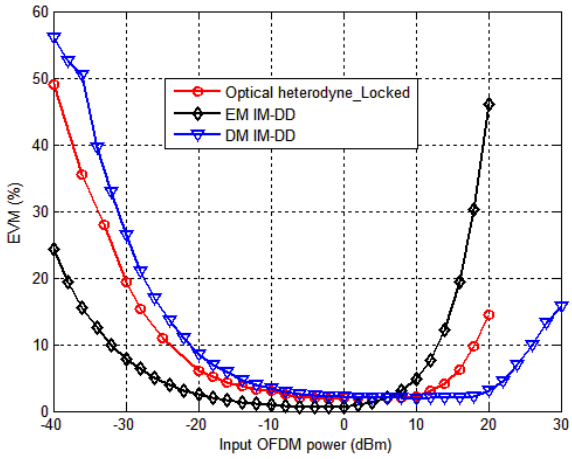

Fig. 8. EVM du signal OFDM en bande millimétrique pour les trois systèmes RoF en fonction de la puissance d'entrée P_{OFDM}.

En conclusion, les études développées dans cette thèse ont deux objectifs. Le premier objectif est de démontrer la possibilité d'analyser et de concevoir des systèmes RoF efficacement en développant des modèles électriques précis de composants RoF. Le deuxième objectif est l'analyse d'un système complexe. Parmi les trois systèmes RoF étudiés, le lien DM IM-DD affiche la meilleure performance en linéarité, mais à puissance d'entrée faible, c'est le lien EM IM-DD qui est plus performant. Comparés au système hétérodyne optique, les systèmes IM-DD montrent des résultats légèrement meilleurs, mais en réalité, indépendamment de leur complexité, les systèmes hétérodynes optiques avec OPLL pourraient démontrer les meilleures performances pour la transmission de signaux OFDM en bande millimétrique.

Cette thèse explore l'approche de modélisation de circuit équivalent des systèmes optiques micro-ondes. Cette approche pourrait également être utilisée pour étudier les performances de différentes techniques de génération à ondes millimétriques tels que ceux décrits dans le chapitre 2 et les comparer. L'autre utilisation potentielle des modèles de circuits équivalents serait d'être une aide pour l'intégration des composants et systèmes photoniques.

7

Bibliography

[1] ITU, "Measuring the Information Society," 2013. [Online]. Available: http://www.itu.int/en/ITU-D/Statistics/Pages/default.aspx. [Accessed 1 11 2014].

[2] A. Ngoma, "Radio over Fiber Technology for broadband wireless communication," PhD. Dessertation, Technische Universiteit Eindhoven, The Netherlands, 2005.

[3] ABIresearch, "Growing Demand for Mobility will Boost Global Wi-Fi," ABIresearch, 2012. [Online]. Available: https:/www.abiresearch.com/press/.

[4] J. Guillory, "Radio over Fiber for the Future Home Area Networks," PhD Thesis, University Paris-Est, Paris, France, 2012.

[5] C. Lim and e. al, "Fiber-Wireless Networks and Subsystem Technologies," *Journal of Lightwave Technology,* vol. 28, no. 4, pp. 390 - 405, 2010.

[6] KEYSIGHT TECHNOLOGIES, "Advanced Design System (ADS) Help," 2011.

[7] C. M. Snowden and R. Miles, in *Compound Semiconductor Device Modelling*, London, Springer-Verlag, 1993, p. 149.

[8] M. Morishita, T. Ohmi and J. Nishizawa, "Impedance characteristics of double-heterostructure laser diodes," *Solide-state Electron,* vol. 22, pp. 951-962, 1979.

[9] J. e. a. Katz, "The intrinsic electrical equivalent circuit of a laser diode," *IEEE Journal of Quantum Electronics,* vol. 17, pp. 4-7, 1981.

[10] C. e. a. Harder, "Noise equivalent circuit of a semiconductor laser diode," *IEEE Journal of Quantum Electronics,* vol. 18, pp. 333-337, 1982.

[11] R. Tucker. and D. Pope, "Circuit Modeling of the Effect of Diffusion on Damping in a Narrrow-strip Semiconductor Laser," *IEEE Journal of Quantum Electronics,* vol. 19, no. 7, pp. 1179-1183, 1983.

[12] Tucker, "Large-signal circuit model for simulation of injection-laser modulation dynamics," *IEEE Proceedings I , Solid-State and Electron Devices,* vol. 128, pp. 180-184, 1981.

[13] H. Elkadi, J. P. Vilcot, S. Maricot and D. Decoster, "Microwave circuit modeling for semiconductor lasers under large and small signal conditions," *Microwave and Optical Technology Letters*, vol. 3, no. 11, pp. 379-382, 1990.

[14] W. Way, "Large signal nonlinear distortion prediction for a single-mode laser diode under microwave intensity modulation," *Journal of Lightwave Technology*, vol. 5, no. 3, pp. 305-315, 1987.

[15] C. Rumelhard, C. Algani and A.-L. Billabert, in *Microwave Photonic Links: Components and Circuits*, Wiley-ISTE, U.K, 2011, pp. 321-363.

[16] S. Zhang, N. Zhu and Y. Liu, "Compact circuit modeling of semiconductor lasers for analog optical link simulations," *Proceeding of SPIE*, vol. 6824, 2007.

[17] S. Ghoniemy, L. MacEachern and S. Mahmoud, "Extended Robust Semiconductor Laser Modeling for Analog Optical Link Simulations," *IEEE Journal of Selected Topics in Quantum Electronics*, vol. 9, pp. 872-878, 2003.

[18] A.-L. Billabert, M. Chtioui, C. Rumelhard, C. Algani, M. Alouini, Q. Levesque, C. Feuillet, A. Marceaux and T. Merlet, "Simulation of Microwave optical links and demonstration of noise figure lower than electrical losses," *International Journal of Microwave and Wireless Technologies*, vol. 2, no. 06, pp. 497-503, 2010.

[19] A.-L. Billabert, Q. Levesque, M. Chtioui, C. Algani, C. Rumelhard, A. Marceaux and T. Merlet, "Comparison of theoretical and measured P1dB of a photonic microwave link :influence of some physical parameters of the DFB laser," in *Annals of telecommunications*, 2012.

[20] A. Bdeoui, A.-L. Billabert, J. Polleux, C. Algani and C. Rumelhard, "A new definition of opto-microwave S-parameters and noise figures for an IM-DD microwave photonic link," in *Proceedings of the European Microwave Association, Special issue on Microwave Photonics II*, 2008.

[21] M. Faugeron, M. Tran, O. Parillaud, M. Chtioui, Y. Robert, E. Vinet, A. Enard, J. Jacquet and F. van Dijk, "High-Power Tunable Dilute Mode DFB Laser With Low RIN and Narrow Linewidth," *IEEE Photonics Technology Letters*, vol. 25, no. 1, pp. 7-10, 2013.

[22] H. Ogawa, D. Polifko and S. Banba, "Millimeter-wave fiber optics systems for personal radio communications," *IEEE transaction on microwave theory and techniques*, vol. 40, no. 12, pp. 2285-2293, 1992.

[23] P. Chanclou, F. Bourgart, B. Landousies, B. Gosselin, B. Charbonnier, N. Genay, A. Pizzinat, F. Saliou, B. Capelle, Q. Trung, F. Raharimanitra, A. Gharba, L. Anet Neto, J. Guillory and B. Le Guyader, "Technical options for NGPON2 beyond 10G PON," in *European Conference and Exposition on Optical Communications (ECOC°*, Geneva, Switzerland, 2011.

[24] K. Garenaux, T. Merlet, M. Alouini, J. Lopez, N. Vodjdani, R. Boula-Picard, C. Fourdin and J. Chazelas, "Recent Breakthroughs in RF Photonics for Radar Systems," *IEEE Aerospace and Electronic Systems Magazine* , vol. 22, no. 2, pp. 3-8, 2007.

[25] B. Walke, R. Seidenberg and M. Althoff, in *UMTS: The fundamentals*, Wiley & Sons, England, 2003.

[26] International Telecommunication Union, "IMT-Advanced (4G) Mobile wireless broadband on the anvil," 2011. [Online]. Available: http://www.itu.int/net/pressoffice/press_releases. [Accessed 1 11 2014].

[27] P. Hatami and A. Yari, "A comparative study of wireless broad band access technologies," in *7th International Symposium on Telecommunications (IST)*, 2014.

[28] International Tlecommunication Union, "Evolution of Wireless Mobile Communication," 2009.

[29] Wi-Fi Alliance, "Wi-Fi CERTIFIED™ n: Longer-Range, Faster-Throughput, Multimedia-Grade Wi-Fi® Networks," 2009. [Online]. Available: http://www.wi-fi.org/file/wi-fi-certified-n-longer-range-faster-throughput-multimedia-grade-wi-fi-networks-2009. [Accessed 1 11 2014].

[30] IEEE 801.15 WPAN Task Group 1, "IEEE 802.15.3 Bluetooth standard for wireless personal area networks," 2002. [Online]. Available: http://ieee802.org/15/pub/ TG1 .html. [Accessed 1 11 2014].

[31] "IEEE 802.15.3 Standard for low rate wireless personal area networks," 2006. [Online]. [Accessed 1 11 2014].

[32] Agilent Technologies, "Wireless LAN at 60 GHz - IEEE 802.11ad Explained : Application Note".

[33] Agilent Technologies, "Wireless LAN at 60 GHz - IEEE 802.11ad," 2013. [Online]. Available: http://cp.literature.agilent.com/litweb/. [Accessed 1 11 2014].

[34] S. Emami, in *UWB Communication Systems: Conventional and 60 GHz Principles, Design and Standards*, Springer, 2013, pp. 1-39.

[35] Federal Communications Commission (FCC), "Revision of Part 15 of the Commission’s Rules Regarding Ultra Wideband Transmission Systems," 2002.

[36] A. Balakrishnan, A. Batra and A. Dabak, "A multi-band OFDM system for UWB communication,," in *Proceedings IEEE Conference on Ultra Wideband Systems and Technologies*, 2003.

[37] Y. Guo, B. Luo, C. Park, L. Ong, M.-T. Zhou and S. Kato, "60 GHz Radio-over-Fiber for Gbps Transmission," in *Global Symposium on GSMM*, 2008.

[38] N. Guo, R. Qiu, S. Mo and K. Takahashi, "0-GHz Millimeter-Wave Radio: Principle,

Technology, and New Results," *EURASIP Journal on Wireless Communications and Networking,* pp. 1-8, 2007.

[39] FTTH Council Europe, "Creating a brighter future," http://www.ftthcouncil.eu/, Stockholm, weden, 2014.

[40] D. Gutierrez, S. Wei-Tao, A. Fu-Tai and S. Kyeong, "Next-Generation Optical Access Networks," *Journal of Lightwave Technology,* vol. 25, no. 11, pp. 1-5, 2007.

[41] A. Seeds and K. Williams, "Microwave Photonics," *Journal of Lightwave Technology,* vol. 24, no. 12, pp. 4628-4641, 2006.

[42] J. Yao, "Microwave Photonics," , vol.27, no.3, pp.314,335, Feb.1, 2009," *Journal of Lightwave Technology,* vol. 27, no. 3, pp. 314-335, 2009.

[43] S. Iezekiel, "Microwave Photonics – an Introductory Overview," in *Microwave Photonics Devices and Applications,* John Wiley & Sons, Ltd, 2009, pp. 3-41.

[44] D. Mynbaev and L. Scheiner, Fiber Optic Communications Technology.

[45] H. Al-Raweshidy and S. Komaki, Radio over Fiber Technology for Mobile Communications Networks, Norwood, MA 06062: Artech House, 2002.

[46] M.-F. Huang, A. Chowdhury, Y.-T. Hsueh, J. Yu and Gee-Kung Chang, "Integration of RoF with WDM-PON for lightwave centralized access networks," in *Opto-Electronics and Communications Conference (OECC),* 2011.

[47] T. Kuri, H. Toda and K. Kitayama, "Radio over fiber: DWDM-based analog/digital access networking and its enabling technologies," in *IEEE Radio and Wireless Symposium*, 2008.

[48] V. Urick, F. Bucholtz, J. McKinney, P. Devgan, A. Campillo, J. Dexter and K. Williams, "Long-Haul Analog Photonics," *Journal of Lightwave Technology,* vol. 29, no. 8, pp. 1182-1205, 2011.

[49] P. Devgan, V. Urick, J. McKinney and K. Williams, "Cascaded Noise Penalty for Amplified Long-Haul Analog Fiber-Optic Links," *IEEE Transactions on Microwave Theory and Techniques,* vol. 55, no. 9, pp. 1973-1977, 2007.

[50] I. A. Edward and H. Charles, "Analogue Microwave Fibre-optic Link Design," in *Microwave Photonics: Devices and Applications*, John Wiley & Sons, Ltd, 2009, pp. 133-169.

[51] D. Novak, A. Nirmalathas, C. Lim and R. Waterhouse, "Fibre Radio Technology," in *Microwave Photonics: Devices and Applications*, John Wiley & Sons, Ltd, 2009, pp. 169-191.

[52] A. Stohr and D. Jager, "Photonic Oscillators for THz Signal Generation," in *Microwave Photonics: Devices and Applications*, John Wiley & Sons, Ltd, 2009, pp.

85-111.

[53] Cox et al., "Limits on the performance of RF-over-fiber links and their impact on device design," *IEEE Transactions on Microwave Theory and Techniques,* vol. 54, no. 2, pp. 906-920, 2006.

[54] L. Kazovsky, J. Fan, T. Fong, R. Kalman, D. Sabido and M. Tabara, "Linewidth-Insensitive Coherent Analog Optical Links," Stanford University, New York, 1994.

[55] O. Kjebon, R. Schatz, S. Lourdudoss, S. Nilsson, B. Stalnacke and L. Backbom, "30 GHz direct modulation bandwidth in detuned loaded InGaAsP DBR lasers at 1.55 μm wavelength," *Electronics Letters,* vol. 33, no. 6, pp. 488-489, 1997.

[56] S. Hwang, J. Liu and J. White, "35-GHz intrinsic bandwidth for direct modulation in 1.3-um semiconductor lasers subject to strong injection locking," *IEEE Photonics Technology Letters,* vol. 16, no. 4, pp. 972-974, 2004.

[57] R.-P. Braun, G. Grosskopf, H. Heidrich, C. von Helmolt, R. Kaiser, K. Kruger, U. Kruger, D. Rohde, F. Schmidt, R. Stenzel and D. Trommer, "Optical microwave generation and transmission experiments in the 12- and 60-GHz region for wireless communications," *IEEE Transactions on Microwave Theory and Techniques,* vol. 46, no. 4, pp. 320 - 330, 1998.

[58] K. Williams, L. Goldberg, R. Esman, M. Dagenais and J. Weller, "6-34 GHz offset phase-locking of Nd:YAG 1319 nm nonplanar ring lasers," *Electronics Letters,* vol. 25, no. 18, pp. 1242-1243, 1989.

[59] F. Fan and M. Dagenais, "Optical generation of a megahertz-linewidth microwave signal using semiconductor lasers and a discriminator-aided phase-locked loop," *IEEE Transactions on Microwave Theory and Techniques,* vol. 45, no. 8, pp. 1296-1300, 1997.

[60] R. Steele, "Optical phase-locked loop using semiconductor laser diodes," *Electronics Letters,* vol. 19, no. 2, pp. 69-71, 1983.

[61] L. Langley, M. Elkin, C. Edge, M. Wale, U. Gliese, X. Huang and A. Seeds, "Packaged semiconductor laser optical phase-locked loop (OPLL) for photonic generation, processing and transmission of microwave signals," *IEEE Transactions on Microwave Theory and Techniques,* vol. 47, no. 7, pp. 1257 - 1264, 1999.

[62] U. Gliese, T. Nielsen, M. Bruun, E. Lintz Christensen, K. Stubkjaer, S. Lindgren and B. Broberg, "A wideband heterodyne optical phase-locked loop for generation of 3-18 GHz microwave carriers," *IEEE Photonics Technology Letters,* vol. 4, no. 8, pp. 936-938, 1992.

[63] J. O'Reilly, P. Lane and M. Capstick, "Optical generation and delivery of modulated mmw-waves for mobile communications," in *Analogue optical fibre communications,* 1995.

[64] R. Ramos and A. Seeds, "Comparison between first-order and second-order optical phase-lock loops," *IEEE Microwave and Guided Wave Letters*, vol. 4, no. 1, pp. 6-8, 1994.

[65] A. M. R. Islam, M. Bakaul, A. Nirmalathas and G. E.Town, "Simplification of millimeter-wave radio-over-fiber system employing heterodyning of uncorrelated optical carriers and self-homodyning of RF signal at the receiver," *Optics Express*, vol. 20, no. 5, pp. 5705-5724, 2012.

[66] I. Insua, D. Plettemeier and C. Schaffer, "Simple Remote Heterodyne Radio-Over-Fiber System for Gigabit Per Second Wireless Access," *Journal of Lightwave Technology*, vol. 28, no. 16, pp. 2289-2295, 201.

[67] S. Mikroulis, M. Thakur and J. Mitchell, "Investigation of a robust remote heterodyne envelope detector scheme for cost-efficient E-PON / 60 GHz wireless integration," in *16th International Conference on Transparent Optical Networks (ICTON)*, 2014.

[68] I. G. Insua, P. T. Manoj and J. E. Mitchell, "Simple Remote Heterodyne Radio-Over-Fiber System for Gigabit Per Second Wireless Access," *Journal of Lightwave Technology*, vol. 28, no. 16, pp. 2289-2295, 2010.

[69] D. Wake, C. Lima and P. Davies, "Optical generation of millimeter-wave signals for fiber-radio systems using a dual-mode DFB semiconductor laser," *IEEE Transactions on Microwave Theory and Techniques*, vol. 43, no. 9, pp. 2270-2276, 1995.

[70] T. Nagatsuma, A. Hirata, N. Shimizu, H.-J. Song and N. Kukutsu, "Photonic generation of millimeter and terahertz waves and its applications," in *19th International Conference on Applied Electromagnetics and Communications*, 2007.

[71] S. Ginestar, F. Van Dijk, A. Accard, F. Poingt, F. Pommereau, L. Le Gouezigou, O. Le Gouezigou, F. lelarge, B. Rousseau, J. Landreau, J.-P. Vilcot and G.-H. Duan, "Tunable dual-mode DFB laser for millimetre-wave signal generation," *The European Physical Journal Applied Physics*, vol. 53, no. 03, p. 33609, 2011.

[72] A. Hirata, M. Harada, K. Sato and T. Nagatsuma, "Millimeter-wave photonic wireless link using low-cost generation and modulation techniques," in *International Topical Meeting on Microwave Photonics*, 2002.

[73] Y. zhang, K. Xu, R. Zhu, J. Li, J. Wu, X. Hong and Jintong Lin, "Photonic Generation of M-QAM/M-ASK Signals at Microwave/Millimeter-Wave Band Using Dual-Drive Mach–Zehnder Modulators With Unequal Amplitudes," *Journal of Lightwave Technology*, vol. 26, no. 15, pp. 2604-2610, 2008.

[74] G. H. Nguyen, B. Cabon and Y. Le Guennec, "Generation of 60-GHz MB-OFDM Signal-Over-Fiber by Up-Conversion Using Cascaded External Modulators," *Journal of Lightwave Technology*, vol. 27, no. 11, pp. 1496-1502, 2009.

[75] U. Gliese, S. Norskov and T. Nielsen, "Chromatic dispersion in fiber-optic microwave and millimeter-wave links," *IEEE Transactions on Microwave Theory and Techniques,* vol. 44, no. 10, pp. 1716-1724, 1996.

[76] G. Nguyen, V. Dobremez, B. Cabon and Y. Le Guennec, "Optical Techniques for Up-Conversion of MB-OFDM Signals in 60 Ghz Band Using Fiber Bragg Grating," in *IEEE International Conference on Communications*, 2009.

[77] T. Shao, "Study of Converged 60 GHz Radio over Fiber with WDM-PN Access Networks," PhD. Dessertation, Université de Grenoble, 2012.

[78] L. A. Coldren and S. W. Corzine, Diode Lasers and Photonic Integrated Circuits, New York: John Wiley & Sons, inc, 1995.

[79] G. P. Agrawal, "Optical Transmitters," in *Fiber-Optic Communication Systems*, John Wiley & Sons, 2002, p. 108.

[80] G. Agrawal and N. Dutta, "Long-wavelength Semiconductor Lasers," in *Long-wavelength Semiconductor Lasers*, New York, Van Nostrand Reinhold, 1986.

[81] J. Chen, R. Ram and R. Helkey, "Linearity and third-order intermodulation distortion in DFB semiconductor lasers," *IEEE Journal of Quantum Electronics,* vol. 35, no. 8, pp. 1231-1237, 1999.

[82] G. Agrawal, "Effect of gain and index nonlinearities on single-mode dynamics in semiconductor lasers," *IEEE Journal of Quantum Electronics,* vol. 26, no. 11, pp. 1901-1909, 1990.

[83] M.-S. Lin, S.-Y. Wang and N. Dutta, "Measurements and modeling of the harmonic distortion in InGaAsP distributed feedback lasers," *IEEE Journal of Quantum Electronics,* vol. 26, no. 6, pp. 998-1004, 1990.

[84] R. Tucker and I. Kaminow, "High-frequency characteristics of directly modulated InGaAsP ridge waveguide and buried heterostructure lasers," *Journal of Lightwave Technolog,* vol. 2, no. 4, pp. 385-393, 1984.

[85] P. Mena, S.-M. S. Kang and T. DeTemple, "Rate-equation-based laser models with a single solution regime," *Journal of Lightwave Technology*, vol. 15, no. 4, pp. 717-730, 1997.

[86] D. Channin, "Effect of gain saturation on injection laser switching," *Journal of Applied Physics,* vol. 50, no. 6, pp. 3858-3860, 1979.

[87] H.-T. Lin and Yao-Huang Kao, "Nonlinear distortions and compensations of DFB laser diode in AM-VSB lightwave CATV applications," *Journal of Lightwave Technology,* vol. 14, no. 11, pp. 2567-2574, 1996.

[88] T. Keating, X. Jin, S. -L. Chuang and K. Hess, "Temperature dependence of electrical and optical modulation responses of quantum-well lasers," *IEEE Journal of*

Quantum Electronics, vol. 35, no. 10, pp. 1526-1534, 1999.

[89] R. Nagarajan, M. Ishikawa, T. Fukushima, R. S. Geels and J. Bowers, "High speed quantum-well lasers and carrier transport effects," *IEEE Journal of Quantum Electronics*, vol. 28, no. 10, pp. 1990- 2008, 1992.

[90] L. A. Coldren and S. W. Corzine, "Dynamic Effects," in *Diode Lasers and Photonic Integrated Circuits*, John Wiley & Sons, Inc., 1995, p. 241.

[91] C. H. Henry, "Phase Noise in Semiconductor Lasers," *Journal of Lightwave Technology*, vol. 4, no. 3, pp. 298,311, 1986.

[92] K. Kikuchi, "Effect of 1/f-type FM noise on semiconductor-laser linewidth residual in high-power limit," *IEEE Journal of Quantum Electronics*, vol. 25, no. 4, pp. 684-688, 1989.

[93] M. Fukuda, T. Hirono, T. Kurosaki and F. Kano, "1/f noise behavior in semiconductor laser degradation," *IEEE Photonics Technology Letters*, vol. 5, no. 10, pp. 1165-1167, 1993.

[94] A. Dandridge and H. Taylor, "Correlation of Low-Frequency Intensity and Frequency Fluctuations in GaAlAs Lasers," *IEEE Journal of Quantum Electronics*, vol. 30, no. 1726,1738, pp. 1726-1738, 1982.

[95] A. Bdeoui, A.-L. Billabert and C. Rumelhard, "Direct modulation of a laser by a microwave signal: A model for 1/f amplitude and phase noises," in *European Microwave Conference*, 2003.

[96] F.N. Hooge, ""“The relation between 1/f noise and number of electrons”, Physica B, 162, pp. 344-352, 1990.," *Physica*, vol. B, no. 162, pp. 344-352, 1990.

[97] F. Hooge, "1/f noise sources," *IEEE Transactions on Electron Devices*, vol. 41, no. 11, pp. 1926-1935, 1994.

[98] R. Nagarajan, M. Ishikawa, T. Fukushima, R. S. Geels and J. Bowers, "High speed quantum-well lasers and carrier transport effects," *IEEE Journal of Quantum Electronics*, vol. 28, no. 10, pp. 1990 - 2008, 1992.

[99] K. Sum and N. Gomes, "Microwave-optoelectronic modelling approaches for semiconductor lasers," *IEE Proceedings - Optoelectronics*, vol. 145, no. 3, pp. 141-146, 1998.

[100] I. Habermayer, "Nonlinear circuit model for semiconductor lasers," *Optical and Quantum Electronics*, vol. 13, pp. 461-468, 1981.

[101] R. S. L.V. Asryan, "Temperature dependence of the threshold current density of a quantum dot laser," *IEEE Journal of Quantum Electronics*, vol. 34, no. 5, pp. 841-850, 1998.

[102] J. Hu, A. Nkansah, N. Gomes, M. Zhao and Gu,, "Phase Noise Effects on Directly Modulated 64-QAM OFDM Radio-over-Fiber Systems," in *Microwave Photonics, 2011 International Topical Meeting on & Microwave Photonics Conference*, 2011.

[103] S. Singla and K. Arya, "SNR Analysis of RoF Systems based on 64-QAM Including the Impact of Dispersion and Phase noise," *International Journal of Computer Applications*, vol. 40, no. 2, pp. 37-40, 2012.

[104] L. A. and S. W. Corzine, "Gain and Current Relations," in *Diode Lasers and Photonic Integrated CircuitsColdren*, John Wiley & Sons, Inc., 1995, p. 139.

[105] J. Wang and K. Petermann, "Small Signal Analysis for Dispersive Optical. Journal of Lightwave Technology," *Journal of Lightwave Technology*, vol. 10, no. 1, pp. 96-100, 1992.

[106] IEEE Std 1139-1999, "IEEE Standard Definitions of Physical Quantities for Fundamental Frequency and Time Metrology - Random Instabilities," 1999.

[107] S. &. F. V. Camatel, "Narrow Linewidth CW Laser Phase Noise Characterization Methods for Coherent," *Journal of Lightwave Technology*, vol. 26, no. 17, p. 3048–3055, 2008.

[108] Llopis et al., "Phase noise measurement of a narrow linewidth CW laser using delay line approaches," *Optics Letters*, vol. 36, no. 14, pp. 2713-2715, 2011.

[109] R. Scott, C. Langrock and B. Kolner, "High-dynamic-range laser amplitude and phase noise measurement techniques," *IEEE Journal of Selected Topics in Quantum Electronics*, vol. 7, no. 4, pp. 641-655, 2001.

[110] F. M. D. M. V. Rizzoli, "General noise analysis of nonlinear microwave circuits by the piecewise harmonic-balance technique," *IEEE Trans. Microwave Theory and Techniques*, vol. 42, no. 5, pp. 807-819, 1994.

[111] G. P. Agrawal., in *Lightwave Technology: Components and Devices.* , New Jersey, USA, JohnWiley & Sons, Inc,, 2005.

[112] A. Carena, "Modulation Formats for Optical Communications," optcom.polito.it, Torino, Italy, 2009.

[113] Photline Technologies, "MX-LN Series Lithium Niobate Intensity Modulators," http://www.lasercomponents.com/.

[114] Z. Abdallah, A. Rumeau, A. Fernandez, G. Cibiel and O. Llopis, "Nonlinear Equivalent-Circuit Modeling of a Fast Photodiode," *IEEE Photonics Technology Letters*, vol. 26, no. 18, pp. 1840-1842, 2014.

[115] G. Ghione, "Detectors," in *optoelectronics, Semiconductor devices for high-speed*, New York, Cambridge University Press, 2009, pp. 189-199.

[116] A. Madjar, N. Koka, J. Bloch, P. Yu, A. Stoehr and D. Jaeger, "A Novel Analytical Model as a Design Tool for Uni-Traveling-Carrier Traveling Wave Photo Detectors Approaching 1 THz," *IEEE Transactions on Microwave Theory and Techniques,* vol. 57, no. 1, pp. 223-230, 2009.

[117] A. Stohr, S. Babiel, P. Cannard, B. Charbonnier, F. Van-Dijk, S. Fedderwitz, D. Moodie, L. Pavlovic, L. Ponnampalam, C. C. Renaud, D. Rogers, V. Rymanov, A. Seeds, A. Steffan, A. Umbach and M. Weiss, "Millimeter-Wave Photonic Components for Broadband Wireless Systems," *IEEE Transactions on Microwave Theory and Techniques,* vol. 58, no. 11, pp. 3071-3082, 2010.

[118] E. Rouvalis, C. C. Renaud, D. G. Moodie, M. J. Robertson and A. J. Seeds, "Traveling-wave Uni-Traveling Carrier Photodiodes for continuous wave THz generation," *Optics Express,* vol. 18, no. 11, pp. 11105-11110, 2010.

[119] J. Gao, B. Gao and C. Liang, "A PIN PD microwave equivalent circuit model for optical receiver design," *Microwave and Optical Technology Letters,* vol. 38, no. 2, pp. 102-104, 2003.

[120] G. Wang, T. Tokumitsu, I. Hanawa, Y. Yoneda, K. Sato and M. Kobayashi, "A time-delay equivalent-circuit model of ultrafast p-i-n photodiodes," *IEEE Transactions on Microwave Theory and Techniques,* vol. 51, no. 4, pp. 1227-1233, 2003.

[121] C. Fritsche and V. Krozer, "Large-signal PIN diode model for ultra-fast photodetectors," *European Microwave Conference,* vol. 2, pp. 4-6, 2005.

[122] Emcore Corporation, "Microwave packaged photodiode," www.emcore.com, 2011.

[123] C. Lethien, C. Loyez and J.-P. Vilcot, "Potentials of radio over multimode fiber systems for the in-buildings coverage of mobile and wireless LAN applications," *IEEE Photonics Technology Letters,* vol. 17, no. 12, pp. 2793-2795, 2005.

[124] D. Wake and D. Moodie, "Passive Picocell - Prospects For Increasing The Radio Range," in *International Topical Meeting on Microwave Photonics*, 1997.

[125] L. Anet Neto, D. Erasme, N. Genay, P. Chanclou, Q. Deniel, F. Traore, T. Anfray, R. Hmadou and C. Aupetit-Berthelemot, "Simple Estimation of Fiber Dispersion and Laser Chirp Parameters Using the Downhill Simplex Fitting Algorithm," *Journal of Lightwave Technology,* vol. 31, no. 2, pp. 334-342, 2013.

[126] C. H. COX, in *ANALOG OPTICAL LINKS Theory and Practice*, New York, cambridge university press, 2004.

[127] C. H. Cox, "Noise in Links," in *Analog Optical Links Theory and Practice*, Cambridge University Press, 2006, pp. 159-199.

[128] M. Chtioui, C. Feuillet, N. Massad, A. Vidal, J. Louardi, M. Faugeron, F. van Dijk, M. Tran, Y. Robert, E. Vinet, M. Achouche, F. Lelarge, M. Biet, E. Grard, V. Rodrigues, J.-R. Burie, F. Laruelle and A. Marceaux, "Analog microwave photonic

link based on a high power directly modulated laser, a high power photodiode and passive impedance matching," in *International Topical Meeting on Microwave Photonics (MWP),* 2012.

[129] R. Kalman, J. Fan and L. Kazovsky, "Dynamic range of coherent analog fiber-optic links," *Journal of Lightwave Technology,* vol. 12, no. 7, p. 1263, 1994.

[130] S. Ryu, "Receiver Sensitivity Characteristics in Coherent Detection," in *Coherence Lightwave Communication Systems,* London, Artech House, 1995, pp. 41-73.

[131] W. Stephens and T. Joseph, "System characteristics of direct modulated and externally modulated RF fiber-optic links," *Journal of Lightwave Technology,* vol. 5, no. 3, pp. 380-387, 1987.

[132] R. Ram and Helkey, "Linearity and third-order intermodulation distortion in DFB semiconductor lasers," *IEEE Journal of Quantum Electronics,* vol. 35, no. 08, p. 1231–1237, 1999.

[133] M.-B. Bibey, F. Deborgies, M. Krakowski and D. Mongardien, "Very Low Phase-Noise Optical Links—Experiments and Theory," *IEEE Transactions on Microwave Theory and Techniques,* vol. 47, no. 12, pp. 2257-2262, 1999.

[134] V. Rizzoli, F. Mastri and D. Masotti, "General noise analysis of nonlinear microwave circuits by the piecewise harmonic-balance technique," *IEEE Transaction in Microwave Theory and Techniques,* vol. 42, no. 5, pp. 807-819, 1994.

[135] T. Kuri and K. Kitayama, "Laser phase noise free optical heterodyne detection technique for 60-GHz-band radio-on-fiber systems," Microwave Photonics," in *International Topical Meeting on MWP*, 2000.

[136] R. Steed, et al., "Monolithically integrated heterodyne optical phase-lock loop with RF XOR phase detector," *Optics Express,* vol. 19, no. 2, pp. 20048-20053, 211.

[137] M. H. Shahine , "DFB Laser Diode Dynamics with Optoelectronic Feedback, Semiconductor Laser Diode Technology and Applications," in *Semiconductor laser Diode: Technology and Applications*, USA, Intech, 2012, pp. 89-118.

[138] N. Satyan, W. Liang and A. Yariv, "Coherence Cloning Using Semiconductor Laser Optical Phase-Lock Loops," , vol.45, no.7, pp.755,761, July 2009," *IEEE Journal of Quantum Electronics,* vol. 45, no. 7, p. 755, 2009.

[139] N. J. Gomes, M. Morant, A. Alphones, B. Cabon, J. E. Mitchell, C. Lethien, M. Csornyei, A. Stohr and S. Iezekiel, "Radio-over-fiber transport for the support of wireless broadband services," *Journal of Optical Networking,* vol. 8, no. 2, pp. 156-178, 2009.

[140] D. Wake, A. Nkansah and N. Gomes, "Radio Over Fiber Link Design for Next Generation Wireless Systems," *Journal of Lightwave Technology,* vol. 28, no. 16, pp.

2456-2464, 2010.

[141] J. owarth, A. Lauterbach, M. Boers, L. Davis, A. Parker, J. Harrison, J. Rathmell, M. Batty, W. Cowley, C. Burnet, L. Hall, D. Abbott and N. Weste, "60GHz Radios: Enabling Next-Generation Wireless Applications," in *IEEE Region TENCON*, 2005.

[142] C. Anderson and T. Rappaport, "In-building wideband partition loss measurements at 2.5 and 60 GHz," *IEEE Transactions on Wireless Communications,* vol. 3, no. 3, pp. 922-928, 2004.

[143] H. Xu, V. Kukshya and T. Rappaport, "Spatial and temporal characteristics of 60-GHz indoor channels," *IEEE Journal on Selected Areas in Communications,* vol. 20, no. 3, pp. 620 - 630, 2002.

[144] P. H. Moose, "A technique for orthogonal frequency division multiplexing frequency offset correction," *IEEE Transactions on Communications,* vol. 42, no. 10, pp. 2908-2914, 1994.

[145] A. G. Armada, "Understanding the effects of phase noise in orthogonal frequency division multiplexing (OFDM)," *IEEE Transactions on Broadcasting,* vol. 47, no. 2, pp. 153-159, 2001.

[146] S. Wu and Y. Bar-Ness, "OFDM systems in the presence of phase noise: consequences and solutions," *IEEE Transactions on Communications,* vol. 52, no. 11, pp. 1988-1996, 2004.

[147] Keysight Technologies, "Phase Noise and OFDM: Adding the Right Amount in the Right Place," 10 December 2013. [Online]. Available: http://rftest.blogs.keysight.com/2013/12/phase-noise-and-ofdm-adding-the-right-amount-in-the-right-place/. [Accessed 19 March 2015].

[148] B. Dusza, K. Daniel and C. Wietfeld, "Error Vector Magnitude Measurement Accuracy and Impact on Spectrum Flatness Behavior for OFDM-Based WiMAX and LTE Systems," Wireless Communications, Networking and Mobile Computing ", 2009. WiCom '09. 5th International," in *International Conference on Wireless Communications Networking and Mobile Computing*, 2009.

[149] ecma INTERNATIONAL, "High rate 60 GHz PHY, MAC and PALs," 2010.

[150] R. Shafik, S. Rahman and R. Islam, "On the Extended Relationships Among EVM, BER and SNR as Performance Metrics," *International Conference on Electrical and Computer Engineering,* pp. 408-411, 2006.

[151] A. Georgiadis, "Gain, phase imbalance, and phase noise effects on error vector magnitude," *IEEE Transactions on Vehicular Technology,* vol. 53, no. 2, pp. 443-449, 2004.

[152] A. Nassery, S. Ozev, M. Verhelst and M. Slamani, "Extraction of EVM from Transmitter System Parameters," in *16th IEEE European Test Symposium (ETS),*

2011.

[153] Y. Wang, K. Gong and Zhaowu Chen, "Theoretical Analysis of Performance Degradation Due to Phase Noise and I/Q Imbalance in MQAM-OFDM Systems," in *IEEE International Conference on Communications*, 2008.

[154] WiMedia Alliance, "WiMedia PHY Test specification," 18 Dec. 2007. [Online]. Available: www.wimedia.org.

[155] M. I. a. K. P. S. M. I. Jianmin Wang, "Small Signal Analysis for Dispersive Optical," *Journal of Lightwave Technology,* vol. 10, no. 1, pp. 96-100, 1992.

[156] J. Yao, "Microwave Photonics," *Journal of Lightwave Technology*, vol. 27, no. 3, pp. 314-335, 2009.

[157] J. Yu and et. al, "Cost-effective optical millimeter technologies and field demonstrations for very high throughput wireless-over-fiber access systems," *Journal of Lightwave Technology*, vol. 28, no. 16, pp. 2376-2397, 2010.

[158] D. Jäger, R. Heinzelmann and A. Stohr, "Microwave Optical Interaction Devices: From Concept to Applications," in *30th European Microwave Conference*, 2000.

[159] J. Laskar, S. Pinel, s. Sarkar and P. Sen, "The Next Wireless Wave is a millimeter wave," in *Microwave Journal, vol 50, no. 8, p. 22*, 2007.

[160] R. Gaudiono, D. Cardenas, C. B. Bellec, M., N. Evanno, P. Guignard, S. Meyer, A. Pizzinat, I. Mollers and D. Jager, "Perspective in next-generation home networks: Towards optical solutions?," *IEEE communication Magazine,* vol. 48, no. 2, pp. 39-47, 2010.

[161] S. Keyvaninia, S. Verstuyft, L. Van Landschoot, D. Van Thourhout, G. Roelkens, G.-H. Duan, F. Lelarge, J.-M. Fedeli, S. Messaoudene, T. De Vries, E. Geluk, B. Smalbrugge and M. Smit, "III-V/silicon first order distributed feedback lasers integ," in *European Conference and Exhibition on Optical Communication (ECOC)*, Munich, Germany, 2013.

[162] K. Vahala and A. Yariv, "Semiclassical theory of noise in semiconductor lasers: Part II," *IEEE Journal of Quantum Electronics*, vol. 19, no. 6, pp. 1096-1101, 1983.

[163] C. C. Wei and J. J. Chen, " Study on dispersion-induced phase noise in an optical OFDM radio-over-fiber system at 60-GHz band," *Optics Express*, vol. 18, no. 20, pp. 20774-85, 2010.

[164] J. Maeda, T. Katoh and S. Ebisawa, "Effect of Fiber Dispersion on Subcarrier QAM Signal in Radio-Over-Fiber Transmission," *Journal of Lightwave Technology*, vol. 30, no. 16, pp. 2625-2632, 2012.

[165] Kassa, W.; Billabert, A.; Faci, S.; Algani, C., "Electrical Modeling of Semiconductor Laser Diode for Heterodyne RoF System Simulation,"," *IEEE Journal of Quantum*

Electronics, vol. 49, no. 10, pp. 894-900, 2013.

[166] IEEE-SA Standards Board, "IEEE Standard Definitions of Physical Quantities for Fundamental Frequency and Time Metrology— Random Instabilities," Institute of Electrical and Electronics Engineers, Inc, Printed in the United States of America, 1999.

[167] Anthony, "Radio over Fiber Technology for broadband wireless communication," PhD Thesis, Technische Universiteit Eindhoven, The Netherlands, 2005.

[168] "Understanding the effects of phase noise in orthogonal frequency division multiplexing (OFDM)," *IEEE Transactions on Broadcasting*, vol. 47, no. 2, pp. 153-159, 2001.

LIST OF PUBLICATIONS

International Journal papers

W-E.Kassa, A-L.Billabert, S.Faci, C.Algani, « Simulation of heterodyne RoF systems based on 2 DFB lasers: application to an optical phase locked loop design » Int. J. Microw. and Wireless Technologies, Vo. 6, Issue 02, 2013, pp. 207-211.

W-E.Kassa, A-L.Billabert, S.Faci, C.Algani, « Electrical Modeling of Semiconductor Laser Diode for Heterodyne RoF System Simulation », IEEE Journal of Quantum Electronics, Vol. 49, Issue 10, 23 July 2013, pp. 894–900.

International conference proceedings

W-E.Kassa, S.Faci, A-L.Billabert, C.Algani, « Equivalent Circuits of Heterodyne Radio-over-Fiber for Transmission of Wireless Signals in the 60GHz Band » ISMOT 2015, 15th International Symposium on Microwave and Optical Technology, 29 june- 1st july, Dresden, Germany.

W-E.Kassa, S.Faci, A-L.Billabert, C.Algani, « Optical Phase Noise Modeling for Heterodyne Radio over Fiber Systems », EuMW'2014, European Microwave Conference, 5-10 october 2014, Rome, Italie.

A-L.Billabert, S.Faci, A.Kabalan, **W.E.Kassa**, C.Algani, « Advanced photonic components modelling for RoF link design », ICTON 2015, Budapest, 9 july 2014

A-L.Billabert, S.Faci, **W.E.Kassa**, A.Kabalan, C.Algani, « Electrical simulation of RoF systems for telecommunication and defense applications », Comité de management de l'action COST (European Cooperation in Science and Technology) IC1101 OPTICWISE (Optical Wireless Communications-An emerging technology), Graz, Autriche, 7-9 july 2014.

National conferences

W.E.Kassa, A-L.Billabert, S.Faci, C.Algani, « Electrical Simulation of Radio over Fiber Systems », Journée du Club Optique et Microondes de la Société Française d'Optique, 19 juin 2014, Lannion, France.

W.E.Kassa, A-L.Billabert, S.Faci, C.Algani, « Phase Noise Simulation of Semiconductor Laser » Association du Réseau Micro-ondes d'Ile de France (AREMIF), Février 2013, Paris.

W.E.Kassa, A-L.Billabert, S.Faci, C.Algani, « Modélisation de bruit de phase des lasers à semi-conducteur pour les communications optiques ultra haut débit », 18ème journées nationales microondes, JNM'2013, Paris - Mai 2013.